Optimising the transformation and yield to ultimate strength ratio of Nb-Ti micro-alloyed low carbon line pipe steels through alloy and microstructural control

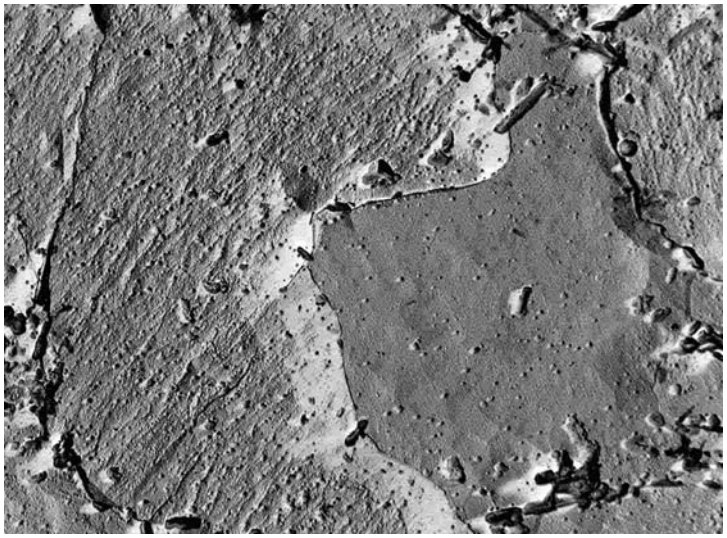

By Zhenghua Tang

Submitted in partial fulfilment of the requirements for the degree

Philosophiae Doctor (Metallurgical Engineering)

in the

Department of Materials Science and Metallurgical Engineering

Faculty of Engineering, Built Environment and Information Technology

University of Pretoria

Republic South Africa

22 May 2006

To my daughter Mingyi

谨此献给我的女儿唐铭艺

Acknowledgments

Firstly, I would like to express my sincere gratitude and appreciation to Professor Waldo Stumpf* for his supervision, invaluable guidance and discussions and professor Chris Pistorius, Head of Department, and the University of Pretoria for the provision of facilities and financial support.

*Membership of national and international bodies:

- Fellow of the South African Academy of Engineering
- Past Chairman of the UN-International Atomic Energy Agency's Standing Advisory Group on Technical Assistance and Co-operation (SAGTAC) in Vienna for the years 2002 to 2005
- Past Member of an Expert Group of the UN-IAEA in 2004/2005 on the non-proliferation considerations of Multi-National Arrangements on Uranium enrichment and spent fuel reprocessing
- Past Honorary President of the South African Branch of the Institution of Nuclear Engineers

I would like to specially thank the following kind people:

Dr N.G. van den Bergh for technical support in shadowing replicas.

Professor G.T.van Rooyen for useful discussions and technical support in the tensile tests.

Mr CF van der Merwe for technical support in much of the work on transmission electron microscopy.

Mr Charl Smal for technical support in tensile tests and others.

Mr Johann Borman for his assistance before his untimely death.

I also wish to thank

Dr Kevin Banks for providing materials for the alloys and making many helpful suggestions.

Mr Francois Verdoorn for training on the Gleeble and Dilatometer.

Mrs Havenga Sarah for her assistance in administrative matters.

Mr Charles Siyasiya for his assistance in editing my English.

I would like also to thank others who gave me assistance.

The provision of financial support from Mittal Steel SA and the NRF through the THRIP program is also greatly appreciated.

Finally, I would like to also specially thank my wife and my daughter Mingyi for they gave me a wonderful and memorable life of four years in far SA and, for their assistance and encouragement.

致谢

首先,我要衷心的感谢我的导师, 南非工程院院士, 2002-2005 维也纳联合国原子能机构技术支持与协助顾问团主席, 2004/2005 联合国多国铀废料回收专家组成员,核工程协会南非分会前名誉主席, 比勒陀利亚大学教授, Stumpf 先生对我的精心指导! 和比勒陀利亚大学材料科学与冶金工程系主任 Pistorius 教授以及大学所给予的设备和资金方面的支持!

特别感谢如下的南非友好人士:

N.G. van der Berg 博士在电镜投影复型方面的技术支持;

G.T.van Rooyen 教授的有益讨论和特殊拉伸试验方面的帮助;

CF van der Merwe 先生在透射电镜实验方面提供的方便;

Charl Smal 先生在拉伸试验和其他方面的帮助;

Johann Borman 先生生前非常友好的帮助;

还要感谢

Kevin Banks 博士提供了实验所需的材料及一些有益的建议;

Verdoorn Francois 先生在 Gleeble 和 Dilatometer 的培训;

Havenga Sarah 女士在行政事务方面的帮助;

Mr Charles Siyasiya 在校正英语方面的帮助;

以及其他给予帮助的人士;

还要感谢南非 Mittal 钢公司及 THRIP 项目所给予的资金支持;

此外,我特别要感谢我的妻子和女儿陪伴我在遥远的南非度过了令我终身难忘的非常快乐的四年海外生活，同时她们也给了我无数的帮助和鼓励。

Optimising the transformation and yield to ultimate strength ratio of Nb-Ti micro-alloyed low carbon line pipe steels through alloy and microstructural control

by Zhenghua Tang (唐正华)

Supervisor: Professor Waldo Stumpf
Department: Materials Science and Metallurgical Engineering
University: University of Pretoria
Degree: Philosophiae Doctor

Abstract

Thinner walled (about 6 mm thickness) line pipe steels for smaller diameter pipelines tend to have a relatively high ratio of yield strength to ultimate tensile strength (YS/UTS) of 0.93 or higher. This study focused on the effect of the microstructures, prior deformation in the austenite, cooling rate, coiling simulation and the additions of some micro-alloying elements on the YS/UTS ratio of a currently produced Nb-Ti and some experimental Nb-Ti-Mo line pipe steels. The experimental research included the design of the chemical compositions for five experimental alloys, simulation of the controlled hot rolling process, the determination of the strain-free as well as the strain affected continuous cooling transformation (CCT) diagrams, phase identification and quantitative assessment of the microstructures by optical microscopy, scanning electron microscopy (SEM) and transmission electron microscopy (TEM), the latter especially on shadowed carbon extraction replicas and, tensile tests etc.

This study indicated that the transformed microstructures of the alloys were a mixture of acicular ferrite plus polygonal ferrite and the volume fraction of acicular ferrite varied from 46.3 to 55.4%. Molybdenum additions did not markedly affect the

formation of acicular ferrite after hot rolling and rapid cooling. The microstructural details of the acicular ferrite were successfully revealed by TEM on shadowed extraction replicas. This technique was useful to distinguish the acicular ferrite from the polygonal ferrite through a more smooth surface relief after etching in 2% Nital of the little etched polygonal ferrite whereas the deeper etched acicular ferrite showed parallel sets of internal striations. This made it possible to measure the volume fraction of acicular ferrite in the mixed microstructures of acicular ferrite and polygonal ferrite.

The continuous cooling transformation behaviors of two alloys with no molybdenum and with 0.22% Mo were constructed with no prior deformation as well as with prior deformation of the austenite. Molybdenum additions shifted the strain-free CCT diagram towards longer times and expanded the region in which acicular ferrite formed from a cooling rate range of 0.3 to 5 $^{o}Cs^{-1}$ (Mo-free) to 0.1 to 15 $^{o}Cs^{-1}$ (with 0.22% Mo). However, its effect was significantly overshadowed by prior deformation in the austenite. The strain affected CCT diagrams for both alloys appear to be similar. The prior deformation had a stronger effect on the CCT diagram than molybdenum additions and promoted acicular ferrite formation, whereas it suppressed the formation of bainite. The prior deformation had two effects in acicular ferrite formation: it promoted nucleation and suppressed its growth and, therefore, resulted in a finer overall grain size.

The effect on the YS/UTS ratio at various cooling rates ranging from 1 to 34, 51, 54 or 60 $^{o}Cs^{-1}$ was investigated in three cases: (i) without prior deformation and coiling simulation, (ii) with no prior deformation but with coiling simulation at 575 and 600 ^{o}C and, (iii) with prior deformation of 33% reduction in the austenite below the T_{nr} followed by coiling simulation at 575 ^{o}C for 1 hour. It was determined that the YS/UTS ratio was a function of the microstructure and cooling rate in the case (treatment (i)) without any coiling simulation and prior deformation. The coarse bainite or acicular ferrite, which was formed at high cooling rates, raised the YS/UTS ratio under conditions of no deformation prior to the transformation. The yield strength and ultimate tensile strength also increased with an increase in cooling rate.

With coiling conditions (treatment (ii)), the ratio was not sensitive to the cooling rate or the microstructure for the reference Mo-free alloy #6 because the coiling allows recovery of dislocations, thereby decreasing the difference in dislocation density that had arisen between a low and a high cooling rate. The YS/UTS ratio ranged from 0.75 to 0.8 after a simulated coiling at 575 ºC and from 0.76 to 0.78 after a coiling simulation at 600 ºC.

Prior deformation (treatment (iii)) in the austenite raised the ratio from 0.81 to 0.86. However, the YS/UTS ratio was not sensitive to cooling rate after coiling at 575 ºC for 1 hour in the cases with and without prior deformation in the austenite. Deformation with a 33% reduction below the T_{nr} prior to the transformation increased the yield strength more than the ultimate tensile strength, leading to a high YS/UTS ratio that ranged from 0.81 to 0.86. The prior deformation, therefore, had a stronger effect on the YS/UTS ratio than the microstructure.

Key words:
line pipe steel, acicular ferrite, microstructure, ratio of yield strength to ultimate tensile strength,, Nb-Ti micro alloyed steel, controlled hot rolling process, CCT diagram, non-recrystallisation temperature, nucleation of acicular ferrite

Table of Contents

List of figures:

List of tables:

CHAPTER 1 INTRODUCTION

The demand for high-performance line pipe steels has resulted in extensive research being conducted towards increasing, firstly, performance of high-strength low alloy steels (HSLA) and secondly, to improve large diameter forming processes to increase the capacity of pipelines used at higher operating pressures. The trends in the technology of line pipe are towards the use of thinner wall thicknesses and UOE pipe-forming, (plate-U-forming-O-bending and shrinking-E-expanding). These demands include the introduction of higher strength and higher toughness steels with lower ductile-to-brittle transition temperatures and higher impact energies. The grades of line pipe steels have, therefore, been developed from X65 grade towards X80 and X100 to meet these requirements.

1.1 Strengthening mechanisms in line pipe steels

The main strengthening mechanisms used in line pipe steels are strengthening by solid solution hardening, by dislocation substructure, by phase transformation strengthening, by precipitation hardening and by grain refinement. The solid solution strengthening result from elements such as manganese and molybdenum, the phase transformation from lower transformation temperature phases such as acicular ferrite and bainitic ferrite or martensite, resulting in finer microstructures with a higher dislocation density. On account of the micro-alloying element additions, carbonitrides of vanadium, niobium and titanium contribute to the precipitation strengthening. Besides dispersion hardening niobium has an added benefit on the refinement of the ferrite grains. Higher pass strains below the non-recrystallisation temperature during the controlled rolling process, also contributes to good ferrite grain refinement.

1.2 Chemical composition of line pipe steels

A special alloying design philosophy is used for line pipe steels. Micro-alloying element additions are necessary to obtain the high strengths, and raise the temperature

above which complete recrystallisation during hot rolling occurs and the recrystallisation of austenite is, therefore, retarded below this temperature. Generally speaking, the relatively low levels of the main chemical elements contribute to a low carbon equivalent (CE) for good weldability, and approximately an 0.15% total micro-alloying element content of vanadium + niobium + titanium is usual[1]. The micro-alloying elements may be only one of these three or a combination of any two or three of the micro-additions (V, Nb and Ti). Molybdenum and niobium are beneficial to the formation of acicular ferrite and they suppress the formation of pearlite[2, 3, 4]. Boron additions are used to form bainitic ferrite and also to suppress the formation of pearlite. Lower carbon contents (below 0.05% or less) are considered to improve weldability, increase the toughness, form less pearlite and increase the strength due to more effective dissolution of niobium.

1.3 Steel making of line pipe steel

The main steel-making procedure for line pipe steels is a combination of converter blowing and ladle treatment[5] or the Electric Arc Furnace (EAF) or the Basic Oxygen Furnace (BOF) route. The cleanliness of the steel and the optimum chemical composition are important for obtaining the specified properties of the line pipe. The main considerations concerning the cleanliness of the steel are the requirements for a low sulphur content for high fracture toughness of the pipe body and the avoidance of clustered alumina inclusions in the vicinity of the weld line. CaSi ladle injection treatment (~0.8 kg/t [2] is often added for this purpose) is vital to reduce the sulphur content and to change the type and morphology of sulphide inclusions. The preferred inclusion composition and morphology is generated when the Ca:Al ratio in the steel is about 0.20[2]. The inclusion shape is also controlled by Ti and rare earth element additions. Vacuum degassing is another method to reduce the impurity content of these steels.

1.4 The controlled rolling of strip steel

The continuously-cast slab is processed after melting by Electric Arc Furnace (EAF) or the Basic Oxygen Furnace (BOF). The major production route of strip for line pipe steels is that of controlled rolling and is most effective with line pipe steels containing micro-alloying elements that raise T_{nr}. Briefly, the entire process involves slab reheating, rough rolling, finish rolling, cooling on the run-out table and coiling.

1.4.1 Rolling schedule

1.4.1.1 Reheating

Of importance here, are the reheating temperature and the presence of undissolved carbide particles: The objective of reheating is to achieve uniformly heated slabs with the complete dissolution of micro-alloyed carbonitrides (Nb,V)(C,N). Slabs are heated uniformly within either walking beam furnaces or pusher-type furnaces. The reheating temperature depends on which micro-alloying elements are present in the steel. It ranges generally from 1150 to 1250 ºC for Nb-containing steels. TiN particles will remain undissolved at these temperatures and serve to inhibit the growth of γ-grains during reheating.

1.4.1.2 Rough rolling

The objective of rough rolling is to achieve the finest possible recrystallised austenite grain size before the T_{nr} is reached[6]. In this stage both recrystallisation and strain hardening will take place[7,8]. The rough-rolling phase is completed above the non-recrystallisation temperature (T_{nr}), typically above about 1030 ºC for X60 to X80 ERW line pipe steels [2, 9]. Specially developed reduction schedules together with TiN particles that inhibit growth of recrystallised austenite grains, are employed for this purpose[6]. For most line pipe steels the temperature of rough rolling is from 1200 down to about 950 ºC[7, 9, 10, 11]. A minimum pass strain of 0.2% is needed for the required austenite grain refinement[12].

1.4.1.3 Finish rolling

The objective of this phase is to accumulate rolling strain within the non-recrystallisation region of the austenite grains so that on subsequent ferrite transformation, ferrite nucleation sites are greatly multiplied in number and a very fine ferrite grain size can be achieved after rolling and during controlled cooling[6]. Finish rolling is, therefore, undertaken in the non-recrystallisation austenite region in the lower temperature range above the A_{r3} temperature (i.e. $T_{nr}>T>A_{c3}$)[9]. NbN also precipitates in this stage due to decreasing solubility of Nb in the austenite. The austenite grains elongate and become "pan-caked" in shape. The starting temperature for controlled rolling ranges from 1050 to 950 ºC and finishes around 730 to 1000 ºC [1] depending on alloying and processing conditions. The total finishing reduction below the T_{nr} should be about 64 to 80% when the initial and final thicknesses of the strip are 110 and 18mm respectively [1,6].

1.4.1.4 Heavy reduction

The heavy reduction (60~85%) during controlled rolling increases the yield strength without an adverse effect on the Charpy ductile-brittle transition temperature (DBTT). Moreover, the heavy reduction followed by rapid cooling on the run-out table remarkably improves both the yield strength and the DBTT[10]. On their own, the heavy reduction results in grain refinement and the rapid cooling increases the fraction of bainitic structure. However, when the heavy reduction is followed by rapid cooling, the microstructure with the increased fraction of bainite becomes significantly grain-refined[10]. These results also showed that the volume fraction of martensite/austenite (M/A) constituents decreased on increasing the total deformation for a steel containing 0.03%C, 0.05%Nb and 0.024%Ti[13].

1.4.2 Cooling rate

The cooling rate (V_c) and the finishing temperature (T_c) of accelerated cooling after finish rolling are important parameters of thermo-mechanically controlled processing for line pipe steels to achieve optimum strength through controlling the influence of transformation microstructure, ferrite grain refinement and precipitation hardening. The effect of T_c and V_c may be attributed to the control of the precipitation of carbonitrides during accelerated cooling[9]. The availability of high cooling rates immediately after finish rolling provides greater microstructural adjustment possibilities, especially for the case of Mo-Nb steel types. The possibilities for adjustment of the relative volume fractions of polygonal and acicular ferrite (and grain size) through the setting of the cooling rate and coiling temperature, are evident in principle[2]. Rapid cooling increases the volume fraction of bainite or M/A islands or acicular ferrite.

1.4.3 Coiling temperature

There is no phase transformation during coiling, but it is very important for precipitation strengthening of these steels, so it requires careful control of the coiling temperature if the maximum degree of precipitation strengthening is to be attained. TiC[5], NbC[12] and V(C,N) precipitate in the ferrite during coiling. The temperature should be sufficiently low (i.e. a high degree of under-cooling) for fine precipitation of these carbides and carbonitrides in the ferrite but not so low that the volume fraction of TiC is reduced through too slow diffusion[5]. When the coiling temperature is too low, precipitation is suppressed, resulting in low strength.

1.5 Pipe forming and welding process

The process of pipe making is through cold forming and cold expansion. There are two possible seam lines for the manufactured pipes, one is a spiral seam and the other longitudinal. Most of the pipelines manufactured globally belong to the former, but, as the quality of the plate has increased, pipelines with longitudinal seams have

increased lately in many manufacturing processes.

The last operation of pipe making is to either weld the seam by submerged arc welding, or by electrical resistance welding as has been preferred in the recent pipeline manufacturing process [6]. Low carbon equivalence improves the weldability.

CHAPTER 2 MICRO-ALLOYING ELEMENTS AND THEIR EFFECTS ON PRECIPITATION

2.1 Vanadium

Vanadium is used in line pipe steels to form vanadium carbonitrides. Its content ranges from 0.03 to 0.05%V[14]. The main action of vanadium in these steels is dispersion hardening, refinement of ferrite grains and inhibiting grain growth of austenite up to 1050 ºC, but it is detrimental to the formation of acicular ferrite[4]. As the solubility of vanadium in austenite is high there is a weak influence of vanadium on the non-recrystallisation temperature (T_{nr}) of austenite. The solubility of vanadium in ferrite, however, is low, and its addition is extremely effective in the precipitation strengthening of ferrite.

The precipitation starting temperature of VN particles is 1005 ºC through the solubility equation of the form log(X%)(Y%)=(-A/T)+B, where X and Y in the equation are mass percentages of the dissolved micro-alloys, A and B are constants, (A and B are 8330 and 3.46 for VN, respectively), T is the absolute temperature[15]. The solubility limit of vanadium in typical line pipe steels is about 0.2% at 1150 ºC[14].

Vanadium carbonitrides will mostly dissolve in austenite at about 900 ºC[9] . Vanadium also inhibits grain growth of austenite up to 1050 ºC. It passes completely into solid solution above 1050 ºC for typical line pipe compositions. Vanadium has no effect on the recrystallisation of hot-deformed austenite above 900 ºC[16].

2.2 Niobium

Niobium carbide is fully dissolved between 1225 and 1250 ºC. It has a greater refinement effect on ferrite grain size, dispersion hardening and reduction of pearlite content. Niobium has a stronger effect on recrystallisation of hot-deformed

austenite[17-19]. Niobium in solution is also considered to suppress the γ/α transformation due to pining of the γ/α interfaces by NbC[20]. The solute niobium strongly segregates to γ/α boundaries and reduces ferrite growth kinetics because of a solute drag effect. Accordingly, niobium additions suppress or delay the formation of polygonal ferrite and pearlite, and promote the formation of acicular ferrite[4] or bainite/martensite-austenite constituents and increases the bainitic hardenability[21]. The solubility temperature of niobium increases from about 1170 ºC in a typical niobium steel to about 1250 ºC, in a Nb-Ti steel. In relation to titanium, the presence of niobium leads to a higher amount of titanium precipitating in the low temperature range, up to the dissolution of complex Ti-Nb carbonitrides. Consequently, it can be concluded that high titanium concentrations present in Nb-Ti steels, exert a significant influence on the grain coarsening behaviour[22]. Some strengthening will result from NbN or Nb(C,N) precipitation in the austenite. However, the most effective precipitation strengthening comes from NbC precipitation in ferrite [12].

The precipitation start temperature of $Nb(C,N)_{0.87}$ is 1181 ºC. The solubility limit is about 0.05% at 1150 ºC[14]. Higher niobium contents enable finish rolling to be carried out at higher temperatures because undissolved NbC provides a finer austenite grain[23] on soaking, which reduces the critical deformation for austenite to dynamically recrystallise. The most rapid precipitation of niobium occurs between 800 and 950 ºC in austenite. The intermediate finish rolling temperature (FRT_s) of 800~850 ºC leads to lower soluble niobium levels than do lower or higher FRT_s[24].

The content of niobium in line pipe steels is usually less than 0.05%. The main effects of niobium in these steels are as follows:

(i) Much greater refinement[25,26] of ferrite grains due to increasing the inhibiting effect of the growth of austenite grains with Nb%;

(ii) Dispersion hardening;

(iii) Reduction of pearlite content due to the binding of carbon in Nb(C,N); and

(iv) Stronger inhibiting effect on recrystallisation[27] of hot-deformed austenite below 950 ºC [16], thereby raising the non-recrystallisation temperature (T_{nr})[12] due to the precipitation of Nb(C,N) during hot rolling[28].

2.3 Titanium

Titanium can refine ferrite grains, suppress recrystallisation of hot-deformed austenite and reduce pearlite formation. Titanium will bind with free N during solidification of the steel. TiN is very stable at high reheating temperatures (such as 1250 ºC), thus retarding grain growth during the reheating process. TiN will also retard grain growth between rolling passes. If it binds all of the free N, this will result in a significant increase in niobium available in the ferrite to precipitate as NbC. The stoichiometric ratio of Ti to N in TiN, is 3.4/1. Titanium can be used to control the sulphide inclusion shape, thus preventing MnS stringer inclusions. The stoichiometric value for Ti/S in TiS ratio is 1.5/1. Therefore, the titanium addition is calculated from[12]

$$Ti=3.4N+1.5S \qquad (2.1)$$

The precipitation start temperature for TiN is 1633 ºC[15] while that of TiC is less than that of TiN' (<1000 ºC[5] for TiC). Therefore, the alloy needs sufficient titanium content for TiC to form (Ti>0.4N)[14]. The stoichiometric ratio Ti/N is 3.4/1 but it may change depending on several factors, such as the reheating temperature before hot rolling and the content of other micro-alloying elements[29].

The main effects of titanium in high-strength low alloy steels are as follows:

(i) ***Refining of ferrite grains***[30,31]: The optimum Ti/N ratio is close to 2 for Nb-free and V-free steels[29]. Titanium at levels of 0.02 to 0.03% has a much greater refinement effect on ferrite grain size. It inhibits the growth of austenite grains by the difficult-to-dissolve TiN and Ti(C,N) during heating[14]. It inhibits grain growth most effectively at 1150 ºC and an addition of 0.015% Ti has a much greater refinement of austenite grains than the addition of the same amount of Nb[16]. Titanium in excess after binding with free nitrogen will be available to bind with sulphur.

(ii) ***Suppression of recrystallisation of hot-deformed austenite***: Titanium has a stronger inhibiting effect on recrystallisation at 1050 ºC than niobium. There is a contradictory result, however, that 0.03% Ti does not have a substantial effect on the recrystallisation of the austenite of low alloy steels due to differences in the composition of these steels[16].

(iii) ***Dispersion hardening***: Because TiC forms at lower temperatures, the titanium content must exceed the bound content from TiN (Ti>0.4N).

(iv) ***Reduction of pearlite formation***

2.4 Molybdenum

The addition of molybdenum in Nb-containing steels can improve transformation hardening (increased volume fracture of acicular ferrite and M/A islands), grain refinement and precipitation hardening. It is mainly the metastable coherent carbide Mo_2C that provides hardening in Mo-containing steels, although the formation of this carbide requires relatively higher levels of addition. Molybdenum also greatly suppresses or delays the formation of polygonal ferrite and pearlite[4] and promotes the formation of acicular ferrite[32]. When the carbon content of the steel is sufficiently low, martensite formation is avoided and fine structures of bainite and acicular ferrite are formed during air-cooling after hot rolling. This will result in very good ductility. Line pipe steels with a discontinuous stress-strain curve lose some yield strength as a result of U-O pipe forming (U-bending and O-bending) and do not completely recover this loss after expansion of the pipe. For steel containing-molybdenum, the stress-strain curve of the as-rolled plate is continuous without an upper yield point. This results in complete control of the detrimental Bauschinger effect during pipe forming and contributes to an increase in the yield strength from plate to pipe. The impact-transition temperature of traditional grades is raised by 10 to 20 ˚C after pipe forming, but does not change for steel with a molybdenum content [33].

The addition of molybdenum in Nb-containing steels has the following purpose in line

pipe steels:

(i)Transformation hardening due to increased acicular ferrite (AF) and martensite/austenite (MA) formation;

(ii) Grain refinement; and

(iii) Precipitation hardening[2].

The addition of molybdenum provides a considerable strengthening advantage over Nb-V steels[2].

2.5 Carbon

Carbon level in these steels is maintained below 0.06% for the following purposes:

(i) Lowering the carbon equivalent (CE) for improved weldability：The maximum CE specification is 0.45;

(ii) High toughness;

(iii) Less micro- and macro-segregation;

(iv) More effective dissolution of niobium: increasing the strength of steels; and

(v) Less pearlite: improving toughness, formability, SSCC (sulphide stress corrosion cracking).

2.6 Manganese

An increase in the manganese content prolongs the incubation time for polygonal ferrite formation. The manganese addition extends the polygonal ferrite curve of continuous cooling transformation (CCT) diagrams. Accordingly, acicular ferrite structures can be obtained at a slower cooling rate with an increase in the manganese content. The addition of manganese delays the precipitation of titanium and niobium, and increases the solubility of NbC by decreasing the diffusivity of niobium in austenite[4]. Manganese also increases the solubility for nitrogen in austenite significantly.

2.7 Copper, Chromium and Nickel

These elements can improve resistance to HIC (hydrogen-induced cracking) and SSCC (sulphide stress corrosion cracking). Chromium and copper have little effect on the mechanical properties of as-rolled plate. Chromium and copper promote the formation of very fine precipitates when used in combination with niobium or vanadium[33]. Steels with a small amount of copper tend to have a somewhat higher corrosion resistance than alloys without copper. As little as 0.05 wt% Cu has been shown to have a significant effect and, usually, the addition of 0.2% Cu can provide increased resistance to atmospheric corrosion. Copper can increase the strength of ferrite through solid solution strengthening and, with 0.5% or more, is precipitated as elemental Cu-particles when the steel is aged within the temperature range of about 425 to 650 °C, thus providing a degree of precipitation hardening by virtue of ferrite strengthening[34].

CHAPTER 3 THE CONTROLLED ROLLING PROCESS OF LINE PIPE STEELS

Line pipe steels with high strength and good toughness properties are produced by using a controlled rolling process. Controlled rolling appears to be vital to produce these steels with optimum mechanical properties. The controlled rolling technique is most effective with steels containing micro-alloying elements that provide a region below which non-recrystallisation will take place during the finishing stages of hot rolling. Micro-alloying additions increase this temperature above where complete recrystallisation occurs and the recrystallisation of austenite below this temperature is retarded during deformation.

3.1 Three stages of deformation for controlled rolling process

Controlled rolling may be divided in principle into three stages[11]:

(1) Deformation in the austenite recrystallisation temperature region;

(2) Deformation in the austenite non-recrystallisation region; and

(3) Deformation in the two-phase austenite-ferrite region.

This is illustrated in figure 3.1[11] along with the structural changes, which occur during the controlled rolling process. Optimum mechanical properties of HSLA steels can be obtained only by the careful control of microstructural changes in each stage of controlled rolling. The principal variables are deformation temperature, amount of deformation and strain rate.

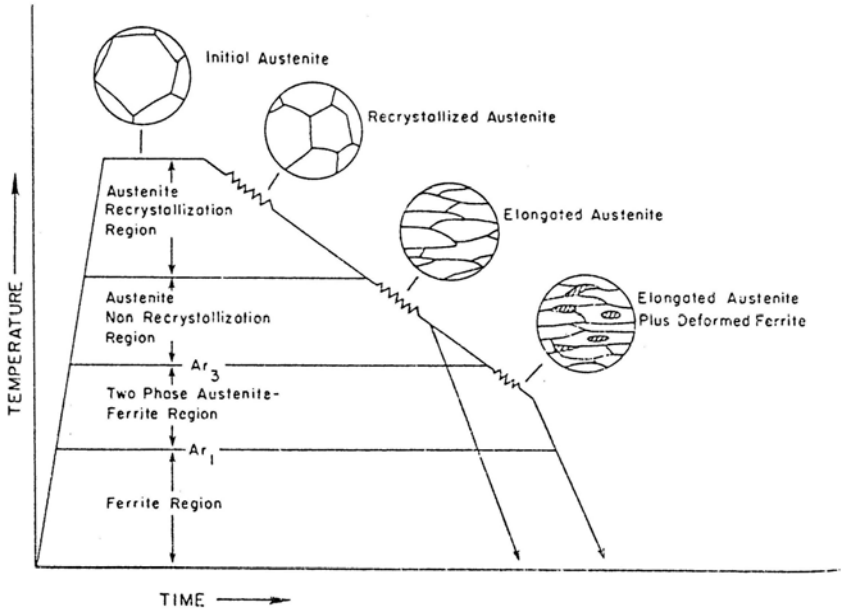

Figure 3.1 Schematic illustration of the three stages of the controlled rolling process[11].

3.1.1 Deformation in the austenite recrystallisation region

The reheating temperature and the solubility of micro-alloying precipitates have a strong influence on the grain size of the initial austenite after reheating and the grain size of the recrystallised austenite before the T_{nr} is reached. The effects of micro-alloying elements depend on the reheating temperature[11]. The recrystallised grain size decreases rapidly as a function of both an increased reduction per pass and a decreasing deformation temperature. The smallest recrystallised austenite grain size can be attained by using deformations above the critical amount required for the initiation of dynamic recrystallisation during hot rolling.

3.1.2 Deformation in the non-recrystallisation region

It is commonly believed that micro-alloying elements retard the recrystallisation of austenite either by solid-solution effects through solute drag or by the pinning effect of strain-induced precipitation. Below the non-recrystallisation temperature, recrystallisation of austenite grains is sufficiently suppressed so that rolling produces deformed elongated austenite grains (also called 'pancake' grains) and deformation

bands within the austenite. Deformation bands also serve as nucleation sites for ferrite[11]. With an increasing amount of deformation, the austenite grains become more elongated, thereby increasing their length-to-thickness ratio, and the number of deformation bands increases and their distribution becomes uniform, giving rise to a fine and uniform final austenite structure and also to the final ferrite structure after transformation on the run-out table.

3.1.3 Deformation in the (α+γ) two-phase region

Deformation in this two-phase region is generally difficult to control because there is a differing deformation resistance in the two-phase region and this type of hot rolling is generally not considered for line pipe purpose. A time-temperature diagram indicating the microstructural processes during hot rolling is shown in figure 3.2[8]. Numerous metallurgical processes take place during hot rolling and subsequent cooling, which determine the final grain size and thus the mechanical properties of the strip.

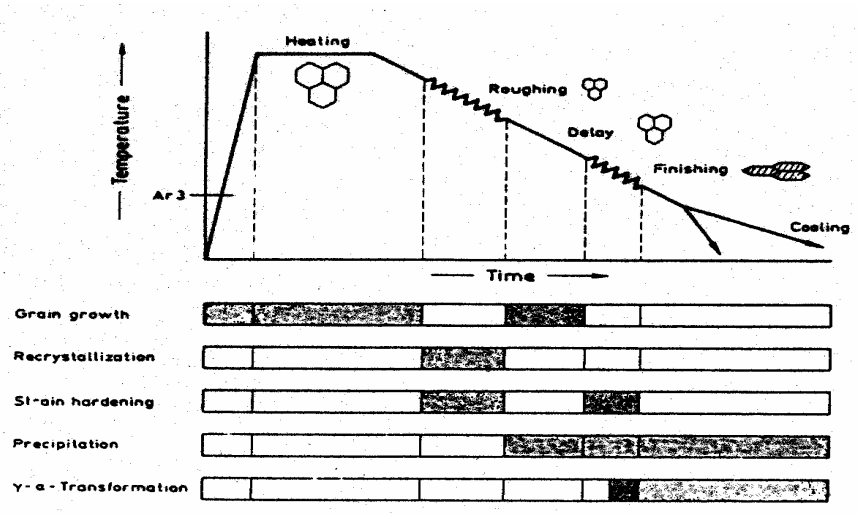

Figure3.2 Metallurgical mechanisms during thermo mechanical hot rolling[8].

3.2 Reheating temperature and undissolved particles

The objective of reheating is to achieve uniformly heated slabs with full dissolution of the micro-alloyed carbonitrides (Nb,V)(C,N). Continuously cast slabs are heated within walking beam furnaces or pusher-type furnaces. The reheating temperature depends on which micro alloying elements are present in the steel. It is generally from 1150 to 1250 ºC for Nb-containing steels, so that most of the alloy carbides and nitrides (except for TiN) are dissolved in the steels in order to obtain maximum dispersion hardening later. The soaking time is usually from 30 to 60 minutes for a slab thickness of 26 to 110 mm[1, 10, 14, 35, 36].

At higher reheating temperatures, most micro-alloying elements will be in solution in the austenite and will precipitate at lower temperatures both in the austenite and in the ferrite as carbides, nitrides, or carbonitrides, thereby increasing the strength of these phases (figure 3.3[24]). However, high reheating temperatures will allow considerable grain growth to occur. At lower reheating temperatures, a larger proportion of micro-alloying precipitates will remain undissolved in the austenite. These precipitates will act as barriers to grain movement. Precipitates formed during deformation will inhibit grain growth of the recrystallised austenite in the same manner as undissolved precipitates[11].

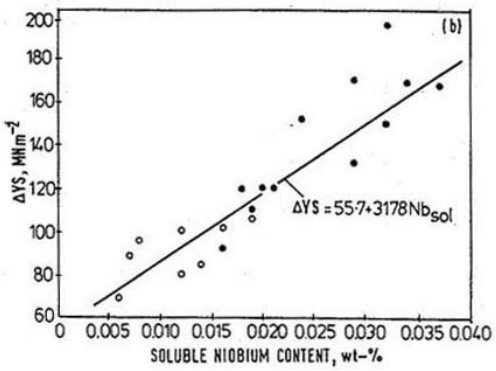

Figure 3.3 Correlation between the increase in yield strength ΔYS and the content of soluble Nb[24] (0.075% C, 043% Si, 1.58% Mn, 0.013% P, 0.005% S, 0.51% Ni, 0.021% Al and 0.106% Nb, and 0.077% C, 0.36% Si, 1.56% Mn, 0.017% P, 0.005%S, 0.47% Ni, 0.020% Al and 0.130% Nb).

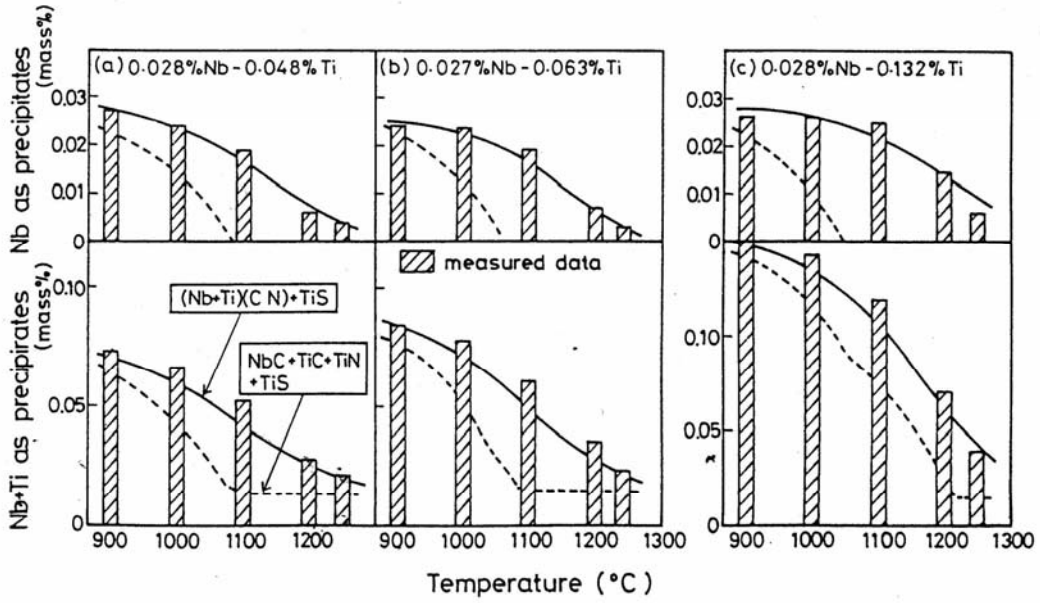

Figure 3.4 Comparison between the calculated and measured quantities of micro-alloying elements as precipitates[37].

Vanadium carbonitride passes completely into solid solution if the reheating temperature is above 1050 ºC[16]. Niobium carbonitride is not fully dissolved in austenite at 1250 ºC and it has a fine spherical shape[38]. Figure 3.4[37] shows that the amount of Nb and (Nb+Ti) present within precipitates in three Nb-Ti bearing steels, decreases with increasing heating temperature[37]. It also shows that there are some undissolved Nb carbonitrides in the matrix even at ~1250 ºC. The measurements also show that only 4 to 27% of Nb was dissolved in the austenite at 1100 ºC for the Nb-Ti steel. This suggests that the mixing of niobium and titanium increases the stability of the precipitates, so that the solubility of precipitates decreases in Nb-Ti bearing steels through the formation of complex precipitates[35,37]. The complex (Nb+Ti) precipitates are more stable than binary Nb carbonitrides so that the coarse precipitates are not dissolved at 1250 ºC[35].

The austenite grain size increases and the quantity of undissolved precipitates decreases with increasing reheating temperature. Accordingly, the grain size after reheating is directly linked to the presence of micro-alloying elements, the dissolution

behaviour of carbonitrides and the heating time and temperature (figure3.5)[39]. The higher the quantity of undissolved precipitates, the more stable the carbonitrides are. So, the austenite grain size becomes finer due to the retarding effect of undissolved particles on the recrystallisation of austenite. The complex micro-alloying precipitates are more stable than binary precipitates. The reheating temperature may, therefore, have to be higher for those steels with complex precipitates.

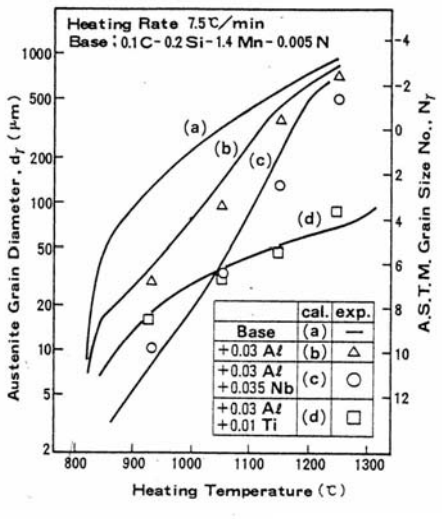

Figure 3.5 Change in austenite grain size during reheating process[39].

3.3 Rough rolling

The objective of rough rolling is to achieve the finest possible recrystallised austenite grain size at the point where the T_{nr} is reached[6]. The rough-rolling stage is completed at a temperature above about 1030 ºC[2], i.e. in the recrystallised austenite region for the X60 to X80 ERW line pipe steels[9] where recovery and recrystallisation of austenite grains take place[7]. Specially developed reduction schedules together with TiN particle control to inhibit growth of recrystallised grains, are employed for this purpose[6]. The transfer bar thickness is typically about 26 to 30 mm for line pipe coils in the final strip thickness range of 5 to 10 mm and effectively sets the non-recrystallisation finish rolling reduction level at about 70 to 80%[2, 6]. However, for most line pipe steels the temperature of rough rolling varies from 1200 to 950 ºC[7,9-11]. Strain hardening also takes place besides recrystallisation in this stage[8].

3.4 Finish rolling

The objective of this stage is to accumulate rolling strain within the austenite grains so that on subsequent ferrite transformation, ferrite nucleation sites are greatly multiplied in number and a very fine ferrite grain size can be generated during controlled cooling[6].

The stage is confined to the non-recrystallised austenite region in the lower temperature range above A_{r3}[9]. The starting temperature for this stage is in the region of about 1050 to 950 ºC and the finish rolling temperature is in the region of 850 to 950 ºC[6, 9 ,10]. The total finishing reduction is usually about 64 to 80% when the initial slab thickness and finishing thickness are 110 and 18 mm, respectively[1]. While further strengthening of the hot strip can be achieved when finish rolling is continued into the intercritical region of austenite and ferrite, there is little resultant benefit to the final pipe strength since the Bauschinger effect is increased in magnitude. Lowering the finish rolling temperature below A_{r3} was effective in one instance, in significantly increasing the strength of the hot strip (figure 3.6[22]). However, almost no further improvement in the corresponding pipe strength was recorded, suggesting that two-phase rolling exacerbates the Bauschinger drop[2]. This “diminishing return” effect led to the consideration of molybdenum additions as a means in which to comfortably reach higher strength levels in X70 and X80 line pipe steels whilst avoiding the use of an excessively high carbon equivalent in the interests of preheat-free welding[2].

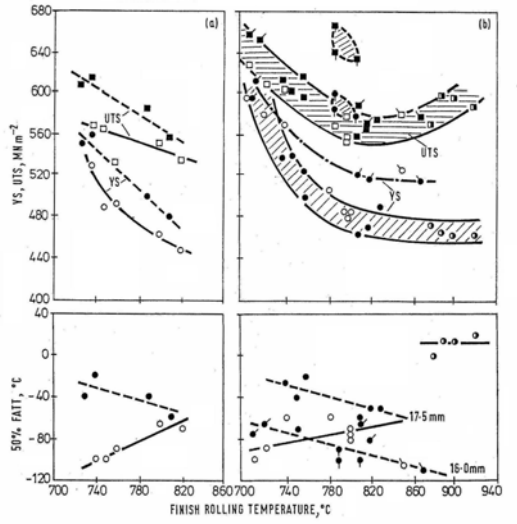

Figure 3.6 Influence of rolling conditions on the mechanical properties of plate and strip of different thicknesses[24].

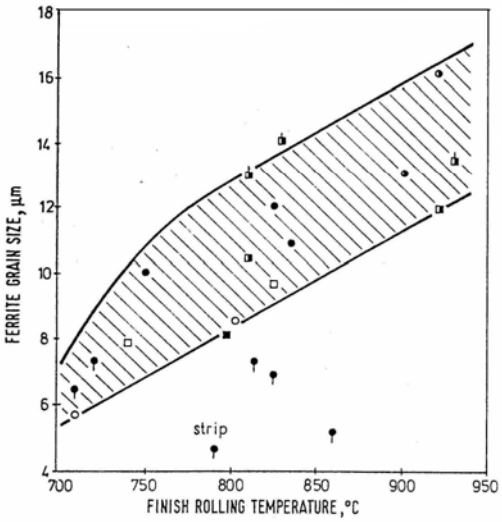

Figure 3.7 Influence of rolling conditions on the average ferrite grain size[24].

The role of the finish rolling temperature on mechanical properties of the steel may be attributed to the acceleration of transformation to ferrite and the refinement of grains by the decrease in the finishing temperature[9]. Therefore, the decrease in finishing temperature will be beneficial to both strength and ductility as shown in the following regression equations determined for a steel of composition: 0.07%C, 0.25%Si, 0.9%Mn, 0.046%Nb, 0.04%V, 0.015%Ti and 40ppm N[9]:

$$YS=0.508T_s-0.231T_f-0.334T_c+1.905V_c+323.6 \qquad R^2=0.94 \qquad (3.1)$$

$$EL=-0.002T_s-0.064T_f-0.086T_c+0.325V_c+121.8 \qquad R^2=0.98 \qquad (3.2)$$

where EL is the elongation in %, T_s is the start rolling temperature (ºC), T_f is the finish rolling temperature (ºC), T_c is the finish cooling temperature (ºC), V_c the cooling rate (ºCs^{-1}) and R^2 is the regression coefficient. In such an approach, however, one needs to strictly control the lowering of the finish rolling temperature as higher mill loads are encountered. It has been reported[9] that when T_f is above a certain lower limit temperature, both the yield strength and the toughness of the steel increase with a decrease of T_f. If T_f is below this critical temperature, a banded microstructure appears which greatly reduces toughness.

Figure 3.7 [24] shows the effect of finish rolling temperature on the final ferrite grain size, showing that the ferrite grain size can be reduced at lower finish rolling temperatures[24, 36]. Some phenomena that appear are strain hardening, precipitation of micro alloying carbonitrides and/or γ-α transformation[8].

3.5 Heavy reduction

A heavy reduction of 60 to 85% in total, increases the yield strength without adversely affecting the Charpy brittle to ductile transition temperature. Moreover, a heavy reduction followed by rapid cooling remarkably increases the yield strength and decreases the Charpy brittle to ductile transition temperature (figure 3.8 [10]). The heavy reduction on its own results in a slight grain refinement and the rapid cooling again increases the fraction of the bainitic microstructure. However the two together, when the heavy reduction is followed by rapid cooling, the microstructure with the increased fraction of bainite becomes grain-refined[10]. The result also showed that the volume fraction of M/A constituents decreased on increasing the deformation for a steel containing 0.03%C, 0.05%Nb and 0.024%Ti (figure 3.9)[13].

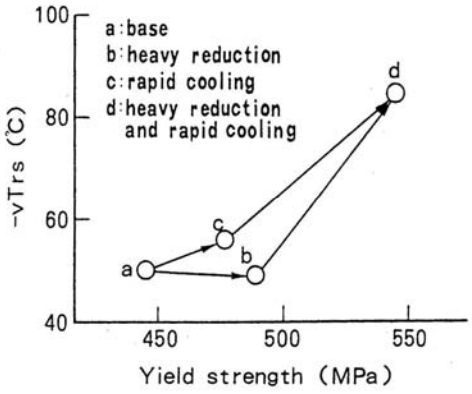

Figure 3.8 Improvement in yield strength and Charpy ductile to brittle transition temperature[10].

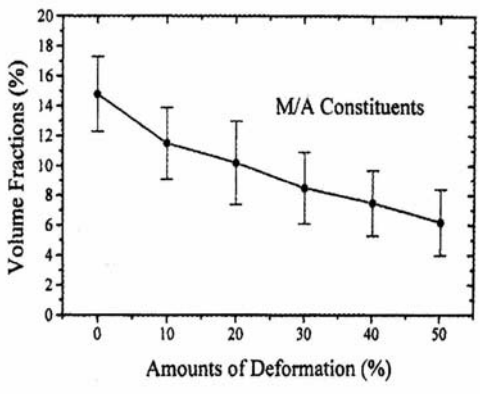

Figure 3.9 Plot of the volume fraction of M/A constituents versus the degree of prior deformation[13].

The total or cumulative reduction of HSLA steels in the hot rolling process is generally between 67 to 84%[1,6,9, 10,14,35,38], while the maximum cumulative reduction is up to 95%[40]. The number of passes of thermo-mechanically controlled processing are generally between 4 to 6 with a maximum of 7 to 9 for an ~0.06%C steel[41]. Table 3.1 shows the typical reduction and passes of hot rolling for line pipe steels.

Table 3.1 Reduction/pass of hot rolling

Steel No	Reduction, %									Ref.
	Pass 1	Pass 2	Pass 3	Pass 4	Pass 5	Pass 6	Rough rolling	Finishing rolling	Total	
1	16	23	29	27	--	--			67	38,42
2	--	--	--	--	--	--	51	64	84	1
3	15	25	25	25	25	25	--	--	80	10
4	21	21	31	30	30	25	--	--	84	10
5	13	30	30	30	30	25	--	--	84	10
6	33	40	40	35	--	--	--	--	84	10
7	16	23	29	27	--	--	--	--	67	35
8	25	33.3	40	33.3	--	--	--	--	73	9

3.6 Strip thickness

The thickness of the final strip has a significant effect on the strength of these steels, especially on the ratio of yield strength to ultimate tensile strength or YS/UTS. Experimental results on X80 line pipe steels showed that the yield strength and tensile strength increased and the YS/UTS ratio also increased from 0.86 to 0.95 with decreasing strip thickness from 9 to 3 mm for an 0.07% C, 0.19% Si, 1.53% Mn, 0.045% Nb, 0.012% Ti and 0.20% Mo steel (figure.10)[6]. A similar relationship between the thickness and the YS/UTS ratio that dropped from 0.89 to 0.76 as the thickness was increased from 13.5 to 50 mm, was found in a X80 steel of composition: 0.075% C, 0.43% Si, 1.58% Mn and 0.106% Nb)[24]. The ratio also dropped from 0.80

to 0.73 as the thickness increased from 10.3 to 32mm for a steel with composition of 0.09% C, ~0.20% Si, ~1.20% Mn, ~0.043% V, ~0.04% Nb and 0.007% Ti[38].

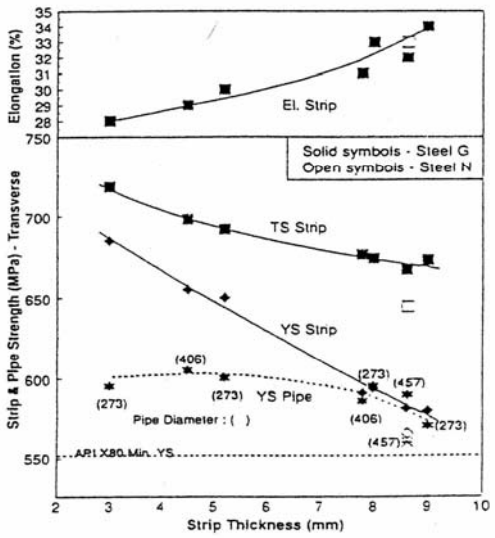

Figure 3.10 Strip and pipe properties for various X80 pipe sizes)[6]. (Steel G: 0.075% C, 1.59% Mn, 0.31% Si, 0.057% Nb, 0.22% Mo, 0.013% Ti and 0.006% N; Steel N: 0.070% C,1.53% Mn, 0.19% Si, 0.045 Nb,0.20% Mo, 0.012% Ti and 0.0045% N.

3.7 Cooling rate after finish rolling

The cooling rate (V_c) and the finishing temperature (T_c) of the accelerated cooling process after finish rolling are important parameters to achieve optimum strength of thermo-mechanically controlled processing for line pipe steels. Controlling the T_c and V_c may lead to the control of precipitation of carbonitrides during accelerated cooling[9]. The availability of high cooling rates immediately after finish rolling provides greater microstructural adjustment possibilities, especially for the case of Mo-Nb steel types. The possibilities for adjustment of the relative volume fraction of polygonal and acicular ferrite (and grain size) through the setting of the cooling rate and coiling temperature are schematically evident in figure 3.11[2]. The rapid cooling increases the fraction of bainitic structure or M/A islands or acicular ferrite. This is because polygonal and pearlite transformations are governed by slow diffusion and have some difficulty in fully transforming during accelerated cooling. The austenite may remain as retained austenite or transform to an acicular ferrite structure because

the transformation to acicular ferrite is a mixed mode of shear and diffusion[4,9,11,43]. The M/A islands are carbon-rich due to the replacement of pearlite by these small islands. The M/A islands also refine the ferrite grain size structure. The ferrite grain size becomes finer when a heavy reduction is followed by rapid cooling (figure 3.12[10]) because the nucleation rate increases and there is not enough time for growth of nuclei of ferrite grains due to increasing under-cooling at a rapid cooling rate. The heavy reduction during finish rolling results in more crystal defects and these provide the nucleation sites for the γ→α transformation.

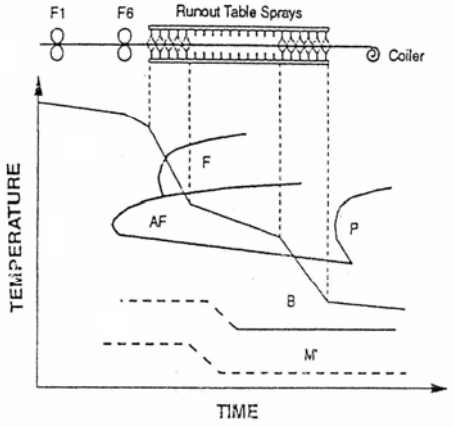

Figure 3.11 Schematic representation of the cooling pattern on the run-out table of a Hot Strip Mill[2].

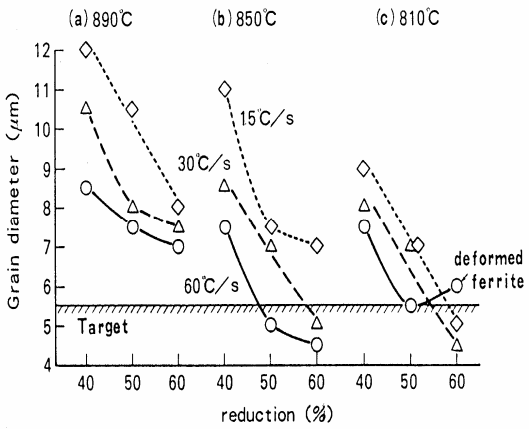

Figure 3.12 Influence of reduction and cooling rate on the ferrite grain diameter[10].

The cooling rate after controlled rolling also has a significant effect on the degree of precipitation[11]. With slower cooling rates the coarsening of precipitates makes them less effective for strengthening while with faster cooling rates, no precipitation occurs and the micro-alloying elements remain in solution. Correctly designed accelerated cooling leads to fine precipitation of Nb(C,N) and also provides ferrite grain refinement[4]. Roberts[5] indicated that a higher yield strength can be obtained at a low carbon equivalent by employing accelerated cooling. In general, an increasing degree of precipitation hardening as the cooling rate is raised, has no detrimental effect on fracture toughness because of the simultaneous refinement of the microstructure and

the replacement of pearlite by small islands of bainite.

An increase in cooling rate from 15 to 30 ºCs^{-1} in a Nb-bearing steel (0.1% C, 0.20% Si, 0.09% Mn, 0.046% Nb and 0.0018% N) enhanced the yield strength by 20 to 30 MPa[10]. This leads to a guideline equation (3.1) above. The yield strength of a line pipe steel can increase by an average of about 2 MPa for every increase of 1 ºCs^{-1} in the cooling rate[9].

The cooling rate on run-out tables for line pipe strip rolling in the laboratory is generally between 10 to 60 ºC s^{-1}[9,10,44].

3.8 Finish temperature of accelerated cooling

The finish temperature of accelerated cooling (T_c) is important in controlling the precipitation of carbonitrides during this cooling. At a temperature just above 500 ºC, V_4C_3 which is the main vanadium carbide in these steels, has the highest nucleation rate and its contribution to precipitation strengthening is most prominent[45]. Therefore, within a certain temperature range just above 500 ºC, a lower T_c is beneficial to both strength and ductility as predicted by formulae (3.1) and (3.2). However, T_c cannot be decreased too low, because it will be detrimental to the fracture toughness of the steel[9].

The pearlite transformation will also be retarded as the finish temperature of accelerated cooling is decreased. Optical microscopy showed that some pearlite is formed when T_c is at 781 ºC, only a little pearlite is formed at 660 ºC and no pearlite is formed below 580 ºC in an 0.08% C, 0.007% Nb, 0.009% Ti steel[39]. When lowering the T_c , ferrite grains become finer and the volume fraction of acicular ferrite increases. Below 580 ºC, however, the ferrite grain size remains largely unaffected because the ferrite transformation is already complete (figure 3.13)[39].

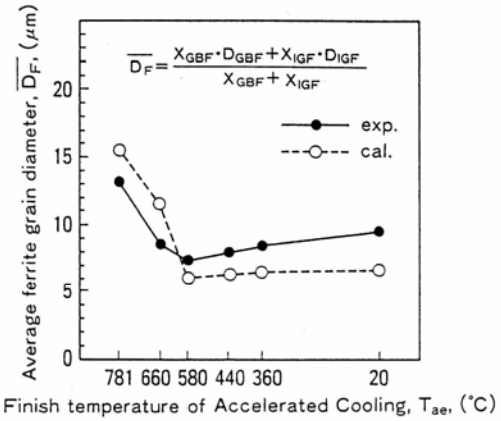

Figure 3.13 Effect of finish temperature of accelerated cooling on the average ferrite grain diameter[39].

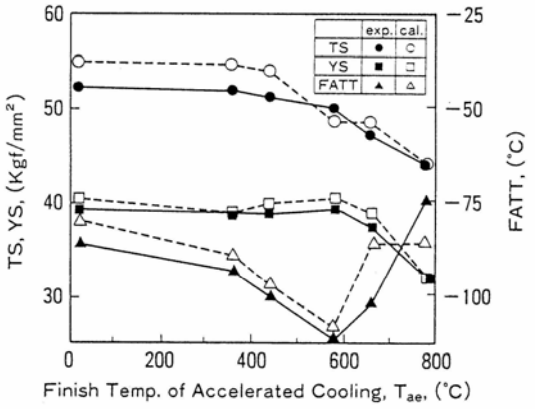

Figure 3.14 Comparison of mechanical properties between the observed and the calculated strengths of micro-alloyed steels[39].

The relationship between T_c and the tensile strength is shown in figure 3.14[39]. It indicates that the yield strength and ultimate tensile strength increase with decreasing T_c until about 580 ºC. But almost no further change in strength is found at T_c < 580 ºC.

The finishing temperature of accelerated cooling (T_c) is, therefore, maintained generally between 550 and 670 ºC[7,8,10,44] although sometimes it may even be as high as 800 ºC (~0.10% C)[36] or even below 500 ºC [9,10].

From the above, it appears that the optimum mechanical properties for a line pipe steel can be obtained when the reheating temperature T_s is approximately 1100 ºC, the finishing temperature T_f is about 890 ºC, the finishing cooling temperature T_c is about 520 ºC and the cooling rate V_c from the T_f to T_c is about 30ºCs^{-1}[9].

3.9 Coiling temperature

The coiling temperature will influence the effectiveness of Nb-precipitation but especially that of V(C,N) precipitation in the ferrite, thus controlling the precipitation strengthening of the steel. The coiling temperature requires careful control if the maximum degree of precipitation strengthening is to be attained. High coiling temperatures result in few and coarse precipitates, which will add very little to the strength, while lower temperatures should be sufficiently low for a fine precipitation, adding to the strength depending on the levels of micro-alloying additions, especially the vanadium and free N in solution. Low coiling temperatures will result in finer ferrite grains because of less ferrite grain growth taking place after transformation, adding to the strength and fracture toughness. Lower finish cooling and coiling temperatures, will suppress pearlite formation and microstructural banding[46]. The temperature, however, should not be too low so that the volume fraction of TiC is reduced by too slow diffusion[5]. Too low a coiling temperature results in low strength because precipitation may be retarded. The optimum coiling temperature for a given composition should preferably be determined experimentally.

Production experience with Nb-Ti-, Nb-V-Ti- and Mo-Nb-Ti-type line pipe steels shows somewhat different sensitivities of coiling temperature with strip strength properties as indicated in figure 3.15[2]. There was little effect in the relationship between coiling temperature and yield strength for these micro-alloying steels. The same tendency is that the yield strength increases with decreasing coiling temperature. Decreasing the coiling temperature has no effect on the yield strength below about 620 ºC for a Ti-Nb-V steel with composition 0.085% C, 0.050% V, 0.045% Nb and 0.013% Ti[2].

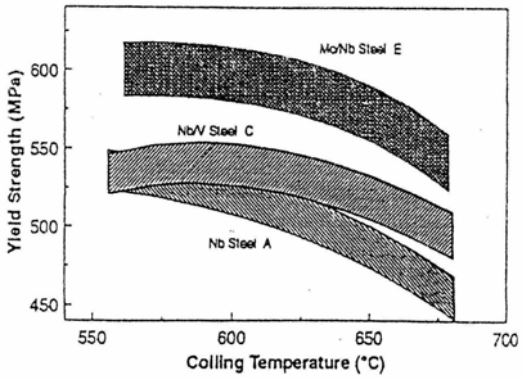

Figure 3.15 Effect of coiling temperature on the YS of hot rolled strip for various types of alloys[2].

3.10 Non-recrystallisation temperature (T_{nr})

The non-recrystallisation temperature (T_{nr}) is also an important parameter for the controlled rolling process of line pipe steels. The rough-rolling process is generally carried out above the T_{nr} temperature, which is associated with the finishing temperature of the rough-rolling stage. During finishing below the T_{nr}, a total of at least 0.8 strain should be applied for effective grain refinement (effective controlled rolling)[46].

A coarse, polygonal ferrite plus pearlite microstructure can be ascribed to insufficient strain below $T_{nr,}$ coupled with higher coiling temperatures, while a coarse acicular ferrite can be ascribed to insufficient strain below T_{nr} coupled with lower coiling temperatures[46].

3.10.1 Effect of alloying elements

Micro-alloying elements have some effect on the T_{nr}. Niobium binds with free nitrogen and precipitates as niobium nitrides at higher temperatures, e.g. during rough rolling. Thus, most of the niobium then becomes ineffective in retarding austenite recrystallisation during finish rolling at lower temperatures. Titanium is, therefore, often used in combination with niobium to tie the free nitrogen in Nb-Ti

micro-alloyed steels and this generally forms (Ti,Nb)N precipitates. Thus, titanium will increase the effect of the niobium on the T_{nr}. Thus titanium and niobium micro-alloying elements will raise the T_{nr} (inhibiting recrystallisation)[47], and cause more effective grain refinement. Titanium appears to accelerate the precipitation of Nb(C,N), and therefore, contributes to the retardation of recrystallisation. Titanium is only 0.31 times as effective as niobium in retarding recrystallisation and aluminium 0.15 times[48]. The T_{nr} temperatures at a strain rate of 3.63 s^{-1} were found to be 918 and 937 ºC for a V-micro-alloyed (0.075% V) and a V-Ti (0.055% V+0.024% Ti) micro-alloyed steel, respectively, while the T_{nr} was about 1042 ºC for a Nb (0.026%) steel deformed at the same strain rate[47]. The T_{nr} decreases with decreasing super-saturation ratio or the [Nb][C] solubility product[48,49]. The addition of Mo, Nb, and (Mo+Nb) increases the T_{nr} in this order[48]. The T_{nr} is increased by boron additions because it accelerates the precipitation kinetics of Nb(C,N), but a maximum in the T_{nr} at a boron concentration of 48 ppm occurs. The results showed that increasing the boron content beyond 48 ppm leads to a decrease in the T_{nr}[48]. This decrease in the T_{nr} was possibly due to an acceleration in the rate of coarsening of the Nb(C,N), as precipitate coarsening of Nb(C,N) is accelerated by the presence of boron[48] and such coarsened particles lose their effectiveness with regard to retarding the recrystallisation. When less than 48 ppm boron was added, the equilibrium segregation of boron to austenite boundaries and the acceleration of Nb(C,N) precipitation can both contribute to increasing the T_{nr}.

3.10.2 Effect of the controlled rolling process

At the same solution reheating temperature, the non-recrystallisation temperature was found to decrease with an increase in the strain rate from 1.09 to 3.63 s^{-1}. This is because a higher strain rate and strain will cause a consequent increase in the density of dislocations, which are beneficial to the onset of recrystallisation through increasing its driving force. Increasing the pass strain and strain rate was found to lead to a decrease in the T_{nr} for Nb-containing, (Nb+Ti)-containing,

(Nb+Ti+Mo)-containing and B-containing steels. The strain rate had a smaller effect on the T_{nr} than the pass strain. These relationships were found to be as follows[48]:

$$T_{nr} \propto \varepsilon^{-0.12} \tag{3.3}$$

$$T_{nr} \propto \dot{\varepsilon}^{-0.01} \tag{3.4}$$

The effect of inter-pass time on the T_{nr} is complicated by the transition from a solute drag effect to retardation by precipitation. In a short inter-pass time range (generally less than 12.5 seconds), the T_{nr} decreases with increasing inter-pass time because niobium solute drag appears to be responsible for the retardation of recrystallisation[48]. The full T_{nr} relationship to process conditions can be expressed as:

$$T_{nr} = A\,\varepsilon^{-0.12} t_{ip}^{-0.1}\,\dot{\varepsilon}^{-0.01} \quad (t_{ip}<12.5\text{ s}) \quad \text{or} \tag{3.5}$$

$$T_{nr} = (A\log[Nb]_{eq}+B)\,\varepsilon^{-0.12} t_{ip}^{-0.1}\,\dot{\varepsilon}^{-0.01} \tag{3.6}$$

where $[Nb]_{eq}$ is the equivalent niobium content given by $[Nb]_{eq}=[Nb+0.31Ti+0.15Al]$, A=88.1 ºC per wt% and B=1156 ºC.

At long inter-pass times, however, the T_{nr} increases with increasing inter-pass time. This is because the volume fraction of precipitates that are formed is time dependent, so that the retardation effect increases with the holding time before precipitate coarsening sets in. The effect of the deformation parameters on the T_{nr} is then as follows:

$$T_{nr} = A'\,\varepsilon^{-0.12} t_{ip}^{0.04}\,\dot{\varepsilon}^{-0.01} \quad (12.5\text{ s}< t_{ip}<30\text{ s}) \quad \text{or} \tag{3.7}$$

$$T_{nr} = (A'\log([Nb][C])+B')\,\varepsilon^{-0.12} t_{ip}^{0.04}\,\dot{\varepsilon}^{-0.01} \tag{3.8}$$

where A′=63.5 ºC per wt%, B′=885 ºC

Strain has the following effect on the T_{nr}[47]:

$$T_{nr}=T_s-P\varepsilon^a\dot{\varepsilon}^b D^c \tag{3.9}$$

where T_s is the solution temperature, ε is the strain, $\dot{\varepsilon}$ is the strain rate and D is the austenite grain size. From the equation above, it appears that a smaller grain size

contributes to raising the T_{nr}.

The effect of micro alloying elements on the T_{nr} is described by the following solute retardation parameter (SRP):

$$SRP = \log\left(\frac{t_x}{t_{ref}}\right)\left(\frac{0.1}{X}\right)100 \qquad (3.10)$$

where t_x is the time required for the start of static recrystallisation in the steel containing the element x, t_{ref} is the equivalent time for a reference plain carbon steel and X is the alloy content of x in at%. The SRP of V, Mo and Nb is 10, 37 and 409, respectively for a static condition or 8.4, 25 and 135, respectively for a dynamic condition with $\dot{\varepsilon}=2\ s^{-1}$ at 1000 ºC[50].

CHAPTER 4 MICROSTRUCTURE AND MECHANICAL PROPERTIES

4.1 Acicular ferrite

4.1.1 Nucleation and growth of acicular ferrite

Microstructures with a significant proportion of acicular ferrite present an optimised combination of mechanical properties if compared with mainly bainitic structures. It is well documented that acicular ferrite formation is enhanced by the presence of non-metallic inclusions in studies in weld pools[51-64], low carbon steels[65] and medium carbon forging steels[66-69], and is characterized by elongated grains that are "chaotically" arranged[4]. These second-phase particles act as point sites on which the intragranular nucleation[70,71] of ferrite units develops. There may also be some M/A islands present with a high dislocation density[11]. Acicular ferrite is a non-equiaxed structure phase with an interior that contains a dense substructure of dislocations[4,72]. The carbon content in the M/A islands is higher than that in the surrounding matrix. Accordingly, the M/A islands are carbon-enriched, whose formation may be attributed to the partitioning of carbon during the transformation to acicular ferrite and the post-transformation of carbon-enriched austenite. When the specimen is deformed in the non-recrystallisation austenite region, high densities of substructure and dislocations will be formed in the austenite, which increase the nucleation rate of acicular ferrite, impedes the growth of the coherent and/or semi-coherent γ/α interfaces and accelerates diffusion of carbon to these γ/α interfaces, which leads to carbon-enriched austenite. During the accelerated cooling after finish rolling and followed by the coiling process, part of the carbon-enriched austenite transforms to martensite and the retained austenite coexists with the martensite[73]. The transformation model is, therefore, a mix of diffusion and shear transformation[4,9,11,43]. The start temperature of the transformation to acicular ferrite is slightly higher than that of an upper bainite[4,11].

Acicular ferrite always has an orientation relationship with the austenite grain, such

that one of its close packed $\{110\}_{AF}$ planes is nearly parallel to the close-packed $\{111\}_{\gamma}$ plane of the parent austenite. Within these parallel planes, a close-packed $<11\bar{1}>_{AF}$ direction of the acicular ferrite is found to be near to a close-packed $<\bar{1}01>_{\gamma}$ direction of the austenite[74]. This demonstrates that the growth of acicular ferrite occurs by a displacive transformation and its growth, therefore, takes place without carbon diffusion. The excess carbon in ferrite is probably rejected into the austenite soon after nucleation. Acicular ferrite plates are never found to grow across austenite grain boundaries and this is also consistent with the displacive transformation mechanism, since the necessary co-ordinated movements cannot be sustained across austenite grain boundaries. TEM work has revealed that the ferrite units belonging to the same sheaf have the same crystallographic orientation in most cases[75].

As regards the carbon concentration of acicular ferrite structures during transformation, experiments and thermodynamic theory have demonstrated that the growth of acicular ferrite is diffusionless with the ferrite inheriting the chemical composition of the parent austenite. The excess carbon in the acicular ferrite is rejected into the retained austenite after transformation and can apparently occur within a few seconds[74].

4.1.2 Two types of acicular ferrites: Upper and lower acicular ferrite

There are two different microstructural morphologies of acicular ferrite (AF) in medium carbon micro-alloyed steels, depending on the isothermal treatment temperature[75]. One is upper acicular ferrite, the typical acicular ferrite with an interlocked microstructure (plate morphology) that is formed at high isothermal treatment temperatures of typically 450 ºC. The secondary, is of acicular plates of ferrite that had nucleated at the interface between the primary ones and the austenite and are inclined at a high angle with respect to the substrate unit.

Another sheaf morphology of lower acicular ferrite, is composed of packets of plates

following the same growth direction at lower isothermal treatment temperatures of typically 400 ºC. A significant change in the morphology of the acicular ferrite is, therefore, clearly apparent with a lowering of the formation temperature. It is observed that the nucleation of the primary plates takes place intragranularly on the same second-phase particles. These significant differences between the morphologies of the two types of acicular ferrite can be distinguished in the early stages of the transformation. At a high nucleation temperature of 450 ºC, single plates form at second phase particles while at temperatures lower than 400 ºC, individual parallel platelets are formed with residual phases in between them.

There may be two reasons for the formation of parallel AF units at low temperatures. Firstly, the lower stability of the austenite close to the tip of the ferrite plate and secondly, the strain field produced by the invariant plane-strain shape transformation, both favour the formation of the same variant as that of the primary plate at these sites. Further growth of these subunits seems to be possible parallel to the primary plate, leaving a thin layer of carbon-enriched retained austenite between the different subunits. Afterwards, these regions of austenite lead to the precipitation of interlath cementite between the ferrite plates[75].

The autocatalytic formation of new plates of acicular ferrite is expected to depend strongly on the carbon concentration profile of the parent austenite ahead of the interface with the primary AF plates. This concentration profile will become more pronounced as the transformation temperature decreases and the diffusion in the austenite of the carbon rejected from the ferrite, becomes slower. Close to the acicular ferrite tips, the carbon enrichment of the austenite could be low enough to allow the transformation to proceed, leading to the formation of elongated sheaves. At high transformation temperatures, the diffusion of carbon is more rapid and plate formation on interfaces is more likely[75].

4.1.3 Effect of the hot rolling process on acicular ferrite formation

Hot deformation will promote the subsequent formation of acicular ferrite. This is because high densities of substructure and dislocations are formed in the austenite during deformation of austenite in the non-recrystallisation region, which increases the nucleation sites for acicular ferrite and promotes the acicular ferrite transformation[4]. The temperature range for the nucleation of acicular ferrite moves slightly towards higher temperatures and shorter times with hot deformation of austenite if compared to an equivalent austenite without hot deformation. The growth of acicular ferrite, however, is retarded in plastically deformed austenite[76]. With an increase in the cooling rate after hot rolling, the fraction of polygonal ferrite decreases and the fraction of acicular ferrite increases in volume and the grain size of the ferrite becomes smaller[73].

4.2 Acicular ferrite and bainite

Bainite forms typically at temperatures between pearlite and martensite and the transformation model is also a displacive mechanism. There are three kinds of microstructure: upper bainite, lower bainite and granular bainite. Carbides precipitate in-between the laths within upper bainite (which often results in a lower toughness), while carbides are finely distributed within the bainite sheaths at a fixed orientation within lower bainite together with some minor interlath formation of carbides also here. Both forms of carbides have a specific orientation relationship between the bainite lath and the carbides in lower bainite[11].

Bainitic ferrite is very different from acicular ferrite in its shape. It possesses largely parallel sheaves of ferrite with a lath-like structure with some granule-like or rod-like cementite particles alongside or within the laths and along the prior austenite grain boundary network that can be seen clearly. The ferrite in bainite nucleates at the austenite grain boundaries[66,77-80], forming sheaves of parallel plates with the same

crystallographic orientation with respect to the parent austenite. Interlath carbide particles in upper bainite precipitate from the carbon-enriched retained austenite trapped in-between the platelets, or in the lower bainite, from within the supersaturated ferrite within the bainite lath[74].

Acicular ferrite micrographs, on the other hand, have been studied[81] in which the acicular ferrite transformation starts through the nucleation of the primary plates at non-metallic inclusion particles[33,52,54,56,82,84] and progresses by the formation of a new generation of secondary plates of ferrite nucleated at the interfaces of the austenite/AF primary plates[78]. Therefore, inclusions play an important role in the formation of acicular ferrite in low alloy welded metals[85,86] because they provide preferential sites for the nucleation[87-89] of the AF. The acicular ferrite matrix is characterized by a fine non-equiaxed ferrite or interwoven nonparallel ferrite laths[66,73,78,90], which have various sizes distributed in a random manner, very often described as a "chaotic arrangement" of plates showing fine-grained interlocking morphologies[78]. The prior austenite grain boundary network is completely eliminated and some fine M/A island constituents are scattered throughout the matrix[4]. This is due to the partitioning of carbon near the austenite/ferrite interface during the growth of acicular ferrite. The carbon content in the austenite will be increased and accordingly, the austenite's stability will be increased. As a result, the partial austenite that is carbon-enriched, remains and transforms to martensite during the subsequent cooling process, resulting in the M/A island constituent.

4.3 Mechanical properties of line pipe steel

4.3.1 The ratio of yield strength to ultimate tensile strength (YS/UTS)

A low YS/UTS ratio a very important parameter in the API specifications for line pipe steels as a high work hardening rate is required for this application. The lack of strain hardening in high YS/UTS steels means that there is a reduced potential for strain redistribution in thinned areas (thinned by corrosion or weld dressing) during service.

A high strength is, of course, required for line pipe to transport oil or natural gas at higher pressures. The American Petroleum Institute (API) specifies a YS/UTS ratio not greater than 0.93 for an application involving pipelines. The 11 mm line pipe strip steel currently produced by MITTAL Steel (South Africa) tends to have a slightly high YS/UTS ratio of typically 0.93. This ratio is affected by the microstructure of the steel and an optimised microstructure (such as acicular ferrite[32]) is, therefore, beneficial in achieving a lower YS/UTS ratio by carefully controlling the hot rolling, cooling and coiling schedules. This ratio is also an important issue in the development of higher grades of line pipe steels. The specification of line pipe steels of the America Petroleum Institute (API) is shown in table 4.1.

Table.4.1 Specification of line pipe steels of API[12]

Grades of steels	Minimum yield strength (MPa)	Minimum tensile strength (MPa)	Minimum Elongation (%)	Maximum YS/UTS
X65	448	530	20.5	0.93
X70	482	565	19	0.93
X80	551	620	17.5	0.93
X90	601	650	17.5	0.93

Some results showed that there is a slightly higher volume fraction of about 7% of martensite/austenite (M/A) constituent with a higher finish rolling temperature and, therefore, a more rounded stress-strain curve and a higher strain-hardening rate on this curve[1]. It is beneficial to lower the YS/UTS ratio and that author found that when the finish rolling temperature was 720 ºC the ratio was 0.69 and at 780 ºC, the YS/UTS was 0.65 and the volume fractions of M/A constituents were 4.6 and 7.0% respectively for a steel with composition 0.057% C, 0.27% Si, 2.04% Mn, 0.040% Nb, 0.112% Ti and 0.001% B[1].

4.3.2 Toughness

The Charpy toughness specification for the control of fracture initiation normally does not prove too onerous a requirement for higher grade line pipe. Toughness is also important for line pipe steels. Higher toughness can be obtained by lowering the carbon content and refining the ferrite grain size[38]. Niobium can improved Charpy toughness[25,26] at lower finishing temperature below 980 ºC[91]. A lower vanadium content is also useful to increase the toughness[38]. Acicular ferrite microstructures resulted in an improvement of the Charpy toughness with no deterioration of the strength[65,92] whereas bainite resulted poor toughness[66].

4.3.3 U-O pipe forming and Bauschinger effect

During U-O pipe forming, the plate materials are subjected to different cyclic strains, depending on the location along the circumference and in the wall. Typical examples of cyclic strain at locations 180˚ and 30˚ from the longitudinal seam are illustrated in figure 4.1[93].

At the 180˚ location where mill tensile test specimens are usually taken, the outer layer receives a tensile force during U-bending, a compressive force during O-bending, a compressive force during shrinking, and a tensile force during expansion. At the same time, the inner layer is subjected to a cyclic strain of compression, tension, compression and tension.

The total process from U-bending to expansion is not a simple work-hardening process but is actually very complex. On the other hand, during the flattening of a curved pipe section for tensile specimens, the Bauschinger effect and work hardening occur in the outer and inner layer respectively.

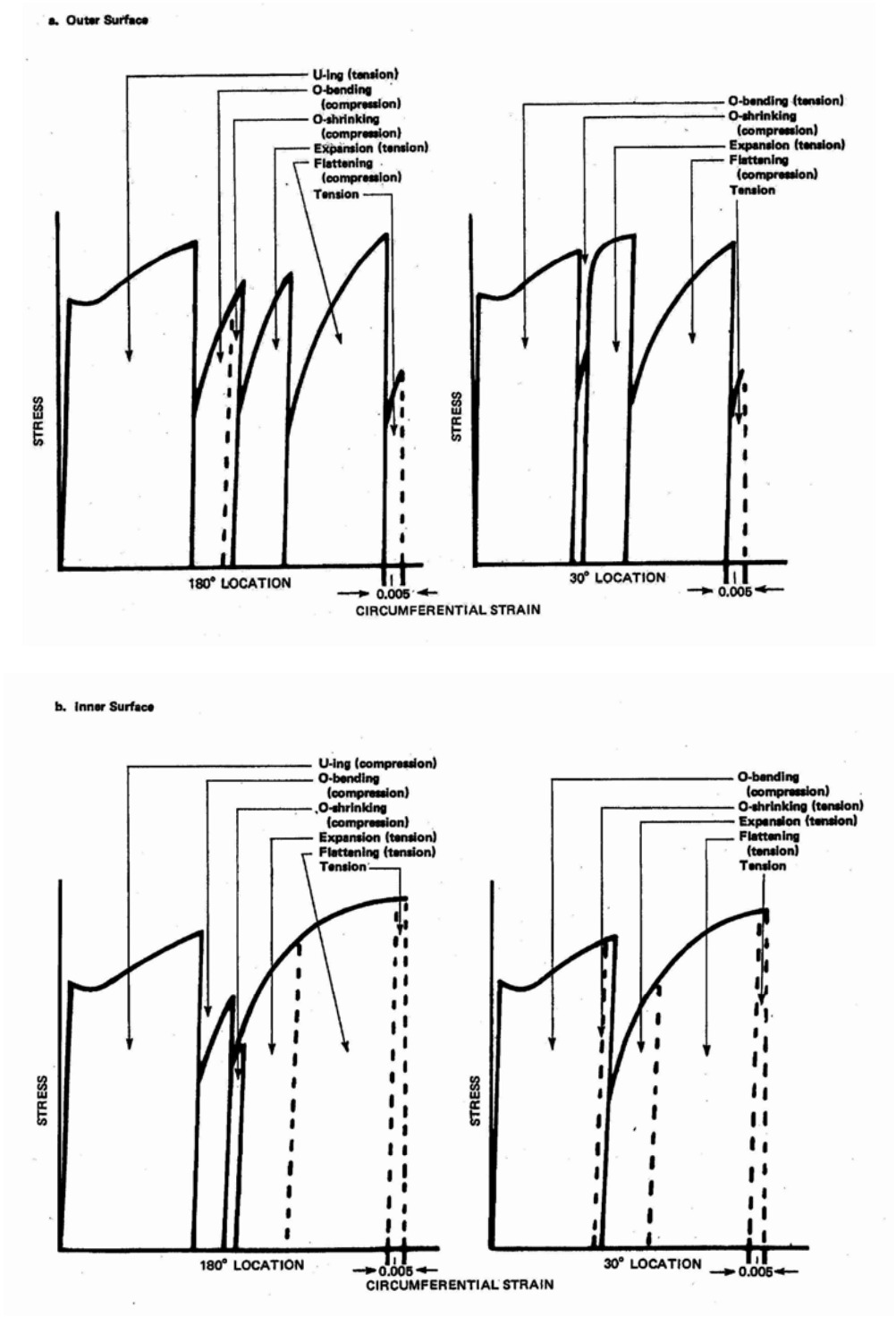

Figure 4.1 Schematic stress-strain curves for the outer (top) and inner (bottom) material during the U-O pipe forming process, with (left) at 180º and (right) at 30º from the welding line[93].

The Bauschinger effect is a characteristic material behavior that is highly dependent on testing conditions[94]. It results in the lowering of a proof-stress value after a

previous single uniaxial initial loading in the opposite direction. When hot rolled strip is converted into ERW line pipe, the pipe forming and sizing strains can significantly modify the pipe yield strength by virtue of the Bauschinger phenomenon. Various steels have different responses to the Bauschinger effect due to different stress-strain curves. Steels with a yield plateau have a Bauschinger strain equal to that corresponding to the strain equal to the yield elongation[95].

The Bauschinger effect is largely controlled by the carbon content and, to a considerably smaller degree, by the manganese content (figure 4.2). Grain size appears to have a minor influence, while the influence of residual-stress conditions is strong (figure 4.3)[94].

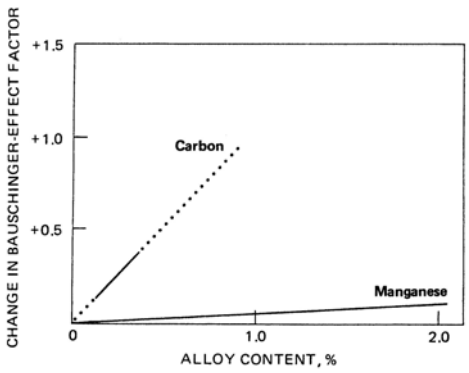

Figure 4.2 The change of the Bauschinger effect factor with carbon and manganese content[94].

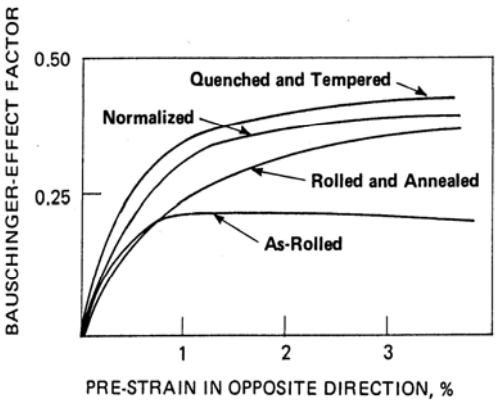

Figure 4.3 The Bauschinger effect in micro-alloyed steel. The upper two curves are for steels with 0.2% C, 0.4% Mn, unalloyed or alloyed respectively with Al, V or Nb. The lower two curves are for low-pearlite steels with less than 0.1% C, 2% Mn, and alloyed with Mo, Nb and Ti[94].

Work-hardening and the Bauschinger effect occur during the pipe-forming process and during the flattening of the tensile test pieces before the tensile test. In the pipe-forming process, work hardening by pipe expansion is more important than the Bauschinger effect, while the reverse is true during sample flattening. The ring-expansion test is used in measuring work hardening. The pipe after forming, has a considerably higher yield strength than the plate, which indicates that work hardening has taken place during pipe forming[96].

CHAPTER 5 BACKGROUND OF CURRENT SOUTH AFRICA LINE PIPE PRODUCTION

5.1 Line pipe steel composition of Mittal Steel (South Africa)

The chemical composition of the current Mittal Steel (SA) line pipe steel is provided in table 5.1.

Table 5.1 Typical chemical composition of the current 11 mm line pipe steel of Mittal Steel, (wt%)

C	Si	Mn	P	S	Cr	Ni	Mo	Cu	Al
0.066	0.258	1.583	0.011	0.004	0.021	0.007	0.001	0.007	0.037

V	Nb	Ti	Sn	B
0.062	0.037	0.017	0.001	0.0002

5.2 Parameters of the hot rolling process at Mittal Steel (SA)

The parameters of hot rolling of line pipe steels at Mittal Steel are shown in table 5.2.

Table 5.2 The parameters of the hot rolling process at Mittal Steel

Pass No		Reheating temperature, °C)	R1	R2	R3	R4	R5	R6	F1	F2	F3	F4	F5	F6
Force (tons)									1860	1552		1150	1076	1053
Temperature (°C)	in	1200	1150						1042	1008		938	915	896
	out							1050	1008	969		915	896	879
Gauges (mm)	in		240	195	160	120	85	60	40	28.87		21.02	15.76	13.51
	out		195	160	120	85	60	40	28.87	21.02		15.76	13.51	11.70
Strain/pass, ε			0.21	0.20	0.29	0.34	0.35	0.40	0.32	0.32		0.29	0.15	0.14
Total strain			1.79						1.22					
Strain rate (s^{-1})									9.4	16.1		22.6	20.9	26.2
Roll speed, V (ms^{-1})				~1.5	~1.5	~1.5	~1.5	~1.5		1.8		2.7	3.3	3.9
Inter-pass time, t, (s)				10	10	10	10	10		2.7	1.8	1	1.5	1.3
Inter-pass cooling rate (°Cs^{-1})				3	3	3	3	3						
Cooling rate after finishing (°Cs^{-1})			40 °Cs^{-1} —for 6mm of the final thickness of strip 20 °Cs^{-1} —for 11.5mm 50 °Cs^{-1} —for 5mm											
t/D (Thickness/Diameter)			~2.4%											

NB: F3-dummy for rolling

5.3 Typical microstructures and existing developments within Mittal Steel for line pipe steel

The optical microstructure of the current 11 mm wall thickness line pipe steel for Mittal Steel is shown in figure 5.1. This is the alloy that was used for a major part of the pipe-line for large-scale gas transportation from Mozambique to Secunda in a 2.5 meters diameter pipe line. The microstructure is a mixture of polygonal ferrite, acicular ferrite and pearlite.

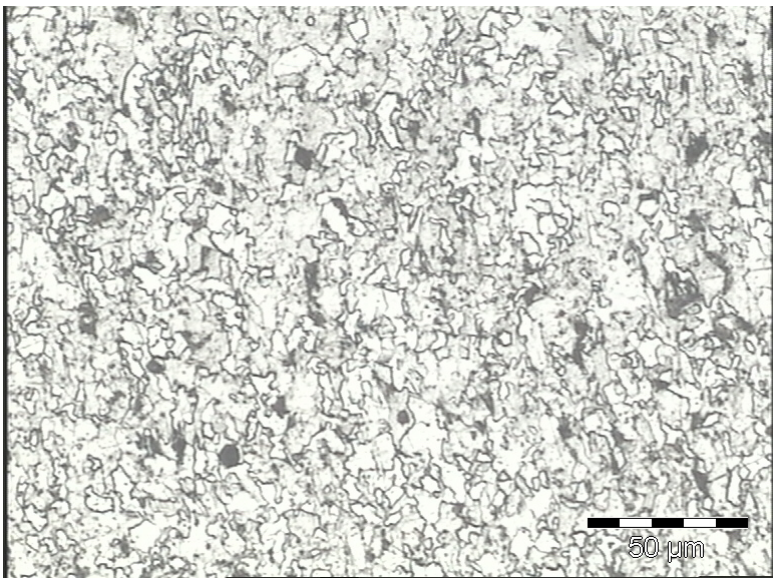

Figure 5.1 The optical microstructure of cast #521031, Mittal Steel line pipe

Smaller thin walled (about 6 mm thickness) pipelines may be used in future within South Africa for smaller scale gas distribution and reticulation to consumers. The current steel produced by Mittal Steel tends to have a slightly high YS/UTS ratio of 0.93, which is on the maximum limit of the specification of the American Petroleum Institute (API) of 0.93 for an application involving pipelines. The current line pipe steel consists typically of about 0.06% carbon with micro-alloying elements of titanium, niobium and vanadium (generally less than 0.05% for each) and is produced either via the Electric Arc Furnace (EAF) or Basic Oxygen Furnace (BOF) route.

5.4 The hypothesis for this study

The objective of this study is to establish the relationship between micro-alloying elements, the microstructure and deformation in austenite on the ratio of YS/UTS and other mechanical properties. Therefore, a study is to be undertaken on the austenite to acicular ferrite transformation with particular emphasis on the kinetics of the acicular ferrite formation and as affected by the above process variables. The experimental research would include a redesign of the chemical composition, dilatometer analyses, simulation of the controlled rolling process on a Gleeble 1500 (initially the work was started on a Gleeble 1500^{TM} model but halfway through the study, the Gleeble was upgraded to a Gleeble 1500^{D} DSI), microstructural observations, tensile tests, SEM and TEM investigations, etc.

5.4.1 Design of the chemical compositions of the investigated alloys

The V-content in the steel was decreased in this study because it only contributes to dispersion hardening as V(C,N) in ferrite. Its dispersion hardening is less than that of Nb in steels.

Niobium is a very important micro-alloying element in line pipe steels and formed one of the main-alloying elements considered in this study. It contributes to dispersion hardening (NbC in ferrite), promotes acicular ferrite formation (reduction of pearlite) and raises the T_{nr} (“pancake” of austenite). The niobium concentration was increased to about 0.045%wt (which is more than the 0.037% used currently by Mittal Steel).

Titanium is another micro-alloying element that retards austenite grain growth during reheating. The reheating temperature may be as high as 1225 ºC due to undissolved TiN. If titanium binds the free nitrogen in the steel, more niobium will be available in the ferrite to precipitate as NbC and will increase the precipitation hardening. Titanium can also control the shape of sulphide inclusions (TiS). Accordingly, the titanium addition was kept at levels of 0.017 to 0.022% in this study.

Molybdenum contributes to phase transformation hardening and can be used instead of V in the hardening of steels. It might benefit the increase in volume fraction of acicular ferrite and M/A islands that are useful to lower the ratio of YS to UTS. Molybdenum can diminish the Bauschinger effect during pipe forming. Thus, molybdenum was added to the experimental alloys in this study. The molybdenum additions considered here were 0.10%, 0.15% and 0.25%, respectively.

Carbon was slightly decreased to 0.05% C in this study for the purpose of improving the weldability of steel.

Summarising the target analysis above, the chemical compositions of the experimental alloys were designed as follows (Table 5.3):

Table 5.3 Design of chemical composition ranges of alloys that were investigated (in wt%)

C	Si	Mn	S	P	V	Nb	Ti
0.05	0.2-0.25	1.0-1.2	<0.005	<0.01	0	0.045	0.022

N	Cu	Ni	Al	Cr	Ca	Mo
0.006	0.007	0.007	0.03	0.02	0.002	0.1-0.25

5.4.2 Design of the controlled hot rolling process

The austenite grain size of the current Mittal Steel alloy, reference alloy #6 (Mo-free) was found to be 57 and 63 μm at 1225 ºC for 60 and 120 minutes respectively. Therefore, the reheating temperature of 1225 ºC was chosen for this study to provide almost complete dissolution of the niobium carbonitrides to achieve maximum precipitation hardening, but little austenite grain size coarsening.

In this study, the finish rolling temperature was maintained at about 870 ºC, i.e. above the A_{r3} and, therefore, with no deformation in the (α+γ) two-phase region.

The temperature range for rough rolling was chosen to be from about 1190 to 1000 ºC in this study, which is above the non-recrystallisation temperature T_{nr}. The total or cumulative true strain in the rough rolling stage was chosen to be about 1.4 with individual pass strains of more than 0.2.

The final temperature for the finish rolling stage was between 840 to 870 ºC. The finish rolling temperature in this stage was maintained above the A_{r3} temperature. The deformation for this stage was, therefore, carried out in the austenite non-recrystallisation region. The total strain in the finish rolling stage was about 0.54 in order to accumulate enough rolling strain within the austenite grains for the subsequent ferrite transformation, leading to a pass strain of more than 0.2 as well.

The initial and final thicknesses of the ingot and plate for laboratory hot rolling were planned to be 43 and 6 mm respectively, with a total heavy reduction of 86%.

The cooling rate after finish rolling has a significant effect on the subsequent microstructure of the line pipe steel. Rapid cooling is useful to increase the volume fraction of acicular ferrite and this contributes to good mechanical properties. It results in a continuous stress-strain curve, decreases the Bauschinger effect during pipe-forming and leads to a low ratio of YS/UTS. In this study, various cooling rates and with/without prior deformation in the austenite on the Gleeble were used to establish the effect of these parameters on the ratio of YS/UTS. For this purpose, the experimental challenge was how to measure the volume fraction of acicular ferrite?

The coiling temperature is also very important to the degree of precipitation hardening of line pipe steels. If the coiling temperature is too high, the precipitates become too

coarse. At low temperatures acicular ferrite may form, but the temperature cannot be too low because the precipitation requires diffusion, and in this study two coiling temperatures of 600 and 575 ºC were chosen. These are also the previous and the current coiling temperatures respectively used by Mittal Steel in their 11 mm strip steel for line pipe.

In this study a hypothesis that the acicular ferrite or an optimised mixture of acicular ferrite and polygonal ferrite, is the most suitable microstructure for decreasing the ratio of YS/UTS of steels, was, therefore, tested.

A series of tests on the Gleeble were also carried out to study the effect of cooling rate, coiling temperatures and deformation prior to transformation on the ratio of yield strength to ultimate tensile strength.

CHAPTER 6 EXPERIMENTAL PROCEDURES

This chapter describes the experimental procedures for the investigation, including the alloy design, the melting and casting of the ingots, the hot-rolling process, the testing of the austenite grain size and the presence and identification of undissolved particles, the determination of the non-recrystallisation temperature, the determination of the strain-free and the strain affected CCT diagrams and the determination of the mechanical properties, etc. Distinguishing between the acicular ferrite and polygonal ferrite in the microstructures of the samples was done by TEM through shadowed carbon extraction replicas and thin foils. The chemical compositions of the experimental alloys were typical of commercial line pipe steels with Nb-V-Ti micro-alloying elements with the current line pipe steel from Mittal Steel as the reference steel.

6.1 Alloy design

As indicated earlier and briefly summarised here again, the design of the experimental alloys was based on the considerations set out below.

1. The chemical compositions of HSLA line pipe steels are normally low in carbon and contain some micro-alloying elements that may be only one, or a combination of any two or three of the micro-additions (vanadium, niobium and titanium). A low carbon level was selected for improving the weldability and toughness, to provide less pearlite and more effective dissolution of niobium during reheating that will increase the precipitation hardening of these steels.
2. Niobium has strong dispersion hardening characteristics due to the formation of NbC in ferrite. It promotes the transformation to acicular ferrite that can be beneficial to lower the ratio of yield strength to ultimate tensile strength of these steels. Niobium also causes refinement of the austenite grains during the rolling process by raising the non-recrystallisation temperature (T_{nr}). Accordingly, a little more niobium was considered than in the current Mittal Steel alloy while

vanadium was reduced or left out, which decreases the non-recrystallisation temperature.

3. Titanium can retard the austenite grain growth during reheating of slabs due to the presence of TiN particles. As described above, considering the stoichiometric ratio of Ti to N (3.4 /1) and preventing MnS stringer inclusions, (which requires Ti/S in TiS of 1.5/1), the ideal titanium addition was calculated from equation (2.1).
4. The addition of molybdenum in Nb-containing steels can improve transformation hardening (increased volume fraction of acicular ferrite and M/A islands), can provide grain refinement and precipitation hardening. It also greatly suppresses or delays the formation of polygonal ferrite and pearlite[4]. Additions of molybdenum were, therefore, considered instead of the usual vanadium for enhancing the strength of the steels. In steels with molybdenum, the stress-strain curve of the as-rolled plate is usually continuous, without an upper yield points[33]. This may provide control of the Bauschinger effect and contribute to an increase in yield strength from plate to pipe.

Thus, the newly designed alloys that were made up, all had the same low carbon, niobium and titanium levels but were made with and without vanadium, and also had varying amounts of molybdenum.

6.2 The melting of the experimental alloys

Sections from the currently produced line pipe steel from Mittal Steel were used as feed stock material for the melting of the new alloys in a 50 kg vacuum induction melting furnace at Mintek. The liquid steel was cast into ingots of 43 × 66 × 235 mm. The chemical compositions of the five new alloys are listed in table 6.1. The Mittal Steel line pipe steel is included in the table as a reference.

Table 6.1 Chemical compositions of the experimental alloys, in wt.%

Alloy #	C	Si	Mn	P	S	Cr	Ni	Mo
1	0.05	0.29	1.21	0.014	0.011	0.07	0.07	0.01
2	0.06	0.25	1.29	0.018	0.01	0.05	0.04	0.09
3	0.05	0.23	1.05	0.019	0.011	0.04	0.04	0.09
4	0.05	0.24	1.31	0.019	0.011	0.05	0.04	0.12
5	0.05	0.25	1.14	0.019	0.011	0.05	0.04	0.22
6(Mittal Steel)	0.066	0.26	1.583	0.011	0.004	0.021	0.007	0.001

Cu	Al	Co	V	Nb	Ti	Sn	B	Free-N
0.02	0.004	0.006	0.06	0.055	0.017	--	0.0001	0.0068
0.03	0.055	0.009	<0.005	0.05	0.019	0.003	0.0003	0.0035
0.03	0.054	0.008	<0.005	0.051	0.019	0.003	0.0002	0.0032
0.02	0.055	0.009	<0.005	0.052	0.019	0.003	0.0003	0.0032
0.02	0.065	0.01	<0.005	0.055	0.021	0.003	0.0003	0.0027
0.007	0.037	--	0.062	0.037	0.017	0.001	0.0002	--

6.3 The effect of reheating temperature and soaking time on the austenite grain sizes

The samples from the cast ingots were machined into cubes of about 10 × 10 × 10 mm. Two methods were used to process these samples in order to measure the austenite grain size. The first was to reheat the samples at temperatures of 1150, 1200, 1225 and 1250 °C, respectively, and then quench them into water. The samples were etched using many different etchants (see table 6.2), but the results revealed that these etchants were not suitable to reveal the prior austenite grain boundaries for the alloys studied. The carbon content of the alloys was probably too low for this. The more successful technique was a modified McQuaid-Ehn method by carburising the samples after reheating in argon, in-situ within the austenite region in a dry carbon monoxide gas atmosphere at 927 ºC for up to 5 hours directly after reheating at the above four austenitisation temperatures, i.e. without going through the ferrite transformation. Pro-eutectoid cementite formed on the prior austenite grain boundaries during very slow cooling from the carburisation temperature at 927 ºC down to 690 ºC at which temperature the sample was removed from the furnace. Thus,

the cementite layers indicated the sites of the original austenite grain boundaries, which then became easy to measure. The carburising process is illustrated in figure 6.1. After carburisation, the samples were polished and etched in a 2% Nital solution and then the original austenite grain sizes were measured by the mean linear intercept method[97].

Table 6.2 The composition of the etchant solutions

Solution Number	**Chemical**	**Quantity**
#1	Picric acid	1 g
	Hydrochloric acid	5 ml
	Ethanol alcohol	95%
#2	$FeCl_3$	1 g
	H_2O	100 ml
#3	$FeCl_3$	1 g
	Hydrochloric acid	5 drops
	H_2O	100 ml
#4	Sodium bisulphite	34 g
	H_2O	100 ml
#5	Hydrochloric acid	40 ml
	Sulphuric acid	10 ml
	H_2O	50 ml
#6	10% aq. Oxalic acid	28 ml
	H_2O_2(30%)	4 ml
	H_2O	80 ml

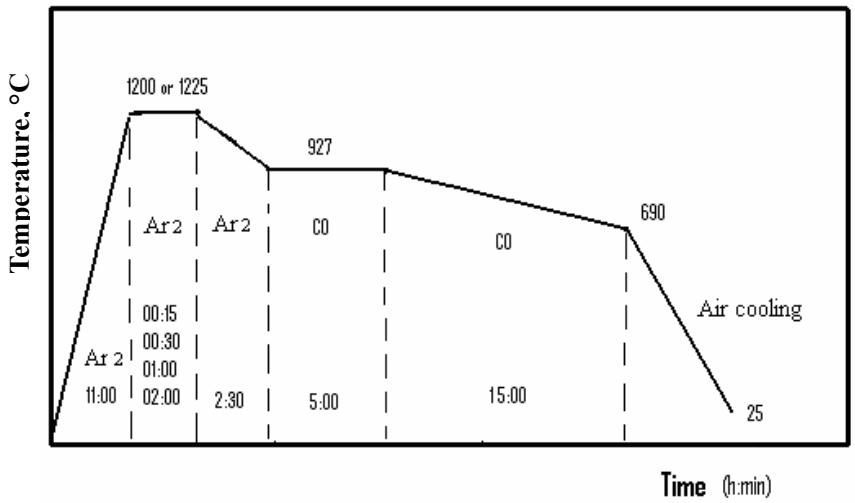

Figure 6.1 Schematic of the modified McQuaid-Ehn carburising process of the samples directly after reheating.

6.4 Measuring the presence and composition of undissolved particles

During reheating, any undissolved small particles will retard the austenite grain growth. Before entering the first rough rolling pass, a fine austenite grain size is beneficial to the later strength and toughness of the steels. The quantity and the size of the undissolved particles are related to the reheating temperature. Austenitisation temperatures ranging from 1150 to 1250 °C were employed, together with soaking times of 15 to 120 minutes for this part of the investigation. The samples were quenched into water or were fast cooled in helium gas. The details of these treatments are listed in table 6.3 below. The samples were mechanically ground and polished after the treatment, then were lightly etched in a 2% Nital solution without an apparent visible optical microstructure of the matrix, and vacuum coated with carbon. The shadowed carbon extraction replicas were similarly made, also after light etching in 2% Nital, then the vacuum application of Au-Pd shadowing at an angle between 20 to 40º before vertical coating of the carbon. The size of the particles was measured on the micrographs obtained from the transmission electron microscope (TEM) and their volume fraction calculated using the following equation[98]:

$$f = \frac{\pi}{6} N_s (\overline{\chi}_{Al}^2 + \sigma_{Al}^2) \qquad (6.1)$$

$$\sigma_{Al}^2 = \frac{n\Sigma x_{Al}^2 - (\Sigma x_{Al})^2}{n(n-1)} \quad (6.2)$$

where $\overline{x}_{Al}$ is the planar arithmetic mean of the particle diameter;

f is the volume fraction of particles;

N_s is the total number of particles intersecting a unit area;

σ_{Al}^2 is the standard deviation of the particle size distribution;

x_{Al} is the diameter of a particle;

n is the total number of particles measured.

Table 6.3 Temperatures and soaking time of the treatment for undissolved particles

Temperature (ºC)	**Time (min)**		
1150	15	60	120
1200	15	60	120
1225	15	60	120
1250	15	60	120

6.5 Non-recrystallisation temperature (T_{nr})

The finishing temperature of rough rolling is associated with the non-recrystallisation temperature (T_{nr}) and heavy reductions must take place within this recrystallisation region at temperatures higher than the T_{nr} in order to obtain a fine recrystallised austenite grain size at the start of finish rolling below the T_{nr}. This is beneficial to high strength and good toughness of the steels. Accordingly, the non-recrystallisation temperature is an important parameter that should be considered when the hot rolling process is designed. Many researchers have studied the recrystallisation of austenite[99-107] and some mechanisms have been proposed[108-110]. The

non-recrystallisation temperature may be a function of the parameters[99,111-113] of the rolling process, such as pass strain[114,115], strain rate and inter-pass time[48], and may also depend on the content of micro-alloying elements[116], etc. The hot torsion test has been widely used to simulate industrial hot rolling processes[117-121]. In this study, the recrystallisation behaviour of the steel was investigated during multi-pass compression deformation on a Gleeble hot working facility on cylindrical samples of 8 mm in diameter and 15 mm in length that were machined from the as-cast ingots.

6.5.1 Testing schedule for the determination of the T_{nr}

Reheating temperatures should be high enough to dissolve all the precipitates (mainly the Nb precipitates, but except the TiN) because the micro-alloying elements affect the non-recrystallisation temperature. The reheating temperature for Nb precipitates can be determined from the following equation[122,123]:

$$\log[Nb]\left(C+\frac{12}{14}N\right)=2.26-\frac{6770}{T} \qquad (6.3)$$

The calculated solution temperatures for Nb(C,N) in the experimental alloys are listed in table 6.4.

Table 6.4 Calculation equilibrium Nb carbonitride solution temperature

Alloy number	Solution temperature of Nb(C,N) (ºC)
1	1145
2	1149
3	1179
4	1130
5	1137

Laasraoui[124] reported that the niobium carbonitrides remained undissolved at reheating temperature of 1100 ºC for an 0.04% Nb steel. Thus, a maximum reheating temperature of 1225 ºC was selected here.

Samples of alloy #6 (the current Mo-free Mittal Steel alloy) were heated to 1225 °C at a heating rate of 100 °Cmin^{-1} and held at this temperature for 15 minutes. The multi-pass compression tests were carried out using the test parameters shown in tables 6.5 and 6.6. Pass strains, ranging from 0.15 to 0.32, and inter-pass times ranging from 4 to 50 seconds were employed, at a constant strain rate of 1 s^{-1}. In two particular tests, the inter-pass time and pass strain were held constant. Another test of strain rate ranging from 0.1 to 2.22 s^{-1}, was also employed at a constant pass strain of 0.2 and constant inter-pass time of 8 seconds (see table 6.7). Such a multi-pass compression testing schedule is illustrated schematically in figure 6.2 below.

Table 6.5 Testing parameters for T_{nr} at strain ranging from 0.15 to 0.32

Inter-pass time (s)	8	8	8	8	8	8
Strain rate (s^{-1})	1	1	1	1	1	1
Strain/pass	0.15	0.2	0.24	0.28	0.30	0.32

Table 6.6 Testing parameters for T_{nr} at inter-pass times ranging from 4 to 50 seconds

Inter-pass time (s)	4	6	8	15	20	30	35	40	50
Strain rate (s^{-1})	1	1	1	1	1	1	1	1	1
Strain/pass	0.2	0.2	0.2	0.2	0.2	0.2	0.2	0.2	0.2

Table 6.7 Testing parameters for T_{nr} at strain rate ranging from 0.1 to 2.22 s^{-1}

Inter-pass time (s)	8	8	8	8	8	8	8	8	8
Pass strain, ε	0.2	0.2	0.2	0.2	0.2	0.2	0.2	0.2	0.2
Strain rate (s^{-1})	0.1	0.47	0.9	1.22	1.38	1.67	1.80	2.0	2.22

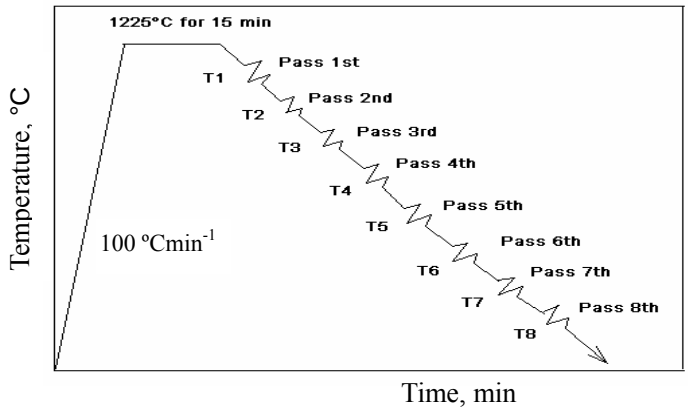

Figure 6.2 Schematic schedule employed in the multi-pass compression tests for the T_{nr}.

6.5.2 The determination of the non-recrystallisation (T_{nr})

A typical set of curves of the true flow stress versus true strain from a multi-pass compression test is illustrated in figure 6.3.

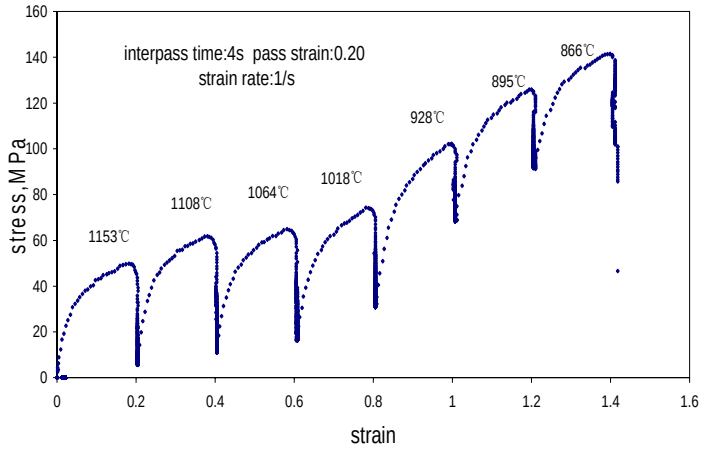

Figure 6.3 The curves of flow stress versus strain in a multi-pass compression test on alloy #6.

The mean flow stress of each pass was calculated from the following equation and the flow stress-strain curve (see figure 6.3):

$$\bar{\sigma} = \frac{1}{\varepsilon_b - \varepsilon_a} \int_{\varepsilon a}^{\varepsilon b} \sigma d\varepsilon \qquad (6.4)$$

The non-recrystallisation temperature was determined from the relationship between the mean flow stress (MFS in MPa) of each pass and the inverse temperature (1/T in K^{-1}) of the compression deformation, as illustrated in figure 6.4. This typical curve is divided into two stages by a slope change in the two straight line sections. In the lower slope stage (which corresponds to a high temperature deformation), full recrystallisation takes place during the pass because there is no strain accumulation and the increase in the mean flow stress is solely due to the decrease in temperature of the inherent strength of a well annealed microstructure. However, in the higher slope stage (deformation below the T_{nr}), there is only partial dynamic recrystallisation, or no recrystallisation at all, indicating that the strain is accumulated from pass to pass, and the mean flow stress increases more rapidly with decreasing temperature[125]. The intersection of two straight lines provides the T_{nr}.

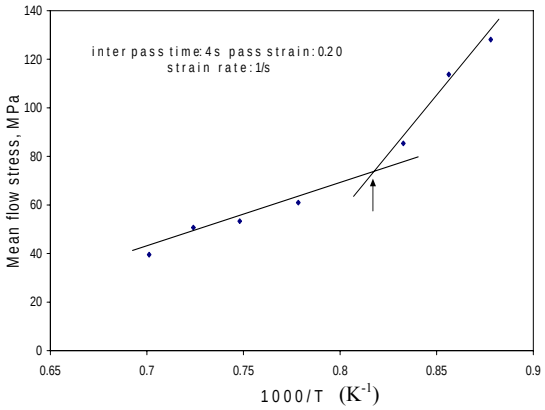

Figure 6.4 Determining T_{nr} from the mean flow stress in MPa versus the inverse pass temperature in K, during a multi-pass compression test on alloy #6.

6.6 CCT-diagram

The alloys used for the CCT diagrams, were the as-cast alloy #5 (with 0.22% Mo) and alloy #6 (Mo-free) (Mitall Steel reference alloy). The chemical compositions of alloys #5 and #6 were listed in table 6.1. Samples of with a size of a 15 to 16 mm long cylinder with a diameter of 7 mm were used for the strain affected CCT tests, and a 8 to 9 mm long cylinder with a diameter of 7 mm for the strain-free CCT test were used. The temperatures of phase transformations were measured by the C-strain facility on the Gleeble which measures the change in diameter of the sample during cooling for the strain affected CCT tests.

6.6.1 The A_{c1} and A_{c3} test

The A_{c1} and A_{c3} are the important critical equilibrium temperatures for starting and completion of the austenitisation transformation during phase transformation of low carbon hypoeutectoid steels (less than 0.77% C). The determination of the A_{c1} and A_{c3} temperatures were made on a single-LVDT THETA dilatometer facility. Phase transformations are normally associated with a non linear volume change in the temperature range of the transformation. The linear thermal expansion or contraction of the samples, therefore, takes place in a manner that allows the subtraction of the linear relationship between dilatometry and temperature from the non-linear transformation portions. A schematic sketch of the dilation with temperature is represented in figure 6.5[126]. Figure 6.6 shows the schematic determination of the A_{c1} and A_{c3} temperatures of steels on the heating curve of dilation versus the testing temperature. In order to completely dissolve all the Nb-alloyed precipitates in this study, e.g. the Nb(C,N), the reheating temperature was chosen as 1225 ºC for 15 minutes with a heating or cooling rate to and from this temperature of 3 ºCmin^{-1} for equilibrium conditions. Samples for the THETA dilatometer were cylinders with a 7 mm diameter and a 10 mm length. The chamber containing the samples was kept at a vacuum of 10^{-4} torr, to prevent any significant oxidation of the samples.

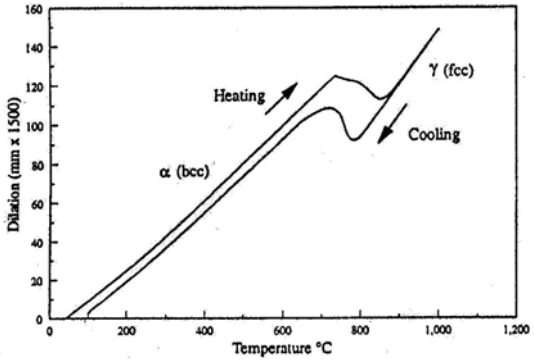

Figure 6.5[126] Schematic dilation as a function of testing temperature.

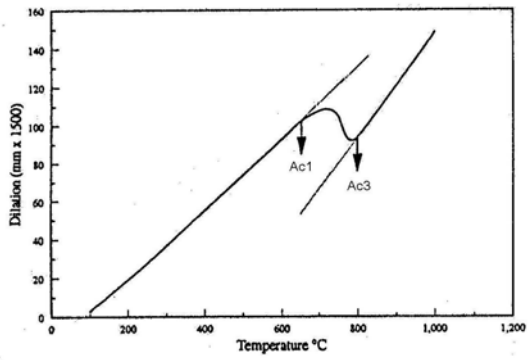

Figure 6.6[126] Schematic determination of the A_{c1} and A_{c3} temperatures on the heating curve.

6.6.2 CCT diagram without prior deformation

The continuous cooling transformation (CCT diagram) without prior deformation was also made on the THETA Dilatometer. The reheating rate was taken as 100 ºCmin^{-1} up to 1225 ºC and held for 15 minutes at this temperature for the purpose of complete dissolution of the Nb-precipitates. The samples were subsequently cooled down to 980 ºC at a rate of 5 ºCs^{-1} and held for 5 minutes at this temperature before finally, cooling down to 25 ºC at the various almost linear cooling rates of 0.1, 0.2, 0.5, 1, 2, 5, 8, 10 and 20 ºCs^{-1}, respectively. The sample chamber was evacuated before cooling after 980 ºC and the cooling media was either flowing argon or helium gas, depending on the required cooling rate. The chamber of the THETA dilatometer and the schematic test schedule are illustrated in figures 6.7 and 6.8, respectively. After cooling, samples were polished and etched in 2% Nital and the microstructures examined with an Olympus PMG3 optical microscope. A combination of the optical micrographs and the cooling curves of dilation with the test temperature, were used to determine the phase transformation temperatures. The CCT diagram was then constructed from the various curves of temperature on a linear scale with the test time on a log scale and the phase transformation temperatures indicated on these.

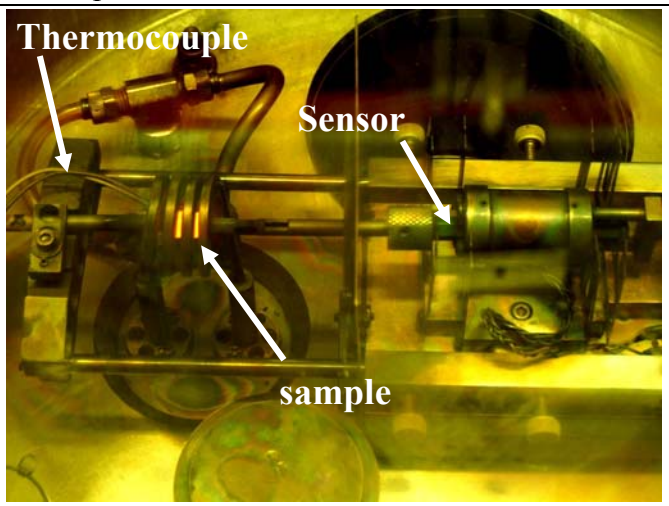

Figure 6.7 Dilatometer chamber

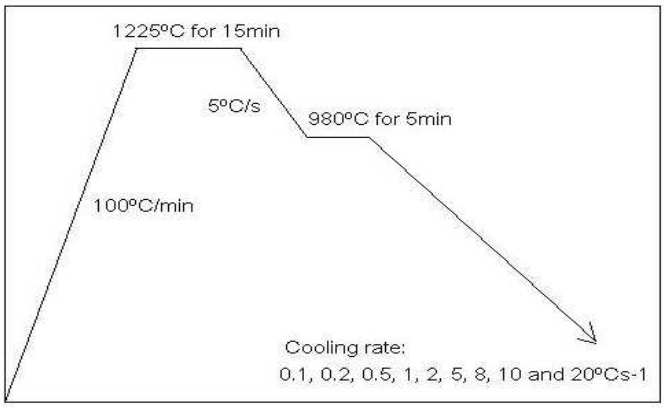

Figure 6.8 Schematic schedule of the test for the CCT diagram on the THETA Dilatometer.

6.6.3 Strain affected CCT diagram

The stain affected CCT diagram with prior deformation, was carried out on Gleeble 1500^{D} DSI hot simulator. The reheating rate was also 100 ºCmin^{-1} up to 1225 ºC and held for 15 minutes at this temperature for the complete dissolution of precipitates in an argon atmosphere. The samples were then cooled down to 860 ºC at 10 ºCs^{-1}, and held for 5 minutes at this temperature. The samples were then compression deformed with a strain of 0.6 (45% reduction below the T_{nr}) at 860 ºC at a strain rate of 0.5 s^{-1}. Samples were finally cooled down to room temperature after deformation, at the various linear cooling rates of 0.1, 0.2, 0.5, 1, 2, 5, 8, 10, 20 and 40 ºCs^{-1}, respectively. The cooling media was also argon (for a slow cooling rate) or helium gas (for a rapid

cooling rate). The steps for preparing the micrographs were the same as for the strain-free CCT diagram above. The chamber of the Gleeble hot simulator and the schematic test schedule are illustrated in figures 6.9 and 6.10, respectively. The C-gauge facility of the Gleeble was used to measure the dilation of the sample during cooling after compression deformation.

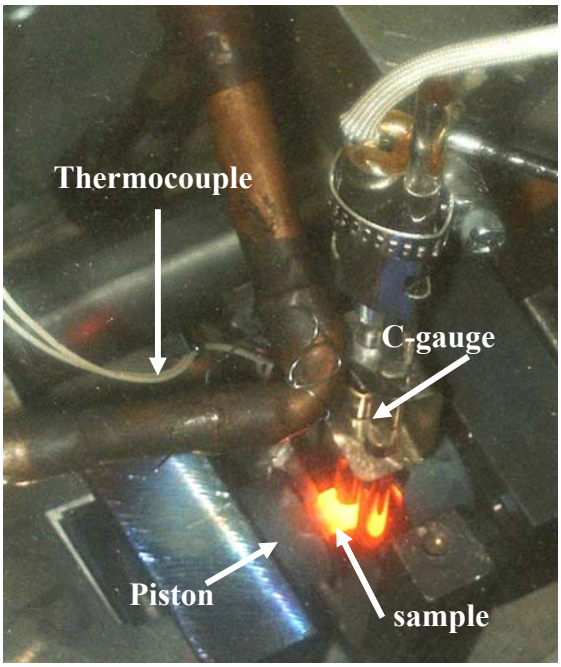

Figure 6.9 Chamber of the Gleeble 1500^{D} DSI

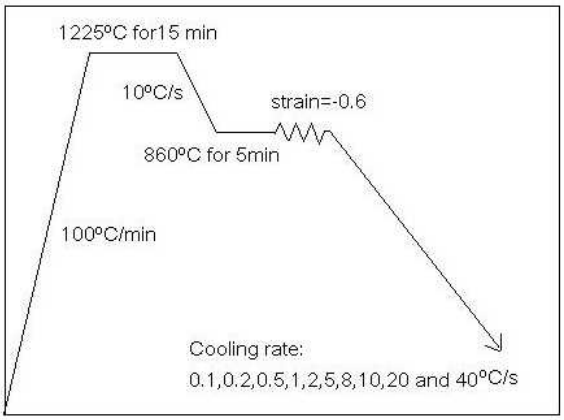

Figure 6.10 Schematic schedule of the test for the strain affected CCT diagrams on the Gleeble.

6.7 The thermo-mechanical process

6.7.1 Cooling unit

A specially constructed cooling unit was used to cool the laboratory melted ingots after hot rolling in a controlled manner. The cooling unit consists of nozzles, a water pump, control valves, and a water box etc. The experimental arrangement is shown in figure 6.11. The coolant is fed with compressed air and sprayed onto the cooling samples through nozzles. The linear distance between the nozzles was about 70 mm, so that uniform cooling of samples of about 100 × 300 mm could be attained. The cooling rate, for instance, was 21 °Cs^{-1} using fresh water at 24 °C as the coolant and with compressed air spraying of the water with an air pressure of 580 MPa. A higher figure of 47 °Cs^{-1} was achieved with a 10% NaCl aqueous solution instead of water.

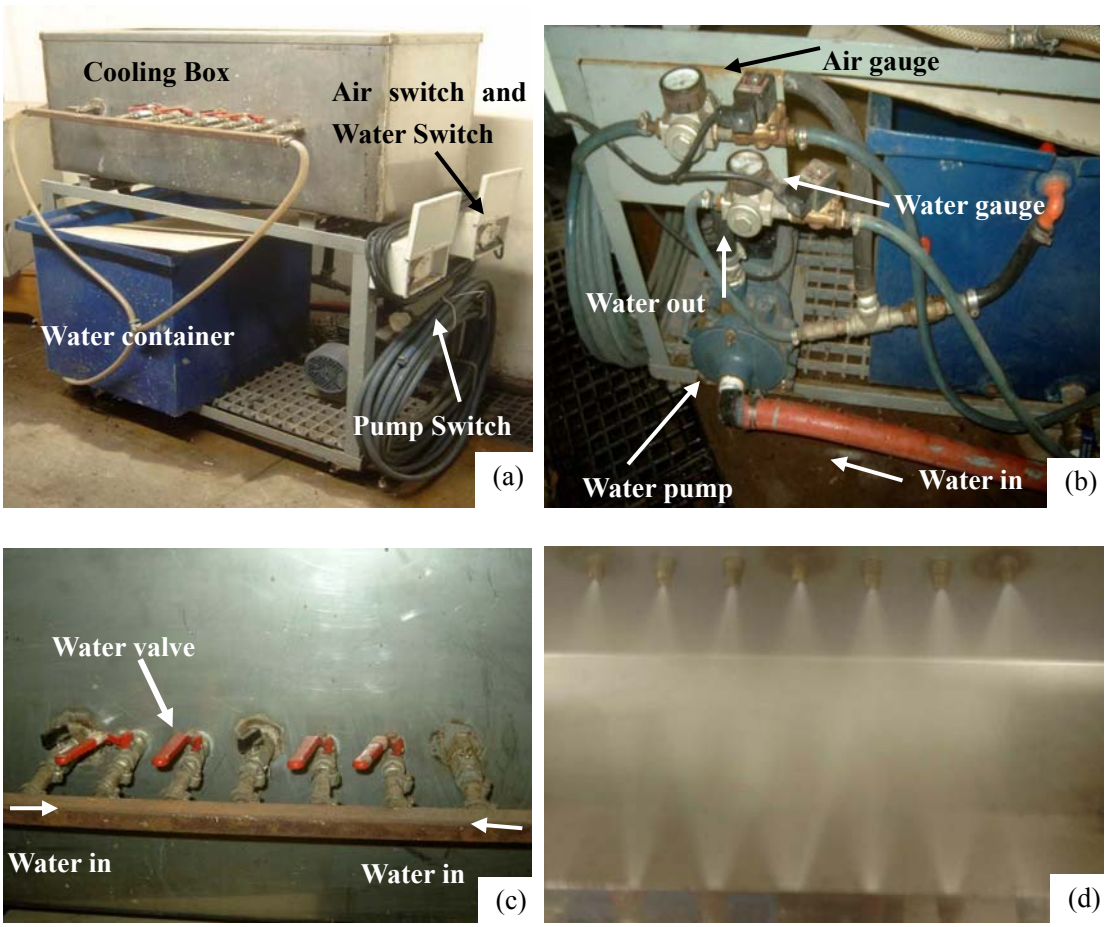

Figure 6.11 Experimental arrangement of the cooling unit for controlled cooling: (a) overall view, (b) controller for mixing of gas and water, (c) valves for the nozzles and, (d) cooling spray in the chamber from the spraying jets.

6.7.2 Hot rolling process of the laboratory ingots

The schedule for the laboratory hot rolling of the ingots, i.e. the pass strain, the total reduction and inter-pass times etc., were controlled as far as possible to optimise the process for austenite grain refinement[114,115]. The experimental casts were hot rolled on a two-stand laboratory hot rolling mill equipped with 10 inch rolls. The ingots of a machined 43 × 90 × 66 mm size for the alloys #1 to #6 were reheated and hot rolled to 6 × 100 × 300 mm plates with the final thickness of 6 mm chosen to simulate a possible future reduced gauge for Mittal Steel from their current 11 mm strip.

6.7.2.1 Reheating before laboratory hot rolling

From the results of the study of the effects of temperature and time on the austenite grain size, a reheating temperature of 1225 °C and a time of 60 minutes were taken. This is quite safe as it has been reported that austenite grains will not coarsen unduly before an austenitisation temperature of about 1250 °C is reached in V-Nb-Ti micro alloyed steels[35].

6.7.2.2 Rough rolling of the laboratory hot rolling

As indicated before, the metallurgical function of roughing is to refine the coarse austenite grains after the reheating and soaking to achieve the finest possible dynamically recrystallised grains before entering the finish rolling below the T_{nr}. Pass strains should, therefore, be at least 0.2 or higher to promote Dynamic Recrystallisation (DRX) during rough rolling to produce finer recrystallised grains. The starting temperature for rough rolling of the laboratory cast ingots was between 1148 and 1190 °C and five passes in this roughing stage were undertaken, with a total roughing strain of 1.43.

6.7.2.3 Finish rolling of the laboratory hot rolling

As before, the objective of this stage is to accumulate sufficient rolling strain within the austenite grains to promote a finer ferrite transformation after rolling. Ferrite nucleation sites are, therefore, greatly multiplied in number and a very fine ferrite grain size can be generated during the subsequent controlled cooling[6]. In this study three passes were used with a total strain of 0.54 and the finish rolling temperature was maintained between 857 and 865 °C.

6.7.2.4 Cooling rate after laboratory finish rolling

The cooling rate (V_c) and the finishing temperature (T_c) of the accelerated cooling after finish rolling, are important parameters of the thermo-mechanically controlled processing for the experimental alloys to achieve their optimum strength and controlling the T_c and V_c may lead to the control of the precipitation of carbonitrides during the accelerated cooling[9]. A rapid cooling rate helps to promote finer precipitation of Nb(C,N), ferrite grain refinement and acicular ferrite formation. The latter is preferred for a low ratio of yield strength to ultimate tensile strength[4], and it also avoids the development of any pearlite in the microstructure. A rapid cooling rate of 47 $°Cs^{-1}$could be achieved in the cooling box by using an aqueous solution of 10% NaCl for alloys #1 to #5 while a rate of 39 $°Cs^{-1}$could be obtained for the Mo-free alloy #6.

6.7.2.5 Simulation of coiling after laboratory hot rolling

The coiling temperature will influence the effectiveness of Nb-carbonitride but especially V(C,N) precipitation in the ferrite, thus controlling precipitation strengthening of these steels. If the coiling temperature is high, the precipitates will become coarser during coiling. A coiling temperature of 600 °C was selected for the study of these alloys as this was also the temperature used in the past by Mittal Steel before they recently lowered it to 575 ºC. After reaching 600 °C in the cooling box, the small plates were placed in a furnace at 600 °C until the temperature became

uniform throughout the plate. Thereafter they were well insulated for 24 hours using a generous covering of vermiculite for a slow cool simulating the actual coiling process in the plant.

6.7.2.6 Hot-rolling process curve

The hot-rolling process schedule is illustrated schematically in figure 6.12. The symbols R and F in the figure refer to the rough and finishing passes, respectively,

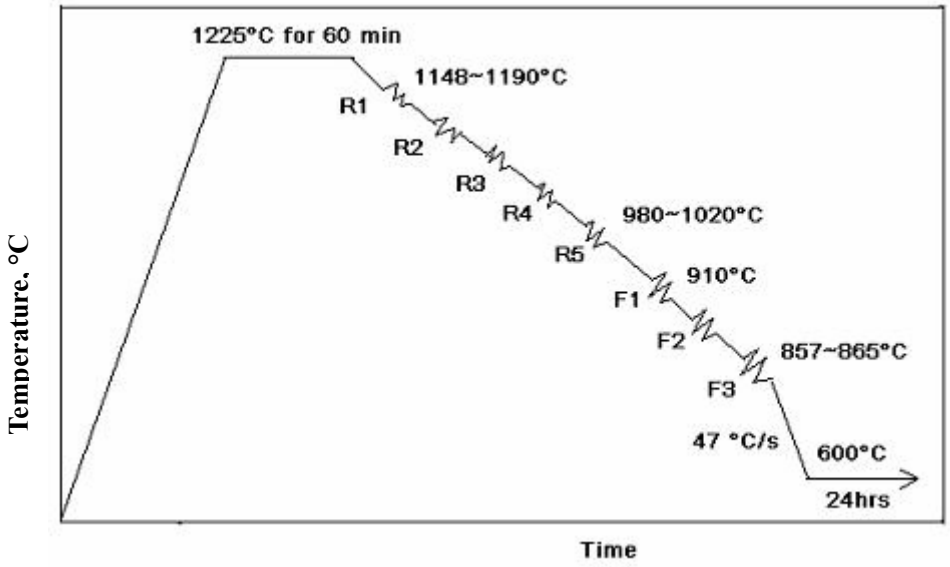

Figure 6.12 Schematic schedule of the hot rolling process on the experimental alloys.

6.8 The identification of acicular ferrite

The optimum microstructure of line pipe steels appears to be one that contains acicular ferrite and some polygonal ferrite. Acicular ferrite is very different from polygonal ferrite and bainitic ferrite. Polygonal ferrite, as the name implies, has polygonal boundaries with a carbon concentration in the ferrite that is almost uniform together with a lower dislocation density. Acicular ferrite, on the other hand, is characterised by fine non-equiaxed or interwoven nonparallel ferrite laths, which have various grain sizes and are arranged in a random manner[78]. Some M/A (martensite/austenite) islands and a high density of dislocations in-between the AF are common[11]. The carbon content in the M/A islands is higher than that in the surrounding matrix and accordingly, these islands are carbon-enriched

martensite/austenite islands whose formation may be attributed to the partitioning of carbon during the transformation to acicular ferrite and the post-transformation of carbon-enriched austenite. During accelerated cooling followed by the coiling process, part of the carbon-enriched austenite transforms to martensite and the remaining austenite will coexist with the martensite[73]. The accepted transformation model of acicular ferrite is a mix of diffusion and shear transformation[4,9,11,43].

Acicular ferrite contributes to a low yield strength and a higher tensile strength due to the lower carbon in the matrix and the M/A islands having a high density of dislocations and this, therefore, leads to a lower YS/UTS ratio. It was found initially that it was easy to confuse acicular ferrite with polygonal ferrite under an optical microscope when samples were etched in 2% Nital because the grain boundaries between them do not become clearly etched. Therefore, one of the key aspects of the experimental techniques in this study was how to distinguish between acicular ferrite and polygonal ferrite in low carbon, Nb-Ti micro-alloyed steels. Various techniques were initially attempted to identify the acicular ferrite, including the use of optical microscopy, Scanning Electron Microscopy (SEM), Transmission Electron Microscopy (TEM) using carbon extraction replicas with and without shadowing and finally, thin foil TEM samples.

6.8.1 Observation with optical microscopy and by SEM

Samples taken after hot rolling that were etched in a 2% Nital solution, were examined with an Olympus PMG3 optical microscope, both JEOL 5800LV and 6000F high resolution SEM, respectively. Acicular ferrite could not be distinguished from polygonal ferrite on the micrographs after etching with a light (5 seconds) or a deep etch (up to 120 seconds) under the optical microscope and SEM.

6.8.2 Observation of replicas by TEM

6.8.2.1 Preparing replicas without shadowing

Firstly, the polished samples were deeply etched from 30 to 60 seconds in a 2% Nital solution and thoroughly washed to remove all loose etching debris from the surface. Carbon coating was done under vacuum on the etched surface of the samples and the coating separated from the sample's surface in a mixture of 7 ml nitric acid and 75 ml ethanol before floating-off in distilled water.

6.8.2.2 Preparing shadowed carbon extraction replicas

The etched surface of the samples was first shadowed through vacuum evaporation with a gold-palladium alloy before the vertical deposition of carbon. Deep etching from 30 to 60 seconds was employed before the shadowing and the shadowing angle with respect to the surface was varied from 20° to 40°. The carbon was then coated vertically onto the shadowed layer. The technique used for separating the carbon film from the sample was the same as described above for the replicas without shadowing.

6.8.3 Thin foil TEM samples

Thin foil samples were used to further distinguish between acicular ferrite and polygonal ferrite and to also validate the results of the shadowed replicas in the TEM. Thin slices of material were cut by electro-discharge in a wire-cutting machine in order to reduce any adverse effect of deformation on the dislocation density in the samples that could have formed from mechanical cutting. The disc size was 3 mm in diameter and 0.6 mm in thickness and the procedure for preparing the thin foil samples was as follows:

- The original cylinder of material with dimensions of 3 mm diameter and 15 mm length was machined in a lathe;
- Five discs of 3 mm diameter and 0.6 mm thickness were cut from the cylinder with the electro-discharge wire-machine;
- The disc samples were carefully and lightly polished to between 50 to 80 μm

in thickness on fine grinding paper;

- The final thinning was done by electro-polishing with a solution of 1.25 l acetic acid, 0.08 l perchloric acid and 0.7 g chromium oxide at 25 °C.

All samples for replicas and thin foils were examined in a Philips CM200 TEM, operated at 60 or 200 KV, respectively.

6.9 Test of subsize samples on the Gleeble with various cooling rates, coiling temperatures and prior deformation

In order to study how some parameters of the controlled hot rolling process influence the YS/UTS ratio of steels, a series of experiments were planned. These parameters include cooling rates, coiling temperatures and deformation in the austenite.

The cooling rate after hot rolling has a strong effect on the fraction of acicular ferrite in Nb-Ti micro-alloyed steels and particularly, accelerated cooling after finish rolling helps to increase the volume fraction of acicular ferrite which may, in turn, influence the YS/UTS ratio. The coiling process controls the precipitation of particles in the matrix of these steels which affects dispersion hardening. The reduction during hot rolling also has an effect on the CCT diagram of these steels as well. A series of tests were designed for this purpose.

6.9.1 Hot rolling plates for Gleeble samples

Alloys #3 and #6 were selected for these tests. Casts of these alloys, firstly, were hot rolled to 6 mm thickness (the parameters of the hot rolling for plates are shown in Appendix H). Two types of preliminary samples were machined: the first type A to a rectangular size of 6 ×10 × 100 mm was used to study the effect of cooling rates and coiling temperature without deformation (figure 6.13-(a)), while the other type B shown schematically in figure 6.13-(b), was used to study the effect of prior compression in austenite, from there the shorter gauge length. At this stage, the gauge

lengths had not been machined into the rectangular samples, hence their being called "preliminary".

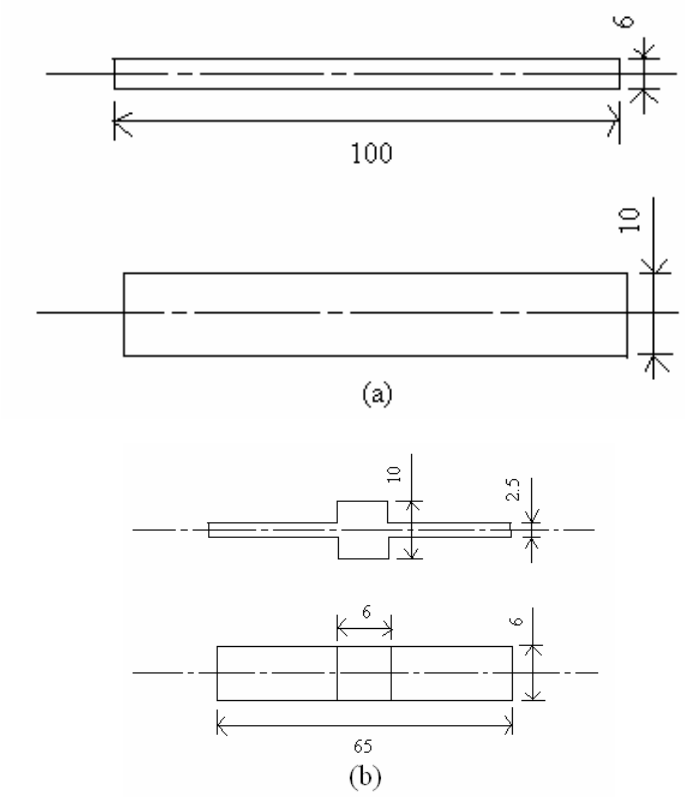

Figure 6.13 Preliminary samples on the Gleeble of (a) type A and (b) type B

6.9.2 Tests on the Gleeble

The first two groups of type A samples were tested at different cooling rates after austenitisation in which the cooling rates ranged from 1 to 51 ºCs^{-1} for the Mo-free alloy #6 (sample #A124) and 1 to 54 ºCs^{-1} for the 0.09% Mo alloy #3 (sample #AF3F). The process graph is shown schematically in figure 6.14.

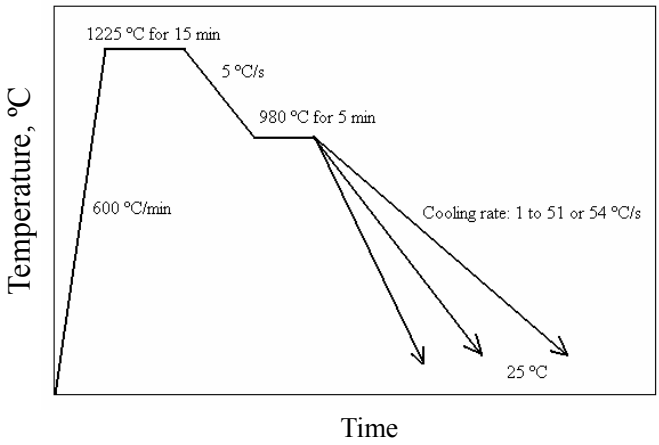

Figure 6.14 Graph of the heating and cooling process on the Gleeble for samples #A124 (the Mo-free alloy #6) and sample #AF3F (the 0.09% Mo alloy #3).

The second two groups of type A samples were subjected to a 60 minutes coiling simulation at 575 (sample #B113) and 600 ºC (sample #A113) for the Mo-free alloy #6, respectively, after cooling in Gleeble. The process graphs are illustrated schematically in figures 6.15.

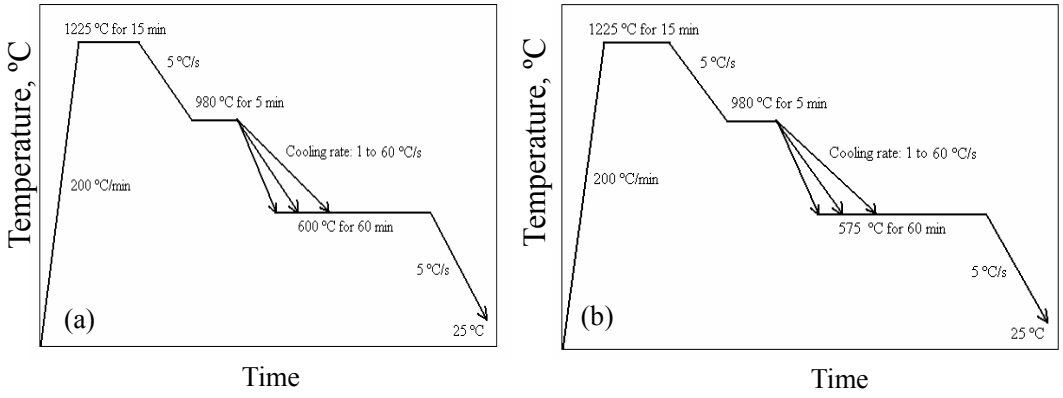

Figure 6.15 Graphs of the heating and cooling cycles in the Gleeble on the Mo-free alloy #6 for samples (a) #A113 and (b) #B113.

The last group, which consisted of type B samples (sample #TEN06 from the Mo-free alloy #6) was tested on the Gleeble with a prior 45% reduction in the austenite (only 33% reduction below the T_{nr}) before cooling and coiling simulation at 575 ºC for 60 minutes. Figure 6.16 shows the test process.

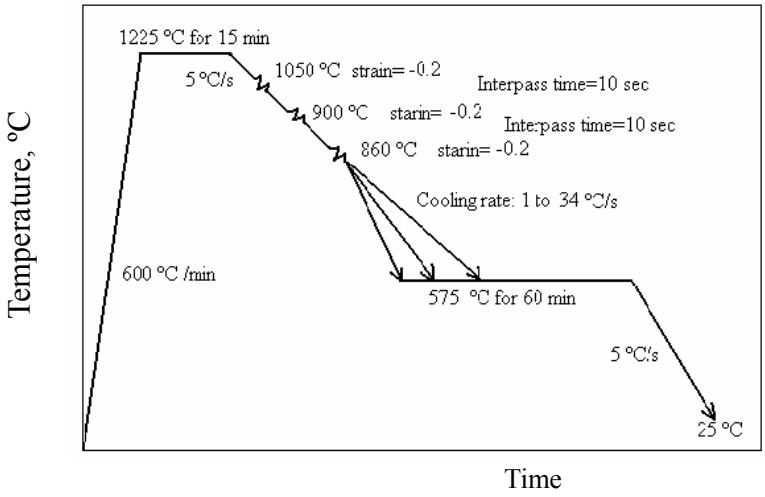

Figure 6.16 Graph of heating, cooling and deformation process in the Gleeble for sample #TEN06 (the Mo-free alloy #6).

6.9.3 Tensile tests

All of these rectangular and preliminary samples that were subjected to the above tests on the Gleeble, were thereafter machined with their gauge lengths to subsize tensile samples of type A (see figure 6.17-(a)) for the tensile test which was done on an INSTRON-8500 Digital Control tensile testing machine for the first four groups of samples and the type B (see figure 6.17-(b)) on a smaller instrumented Hounsfield tensile testing machine.

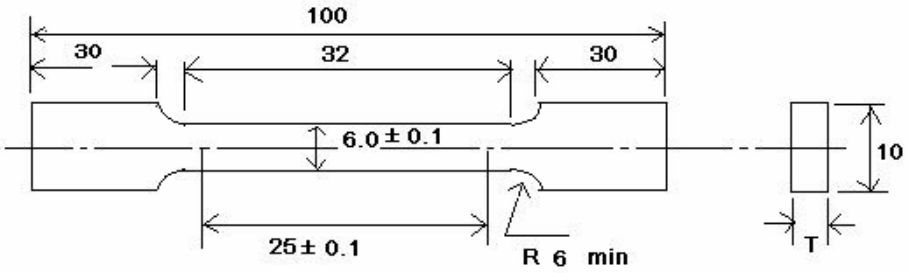

(a)

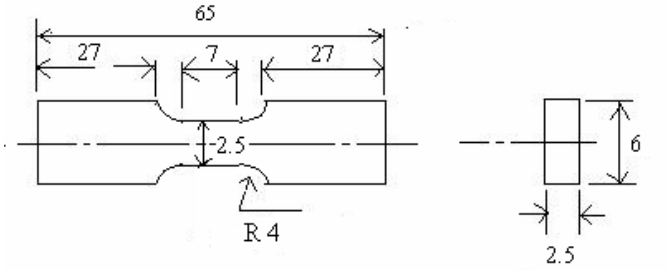

(b)

Figure 6.17 Tensile test samples of (a) type A and (b) type B. T is original thickness of the plates and 6 mm for the as-rolled alloy and the Gleeble samples, respectively.

6.10 Test of mechanical properties on the as-hot rolled alloys

The specimens for the tensile tests from the hot rolled plates were cut from the middle of the rolled plates in the longitudinal and transverse directions and were machined to the subsize tensile of type A (see figure 6.17-(a)). The tensile tests were carried out at room temperature on an INSTRON-8500 Digital Control tensile testing machine with an initial cross-head speed of 0.25 mm min^{-1} until the elongation of 0.5 mm was reached and then a second cross-head speed of 2 mm min^{-1} thereafter.

CHAPTER 7 RESULTS

7.1 The effect of the austenitisation temperature and holding time on the presence of undissolved particles in the V-Nb-Ti-containing alloys

Stable undissolved particles are important in the thermo-mechanically controlled process (TMCP) of line pipe steels. The finer austenite grain size after reheating and before entering the rough rolling stage, result in a good balance of strength and toughness of steels due to the existence of fine undissolved particles. These undissolved particles coarsen with increasing austenitisation temperature, which results in a coarse austenite grain size which is harmful to the final strength and toughness of the steel. The higher austenitisation temperature, however, is beneficial to the thermo-mechanical controlled process as it leads to a low deformation force in the rolling mill. Micro-alloying element additions to high-strength low carbon low alloy line pipe steels are necessary to, firstly, retard the growth of austenite grains at higher austenitisation temperatures and secondly, to retard deformation-induced recrystallisation in the final passes of hot rolling. In order to analyse these particles after reheating, two types of replicas were made in this work: carbon extraction replicas with and without Au-Pd shadowing.

The micrographs of the particles without shadowing are shown in figure 7.1 in which few and relatively small particles can be seen. This suggests that there is a low contrast between the small particles and the carbon film on the extraction replicas made without shadowing. In other words, this technique is not sensitive to small particles of less than 100 nm in diameter. For example, the small dark dot (shown by an arrow in figure 7.1-(b)) can not simply be identified as a particle. Some of the small particles, therefore, could not be included in the count for the calculation of the volume fraction of particles on normal unshadowed carbon replicas, which may have resulted in an error for the measured volume fraction of particles. In order to decrease this error, the technique of shadowed carbon extraction replicas was used to more clearly reveal the smaller particles. The carbon extraction replica with Au-Pd shadowing of alloy #6 after reheating at 1225 ºC for 120 min is illustrated in figure 7.2.

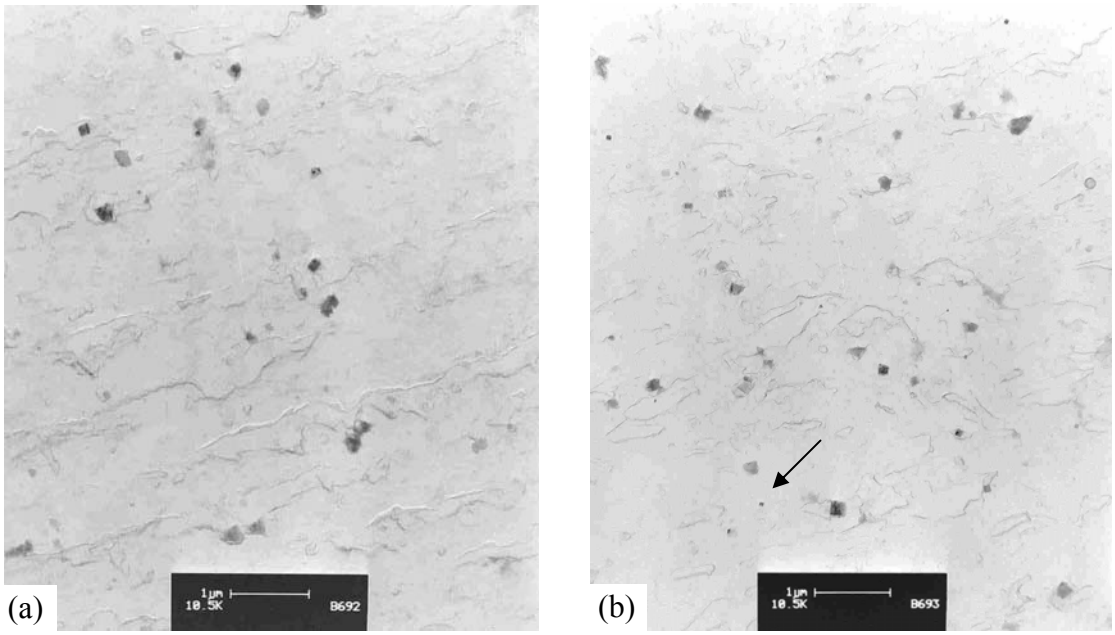

Figure 7.1 Extraction replicas without shadowing with undissolved particles for alloy #6 after reheating at 1200 ºC for 15 min. (Most of the darker spots are not particles but are etching debris on the replicas).

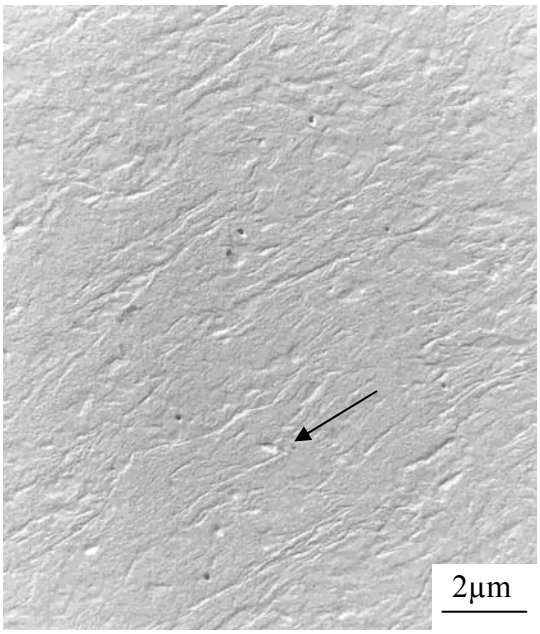

Figure 7.2 Extraction replicas with Au-Pd shadowing for alloy #6 after reheating at 1225 ºC for 120 min.

Comparing figures 7.1 (without shadowing) and 7.2 (with shadowing), the very small particles can be seen more clearly with shadowing, as shown by the small particle of about 52 nm in diameter (shown by an arrow in figure 7.2). It was easy to identify it as an undissolved particle and not etching debris as it contains a shadow beside it,

which indicates that the small particle was protruding from the surface during shadowing and before carbon evaporation. It was, therefore, concluded that the shadowed carbon extraction replica is superior in revealing undissolved particles than carbon extraction replicas without shadowing and this reduced errors in the measuring volume fraction of particles. Comparing the results of the volume fraction measurement of particles with and without shadowing, the measured volume fractions on shadowed replicas were higher than those without shadowing (see table 7.1 below). The volume fraction of particles was calculated in equations (6.1) and (6.2).

Table 7.1 Measured volume fraction of particles on replicas with/without shadowing in alloy #6

Treatment	**Volume fraction (%)**	
	No shadowing	**With shadowing**
As hot rolled	0.31	0.34
1200 ºC 15 min	0.26	0.27
1200 ºC 120 min	0.21	0.22

As may be seen in table 7.1, some smaller particles may not have been counted on unshadowed carbon replicas due to lack of adequate contrast with the carbon film. Therefore, the measured results on the shadowed replicas have a superior precision although both suffer from the effects of a lack of a planar surface after etching[127], which is a pre-requisite in the equation used to calculate the volume fractions.

Some TEM micrographs of particles on the shadowed replicas of alloy #6 after light etching in 2% Nital, are shown in figures 7.3, 7.4, 7.5 and 7.6 for the reheating treatments of 1150, 1200, 1225 and 1250 ºC for different times, respectively. Most undissolved particles are intragranular (marked with “A” in figure 7.6-(a)) and a few particles are on grain boundaries (marked with “B” in figure 7.6-(a)).

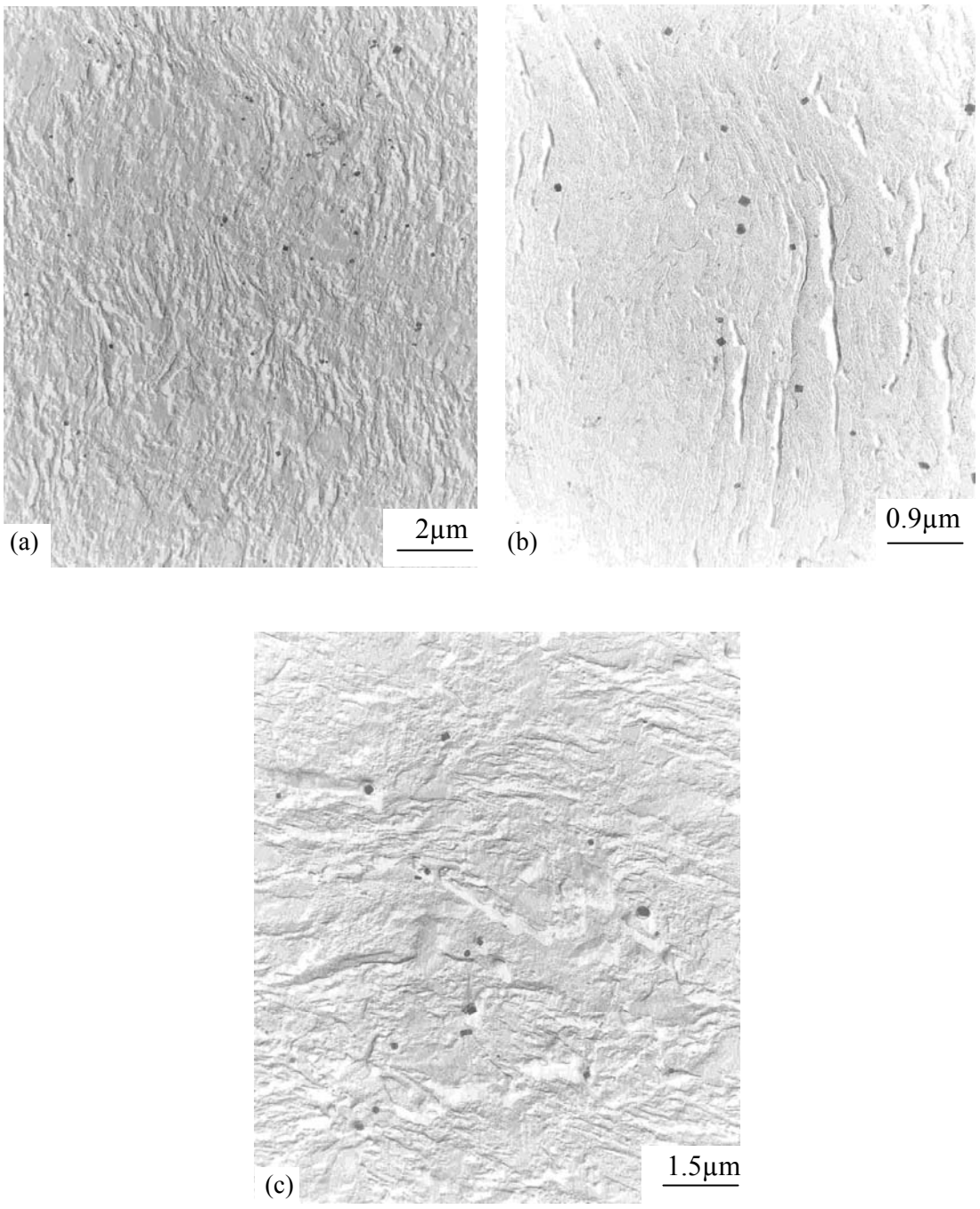

Figure 7.3 TEM micrograph of particles on the shadowed replicas of alloy #6 reheated at 1150 ºC for (a) 15 min, (b) 60 min and, (c) 120 min.

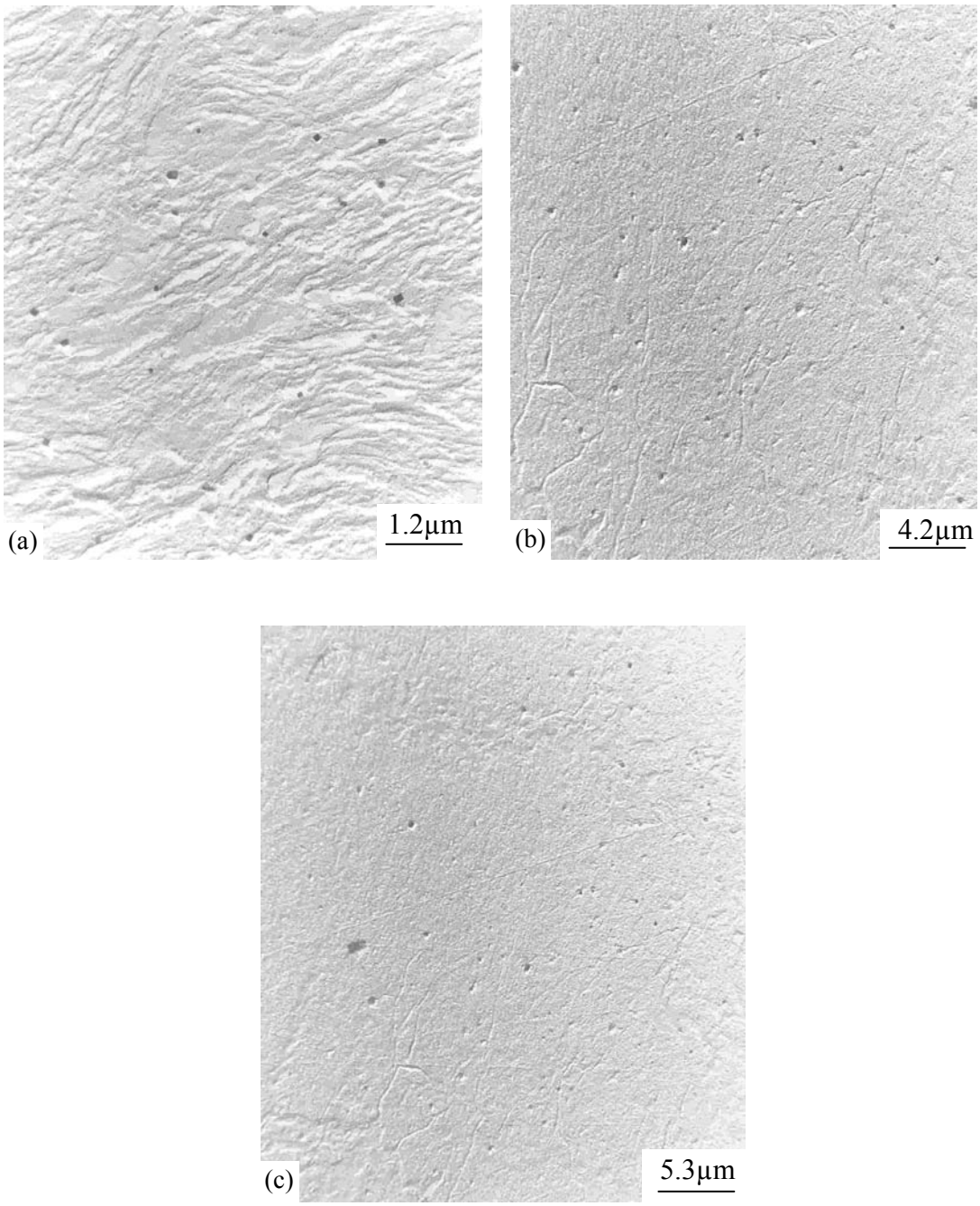

Figure 7.4 TEM micrograph of particles on the shadowed replicas of alloy #6 reheated at 1200 ºC for (a) 15 min, (b) 60 min and, (c) 120 min.

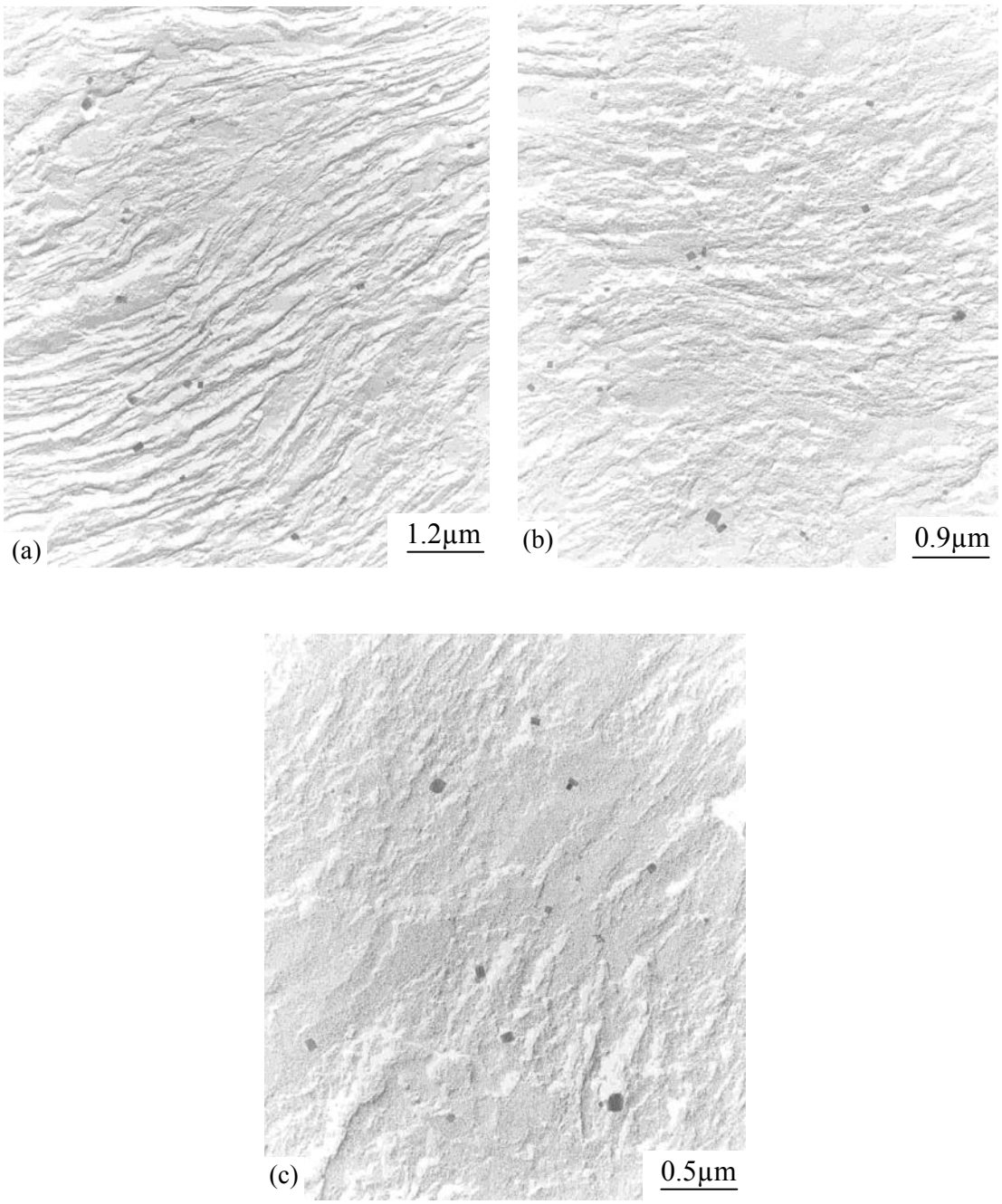

Figure 7.5 TEM micrograph of particles on the shadowed replicas of alloy #6 reheated at 1225 ºC for (a) 15 min, (b) 60 min and, (c) 120 min.

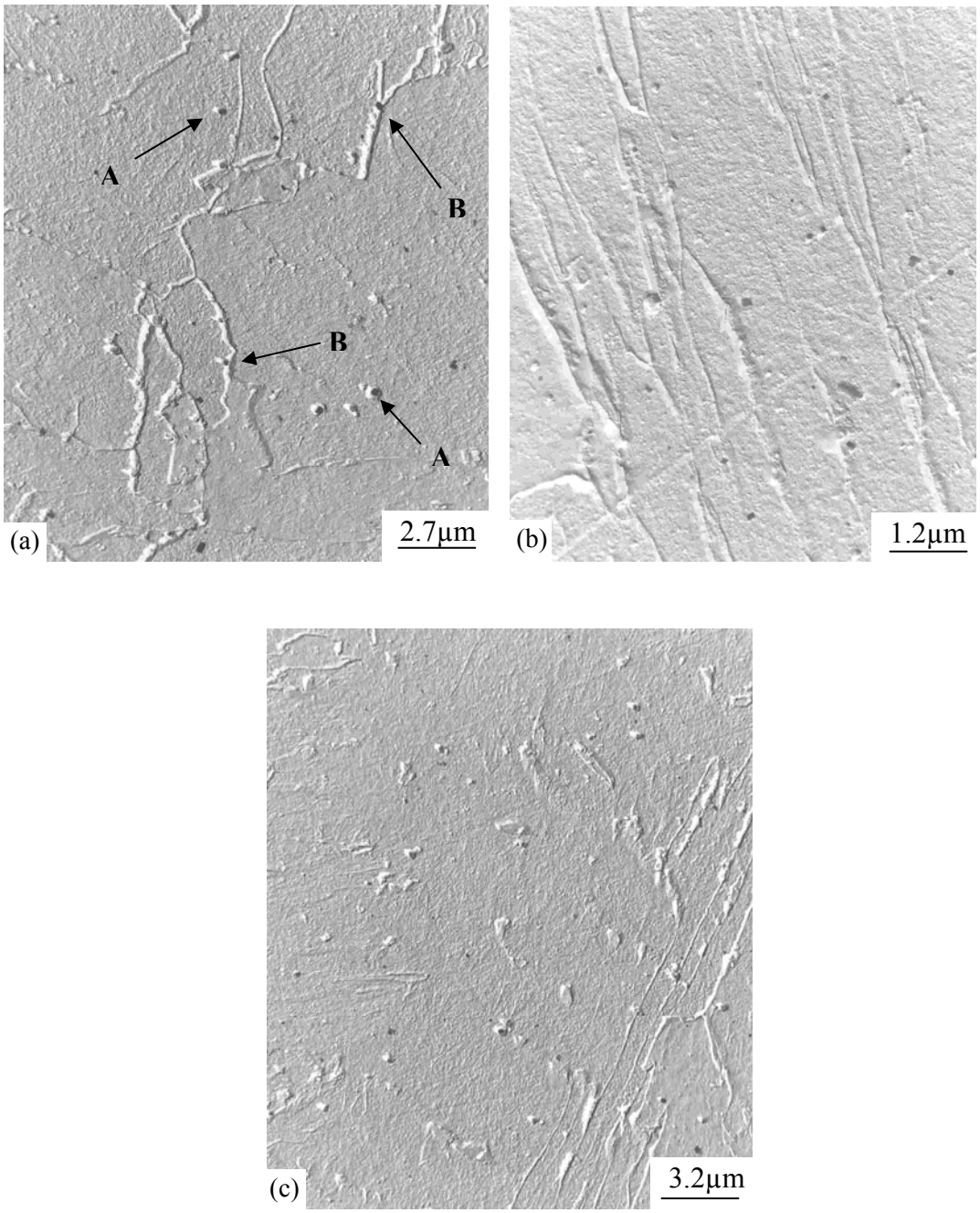

Figure 7.6 TEM micrograph of particles on the shadowed replicas of alloy #6 reheated at 1250 ºC for (a) 15 min, (b) 60 min and, (c) 120 min.

Table 7.2 is a summary of the measured results of undissolved particles observed on the shadowed replicas in the V-Nb-Ti micro-alloyed line pipe steel of Mittal Steel (alloy #6) whose chemical composition was given in table 6.1 in section 6.1.

Table 7.2 Undissolved particles: types and sizes after reheating treatments of alloy #6

Treatment		Type	Size in diameter (nm)	Shape	Nb/Ti Ratio of peak of EDS	Volume fraction (f_v,%)
As-hot rolled		(Ti,Nb)(C,N) (Ti,Nb)C (Nb,Ti)C VN	22~132 33~313 -- --	Square, Ellipsoid Square, Ellipsoid Square, Ellipsoid Square, Rectangle	0.31~0.39 0.22~0.8 4.11 --	*0.34*
1150 ºC	**15 min**	(Ti,Nb)N (Ti,Nb)(C,N)	132 24~94	Ellipsoid Square, Rectangle	0.13 0.21~0.28	0.32
	60 min	(Ti,Nb)(C,N) (Ti,Nb)C	25~132 56	Square Square, Rectangle	0.23~0.26 0.31	0.28
	120 min	(Ti,Nb)(C,N) (Ti,Nb)N (Nb,Ti)C	56~185 73~400 26	Square, Round Round, Square Round, Rectangle	0.21~0.43 0.21~0.27 10.7	0.26
1200 ºC	**15 min**	Ti(C,N) (Ti,Nb)N (Ti,Nb)(C,N)	46~132 182 27~313	Square Square, Rectangle Square	--- 0.18 0.15~0.29	*0.27*
	60 min	(Ti,Nb)(C,N) (Ti,Nb)N	29~330	Square, Rectangle		0.24
	120 min	(Ti,Nb)(C,N) (Ti,Nb)N	22~182 94 ~382	Square, Rectangle Square, Rectangle	0.12~0.16 0.11~0.21	*0.22*
1225 ºC	**15 min**	(Ti,Nb)(C,N) Ti(C,N)	27~322	Square, Rectangle	--	0.22
	60 min	(Ti,Nb)(C,N) Ti(C,N)	25~396	Square, Rectangle	--	0.21
	120 min	(Ti,Nb)(C,N)	30~375	Square, Rectangle	--	0.19
1250 ºC	**15 min**	(Ti,Nb)(C,N) Ti(C,N)	37~428	Square, Rectangle	--	0.21
	60 min	(Ti,Nb)(C,N)	34~403	Square, Rectangle	--	0.20
	120 min	(Ti,Nb)(C,N) Ti(C,N)	46~439	Square, Rectangle	--	0.19

As can be seen from table 7.2, the types of undissolved particles are (Ti,Nb)(C,N), (Ti,Nb)C, (Ti,Nb)N, Ti(C,N) and (Nb,Ti)C. Their respective shapes are cubic or squared, rectangular, rounded and ellipsoidal. There were some VN particles in the as-hot rolled condition but no VN particles were observed after reheating treatments

above 1150 ºC in alloy #6. VN particles were completely dissolved in the austenite above 1150 ºC in this steel and, therefore, can not inhibit the grain growth of the austenite above this temperature.

(Ti,Nb)C and (Nb,Ti)C particles of ellipsoidal and rounded shapes appeared to dissolve at 1200 ºC after 120 min. (Ti,Nb)(C,N) and (Ti,Nb)N remained undissolved at this temperature as indicated by the fact that only square and rectangular particles remained in the steel. It was observed that these squared and rectangular particles were more stable than the ellipsoidal and rounded ones with increasing solution temperature. Some EDS spectra from the transmission electron microscope analyses are presented in figure 7.7.

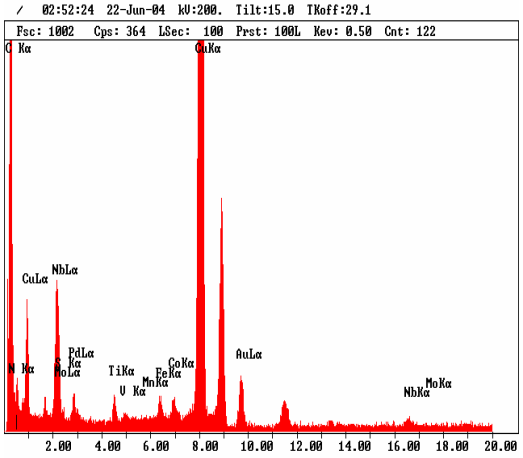

(a) (Nb,Ti)C

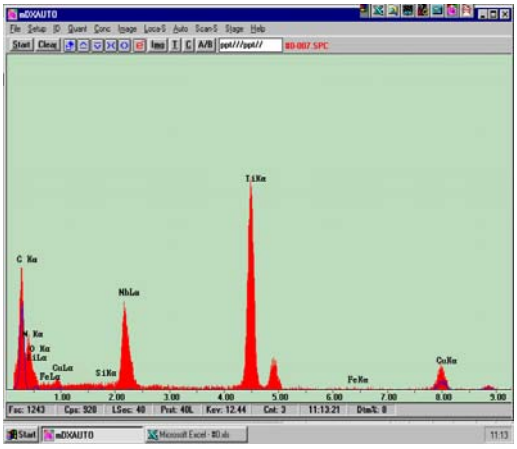

(b) (Ti,Nb) (C,N)

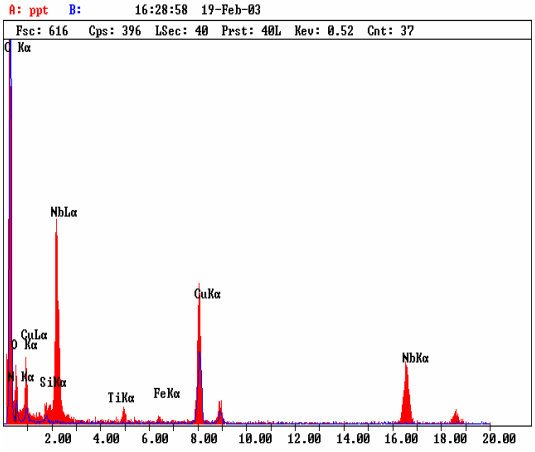

(c) (Nb,Ti) C

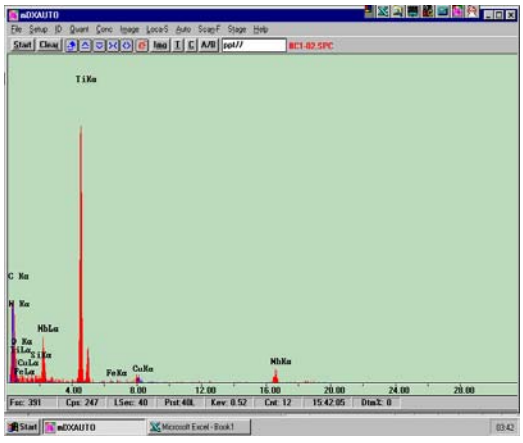

(d) (Ti,Nb)N

Figure 7.7 TEM-EDS results of undissolved particles of alloy #6 after the treatments of (a) as-hot rolled, (b) as-hot rolled, (c) 1150 ºC for 120 min and, (d) 1200 ºC for 15 min.

Some copper peaks in figure 7.7 were probably from the copper grid that supports the carbon coating while a large part of the carbon from the carbon peak (marked with blue) was from the background of the carbon replicas films.

As may be expected in figure 7.8, the volume fractions (f_v) of undissolved particles decreases with an increase in the temperature of solution treatment for all the investigated soaking times, i.e. 15, 60 and 120 min. The curve fitted equations are as follows for the times of 15, 60 and 120 min, respectively.

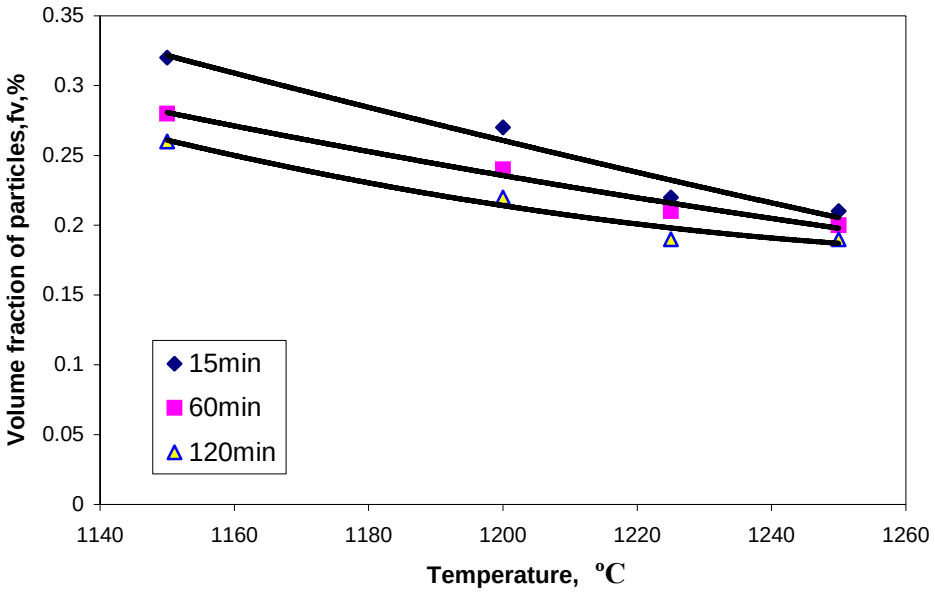

Figure 7.8 The effect of reheating temperature and time on the volume fraction of undissolved particles for alloy #6.

$f_v=10^{-6}T^2-0.0038T+3.2258$ $R^2=0.97$ for 15min soaking time (7.1)

$f_v=10^{-6}T^2-0.0043T+3.3251$ $R^2=0.99$ for 60min soaking time (7.2)

$f_v=4\times10^{-6}T^2-0.0103T+6.862$ $R^2=0.97$ for 120min soaking time (7.3)

where f_v is volume fraction of undissolved particles after the soaking time in %.

T is temperatures of solution or reheating treatment in ºC.

R^2 is the regression fitting coefficient.

As can be seen from equations (7.1) to (7.3), there is a similar trend between the volume fraction of undissolved particles and the solution or reheating temperature at different soaking times. The undissolved particles become less stable at higher

solution temperatures and, therefore, reduce their ability to inhibit any growth of the austenite grains. It can, therefore, be concluded that at high solution temperatures, small particles dissolve and large ones coarsen and the grain boundary pinning effect is reduced or eliminated, leading to austenite grain growth.

There are two effects in the present work: one is coarsening at constant temperature by small particles dissolving and large particles growing by the Lifshitz-Slyosov-Wagner process, such as with the more stable (Ti,Nb)(C,N) and Ti(C,N) that will coarsen above 1250 ºC for 120 min (see table 7.2). The second effect arises from a larger solubility at higher temperatures in which all sizes of particles dissolve, i.e. both small and large ones dissolve, such as with the less stable VN at 1150 ºC and (Ti,Nb)C, (Nb,TI)C at 1200 ºC. This latter type of particle is less stable than the former ones, so that they lose any effect to inhibit the growth of austenite grains.

Table 7.2 shows that the size of the smallest undissolved particles does not significantly change below 1225 ºC. The smallest sizes for the as-received as-hot rolled steel of alloy #6 was 22 nm and after soaking at 1225 ºC for 120 min, this size increased to about 30 nm. The particles started coarsening at a soaking temperature of 1250 ºC for 120 min when a mean particle diameter of 46 nm was observed. It can be concluded that the undissolved particles in alloy #6 containing Nb-Ti-V micro-alloying elements, still had a strong inhibition on the growth of the austenite grains and, therefore, fine austenite grains can still be obtained at reheating temperatures up to about 1225 ºC. The particles of Ti- or (Ti+Nb)-carbonitrides, however, were still undissolved at temperatures above 1200 ºC. All of the V- and Nb-carbides and V-nitrides were dissolved completely at temperatures above 1200 ºC, meaning that only Ti- and (Ti+Nb)-carbonitrides or nitrides contribute to a grain boundary pinning effect to limit austenite grain growth above the temperature of 1200 ºC. In order to get much greater dispersion hardening (Nb- and V-carbides in ferrite) and stronger retarding of austenite grain growth (undissolved particles of Ti- or (Ti+Nb)-carbonitrides in austenite), enough titanium in the steel is needed to bind all free nitrogen, leading to a significant increase in niobium available in the ferrite. In conclusion: if the reheating temperature in the hot rolling process is not more than 1225 ºC, a combination of

greater dispersion hardening and smaller austenite grains after reheating may still be achieved in Nb-Ti micro-alloyed steels.

7.2 Austenite grain size and reheating temperature

The reheating temperature should be high enough to dissolve most of the micro-alloying elements without significant growth of the austenite grains, but also allowing dispersion hardening after the TMCP. The in-situ carburising technique by carbon monoxide gas was used to reveal austenite grain boundaries. The austenite grain size for alloy #6 is shown in figures 7.9 (a)-(d) for reheating conditions at 1150 to 1250 ºC, respectively.

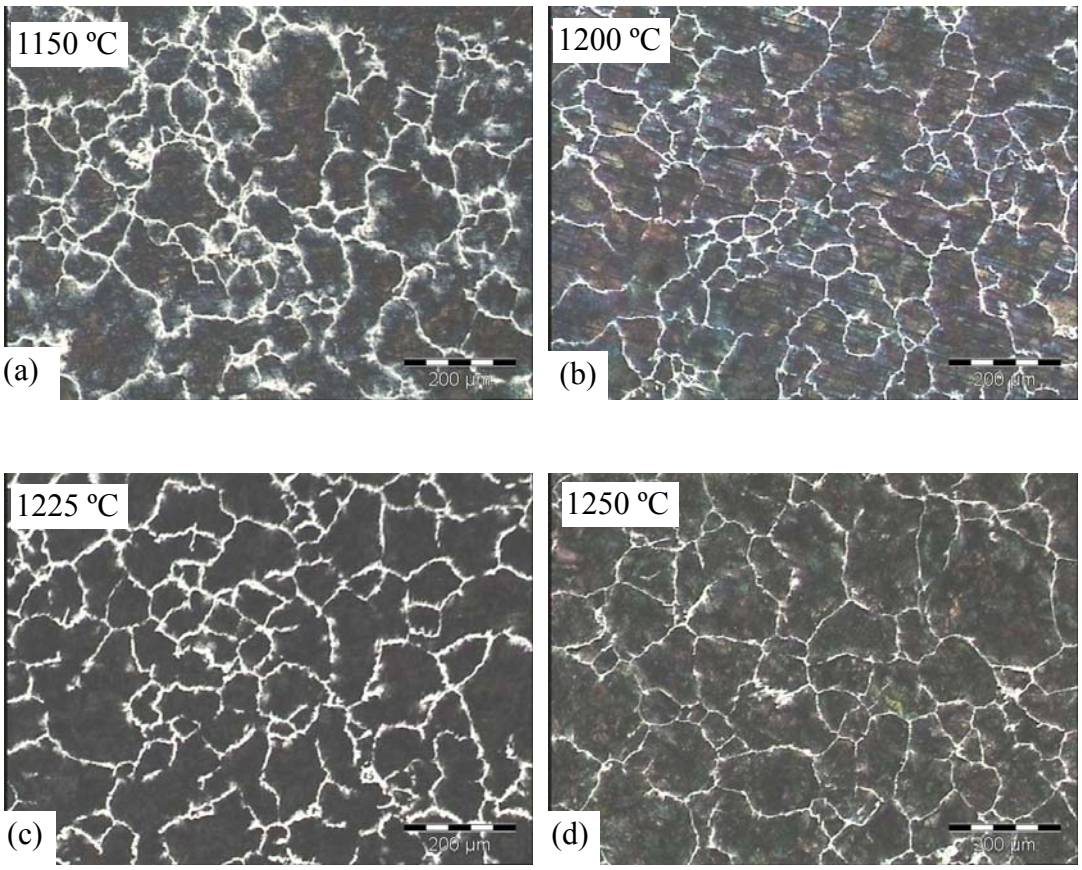

Figure. 7.9 Pro-eutectoid cementite decorates the original austenite grain boundaries in alloy #6 for soaking times of 60 min at different austenitisation temperatures.

The measured intercept length of the austenite grain size for each treatment is shown in table 7.3 below as well as in figures 7.10 and 7.11 while some data from the literature[39] for a steel with composition of 0.1% C, 0.2% Si, 1.4% Mn, 0.005%N, 0.03% Al and 0.01% Ti, have been included in figure 7.10 as a reference.

Table 7.3 Intercept length austenite grain size, in µm, versus reheating temperature and soaking time of alloy #6

Soaking time	1150 ºC	1200 ºC	1225 ºC	1250 ºC
15 min	32.3	41.6	50.4	65.5
30 min	33.9	49.6	52.9	75.0
60 min	48.9	53.0	57.1	76.5
120 min	54.0	58.7	62.9	82.7

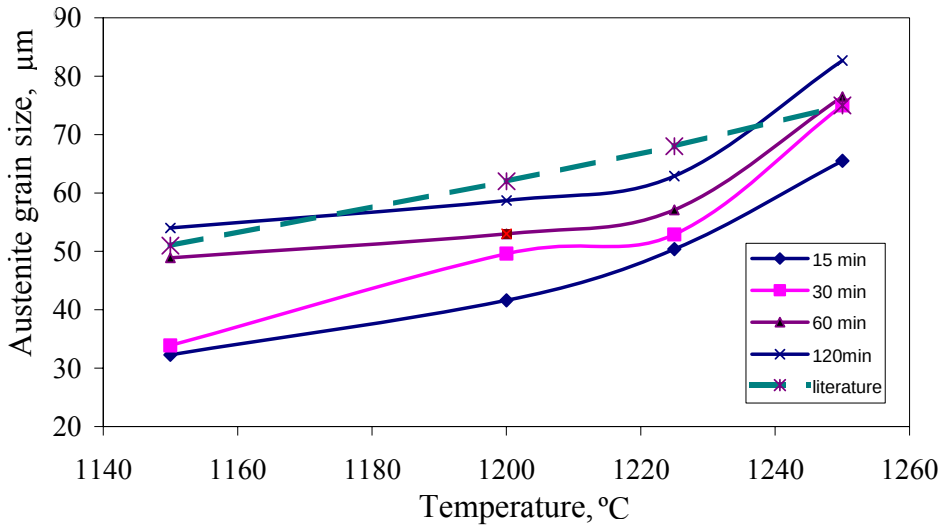

Figure. 7.10 The relationship between the austenitisation temperature and the austenite grain size for alloy #6. The broken line is from published data[39].

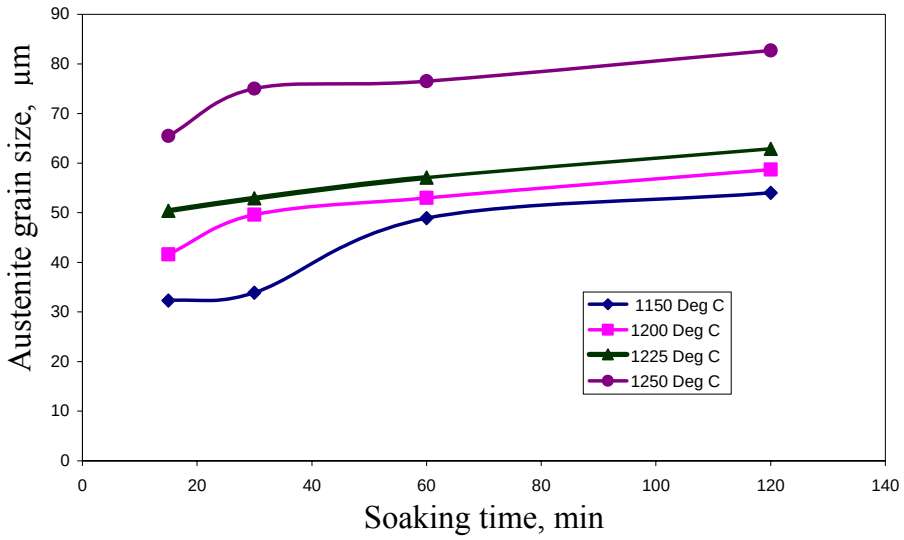

Figure. 7.11 The weak effect of soaking time on the austenite grain size for alloy #6.

As may be seen from figure 7.10, the austenite grain size for alloy #6 increased with increasing austenitisation temperature from 1150 to 1250 ºC, at a constant soaking time. The austenite grains grow slowly, however, below 1225 ºC due to the pinning of the grain boundaries by the stable micro-particles, i.e. (Ti,Nb)(C,N) or (Ti,Nb)N as described in section 7.1, as there is less coarsening of these carbonitrides in the alloy below 1225 ºC. Significant coarsening begins, however, when the carbonitrides dissolve at 1250 ºC (see figure 7.10). As a result, the austenite grains grow sharply with an increase in temperature above 1225 ºC. The growth in austenite grain size is given by an increase of ΔD=19.8 µm from 1225 to 1250 ºC for a soaking time of 120 minutes, compared to a growth by an increase of only ΔD=4.2 µm from 1200 to 1225 ºC. Accordingly, the reheating temperature of the alloys in the present study should not be higher than 1225 ºC for a relatively fine austenite grain size.

Considering much greater dispersion hardening in the ferrite from Nb-bearing precipitates and raising the non-recrystallisation temperature, the niobium should preferably be dissolved completely into the matrix of the steel. The reheating temperature before the hot rolling process should, therefore, not be too low also, but so high that all of the niobium could dissolve into the matrix of the steel. The most effective precipitation strengthening, therefore, can be obtained from NbC precipitation in ferrite[12]. A higher non-recrystallisation temperature (T_{nr}) can also be obtained[12] due to the precipitation of Nb(C,N) during hot rolling[28]. This will, on the

other hand, result in "pancake" austenite grains during hot rolling, providing more nucleation sites as well as sufficient strain accumulation for the following ferrite formation, which results in finer ferrite. Cuddy[114] reported that the broad range of initial austenite grain sizes (53 to 325 μm) converged to a narrow range of grain sizes of 43 to 53 μm after multiple recrystallisation that was produced by a five passes reduction schedule. It was also found that the final austenite grain size before reaching the T_{nr} was dependent mainly on the deformation parameters and was largely independent of the steel's composition, i.e. similar for C-Mn, Nb-bearing and V-bearing steels. Considering a combination of finer austenite grains and greater dispersion hardening, the limit of 1225 ºC was taken as the most appropriate reheating temperature in this study. On the other hand, niobium also raises the T_{nr} because of solute drag by niobium on austenite boundaries if niobium is completely dissolved into the steels. A higher Nb addition, therefore, results in more deformation below the T_{nr} during the hot rolling (if compared to that of lower Nb additions) which induces a finer ferrite grain size.

The soaking time at the austenitisation temperature influences the austenite grain size as well although to a lesser extent than the temperature. The longer the soaking time, the larger the austenite grain size (see figure 7.11). The soaking time is, therefore, largely determined by the slab's section size to achieve uniform temperatures and also to a lesser extent, by the need to dissolve the niobium micro-alloying elements.

7.3 The non-recrystallisation temperature (T_{nr}) and deformation parameters

The non-recrystallisation temperature (T_{nr}) is one of the most important factors in the design of the thermo-mechanically controlled process (TMCP) schedule for line pipe steels. The T_{nr} is the critical temperature below which no dynamic or static recrystallisation will take place during or immediately after hot rolling and this leads to the formation of so-called "pancake" grains. The austenite grains become flattened with consecutive pass reductions as the strain accumulates, up to the Finishing Mill Head where after transformation to ferrite takes place on the run-out table. The finishing rolling is normally carried out below the T_{nr}, which is a function of the alloy content (particularly the Nb alloying addition) as well as parameters of the TMCP, i.e. pass strain (ε), strain rate($\dot{\varepsilon}$) and inter-pass time (t_{ip}).

7.3.1 The T_{nr} and pass strain

Figure 7.12 illustrates for alloy #6 the compression deformation cycles used at various pass strains ranging from 0.15 to 0.32 at the same strain rate of 1 s^{-1} and inter-pass times of 8 seconds.

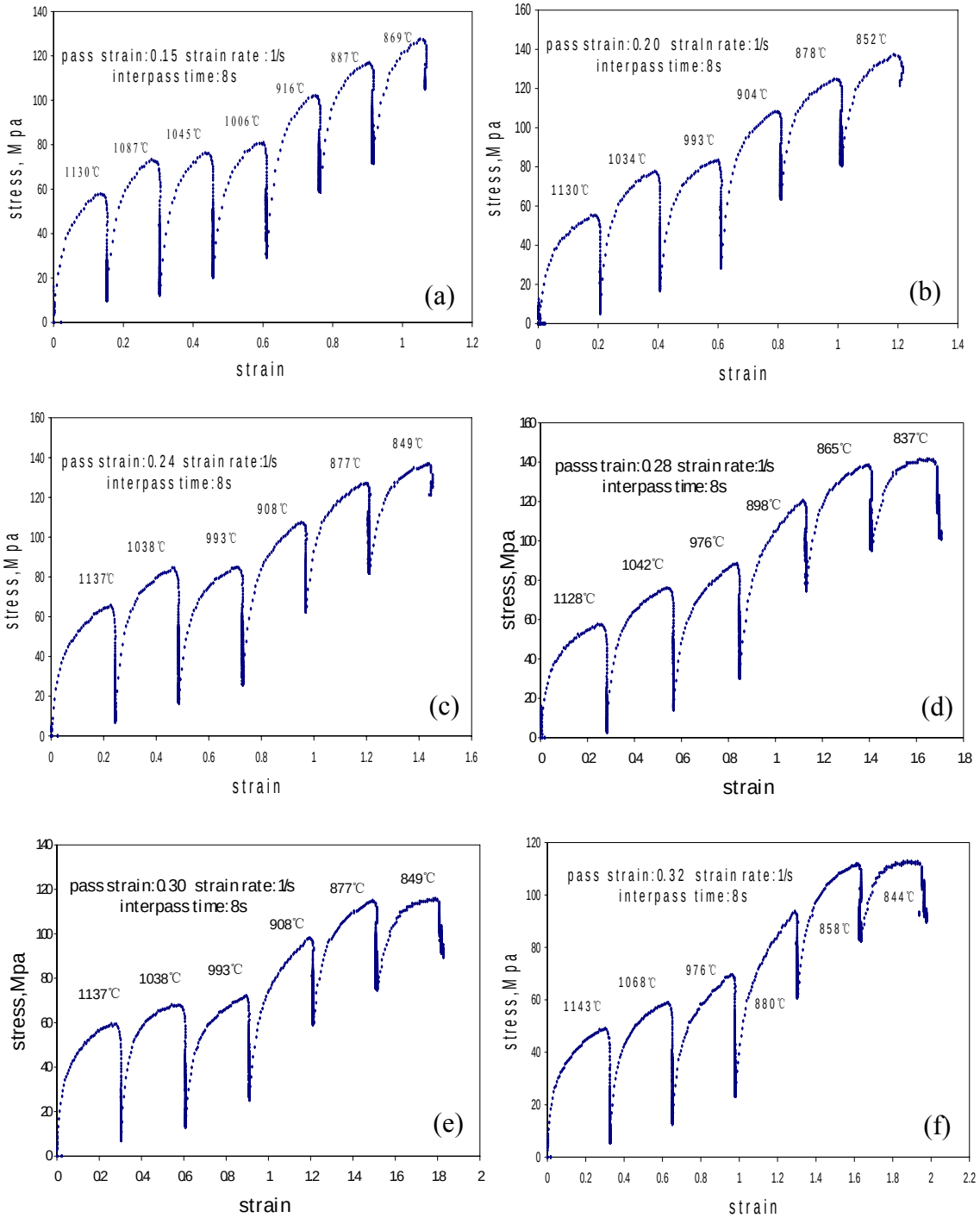

Figure 7.12 Stress-strain curves of multi-pass compression tests of alloy #6 at the same strain rate of 1 s^{-1}, inter-pass time of 8 seconds and different pass strains.

The number of passes in these compression tests was seven at 0.15 strain per pass and 6 passes at more than 0.2 strain per pass. The stress-strain curves for each pass are presented in figure 7.12 with the temperatures of each pass marked on its stress-strain curve. The mean flow stress of each pass was then calculated according to equation (6.4) and the curves of the mean flow stress with the inverse pass deformation temperature plotted as shown in the following figure 7.13. Two straight lines can be obtained here: one has a lower slope at the higher temperature range and the other has a higher slope at the lower temperature range. When the deformation takes place below the T_{nr}, the slope in figure 7.13 increases because of the retained strain hardening within the non-recrystallisation region. As may be seen in figure 7.13, a point of intersection is obtained, which is the non-recrystallisation temperature marked by an arrow (T_{nr}).

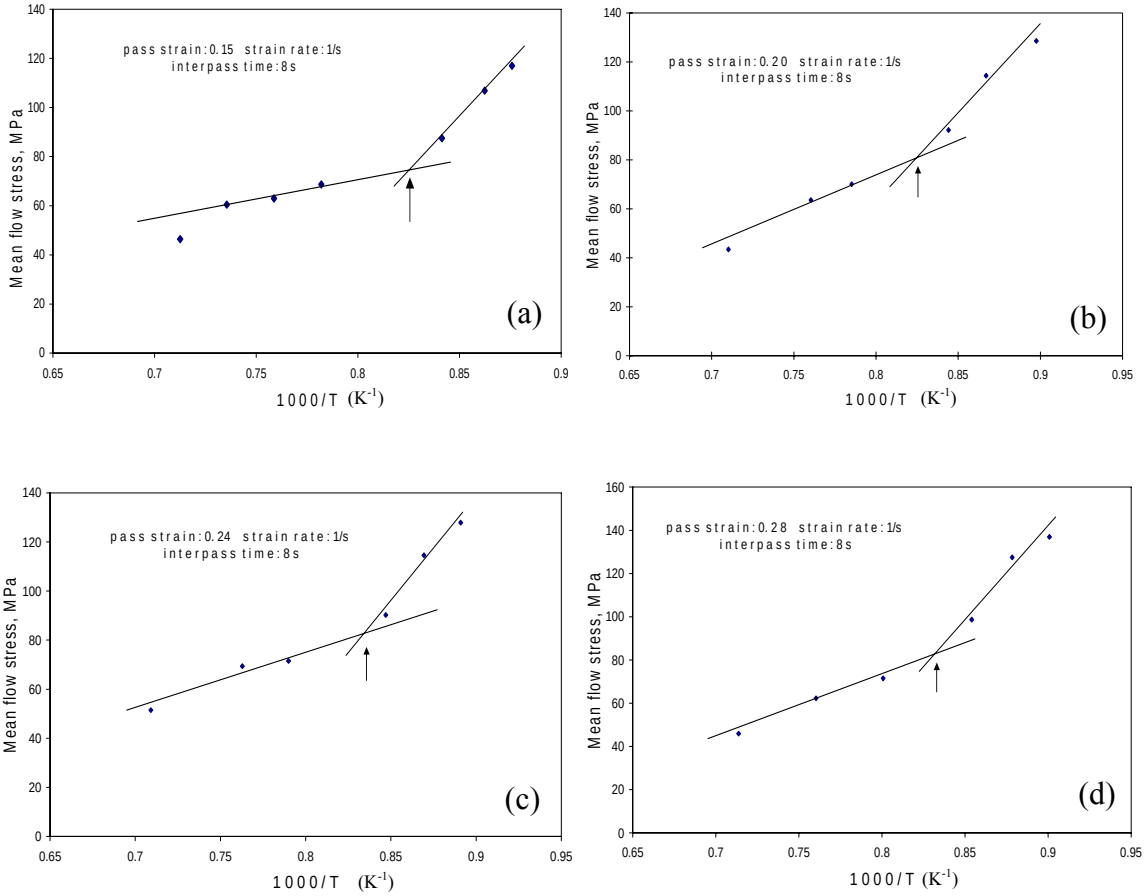

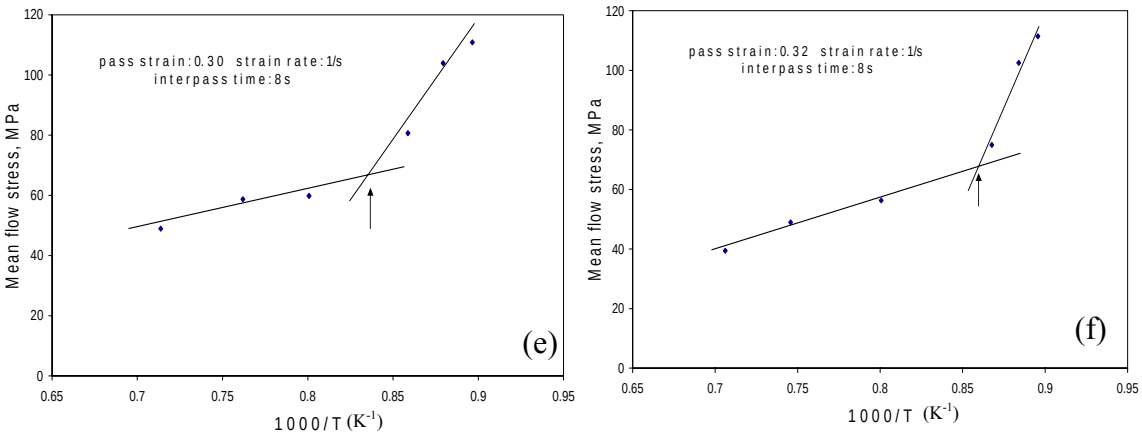

Figure 7.13 Determination of the T_{nr} on the mean flow stress versus inverse temperature curves of alloy #6, all deformed at the same strain rate of 1 s^{-1} and an inter-pass time of 8 seconds but at different pass strains.

As may be seen in figure 7.13, the slope of the straight line below the T_{nr} is lower at a low pass strain of 0.15 than at a strain of 0.32 per pass. The slope of the straight line below the T_{nr}, therefore, appears to increase with an increase in pass strain. This is because the accumulation of retained strain from pass to pass during non-recrystallisation, is higher at higher pass strains. The higher pass strain induces a higher density of dislocations in the flattened austenite grains, which will remain below the T_{nr}, until transformation to ferrite occurs on the run-out table. The results of the T_{nr} at various pass strains are listed in table 7.4 for alloy #6 and are also shown in figure 7.14.

Table 7.4 The non-recrystallisation temperature and pass strains of alloy #6

Sample number	**A15**	**A20**	**A24**	**A28**	**A30**	**A32**
Inter-pass time, t_{ip} (s)	8	8	8	8	8	8
Strain rate (s^{-1})	1	1	1	1	1	1
Pass strain ε	0.15	0.2	0.24	0.28	0.30	0.32
T_{nr} (°C)	937	931	922	916	918	893

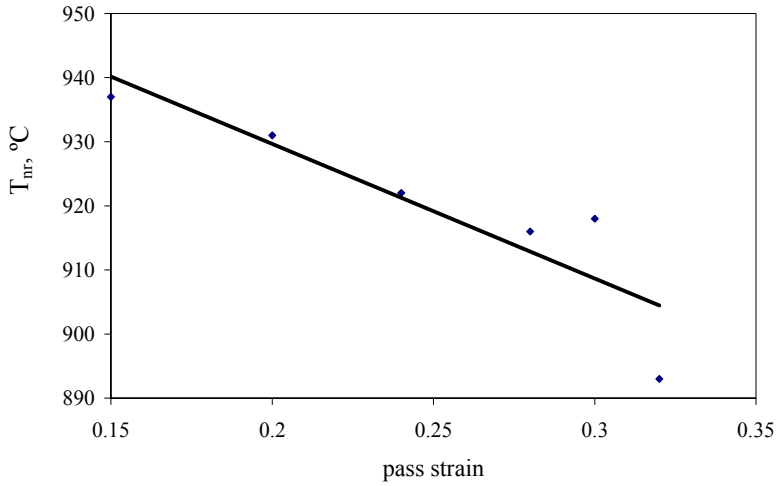

Figure 7.14 The relationship between pass strain (ε) and the non-recrystallisation temperature for alloy #6. Strain rate $\dot{\varepsilon}$=1.0 s^{-1}, inter-pass time t_{ip}=8 s.

The strain rate and inter-pass time were held constant at $\dot{\varepsilon}$=1.0 s^{-1} and t_{ip}=8 s in this series of tests. The T_{nr} in the Mo-free reference alloy #6 decreases with increasing pass strain in an approximately linear relationship. The tendency of the T_{nr} versus pass strain is consistent with the results of Cuddy et al[128] and Bai et al[48,125], i.e., the T_{nr} decreases with an increase in pass strain. This quantitative relationship in alloy #6 can be described by the following equation:

$$T_{nr}= -210\ \varepsilon+972 \qquad R^2=0.79 \qquad (7.4)$$

where T_{nr} is in ºC and the strain ε expressed as the true strain.

Above the T_{nr} grain refinement significantly increases the dislocation density during hot working and this encourages the coarsening of precipitates[111]. As the pass strain increases, austenite grains become finer. The higher dislocation density is associated with a higher stored energy in the austenite, which constitutes the driving force for recrystallisation. Therefore, increasing the pass strain promotes austenite recrystallisation and lowers the T_{nr}. Furthermore, the coarser particles have little effect on retarding the austenite recrystallisation[125]. Weiss and Jonas[112], Bai et al[125] and Speer and Hansen[113] reported that precipitate coarsening during hot deformation takes place as the pass strain increases and these larger particles lose their ability to retard recrystallisation.

7.3.2 The T_{nr} and inter-pass time

The inter-pass time also affects the non-recrystallisation temperature during the hot rolling process. The hot compression results at various inter-pass times ranging from 4 to 50 seconds, with the same pass strain of 0.2 and strain rate of 1 s^{-1} for alloy #6, are shown in figure 7.15.

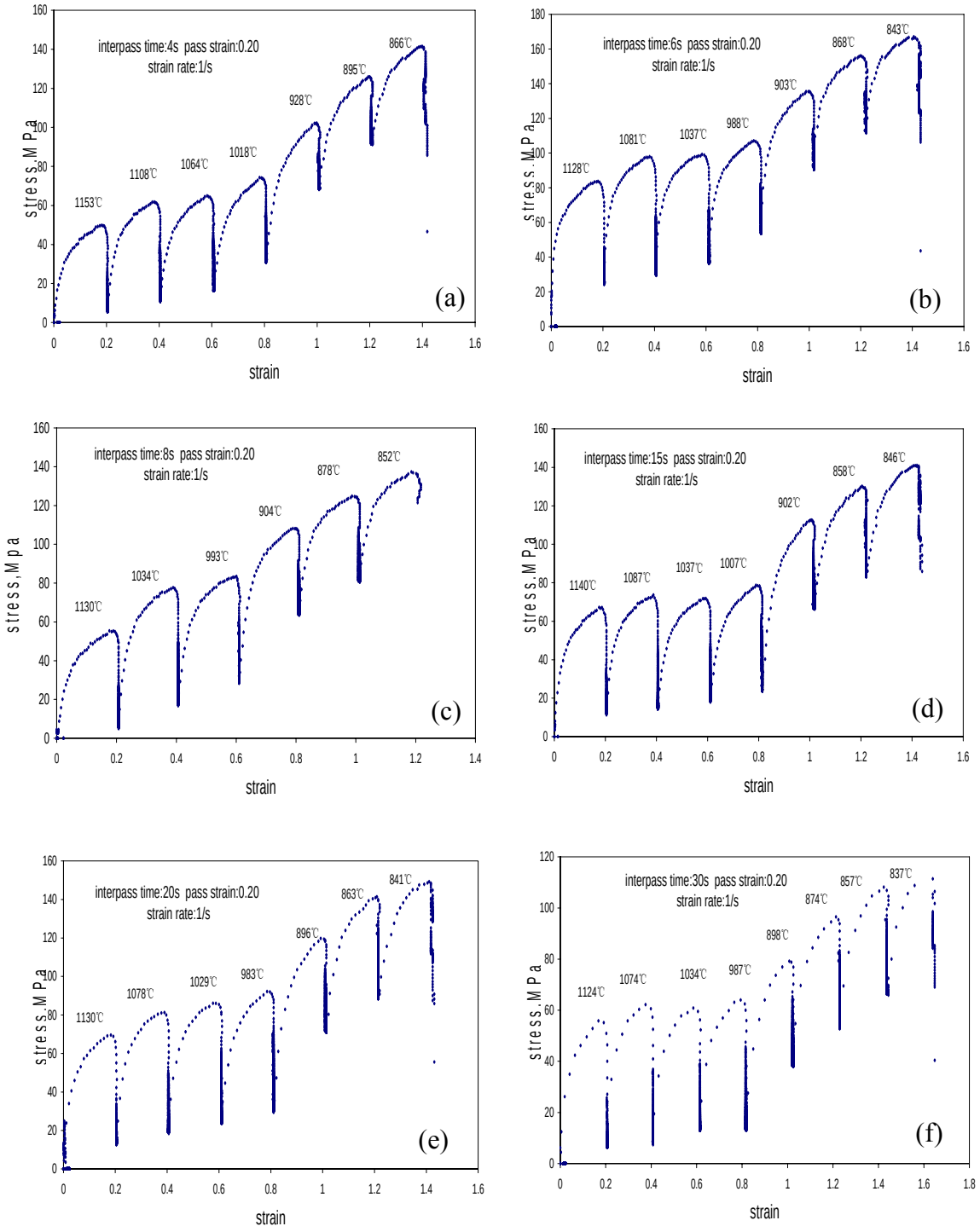

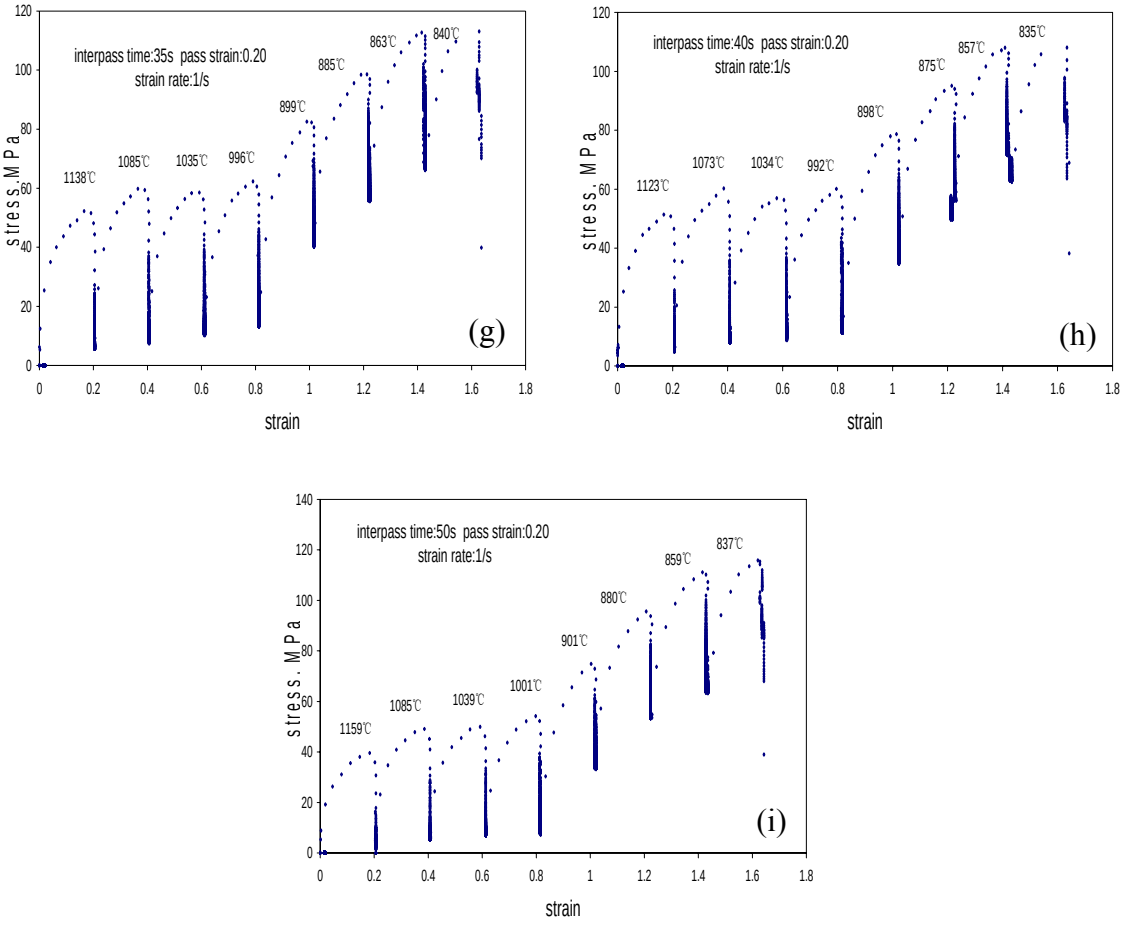

Figure 7.15 Stress-strain curves of multi-pass compression tests on alloy #6 at a constant pass strain of 0.20, a constant strain rate of 1 s^{-1} and a series of inter-pass times ranging from 4 to 50 seconds.

The number of passes in these tests is 6, 7 or 8 (some results were obtained on the Gleeble before its upgrading, others after the upgrading. From there a difference in number of passes arose). The pass temperature is also marked on the respective figures. The mean flow stress values calculated from figure 7.15 is plotted against the inverse pass temperature (in K) in figure 7.16.

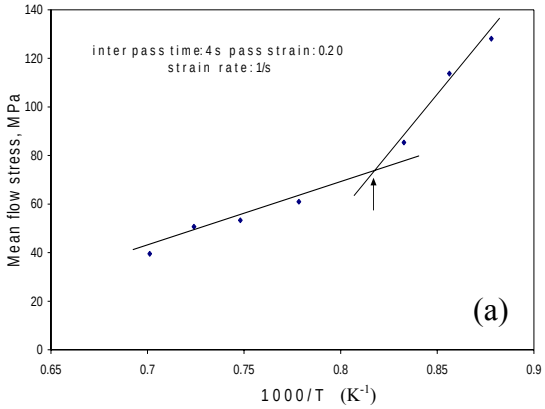
inter pass time:4s pass strain:0.20
strain rate:1/s
Mean flow stress, MPa
1000/T (K-1)
(a)

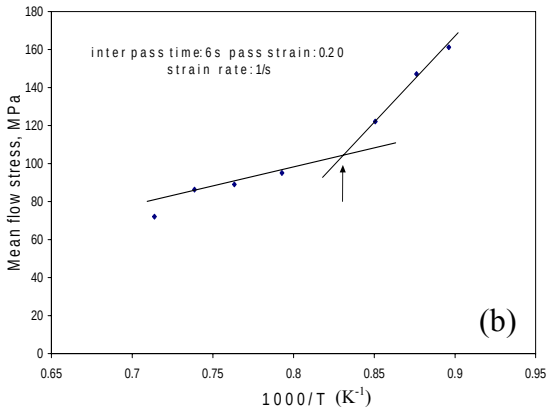
inter pass time:6s pass strain:0.20
strain rate:1/s
Mean flow stress, MPa
1000/T (K-1)
(b)

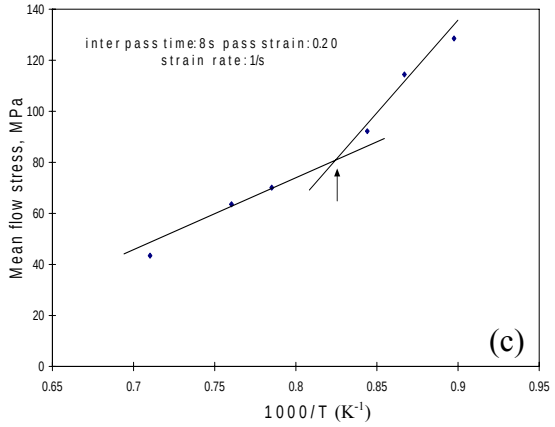
inter pass time:8s pass strain:0.20
strain rate:1/s
Mean flow stress, MPa
1000/T (K-1)
(c)

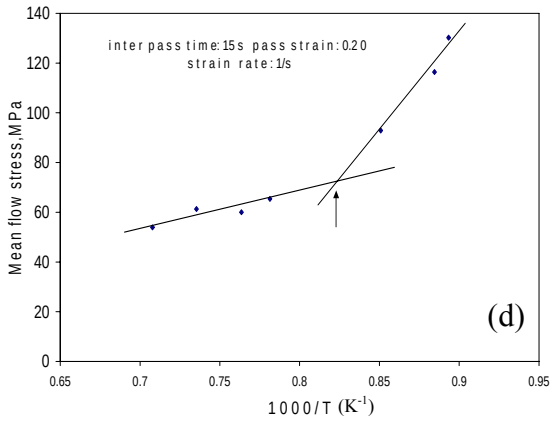
inter pass time:15s pass strain:0.20
strain rate:1/s
Mean flow stress,MPa
1000/T (K-1)
(d)

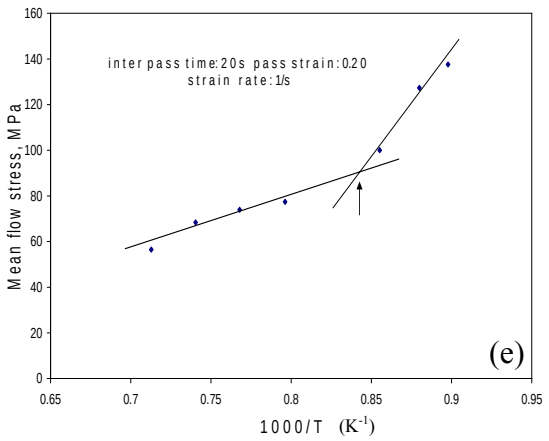
inter pass time:20s pass strain:0.20
strain rate:1/s
Mean flow stress, MPa
1000/T (K-1)
(e)

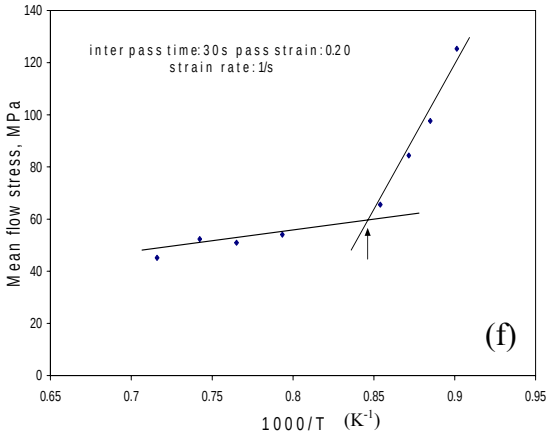
inter pass time:30s pass strain:0.20
strain rate:1/s
Mean flow stress, MPa
1000/T (K-1)
(f)

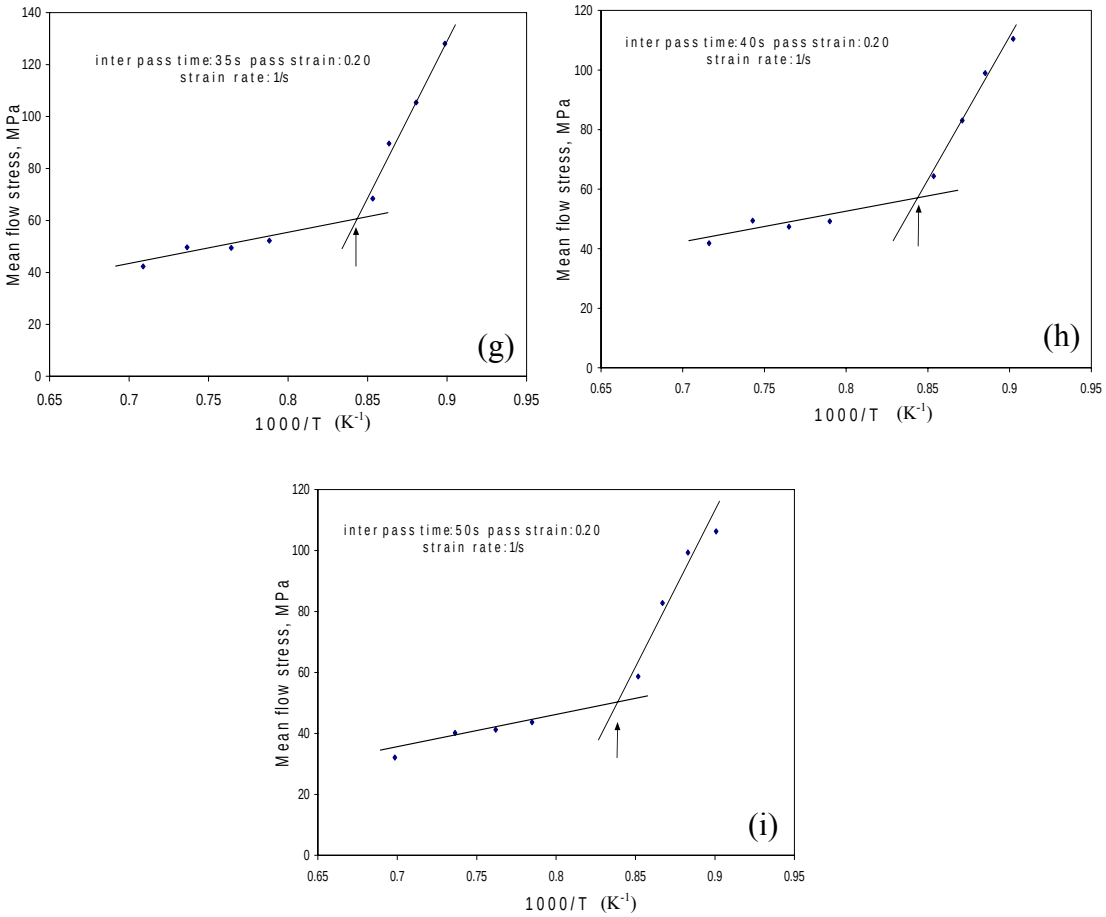

Figure 7.16 The mean flow stress versus inverse temperature curve of alloy #6 during multi-pass compression testing at a constant pass strain of 0.20 and a constant strain rate of 1 s^{-1} but with a variation of the inter-pass times between 4 and 50 seconds.

The values for T_{nr} obtained from figure 7.16 at various inter-pass times are summarised in table 7.5 and figure 7.17.

Table 7.5 The non-recrystallisation temperature of alloy #6 as affected by different inter-pass times

Sample number	**D4a/4b**	**D6**	**D8**	**D15a/15b**	**D20**	**D30**	**D35**	**D40**	**D50**
Pass strain, ε	0.2	0.2	0.2	0.2	0.2	0.2	0.2	0.2	0.2
Strain rate (s^{-1})	1	1	1	1	1	1	1	1	1
Inter-pass time, t_{ip} (s)	4	6	8	15	20	30	35	40	50
T_{nr} (ºC)	934/ 956	938	931	941/ 921	930	914	916	921	913

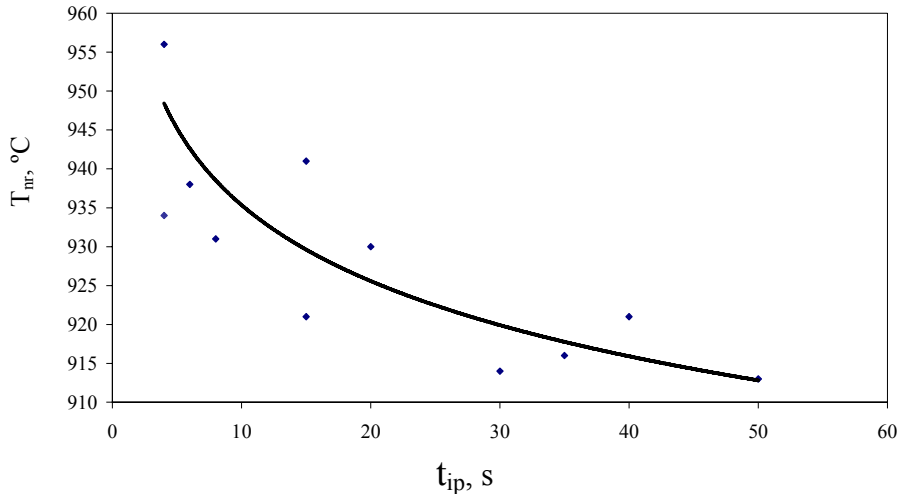

Figure 7.17 The T_{nr} as a function of inter-pass time (t_{ip}) for alloy #6. Strain rate $\dot{\varepsilon}$ =1.0 s^{-1}, pass strain ε = 0.2.

It can be seen that the T_{nr} decreases with increasing inter-pass time from 4 to 50 seconds in alloy #6. Although a large degree of scatter was present, this dependence can be described approximately by the following equation:

$$T_{nr}=961t_{ip}^{-0.0128} \qquad R^2=0.68 \qquad (7.5)$$

The result is different from that of Bai[48,125]. Bai reported that the dependence of the T_{nr} can be divided into three distinct regions: short inter-pass times (less than 12.5 seconds), medium inter-pass times (from 12.5 to 80 seconds) and long inter-pass times (more than 80 seconds). Within the short inter-pass times, the T_{nr} decreases with an increase in inter-pass time up to 12.5 seconds because solute drag by Nb on austenite grain boundaries retards recrystallisation prior to precipitation of NbC. Within the medium inter-pass times, precipitation of NbC occurs and retards recrystallisation and the T_{nr} then increases with an increase in inter-pass time. With a further increase in inter-pass time, the precipitates become coarse and become less effective in retarding the recrystallisation, so that the T_{nr} decreases again with inter-pass time. Some researchers[17,27,129] supported this finding of Bai while another[106] supported the key mechanism of a process of strain induced precipitation.

In this study, it was found that the T_{nr} decreases with increasing inter-pass time within the range of 4 to 50 seconds, probably with both solute drag and precipitation that

affect the recrystallisation. The dependence of the T_{nr} on inter-pass time can be divided into two regions: short inter-pass times (t_{ip}<20 s) and long inter-pass time (20<t_{ip}<50 s). In the short inter-pass times, deformation induces a high density of dislocations and point defects[130] that are beneficial to the nucleation of austenite recrystallisation. Solute drag by Nb on austenite grain boundaries prior to precipitation plays only a retarding role in recrystallisation, which probably is weaker in this range, while dislocations and point defects provide enough driving force for recrystallisation. This means that more recrystallisation will takes place with increasing inter-pass time, leading to a sharp decrease in the T_{nr} with an increase in inter-pass time. With a further increase in inter-pass time, i.e. more than 20 seconds, the effect of inter-pass times on the T_{nr} becomes less. Precipitation takes place and the precipitates are still fine (coarsening is only significant after 80 seconds[125]) in this stage as there is enough time for Nb(C,N) or NbN nucleation on the dislocations introduced from the deformation[130]. These finer precipitates pin the grain boundaries, so that the retarding effectiveness of Nb(C,N) or NbN particles on the recrystallisation is significant. This means that the effect of inter-pass time could become weaker at longer times. Figure 7.17 showed that the effect of the precipitation on the recrystallisation is, therefore, probably stronger than that of solute drag. However, the effect of the precipitates of Nb(C,N) or NbN appears to be not greater than that found by Bai[125].

7.3.3 The T_{nr} and pass strain rate

The T_{nr} can also be affected, besides by the pass strain and inter-pass time, also by the pass strain rate during compression deformation. A group of tests at a pass strain rate ranging from 0.1 to 2.22 s^{-1} was carried out at a constant pass strain of 0.20 and a constant inter-pass time of 8 seconds for alloy #6 and the results are shown in figure 7.18.

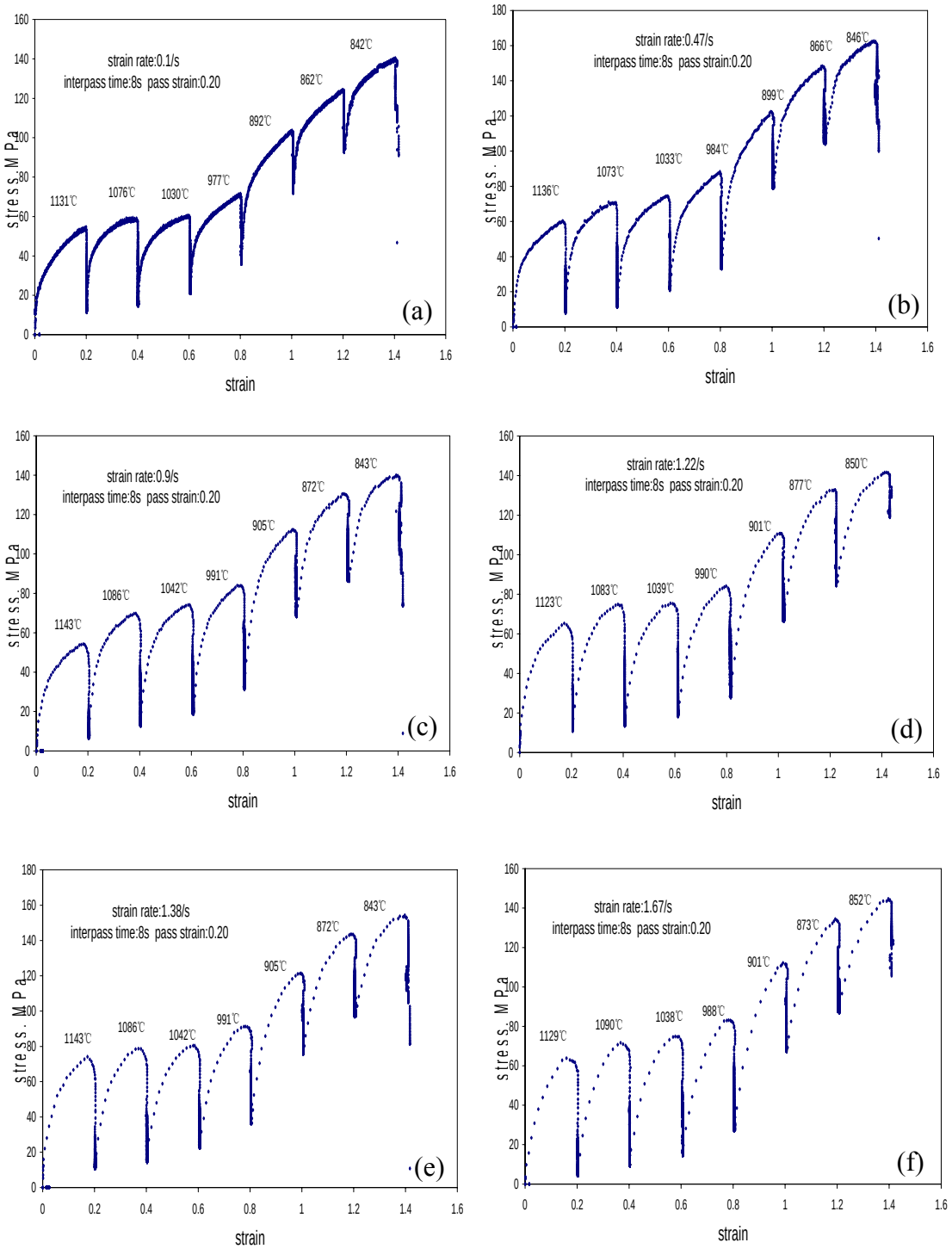

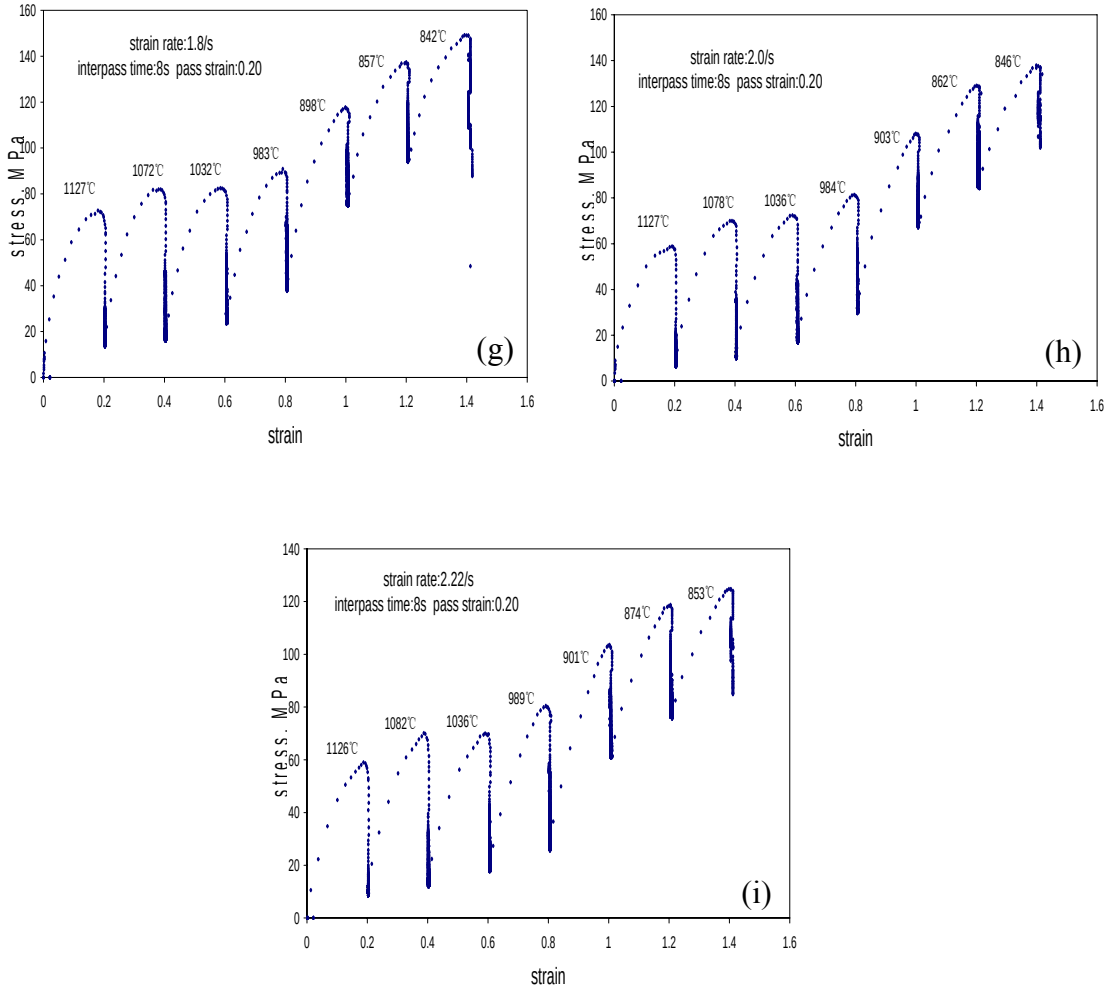

Figure 7.18 Stress-strain curves of compression deformation tests of alloy #6 at a constant pass strain of 0.20 and inter-pass time of 8 s but with a series of strain rates from 0.1 to 2.22 s^{-1}.

The number of passes in this series of tests was seven. The pass deformation temperatures are also marked on figure 7.18. The mean flow stresses calculated from figure 7.18 are plotted against the inverse of pass temperature (in K) in figure 7.19.

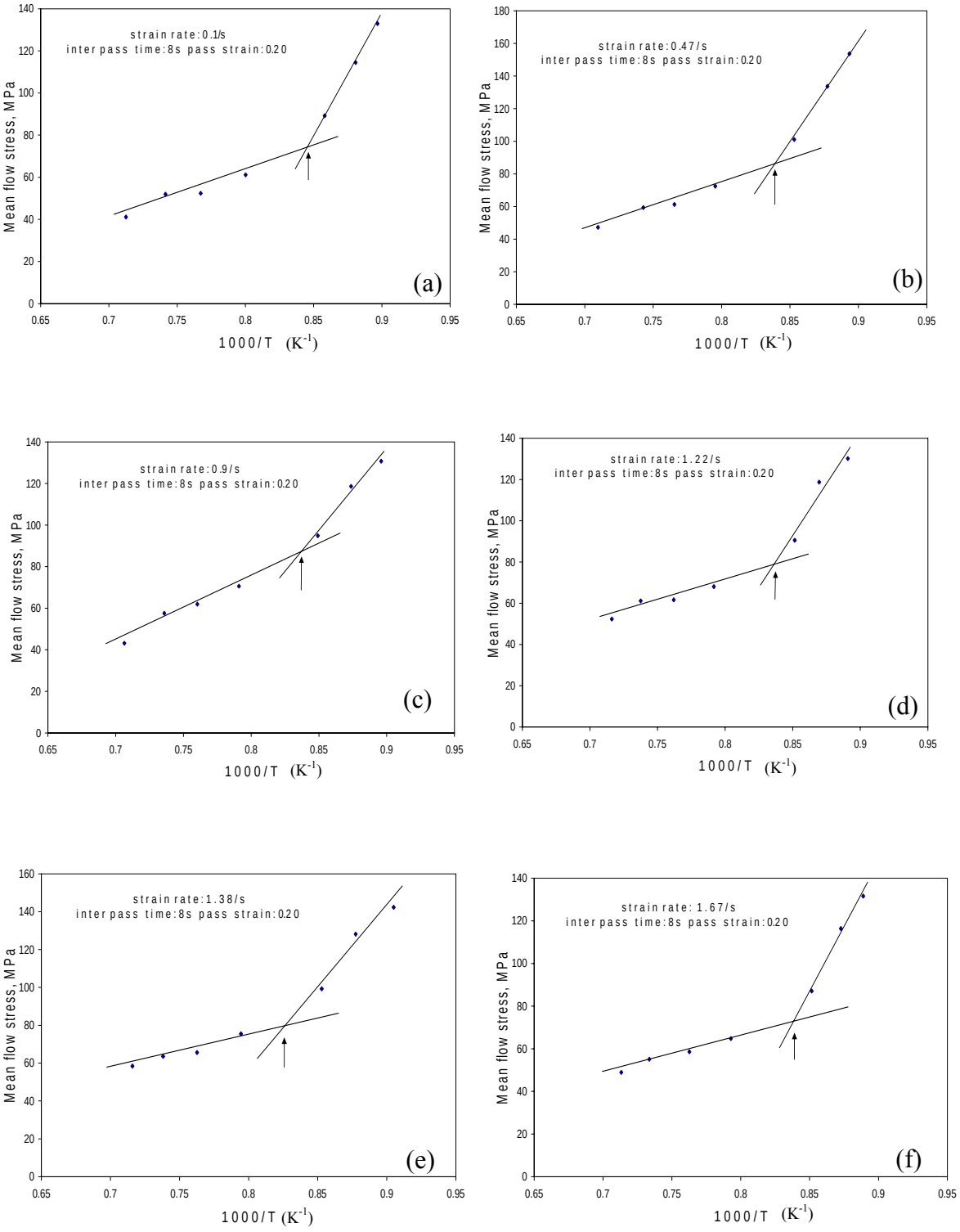

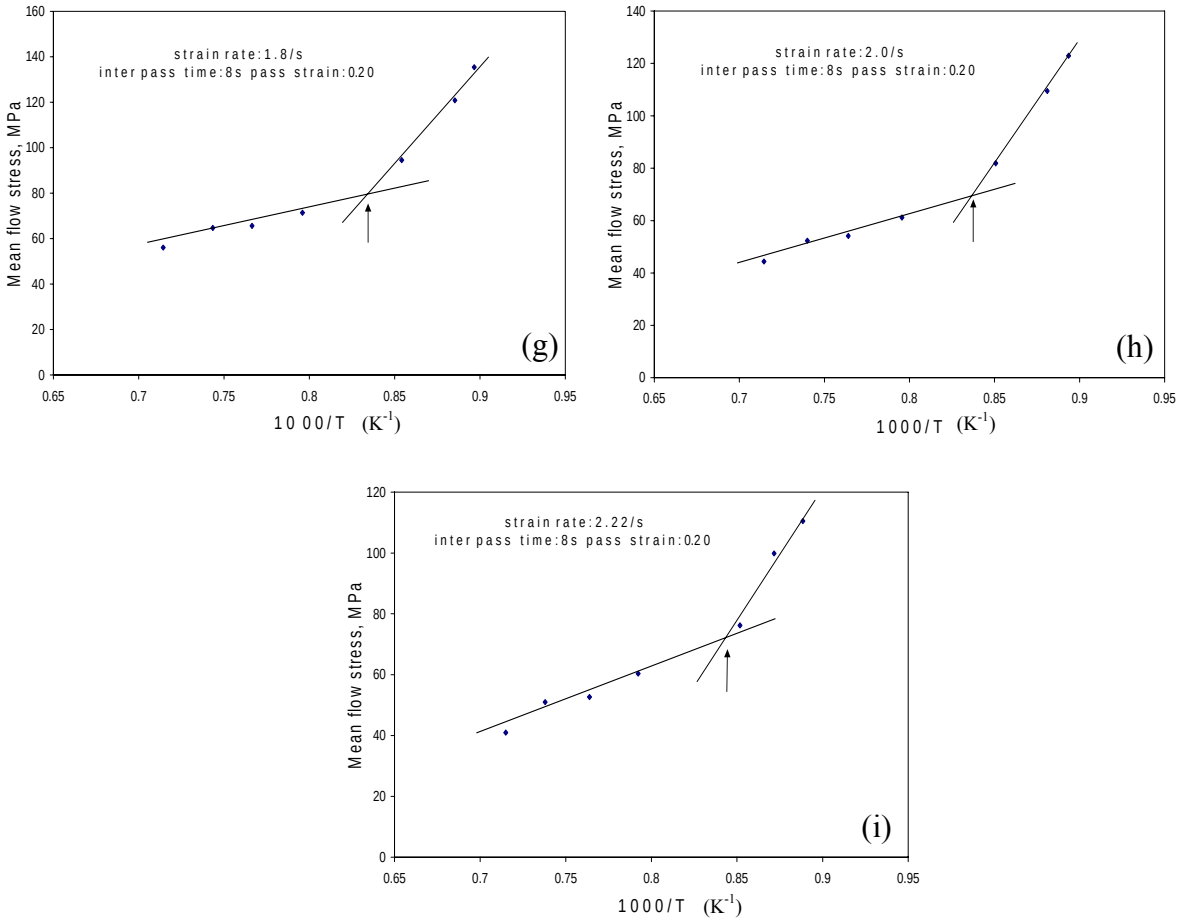

Figure 7.19 The mean flow stress versus inverse test temperature of alloy #6 at a constant pass strain of 0.20 and inter-pass time of 8 s but at a series of strain rates from 0.1 to 2.22 s^{-1}.

Table 7.6 The non-recrystallisation temperature and strain rates of alloy #6

Sample number	**C01**	**C05**	**C1**	**C15**	**C2**	**C3**	**C4**	**C6**	**C8**
Inter-pass time, t_{ip} (s)	8	8	8	8	8	8	8	8	8
Pass strain, ε	0.2	0.2	0.2	0.2	0.2	0.2	0.2	0.2	0.2
Strain rate (s^{-1})	0.1	0.47	0.9	1.22	1.38	1.67	1.80	2.0	2.22
T_{nr} (°C)	914	915	921	929	941	918	920	920	923

The results of the T_{nr} at different stain rates (with ε and t_{ip} constant) are listed in table 7.6 and are plotted in figure 7.20. The austenite should strain harden more at higher

strain rates during a compression test and this should result, theoretically at least, in a larger driving force for recrystallisation and, therefore, should decrease the T_{nr}. However, the opposite tendency was found in alloy #6 (see figure 7.20) and is also different from the results of Bai et al.[125] and Laasraoui[124]. They reported that the T_{nr} decreases with an increase in strain rate when the pass strains are 0.2, 0.3, 0.4 and 0.5. This inconsistency between these results and those obtained by others, may have to be examined further by torsion tests which allow higher strain rates than the highest value of 2.22 s^{-1} used here.

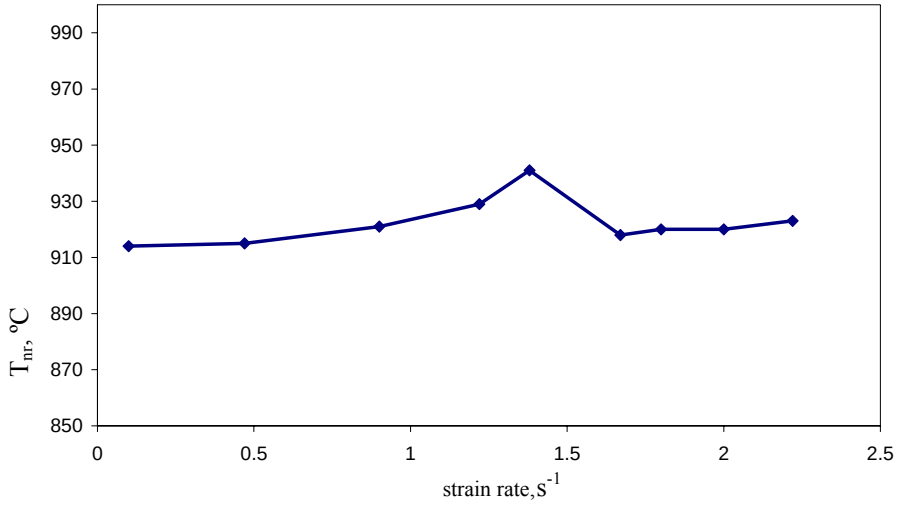

Fig.7.20 Strain rate ($\dot{\varepsilon}$) versus the non-recrystallisation temperature for alloy #6. Pass strain $\varepsilon = 0.2$, inter-pass time t_{ip}=8 s.

7.4. Continuous cooling transformation (CCT diagrams) under strain-free conditions

The aim in manufacturing technology of line pipe steel is to achieve a balance of high strength and toughness. Many researchers[32,65,66,92] have found that the optimal microstructure consists mainly of an acicular ferrite microstructure for optimised mechanical properties in micro-alloyed HSLA steels. Nb and Mo as micro-alloying elements[3,4,32] and thermo-mechanical processes[4,131] can affect the transformation to an acicular ferrite microstructure in line pipe steels. It is important to understand the continuous cooling transformation behaviour of Nb-Mo-Ti micro-alloyed steels, in particular whether an optimal fraction of an acicular ferrite microstructure can be obtained through micro-alloying additions and the hot rolling process. The following sections discuss the CCT diagrams for the experimental alloys #5 (with 0.22% Mo) and #6 (Mo-free) under conditions with and without prior deformation.

7.4.1 CCT diagram for alloy #6 without molybdenum and without prior deformation

The transformed microstructures of alloy #6 without molybdenum and prior deformation are given in figure 7.21.

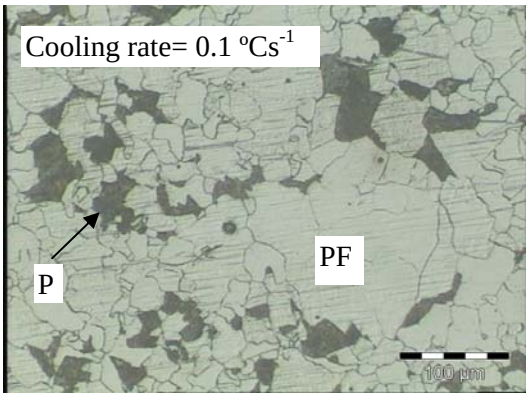

(a) Polygonal ferrite +pearlite

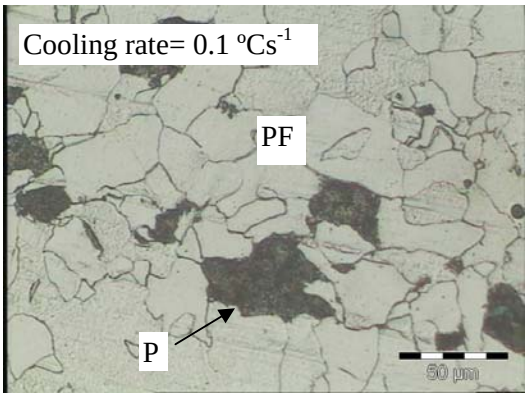

(b) Polygonal ferrite +pearlite

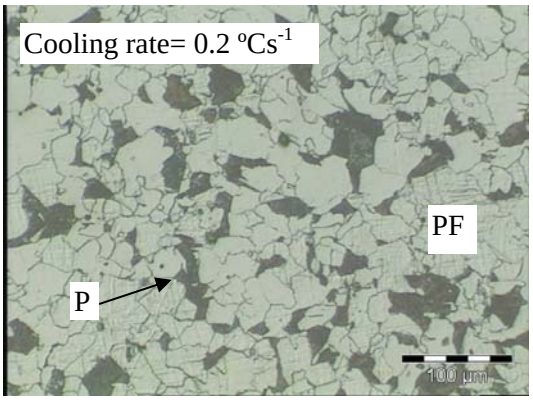

(c) Polygonal ferrite +pearlite

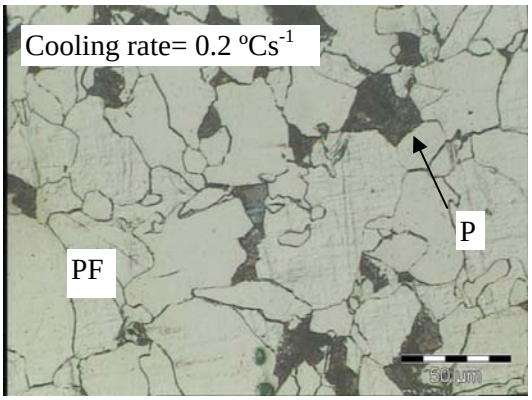

(d) Polygonal ferrite +pearlite

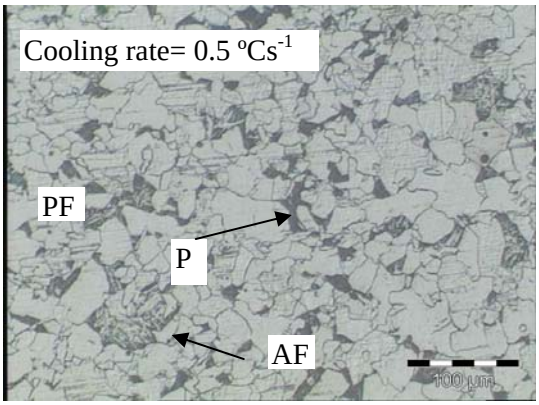

(e) Polygonal ferrite +pearlite + acicular ferrite

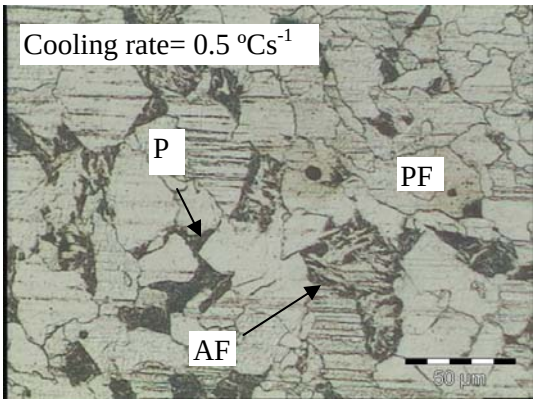

(f) Polygonal ferrite +pearlite + acicular ferrite

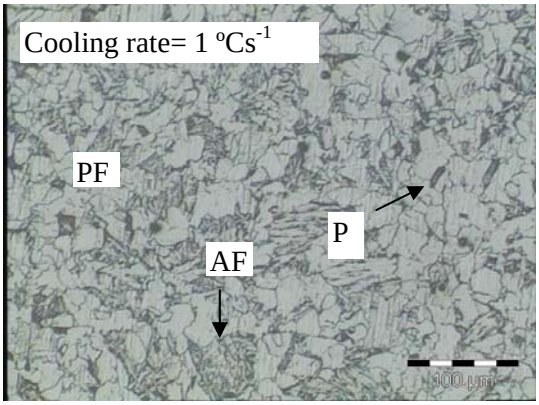

(g) Polygonal ferrite + pearlite + acicular ferrite

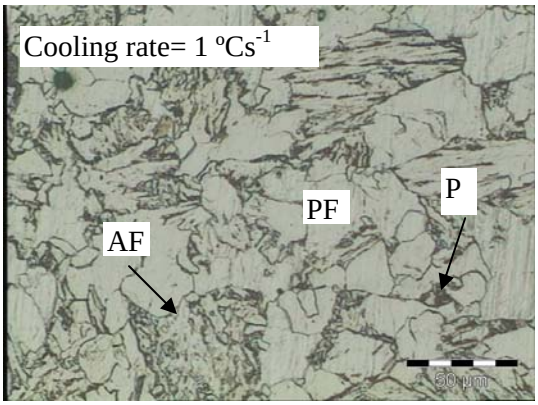

(h) Polygonal ferrite +pearlite + acicular ferrite

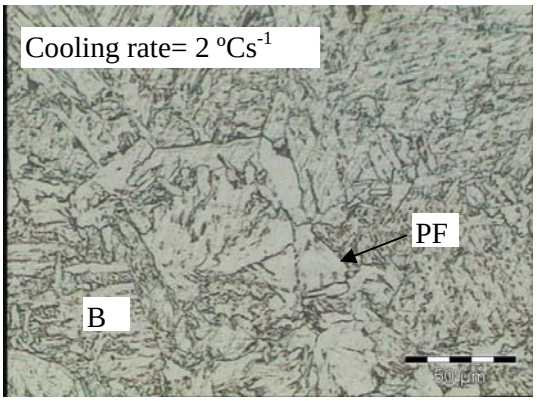

(i) Polygonal ferrite +bainite

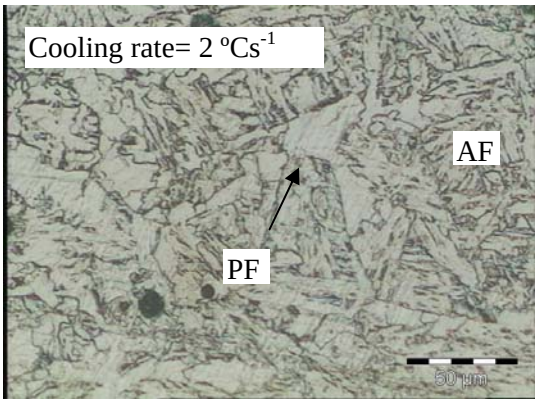

(j) Polygonal ferrite +acicular ferrite

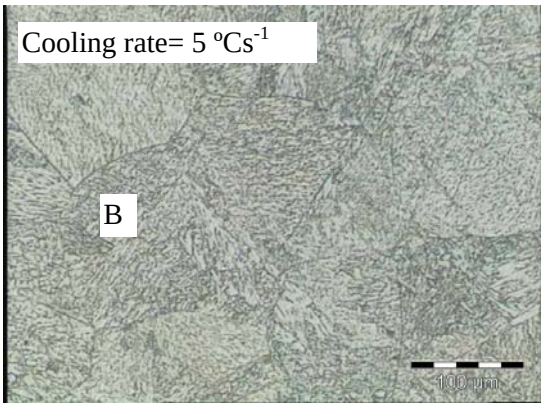

(k) Bainite

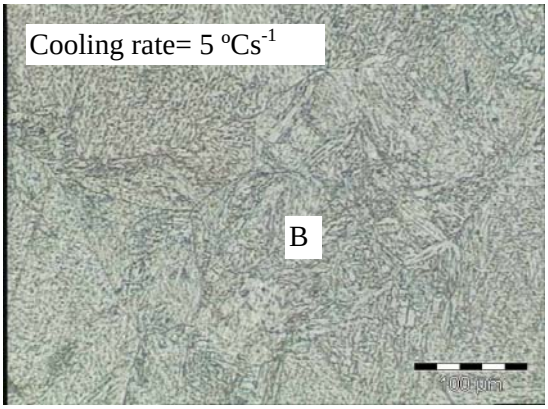

(l) Bainite

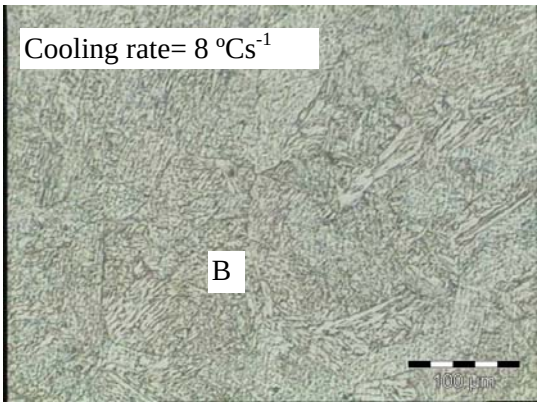

(m) Bainite

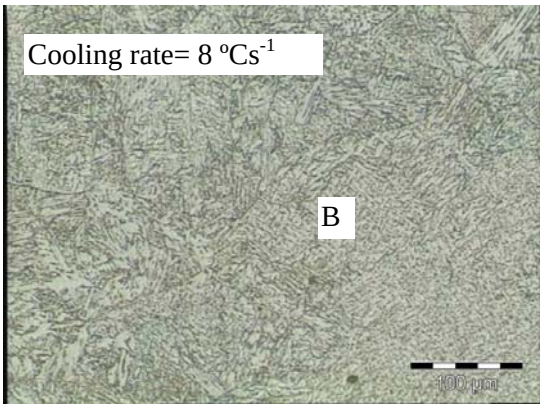

(n) Bainite

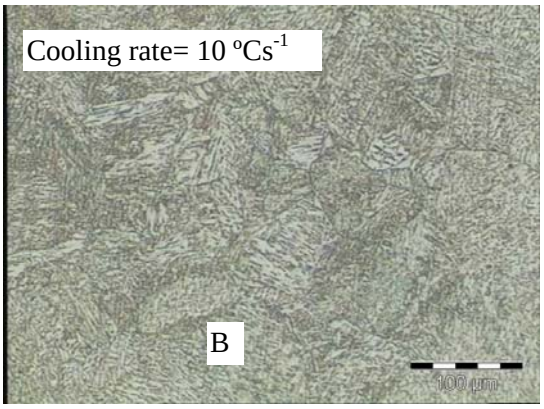

(o) Bainite

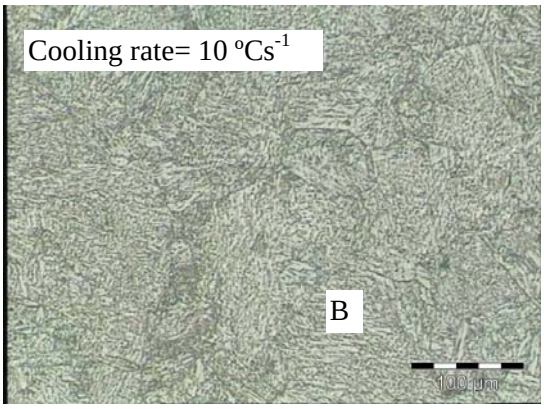

(p) Bainite

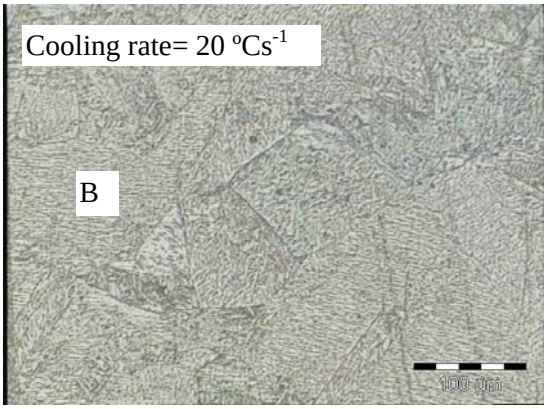

(q) Bainite

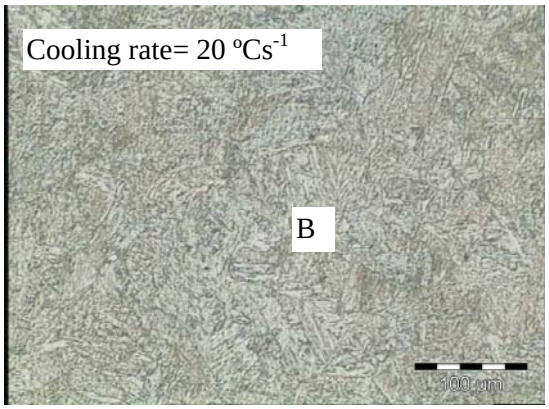

(r) Bainite

Figure 7.21 The optical micrographs (etched in 2% Nital) of the Mo-free alloy #6 and with no prior deformation after continuous cooling. PF-polygonal ferrite, P-pearlite and AF-acicular ferrite microstructure.

The transformed microstructures are affected by the different cooling rates and contain polygonal ferrite, pearlite, an acicular ferrite microstructure or bainitic ferrite. The microstructures contained polygonal and pearlite at low cooling rates, while an acicular ferrite microstructure was obtained at medium cooling rates ranging from about 0.5 to 5 $ºCs^{-1}$. The bainite phase occurred at a cooling rate above about 2 $ºCs^{-1}$ while bainite was practically the only phase above a rate of 5 $ºCs^{-1}$.

The CCT diagrams (with no prior deformation) were constructed through dilatometry and the optical micrographs (figure7.21) after cooling. The CCT diagram of the Mo-free alloy #6 is given in figure 7.22.

The areas of polygonal ferrite, pearlite, an acicular ferrite microstructure and bainite are identified as PF, P, AF and B in the CCT diagram (figure 7.22), respectively. As may be seen, a 100% acicular ferrite microstructure could not be obtained for the reference alloy #6 without prior deformation. A mixture of polygonal ferrite, pearlite and an acicular ferrite microstructure was found within the range of cooling rates between 0.3 and 2 $^{o}Cs^{-1}$, and polygonal ferrite, an acicular ferrite microstructure plus bainite in the range 1.5 to 5 $^{o}Cs^{-1}$. The acicular ferrite microstructure constituent was formed within the cooling rate range of 0.3 to 5 $^{o}Cs^{-1}$ for this Nb-bearing alloy #6 while a 100% bainite transformation occurred above 5 $^{o}Cs^{-1}$.

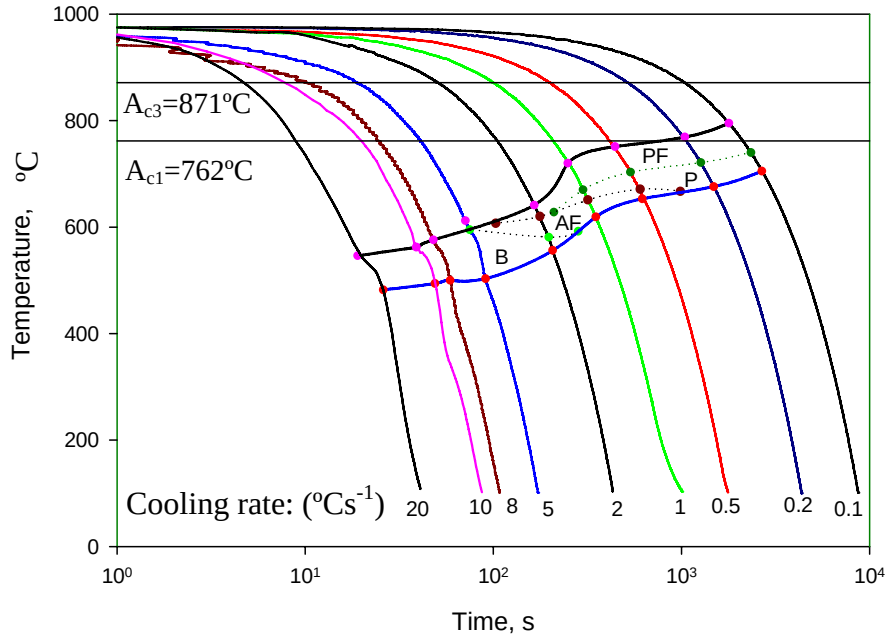

Figure 7.22 The CCT diagram of the Mo-free alloy #6 and no prior deformation. PF-polygonal ferrite, P-pearlite, AF-acicular ferrite microstriucture and B-bainite.

7.4.2 CCT diagram for alloy #5 with 0.22% molybdenum and without prior deformation

The microstructures for alloy #5 with 0.22% Mo and without deformation and transformed at different cooling rates are given in figure 7.23.

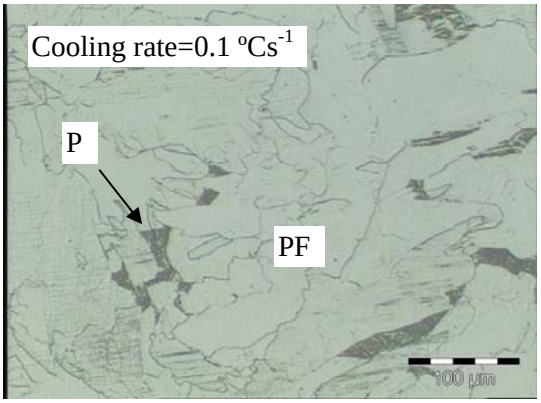

(a) polygonal ferrite + pearlite

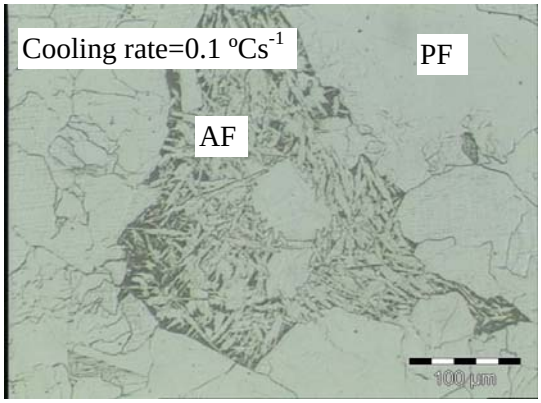

(b) polygonal ferrite + acicular ferrite

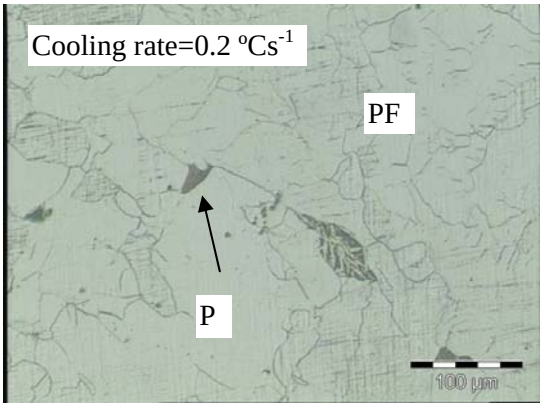

(c) polygonal ferrite + pearlite

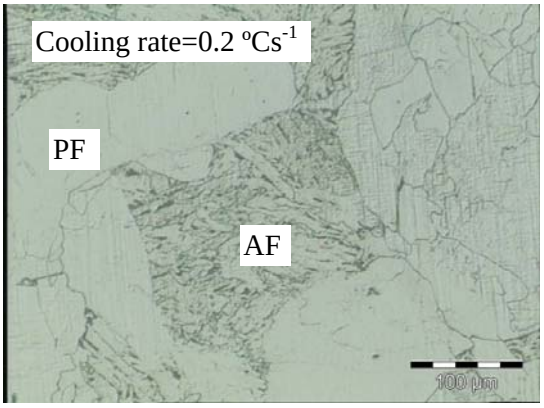

(d) polygonal ferrite + acicular ferrite

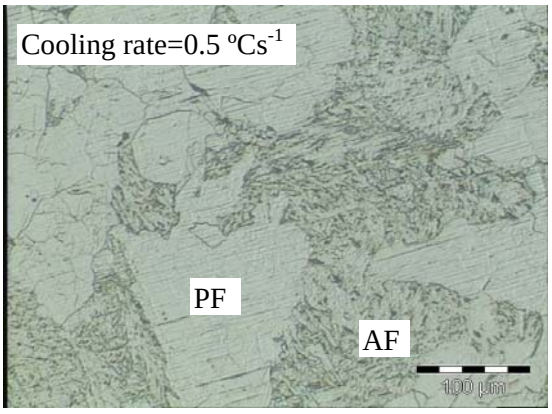

(e) polygonal ferrite + acicular ferrite

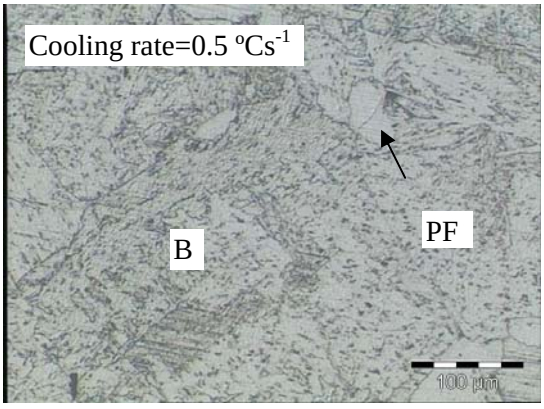

(f) bainite + polygonal ferrite

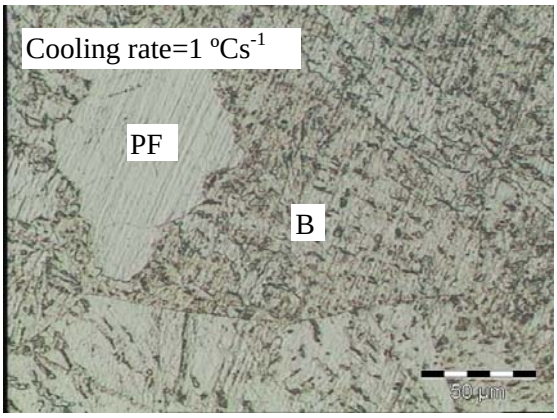

(g) polygonal ferrite + bainite

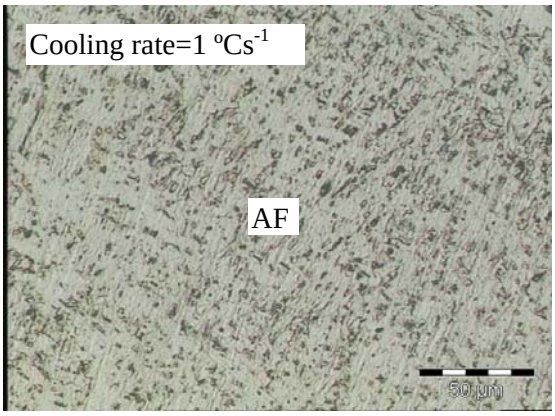

(h) acicular ferrite

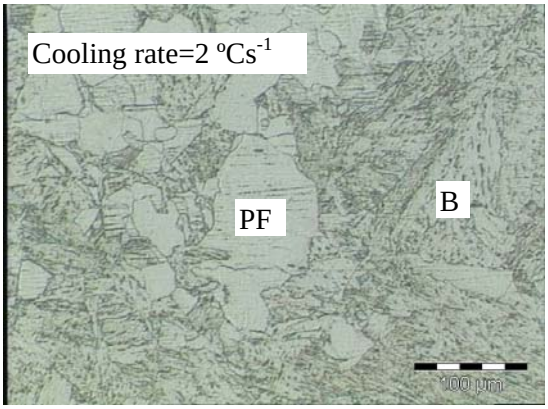

(i) polygonal ferrite + bainite

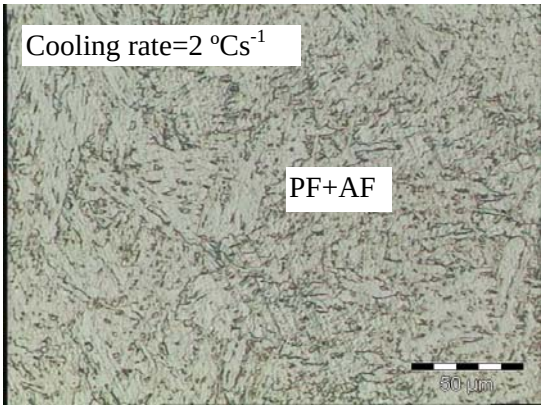

(j) polygonal ferrite + acicular ferrite

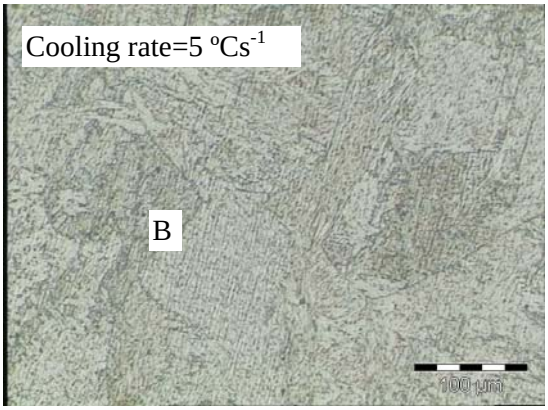

(k) bainite

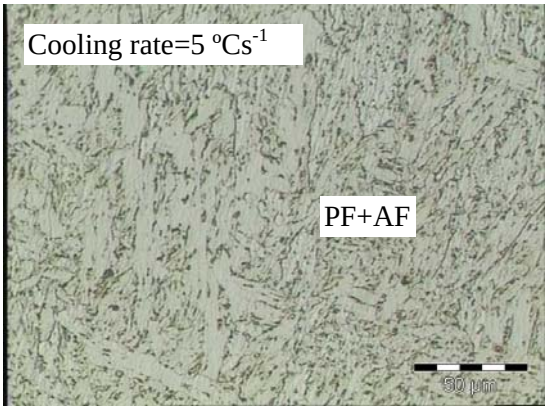

(l) polygonal ferrite + acicular ferrite

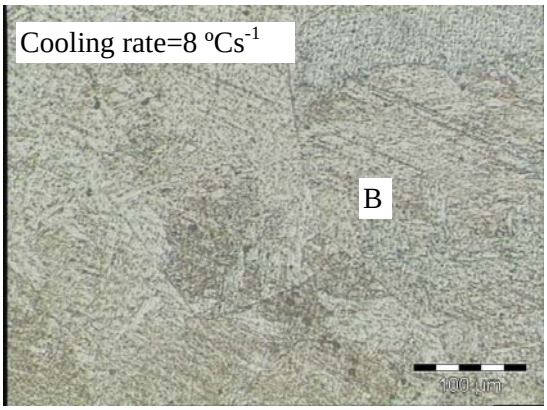

(m) bainite

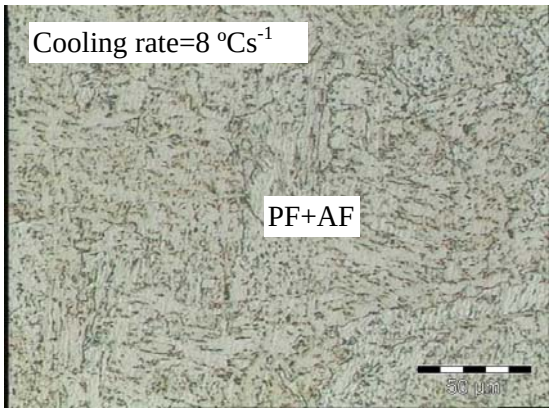

(n) polygonal ferrite + acicular ferrite

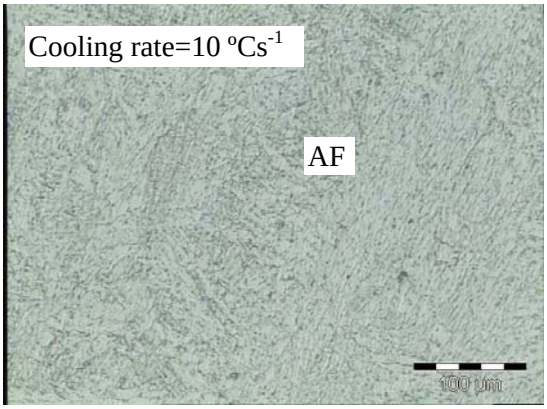

(o) acicular ferrite

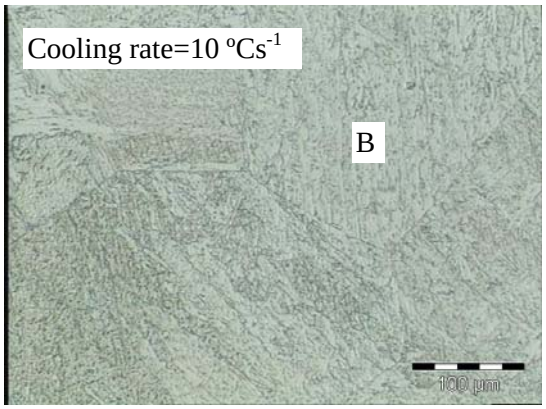

(p) bainite

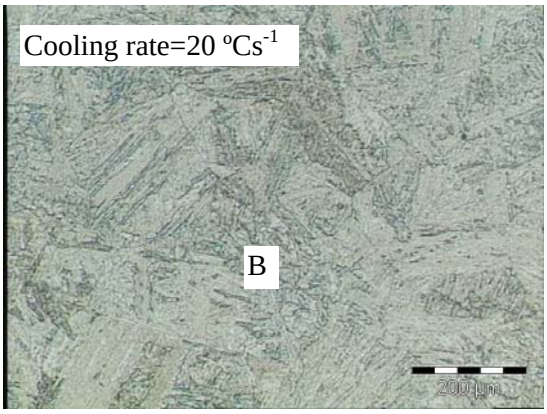

(q) bainite

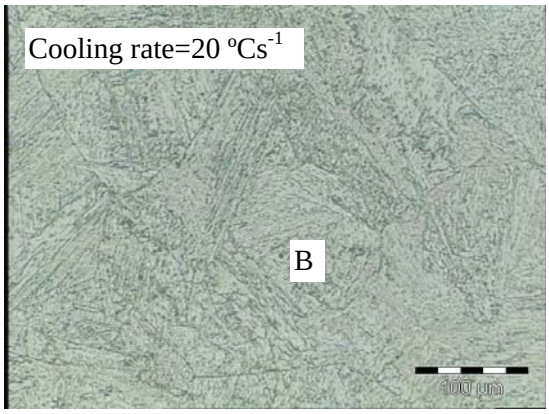

(r) bainite

Figure 7.23 The optical micrographs (etched in 2% Nital) for alloy #5 (with 0.22% Mo) and with no prior deformation after continuous cooling. PF-polygonal ferrite, P-pearlite and AF-acicular ferrite microstructure.

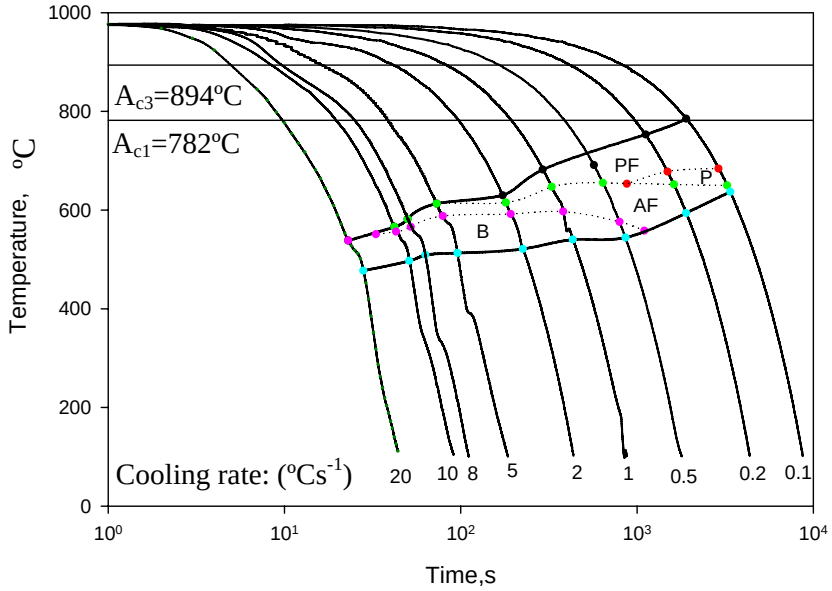

Figure 7.24 The CCT diagram of alloy #5 (with 0.22% Mo) and with no prior deformation. PF-polygonal ferrite, P-pearlite, AF-acicular ferrite microstructure and B-bainite.

The CCT diagram for alloy #5 with 0.22%Mo and without deformation is shown in figure 7.24. By comparing figure 7.22 without molybdenum and figure 7.24 with 0.22% Mo and with no applied deformation in both cases, the two CCT diagrams appear very similar. In both cases, a combination of polygonal ferrite and pearlite was obtained at lower cooling rates. An acicular ferrite microstructure could be obtained in the microstructures with increasing cooling rates. Bainite was the predominant constituent at higher cooling rates, replacing the acicular ferrite microstructure. But closer inspection of the two diagrams reveals some differences between them.

- An acicular ferrite microstructure could be obtained at a cooling rate above approximately 0.3 °Cs^{-1} for the Mo-free alloy #6 while it was obtained already above about 0.1 °Cs^{-1} for alloy #5 (0.22% Mo). The presence of molybdenum, therefore, appears to promote the formation of an acicular ferrite microstructure to some degree, even without prior deformation.
- A bainite phase transformation occurred at lower cooling rates of 0.3 °Cs^{-1} in alloy #5 with molybdenum than in alloy #6, in which a cooling rate of about 1.5 °Cs^{-1} was required. This indicates that molybdenum micro-alloying in the alloy

delays the bainite formation to lower cooling rates. Molybdenum, therefore, shifted the CCT diagram to longer times in the Nb-bearing low carbon alloys without prior deformation.

- An cicular ferrite microstructure formed within a wider cooling rate range from 0.1 to 10 $^{o}Cs^{-1}$ in alloy #5 while in the Mo-free alloy #6, this range was narrower from 0.3 to 5 $^{o}Cs^{-1}$. This means that the cooling rate range for an acicular ferrite microstructure formation for the experimental alloy #5 with 0.22% Mo, is wider than for the Mo-free alloy #6. Molybdenum can, therefore, expand the region of an acicular ferrite microstructure formation to some degree. The molybdenum addition to Nb-containing alloys, therefore, promotes to some degree the formation of an acicular ferrite microstructure in the microstructures without prior deformation. An acicular ferrite microstructure containing microstructure is an optimum microstructure in low carbon low alloyed steels due to its excellent balance of strength and toughness[92].
- Therefore, molybdenum additions to steels can result in superior mechanical properties under conditions of no prior deformation.
- Molybdenum is an alloying element that also promotes the formation of polygonal ferrite. The polygonal ferrite region in the CCT diagram of alloy #5 (figure 7.24) is larger than that of the Mo-free alloy #6 (figure 7.22).
- In contrast, however, the pearlite region in figure 7.24 for alloy #5 is smaller than that for the Mo-free alloy #6 in figure 7.22 and molybdenum additions, therefore, appear to act against the formation of pearlite in these steels without any prior deformation.

7.5 Strain enhanced continuous cooling transformation (CCT diagram) under deformed conditions

Besides chemical composition, deformation in the austenite phase prior to its transformation to ferrite, changes the appearance of the continuous cooling transformation diagram of these alloys. The final phases may vary with deformation parameters, i.e. temperature, strain or reduction, and cooling rate. It is important, therefore, to determine the strain affected CCT diagram after prior deformation.

7.5.1 Strain affected CCT diagram of the Mo-free alloy #6

The optical microstructures for alloy #6 (without molybdenum) are shown in figure 7.25 after a single pass strain of 0.6 at 860 ºC with strain rate of 0.5 s^{-1} and cooling down to room temperature after prior deformation.

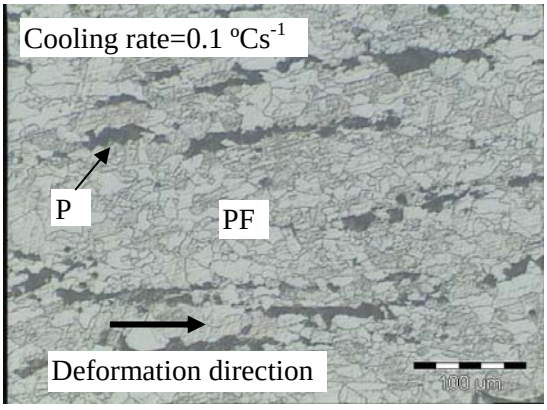

(a) polygonal ferrite + pearlite

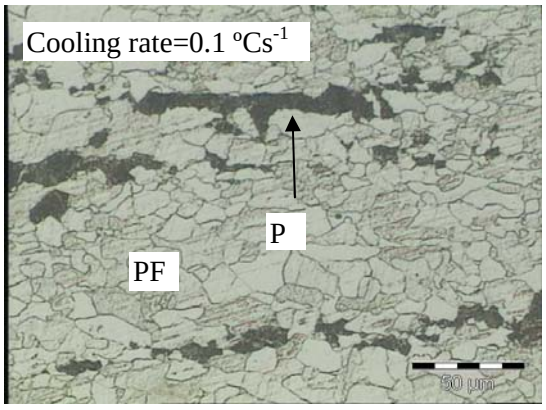

(b) polygonal ferrite + pearlite

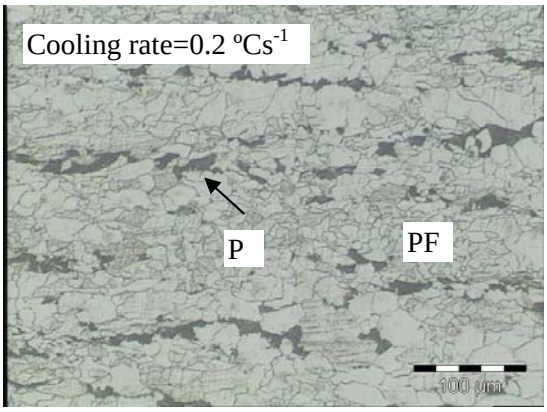

(c) polygonal ferrite + pearlite

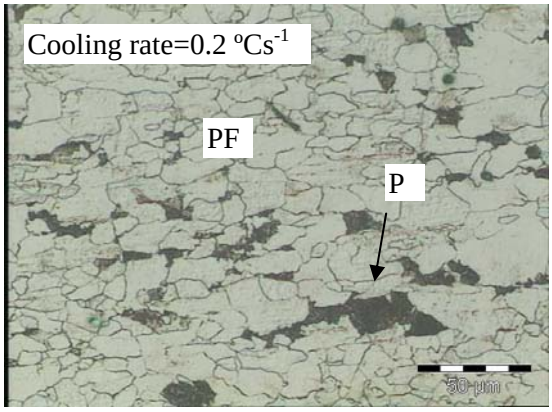

(d) polygonal ferrite + pearlite

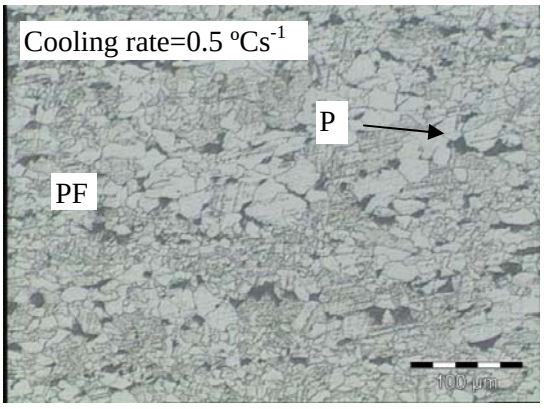

(e) polygonal ferrite + pearlite

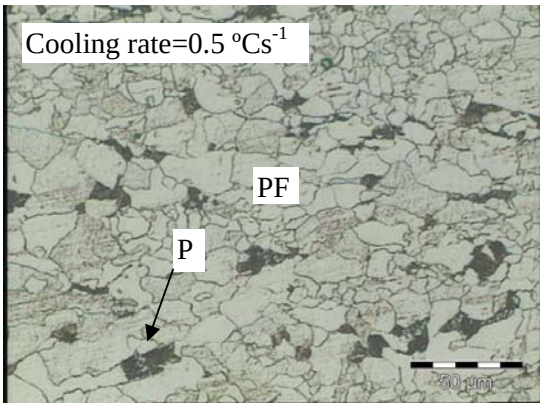

(f) polygonal ferrite + pearlite

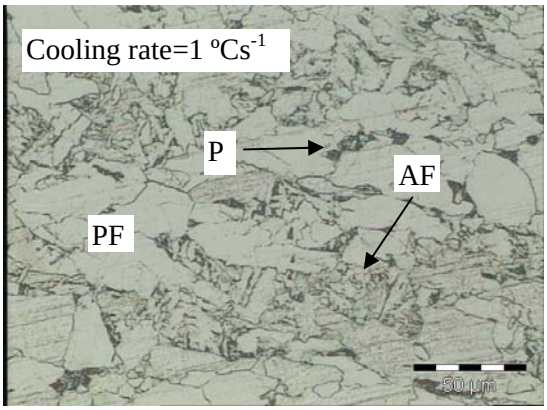

(g) polygonal ferrite + acicular ferrite + pearlite

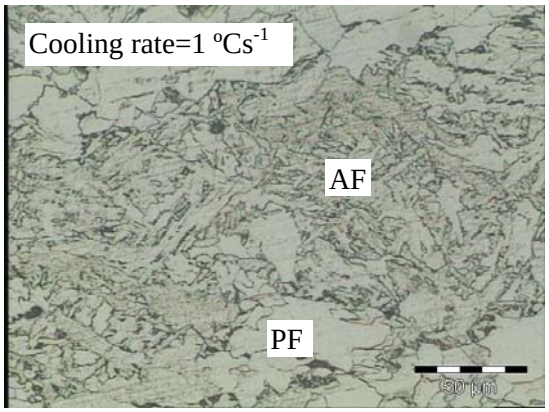

(h) polygonal ferrite + acicular ferrite

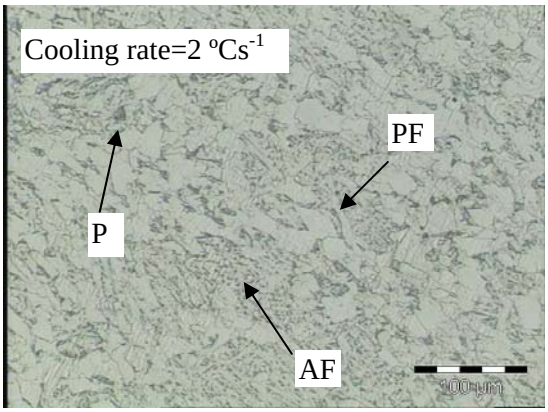

(i) polygonal ferrite + acicular ferrite + pearlite

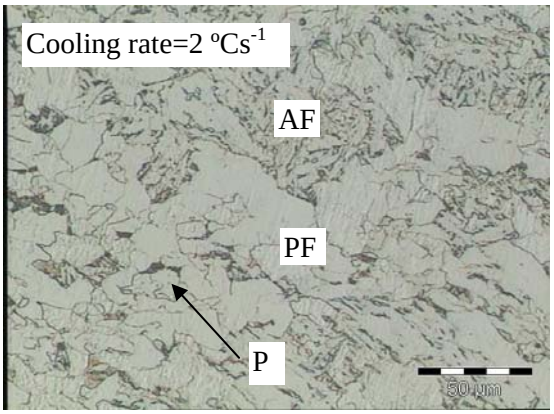

(j) polygonal ferrite + acicular ferrite + pearlite

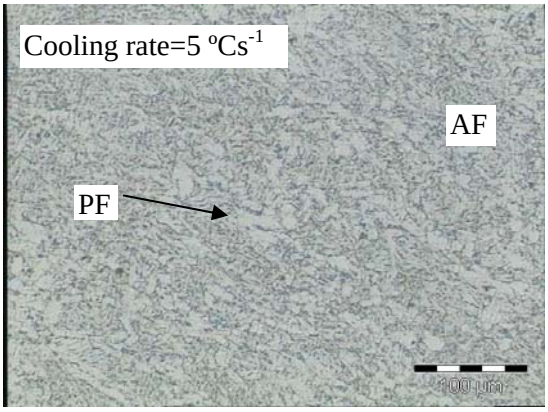

(k) polygonal ferrite + acicular ferrite

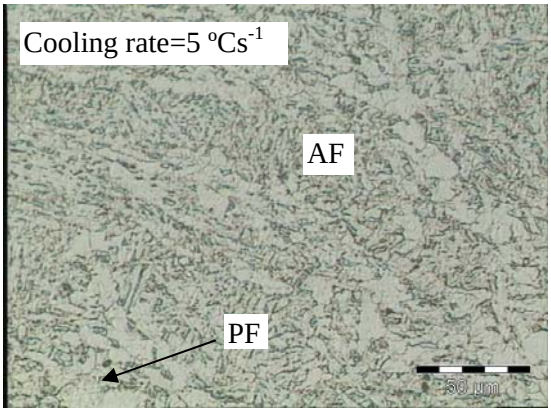

(l) polygonal ferrite + acicular ferrite

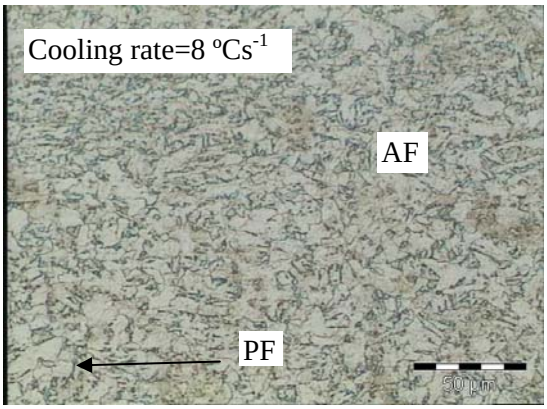

(m) polygonal ferrite + acicular ferrite

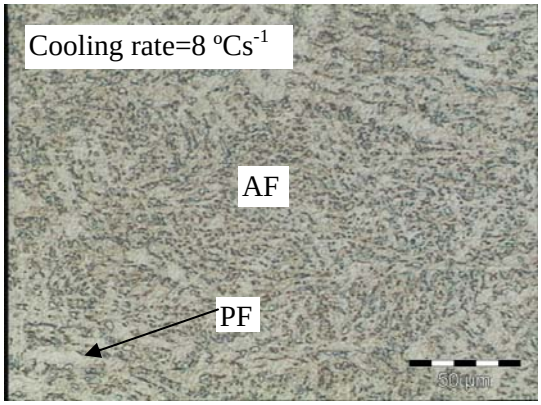

(n) polygonal ferrite + acicular ferrite

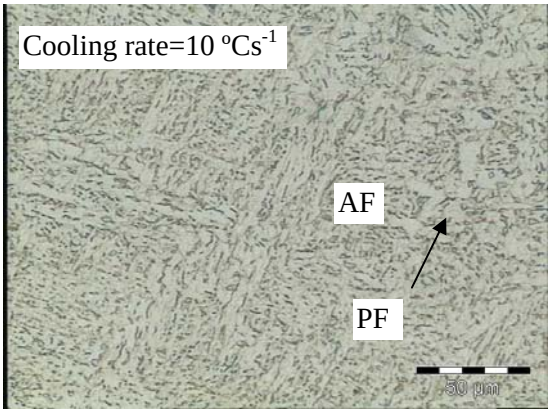

(o) polygonal ferrite + acicular ferrite

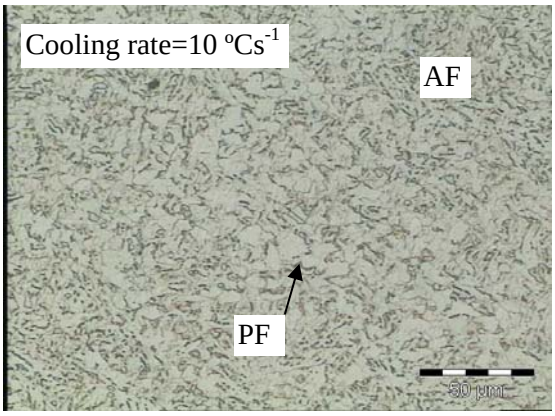

(p) polygonal ferrite + acicular ferrite

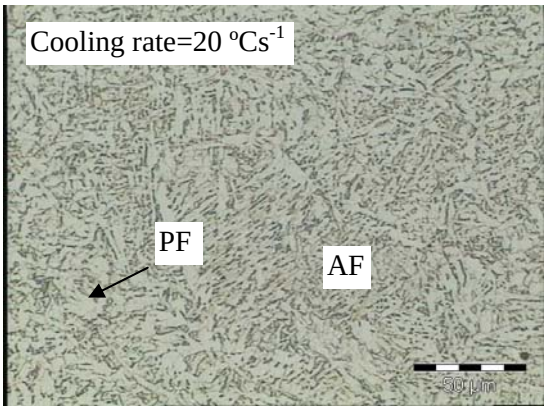

(q) polygonal ferrite + acicular ferrite

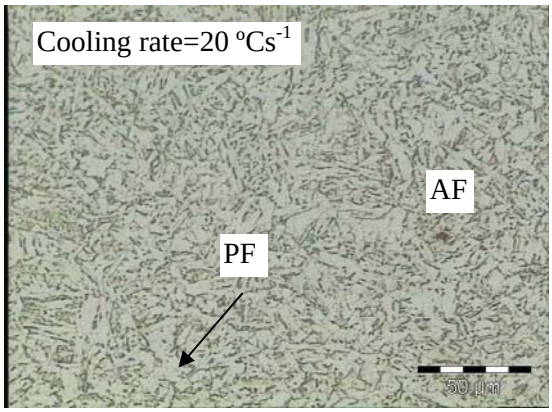

(r) polygonal ferrite + acicular ferrite

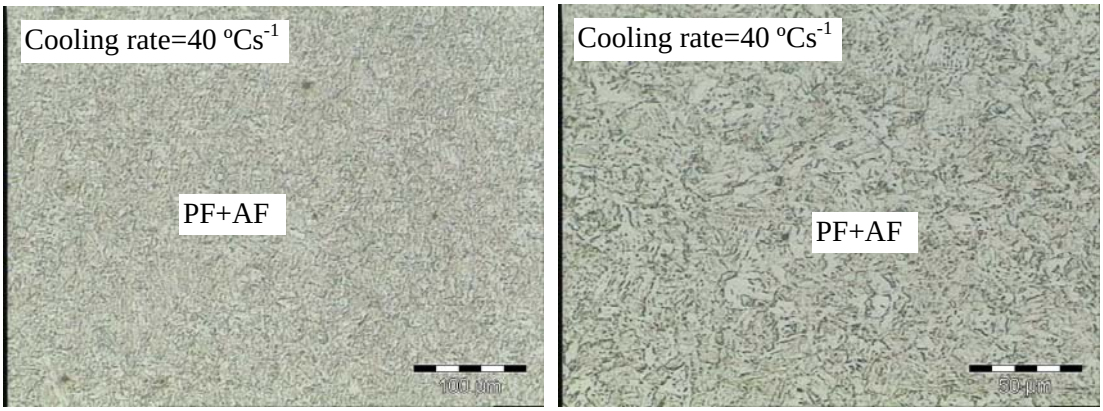

(s) polygonal ferrite + acicular ferrite (t) polygonal ferrite + acicular ferrite

Figure 7.25 The optical micrographs (etched in 2% Nital) of the Mo-free alloy #6 after compression testing with a single pass strain of 0.6 at 860 ºC (which is below the T_{nr}), a strain rate of 0.5 s^{-1} and cooling down to room temperature at different cooling rates. PF-polygonal ferrite, P-pearlite and AF-acicular ferrite microstructure.

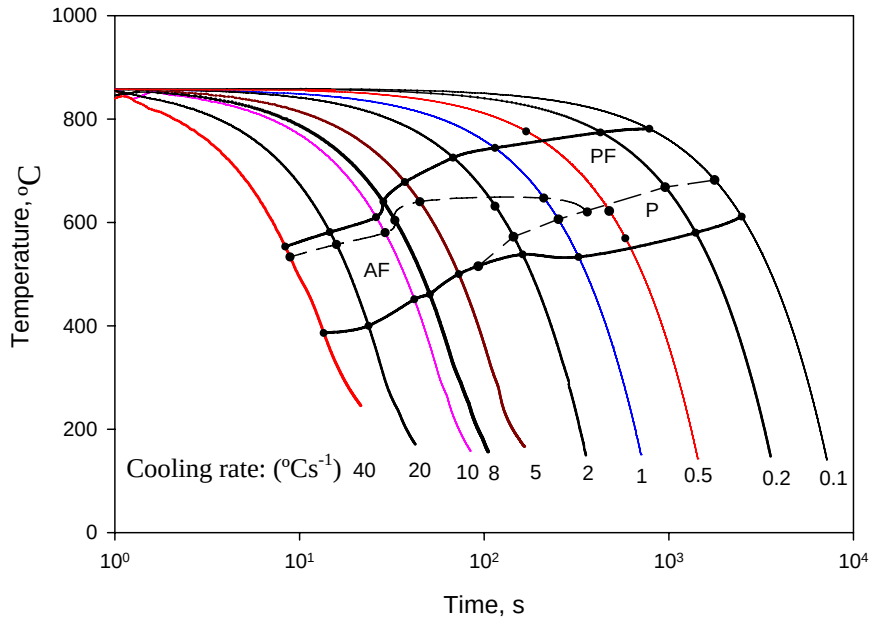

Figure 7.26 The strain affected CCT diagram of the Mo-free alloy #6 after a single pass compression strain of 0.6 at 860 ºC with a strain rate of 0.5 s^{-1}. PF-polygonal ferrite, P-pearlite and AF-acicular ferrite microstructure.

The strain affected CCT diagram of alloy #6 after a single pass strain deformation of 0.6 (equivalent to a 45% reduction) at 860 ºC with strain rate of 0.5 s^{-1} is shown in figure 7.26.

The micrographs of the Mo-free alloy #6 after compression to a strain of 0.6 show a combination of two or three of the phases of polygonal ferrite, pearlite and an acicular ferrite microstructure. This is different from the case of the same alloy but without prior deformation (figure 7.22) where bainite could be obtained at high cooling rates without deformation in this alloy. With prior deformation, however, no bainite is found at all cooling rates ranging from 0.1 to 40 ºCs^{-1} (see figures 7.25 and 7.26). This observation is consistent with the results of others[4,131] and it indicates that bainite transformation is restrained from forming in deformed austenite[132,133]. When a sample is deformed in the austenite region, more dislocations are formed in the austenite and these may act as obstacles in retarding the growth of a bainite packet or sheath in the deformed austenite. In undeformed austenite, on the other hand, there are less of these obstacles during bainite phase formation and as a result, bainite can be found at high enough cooling rates (figure 7.22).

7.5.2 Strain affected CCT diagram of alloy #5 (with 0.22% Mo)

Figure 7.27 shows the results for alloy #5 (with 0.22% Mo) after a prior deformation with a single pass strain of 0.6 at 860 ºC and at a strain rate of 0.5 s^{-1}.

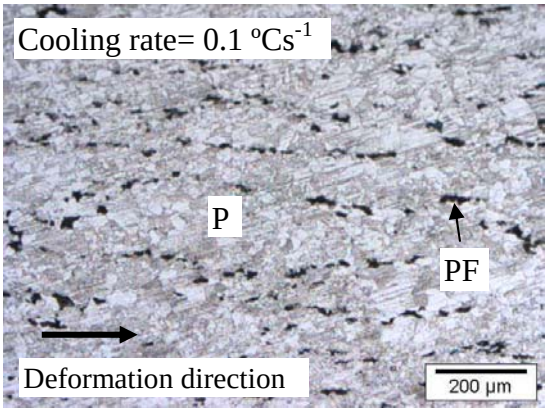

(a) polygonal ferrite + pearlite

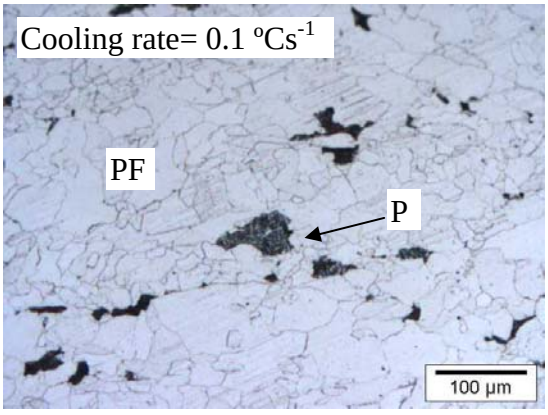

(b) polygonal ferrite + pearlite

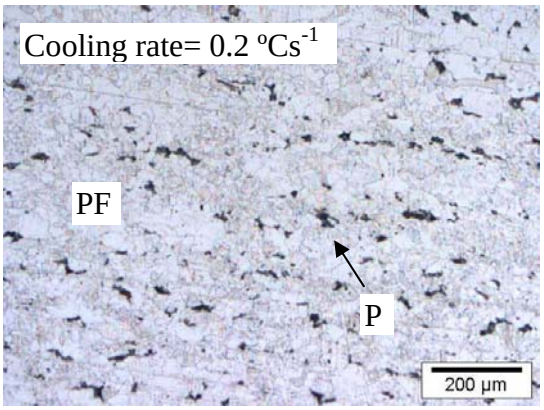

(c) polygonal ferrite + pearlite

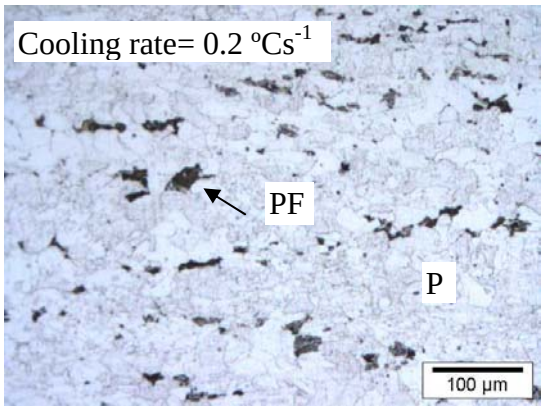

(d) polygonal ferrite + pearlite

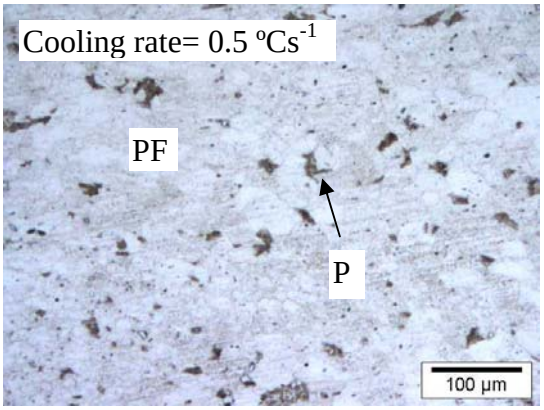

(e) polygonal ferrite + pearlite

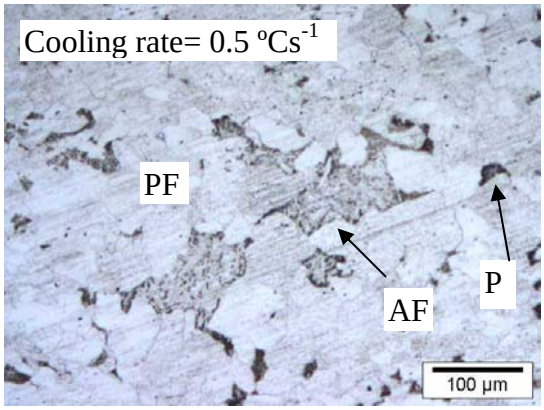

(f) polygonal ferrite + acicular ferrite + pearlite

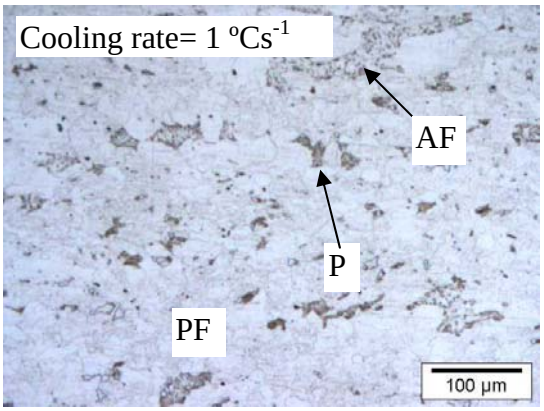

(g) polygonal ferrite + pearlite + acicular ferrite

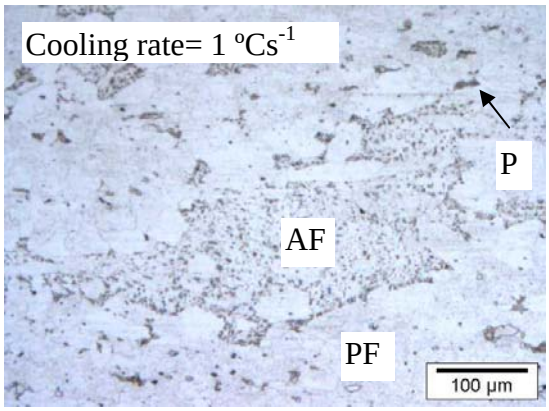

(h) polygonal ferrite + pearlite + acicular ferrite

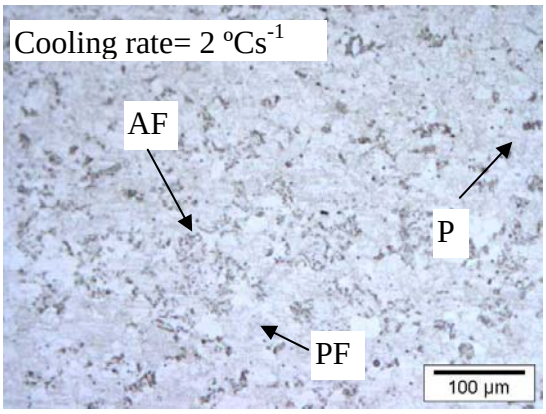

(i) polygonal ferrite + pearlite + acicular ferrite

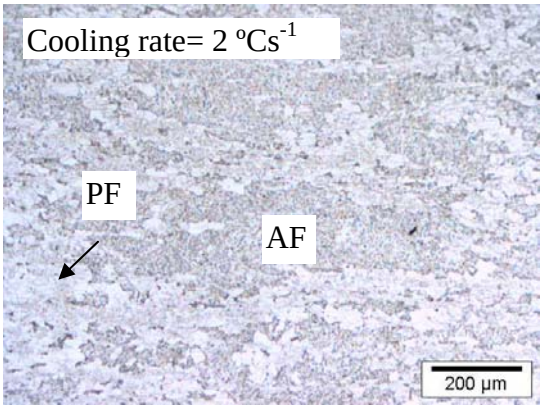

(j) acicular ferrite + polygonal ferrite

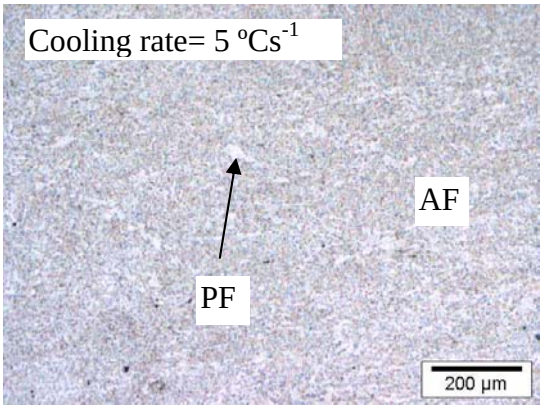

(k) acicular ferrite + polygonal ferrite

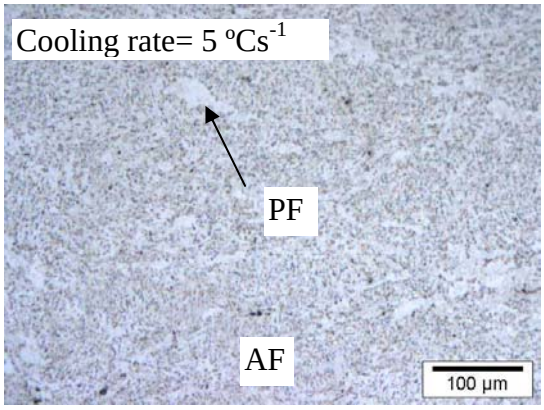

(l) acicular ferrite + polygonal ferrite

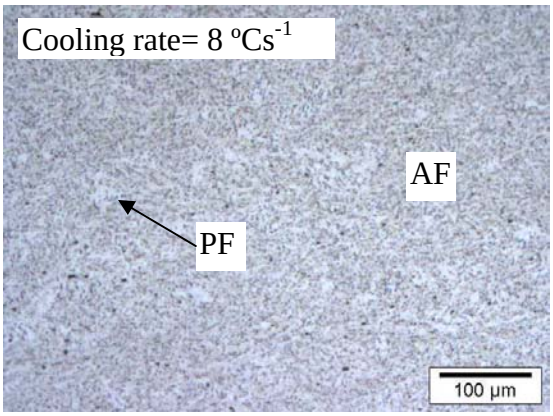

(m) acicular ferrite + polygonal ferrite

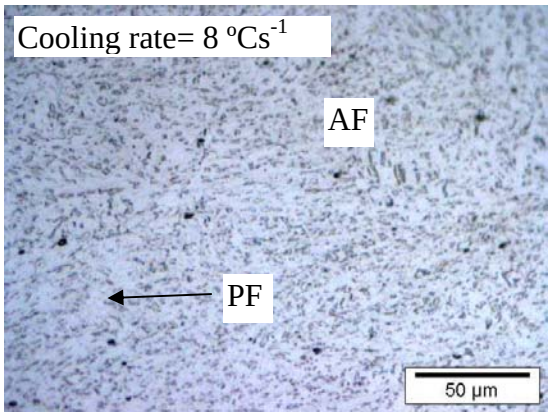

(n) acicular ferrite + polygonal ferrite

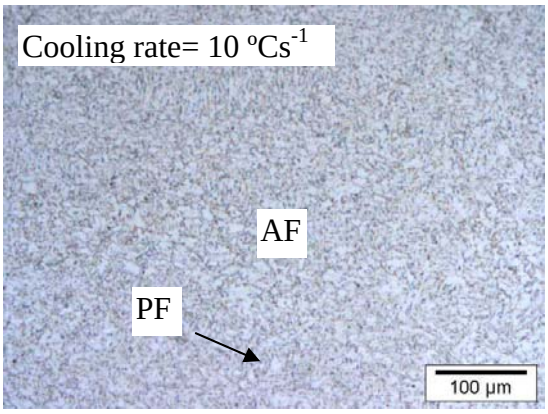

(o) acicular ferrite + polygonal ferrite

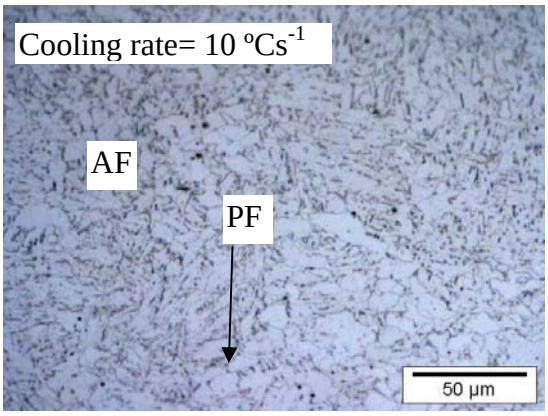

(p) acicular ferrite + polygonal ferrite

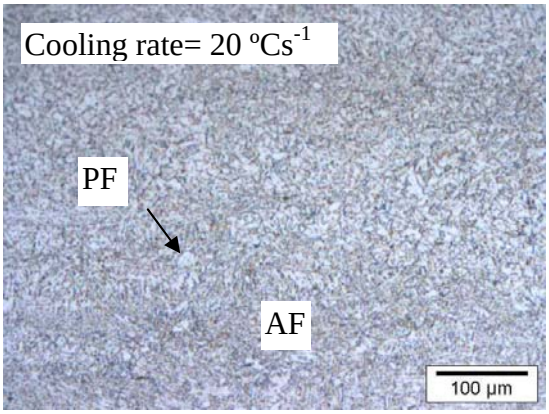

(q) acicular ferrite + polygonal ferrite

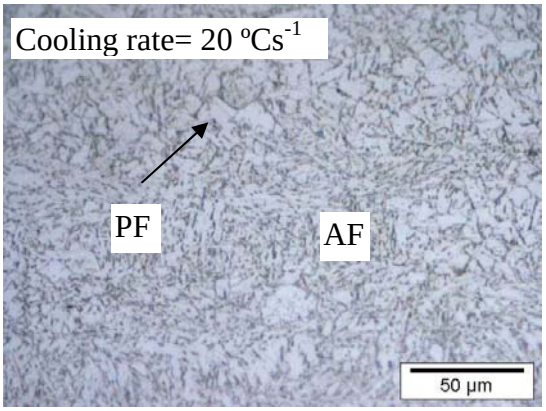

(r) acicular ferrite + polygonal ferrite

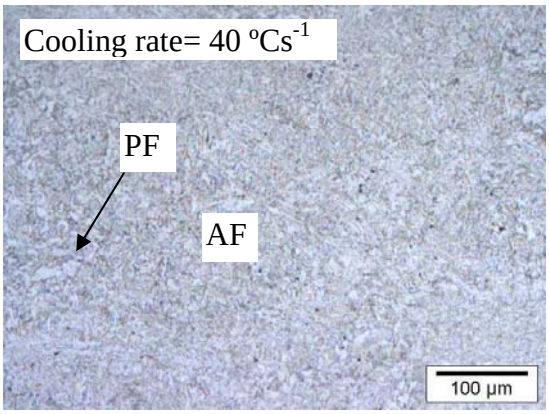

(s) acicular ferrite + polygonal ferrite

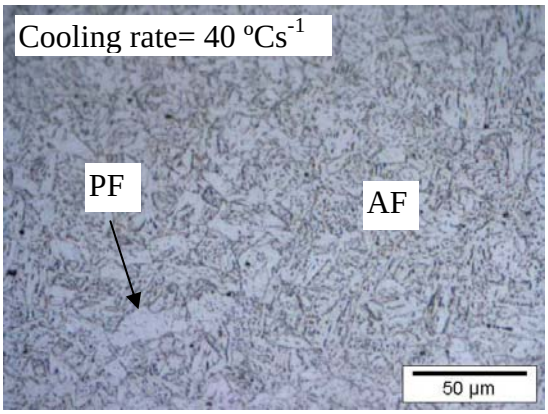

(t) acicular ferrite + polygonal ferrite

Figure 7.27 The optical micrographs (etched in 2% Nital) of alloy #5 (with 0.22% Mo) after a single pass compression of 0.6 strain at 860 ºC and at a strain rate of 0.5 s^{-1} and then cooling at different rates.

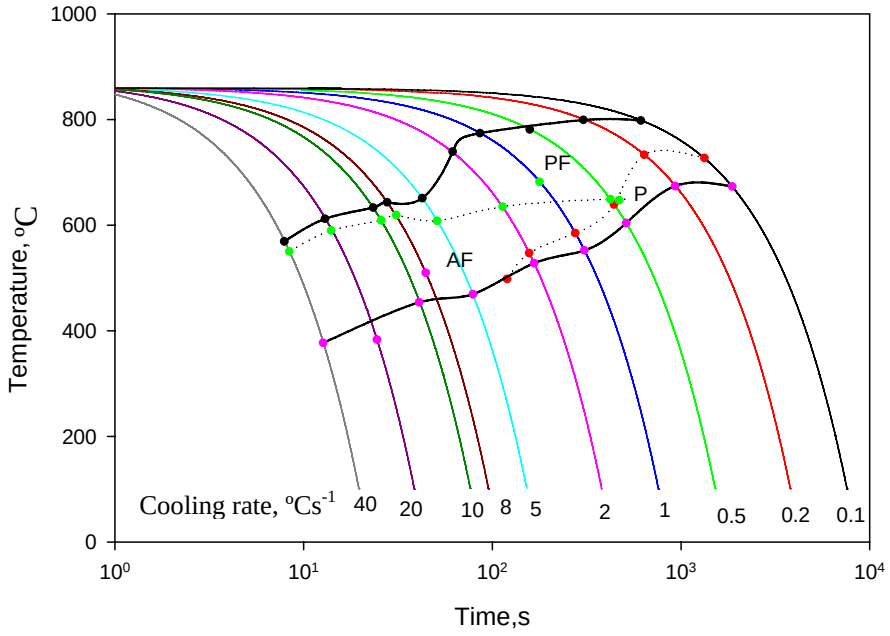

Figure 7.28 The strain affected CCT diagram of alloy #5 (with 0.22% Mo) after a single pass compression of 0.6 strain at 860 °C at a strain rate of 0.5 s^{-1}. PF-polygonal ferrite, P-pearlite and AF-acicular ferrite microstructure.

Figure 7.28 shows that the continuous cooling transformation for alloy #5 (with 0.22% Mo), is similar to alloy #6, the Mo-free alloy. Comparing figures 7.26 and 7.28, an acicular ferrite microstructure is formed at high cooling rates after prior deformation instead of bainite if compared to the case of no prior deformation. It appears that deformation in the austenite region is beneficial to the formation of an acicular ferrite microstructure for Mo-bearing alloys as it impedes the transformation to bainite. It seems, furthermore, that molybdenum additions did not markedly affect the formation of an acicular ferrite microstructure while the prior deformation in austenite had a dominant contribution. This may be from more dislocations resulting from the prior deformation that offered more intragranular nucleation sites for an acicular ferrite microstructure.

Therefore, the following conclusions can be drawn:

- Deformation in austenite promotes an acicular ferrite microstructure formation and hinders bainite formation.
- The effect of molybdenum is less than the effect of prior deformation on promoting an acicular ferrite microstructure formation.
- Bainite could be observed at high cooling rates in steels without prior deformation.

7.6 The results of the laboratory hot rolling process on the YS/UTS ratio

The five alloys #1 to #5 were hot rolled with the same pass numbers, pass strains, pass strain rates and the same total strain in rough and finish rolling on a laboratory mill while the same reheating conditions of 1225 ºC for 60 min were also used. The first rough rolling temperature and the finish rolling temperature, respectively, were very similar for all five experimental alloys. The accelerated cooling rate after finish rolling was also the same at about 47 ºCs^{-1}, for all five experimental alloys, and was 39 ºCs^{-1} for the Mittal steel alloy #6. The simulated coiling after cooling was at a temperature of 600 ºC for 24 hrs. The detailed variables in the hot rolling process for alloys #1 are listed in tables 7.7.

Table 7.7 The laboratory hot rolling parameters for alloy #1

Pass No.		R1	R2	reheating	R3	R4	R5	F1	reheating	F2	reheating	F3
Tempera-ture (ºC)	in	1190	1060	1225 5 min	1140	1070	1020	910	930 5 min	890	930 5 min	890
	out											860
t_{ip} (s)		23	--		16	14	16	--		--		--
Gauge (mm)	in	43	37		28	20	13.6	10.3		8.3		6.9
	out	37	28		20	13.6	10.3	8.3		6.9		6
Pass ε		0.15	0.28		0.34	0.38	0.28	0.22		0.18		0.14
Total ε		1.43						0.54				
Reduction(%)		76						42				
$\dot{\varepsilon}$ (s^{-1})		1.67	2.43		3.15	3.92	4.00	4.07		4.00		3.89

N.B.: The R and F in the table stand for roughing and finishing passes, respectively.

The precise details for the other five alloys #2 to #6, which were very similar to those of alloy #1, are shown in Appendix A. Sample #M1-11 of alloy #6 was taken as a reference to study the microstructures and carry out TEM work.

As can be seen in the table above, the pass strain in the rough rolling stage is more than 0.2 (except for the first pass) in order to obtain a fine recrystallised austenite grain size. The heavy total reduction for alloys #1 to #5, i.e. 76% in rough rolling, 42% in finish rolling and 86% in total, contributes to an optimum combination of strength and toughness through a fine size. Rapid cooling of 47 ºCs^{-1} is useful for the

formation of an acicular ferrite microstructure. The alloy #6 was also used to study the effect of cooling rate, coiling temperature and deformation vis-à-vis the ratio of yield strength to ultimate tensile strength (see Appendix H).

7.7 Volume fraction of acicular ferrite

The volume fraction of acicular ferrite was measured by image-analysis software on shadowed carbon extraction replicas from TEM micrographs taken at 980 times magnification on the experimental alloys #1 to #5. The results are shown in table 7.8 below. Alloy #1 is similar to the Mo-free reference alloy #6 in chemical composition, whereas alloys #2 to #5 contained varying amounts of molybdenum.

Table 7.8 Measured results of volume fraction of acicular ferrite

Alloy #	#1	#2	#3	#4	#5
Molybdenum (%wt)	0.01	0.09	0.09	0.12	0.22
Volume fraction of AF (%)	55.4	46.3	49.4	52.0	46.8
Volume fraction of PF (%)	44.6	53.7	50.6	48.0	53.2

NB. AF-acicular ferrite and PF-polygonal ferrite

Although there appears to be a small effect of molybdenum in affecting the volume fractions of AF and PF, the effect is relatively small and probably needs further study to confirm this.

7.8 Mechanical properties

7.8.1 Results of experimental alloys

The mechanical properties of the five experimental alloys that were hot rolled in the laboratory mill (see section 7.6 above) are given in table 7.9 and the individual curves of strength versus elongation are shown in Appendix G. The longitudinal and transverse (to the rolling direction) values in the table were the average of five samples per direction per alloy except for only four samples for alloy #5 (both directions) and the transverse direction only for alloy #1. The yield strength was taken as the proof strength at 0.5% permanent strain for continuous yielding.

Table 7.9 Mechanical properties of the experimental alloys

Alloy #	Sample direction	YS, MPa	UTS, MPa	YS/UTS	Elongation (%)	Yield type
1	Longitudinal	463	555	0.83	33	D
	Transverse	454	547	0.83	31	D
2	Longitudinal	504	589	0.86	33	D
	Transverse	478	591	0.81	27	D
3	Longitudinal	467	558	0.84	36	D
	Transverse	470	558	0.84	30	D
4	Longitudinal	472	559	0.84	33	D
	Transverse	494	581	0.85	30	D
5	Longitudinal	492	573	0.86	33	D
	Transverse	500	592	0.84	27	C
API specification[12]	X65	≥448	≥530	≤0.93	≥20.5	
	X70	≥482	≥565	≤0.93	≥19	
	X80	≥551	≥620	≤0.93	≥17.5	

NB. YS-yield strength, UTS-ultimate tensile strength, D-discontinuous, C-continuous

7.8.2 Results of mechanical properties for different cooling rates, coiling temperatures and deformation values

7.8.2.1 Effect of cooling rate with no coiling and no prior deformation

The mechanical properties are shown in tables 7.10 and 7.11 for samples subjected to a series of cooling rates after austenitisation and with no prior deformation and no simulated coiling process. Controlled cooling was done by means of helium gas cooling on the Gleeble testing machine at zero load and with conditions of no deformation. The curves of strength versus elongation are shown in Appendix B and C for alloys #6 and #3, respectively.

Table 7.10 Mechanical properties of samples #A124 of the Mo-free alloy #6 with no coiling and no prior deformation

Cooling rate ($^oCs^{-1}$)	YS, MPa	UTS, MPa	YS/UTS	Yield type
1	439	573	0.77	C
5	461	587	0.78	C
10	491	613	0.80	C
21	551	663	0.83	C
40	603	732	0.82	C
51	648	763	0.85	C

Table 7.11 Mechanical properties of samples #AF3F of alloy #3 (with 0.09% Mo) and with no coiling and no prior deformation

Cooling rate ($^oCs^{-1}$)	YS, MPa	UTS, MPa	YS/UTS	Yield type
1	475	593	0.80	C
5	483	579	0.83	C
10	508	606	0.84	C
20	534	625	0.85	C
40	542	640	0.85	C
54	547	648	0.84	C

7.8.2.2 Effect of cooling rate with coiling but without deformation

Results are given in tables 7.12 and 7.13 for the Mo-free alloy #6 treated similarly as above after austenitisation and without prior deformation but with various cooling rates and with subsequent coiling simulations at 600 (sample #A113) and 575 ºC (sample #B113). The individual curves of strength versus elongation are shown in Appendix D and E for 600 and 575 ºC coiling, respectively.

Table 7.12 Mechanical properties of samples #A113 of the Mo-free alloy #6 with 60 min coiling at 600 ºC without prior deformation

Cooling rate ($^oCs^{-1}$)	YS, MPa	UTS, MPa	YS/UTS	Yield type
1	494	635	0.78	C
5	478	619	0.77	C
10	492	650	0.76	C
20	502	650	0.77	C
40	500	651	0.77	C
60	500	646	0.77	C

Table 7.13 Mechanical properties of samples #B113 of alloy #6 with 60 min coiling at 575 ºC without prior deformation

Cooling rate ($^oCs^{-1}$)	YS, MPa	UTS, MPa	YS/UTS	Yield type
1	435	566	0.77	C
5	518	647	0.80	C
10	502	643	0.78	C
20	477	638	0.75	C
40	503	651	0.77	C
60	484	638	0.76	C

7.8.2.3 Effect of cooling rate with 575 ºC coiling and a 33% prior reduction below the T_{nr}

Table 7.14 shows the mechanical properties of the Mo-free alloy #6 with a 575 ºC coiling simulation and a 45% prior reduction in total but 33% reduction below the T_{nr} while the curves of strength versus elongation are shown in Appendix F.

Table 7.14 Mechanical properties of samples #TEN06 for the Mo-free alloy #6 with 60 min coiling at 575 ºC and a 33% prior reduction below the T_{nr}

Cooling rate (ºCs^{-1})	YS, MPa	UTS, MPa	YS/UTS	Yield type
1	434	536	0.81	D
5	528	626	0.84	D
10	514	605	0.85	D
19	568	664	0.86	D
34	528	639	0.83	D

7.9 Transformed microstructures of the alloys

7.9.1 Optical micrographs

The optical microstructures of the five experimental alloys after a rapid cooling rate of 47 ºCs^{-1} and the reference alloy #6, are shown in figures 7.29.

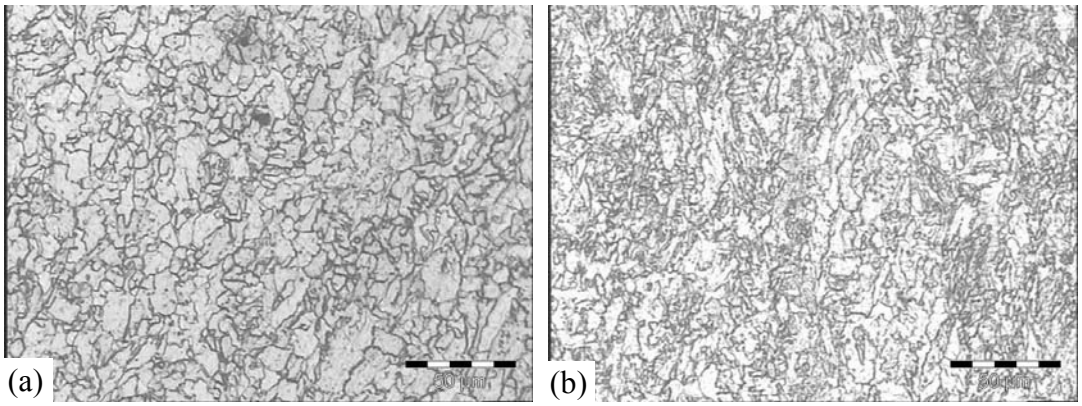

(a) (b)

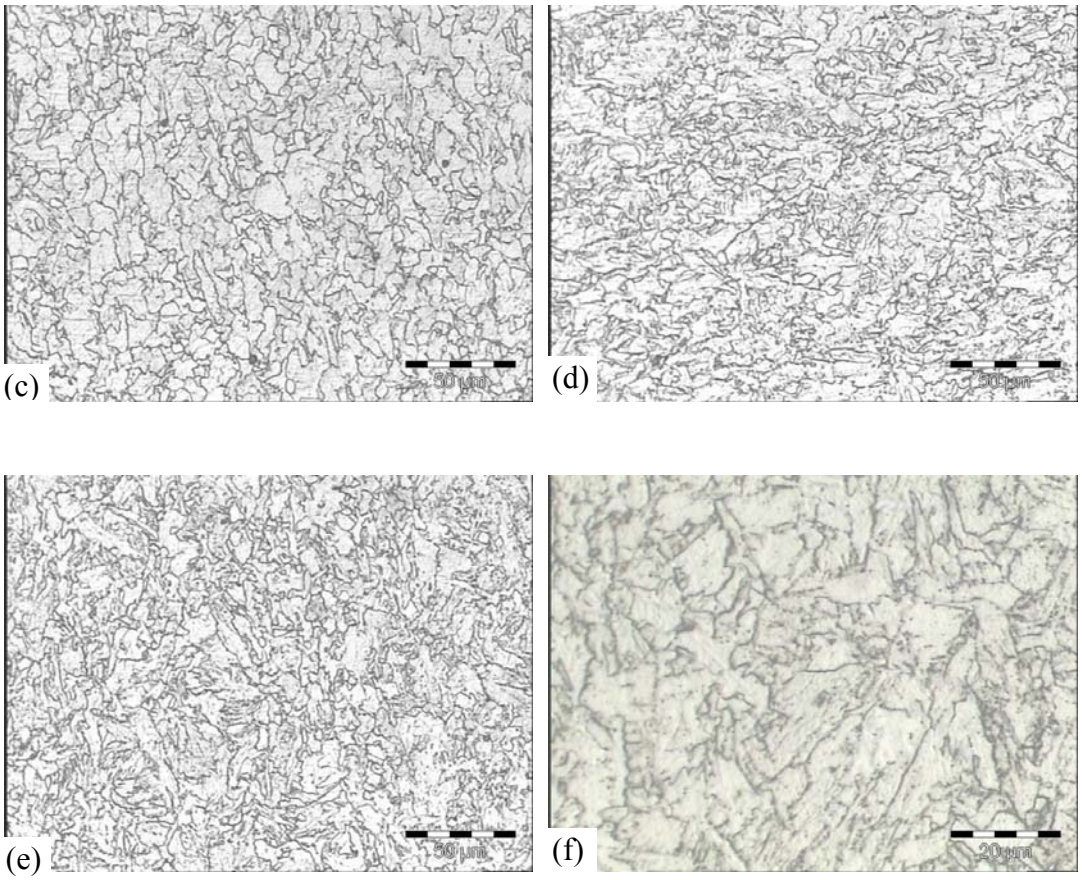

Figure 7.29 The optical microstructure, etched in a 2% Nital solution for 5 seconds, after a rapid cooling rate of 47 ºCs^{-1} for the experimental alloys (a) #1, (b) #2, (c) #3, (d) #4, (e) #5 and, (f) the reference Mo-free alloy #6 cooled at a rate of 39 ºCs^{-1}.

As may be seen in figure 7.29, the optical microstructures for all five experimental alloys #1 to #5 in the as-rolled condition, are similar. They appear to be typical of acicular ferrite, consisting of a "white" phase and an irregular "grey" phase with no clearly etched grain boundaries in the microstructure. In a low carbon low alloyed steel when etched with 2% Nital, polygonal ferrite usually appears as a white coloured phase. From figure 7.29, it is uncertain, however, to establish without any doubt the presence of polygonal ferrite or whether the microstructure shows a 100% acicular ferrite or a mixture of both acicular ferrite and polygonal ferrite. If the polygonal ferrite is mixed within the acicular ferrite structure, it can not be recognised with any confidence. The microstructure of reference alloy #6 consists of a similar microstructure as the five experimental alloys. Accordingly, it was necessary to confirm by other means whether any polygonal ferrite exists in these microstructures.

7.9.2 Microstructures examined by SEM

The Scanning Electron Microscopy (SEM) (Model JEOL JSM-5800LV) was used first in an attempt to identify the presence of polygonal ferrite in the microstructure. The SEM microstructures for the experimental alloys etched in a 2% Nital, are illustrated in figure 7.30 below.

It seemed that there were two different types of microstructures or matrix phases, one is raised above the mean level of the etched plane (marked in "A"), while the other is sunken below this mean plane (marked in "B"). No fine details within each matrix phase can be seen, however, and the SEM was, therefore, not the final answer as to identify the phases which were present.

Next, high resolution SEM (Model JEOL JSM-6000F) micrographs were taken after varying the etching time from 10 to 120 seconds in an attempt to identify these two phases. Figure 7.31 represents the structures of the as-rolled experimental alloys under high resolution SEM after only 5 seconds etching. The microstructures appear relatively similar to those in figure 7.30 although the differences in etching depth between the "raised" and the "sunken" matrix were accentuated. The SEM micrographs after various etching times ranging from 10 to 120 seconds, are shown in figure 7.32. Although the differences in etching depth between the two types of matrix areas are once more, evident, the lack of any finer details of the internal structure within each of the two types of matrix areas did not assist in identifying them conclusively (although one may be tempted to conclude that the deeper etched matrix areas could possibly be acicular ferrite due to its higher dislocation content while the lesser etched matrix areas could possibly be polygonal ferrite with a lower dislocation content). Accordingly, high resolution SEM analysis was also found not to be a totally satisfactory technique to fully identify the matrix microstructures in the present alloys.

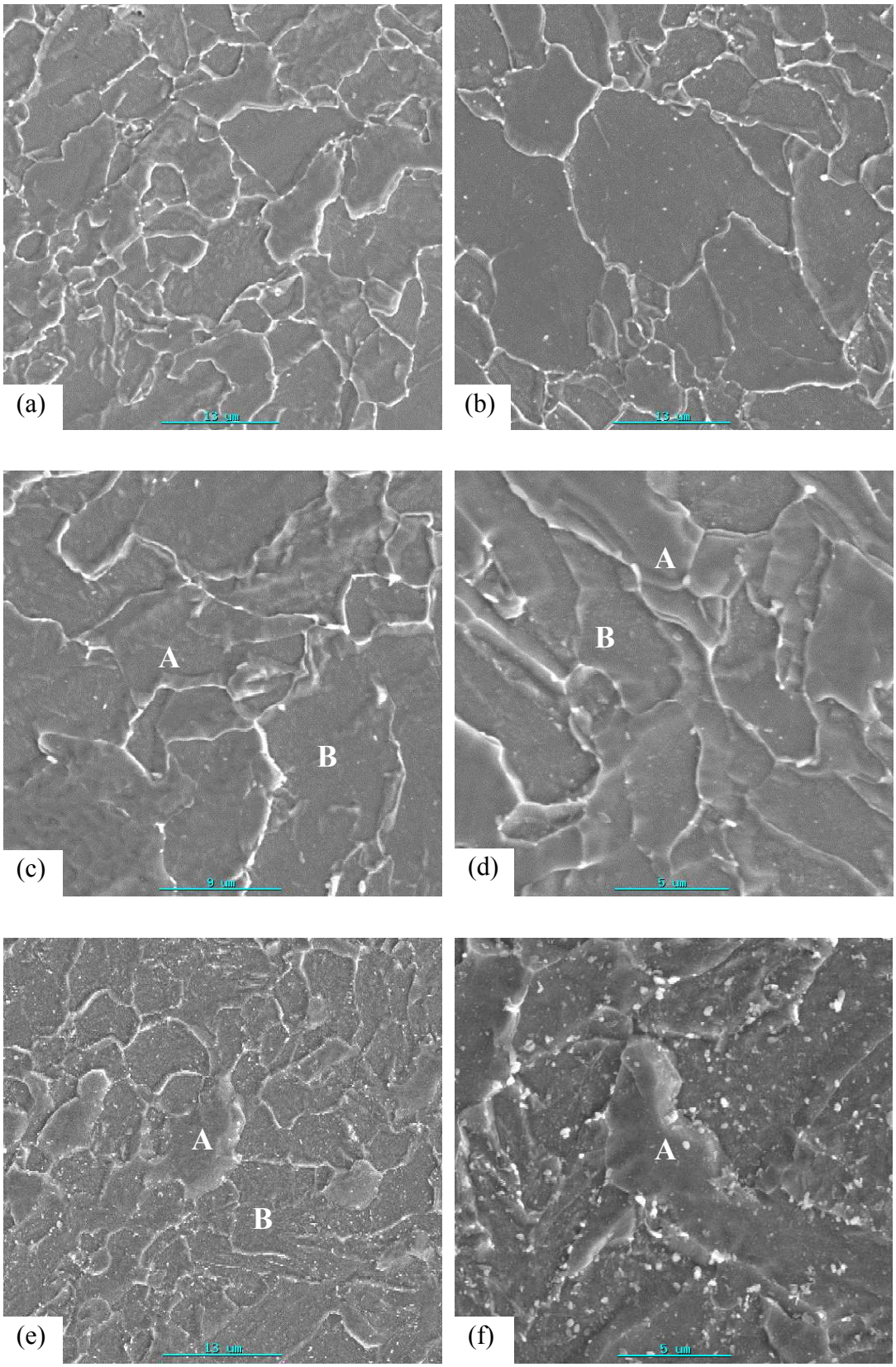

Figure 7.30 The SEM micrographs after a rapid cooling rate of 47 ºCs^{-1}(etched in 2% Nital for 5 seconds) for the experimental alloys (a) #1, (c) #2, (c) #3, (d) #4, (e) #5 and, (f) the reference alloy #6 cooled at a rat of 39 ºCs^{-1}.

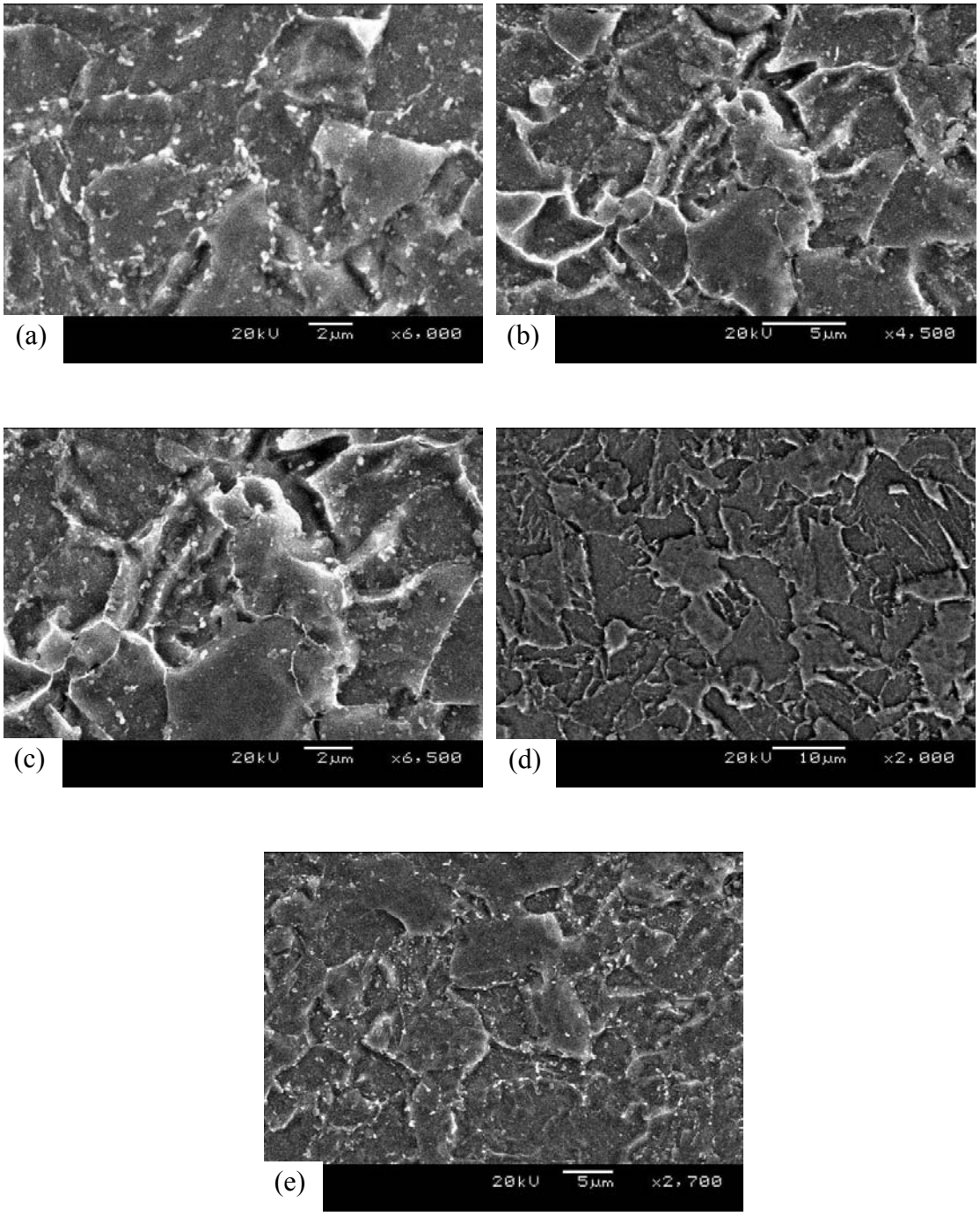

Figure 7.31 The micrographs in the as-rolled condition by high resolution SEM after a rapid cooling rate of 47 ºCs^{-1}(etched in 2% Nital for 5 seconds) for the experimental alloys (a) #1, (c) #2, (c) #3, (d) #4 and, (e) #5.

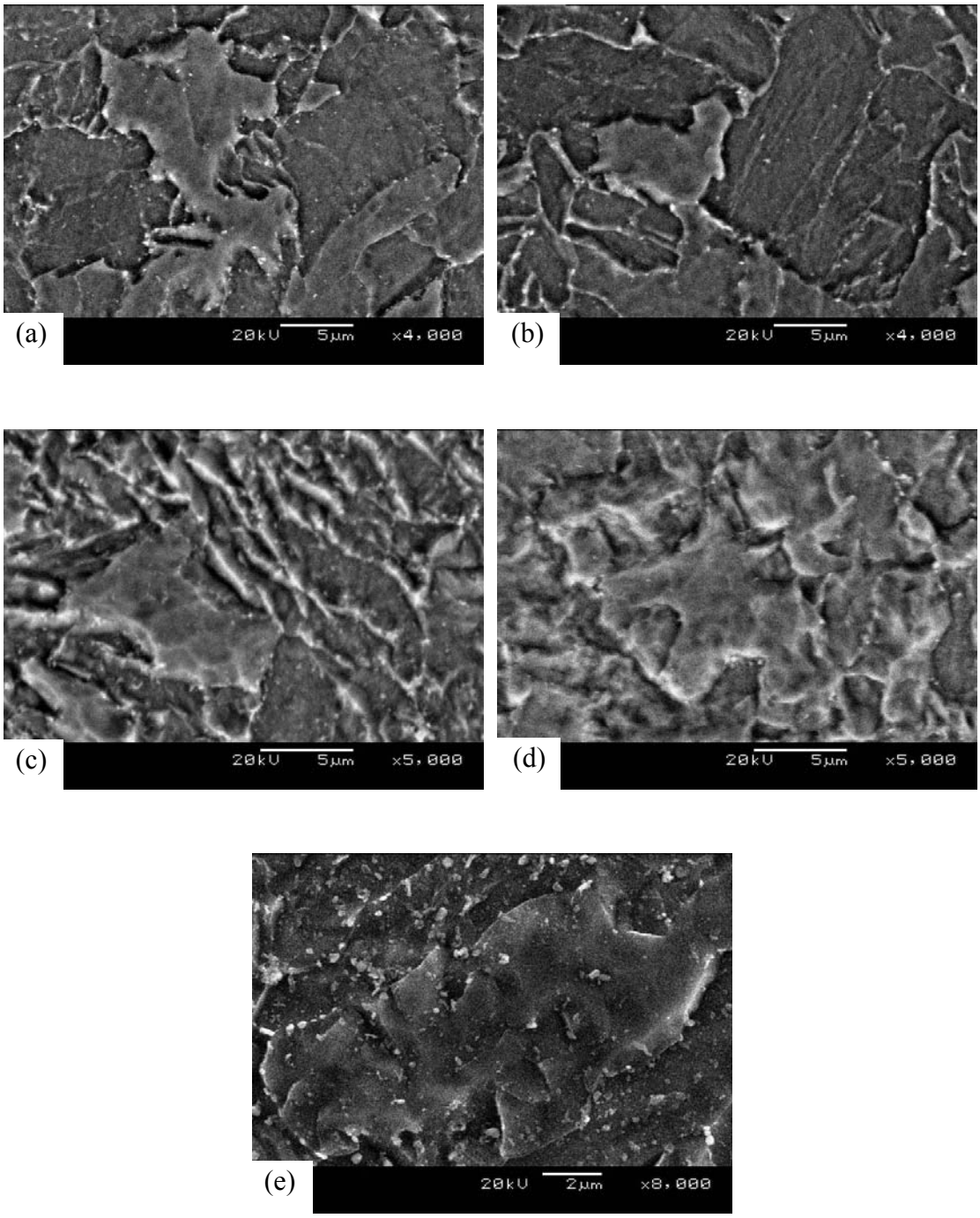

Figure 7.32 The high resolution SEM micrographs in the as-rolled condition after a rapid cooling rate of 47 ºCs^{-1} for the experimental alloy #1 etched in 2% Nital for (a) 10seconds, (c) 15 seconds, (c) 30 seconds, (d) 60 seconds and, (e) 120 seconds.

7.9.3 TEM studies of acicular ferrite on carbon replicas

Carbon extraction replicas with or without Au-Pd shadowing and thin foils were finally used to identify any differences between the matrix phases of acicular ferrite and polygonal ferrite. An etching time from 30 to 60 seconds in a 2% Nital solution was used to obtain a relief on the etched surface on the specimens. A deeply etched relief surface before they are carbon coated, enhances the shadowing of samples.

The TEM micrograph of an unshadowed carbon extraction replica for alloy #6 (reference alloy and Mo-free) is shown in figure 7.33. It appears once more that there are two different matrix phases in the as-rolled reference alloy #6. The quality of the image is a little better than that of the SEM micrographs in figures 7.30 and 7.32. Hence it seemed that carbon extraction replicas may be an improved technique to reveal the finer details of these matrix phases in the alloys, particularly if shadowing by Au-Pd is used before applying the carbon coating to accentuate the relief on the etched surface. Figure 7.34 shows such a shadowed microstructures of alloy #6.

Figure 7.34 shows the marked improvement introduced by shadowing if compared to the unshadowed case in figure 7.33 on the same alloy. The “raised” matrix area (note the direction of the shadow at its edge which is the same as that of protruding carbide particles) has a relatively smooth etched surface revealing some individual carbide particles after being etched in 2% Nital, while the “sunken” matrix areas in the same figure have a very “rough” etched surface which consists of a fine internal and parallel striated structure that has clearly etched very much differently from the “raised” smooth matrix areas.

It may, therefore, be concluded that the raised matrix areas appear to be one phase whereas the sunken matrix areas are clearly another phase or even a multiphase (except for the carbide particles which are present in both types of areas). Consequently, there are apparently two types of matrix phases in alloy #6. Taking all of the above evidence of optical, SEM and TEM observations together, it was concluded that the smooth and raised matrix phase in figure 7.34 is most likely polygonal ferrite (marked with “PF”), whereas the striated and deeper etched one is likely to be acicular ferrite (marked with “AF”). This result was further validated with

thin foil samples in sections 8.3 and 8.4 in the next chapter. As can be seen in figure 7.34, the shadowing is also effective to reveal the smaller precipitates and grain boundaries (marked with "GB") by enhancing their presence.

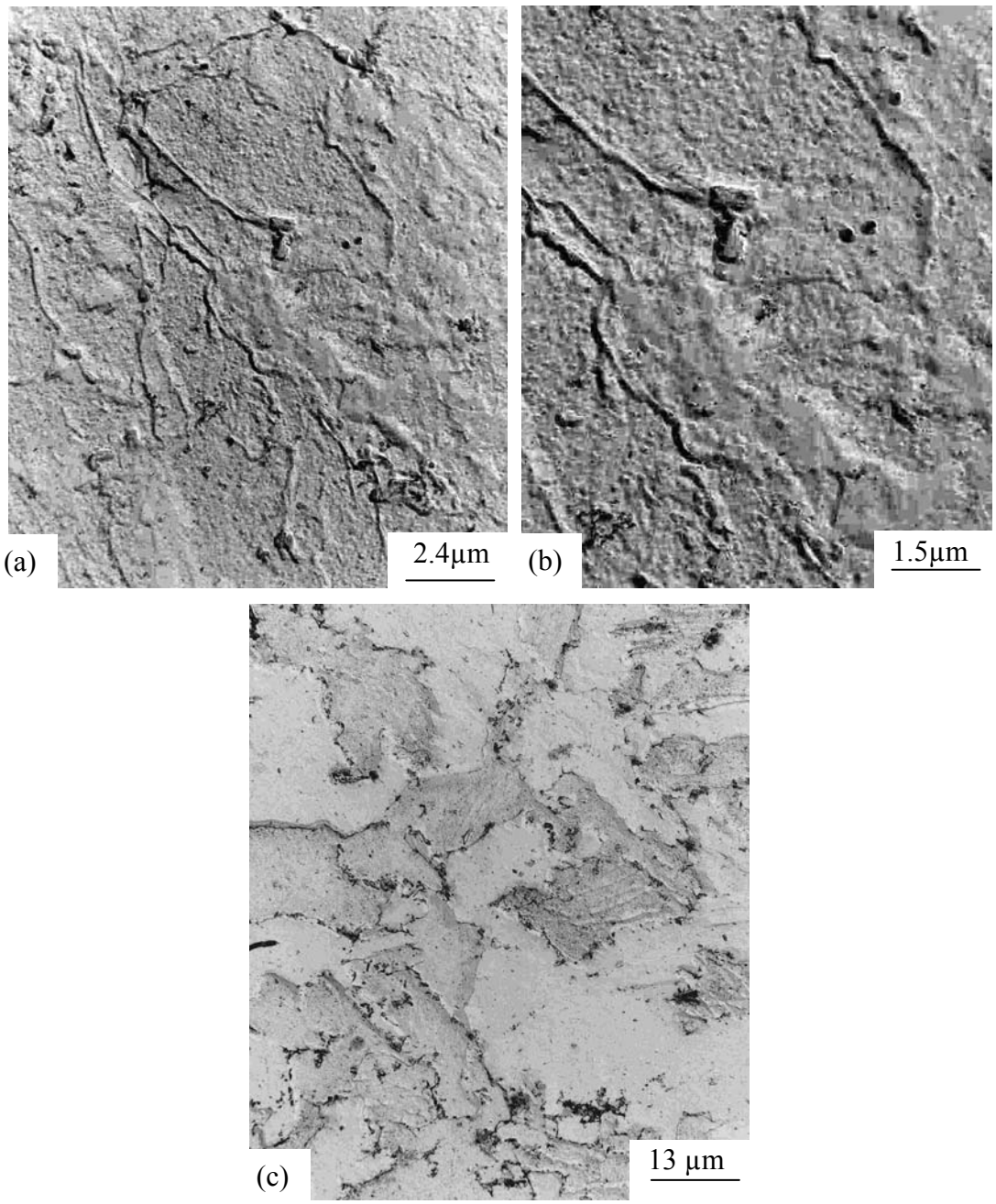

Figure 7.33 TEM micrographs of carbon extraction replicas without shadowing for the reference alloy #6 after hot rolling and rapid cooling at a rate of 39 ºCs^{-1}.

Summarising these results, it was concluded that the shadowing of extraction carbon replicas by applying Au-Pd shadowing at an angle to the etched surface, is an

improved technique to identify the matrix structures in these alloys as both acicular ferrite and polygonal ferrite can be clearly distinguished from each other. The microstructure of reference alloy #6 after hot rolling and rapid cooling at a rate of 39 $^{o}Cs^{-1}$ is, therefore, one of polygonal ferrite plus acicular ferrite with some individual smaller carbides in both these matrix phases.

By this technique, it was also confirmed that the microstructures of the experimental alloys #1 to #5 equally consisted of both polygonal ferrite and acicular ferrite (see figure 7.35) while no structure in the entire study was found with 100% acicular ferrite. The mixed microstructures of the five experimental alloys were, therefore, very similar to that found in the reference Mo-free alloy.

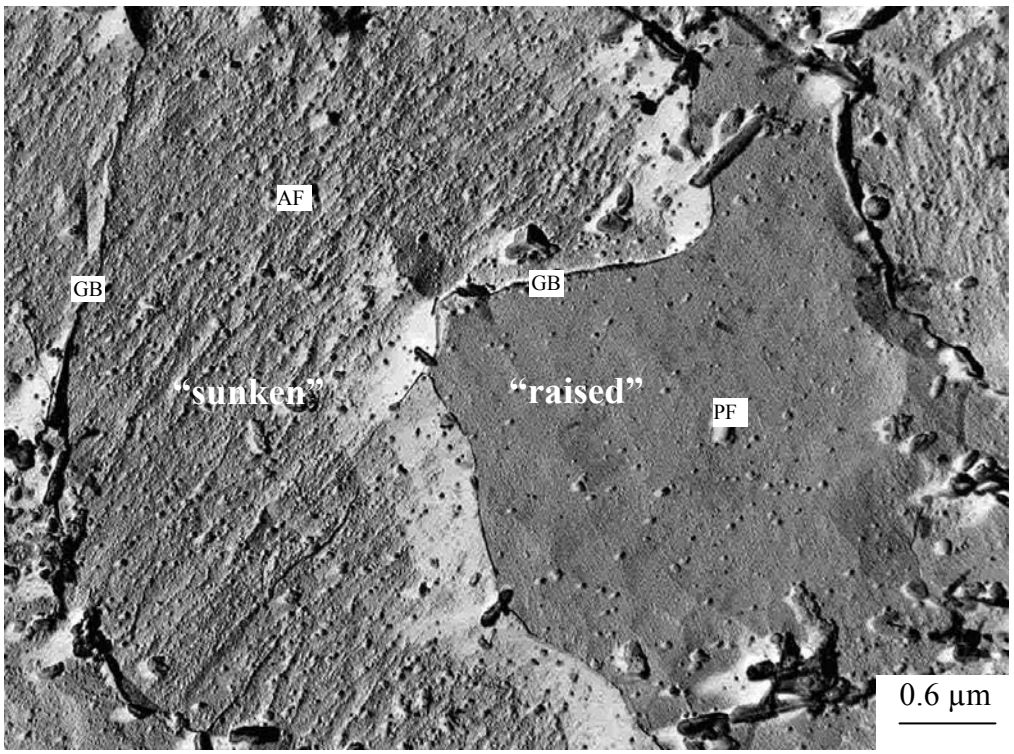

Figure 7.34 The TEM micrograph from a shadowed replica of the Mo-free alloy #6 after hot rolling and rapid cooling at a rate of 39 $^{o}Cs^{-1}$. (AF-acicular ferrite, PF-polygonal ferrite and, GB-grain boundary).

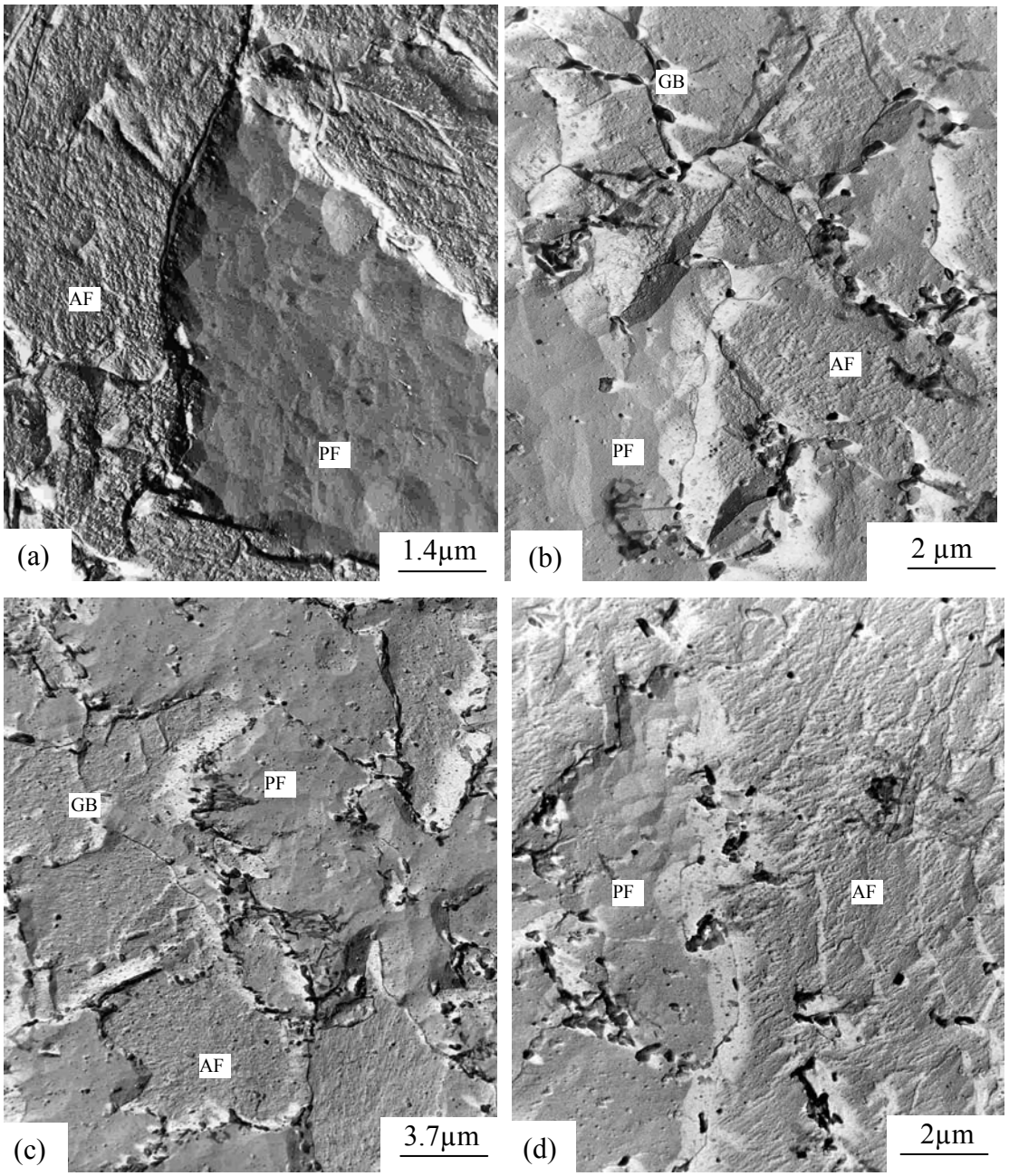
AF
PF
1.4µm
(a)
GB
AF
PF
2 µm
(b)
PF
GB
AF
3.7µm
(c)
PF
AF
2µm
(d)

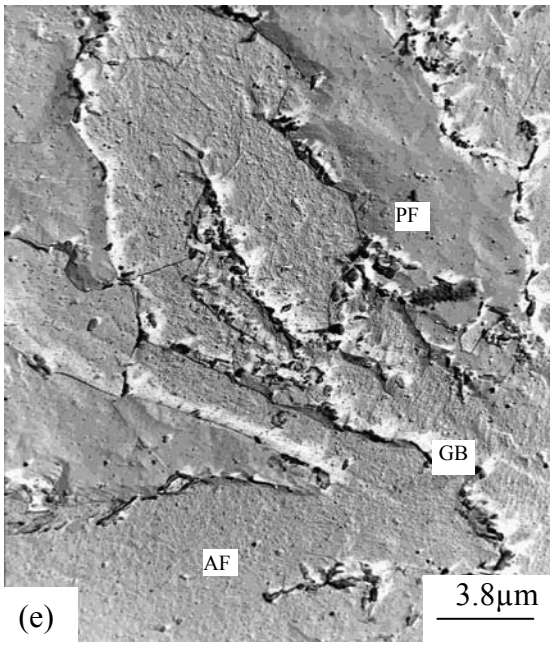

Figure 7.35 TEM micrographs from shadowed replicas of the as-hot rolled and rapidly cooled (at a rate of 47 ºCs^{-1}) experimental alloys (a) #1, (b) #2, (c) #3, (d) #4 and, (e) #5 (AF-acicular ferrite, PF- polygonal ferrite and, GB-grain boundary).

CHAPTER 8 STUDIES OF ACICULAR FERRITE BY THIN FOIL TEM

8.1 Acicular ferrite morphology in experimental alloys

The optical micrographs in figure 7.29 for the alloys after rapid cooling at a rate of 47 $^{o}Cs^{-1}$, show a typical acicular ferrite microstructure, also according to the literature[4,65,131,134]. No researcher in any of these references reported the presence of any polygonal ferrite in an acicular ferrite microstructure, however, even though their optical microstructures appear very similar to those in this study (figure 7.29). Polygonal ferrite is of a "polygonal" shape with a lightly etched colour of "white" in its microstructures under an optical microscope after being etched in a 2% Nital solution. But acicular ferrite also appears as a white plus grey or striated phase in microstructures under some etching conditions. Previous researchers[4,65,131,134] have accepted that optical micrographs like figure 7.29-(b) to (f), consist of only acicular ferrite. As mentioned in section 7.9.3 above, however, the TEM observations on carbon extraction replicas in this study with Au-Pd shadowing, as represented by the microstructures of alloys #1 to #5, are obviously a mixture of polygonal ferrite plus acicular ferrite. A final conclusion based only on the somewhat ill-defined optical microscopy but more clearly confirmed by the observations on shadowed extraction replicas is, of course, not satisfactory in itself and TEM observations on thin foils were done to confirm more details of this apparent anomaly with conclusions reached by other researchers in these microstructures.

Furthermore, it should be recognised that the latest understanding on the nature and origin of acicular ferrite in wrought line pipe steels, is that it may not necessarily be a "unique singular phase" (for instance, the "chaotic morphology" found in welds) but that acicular ferrite should rather be understood as a *collective term* describing a microstructure containing possibly more than one type of ferrite phase, all of which have nucleated intragranularly. It will be seen that this broader concept of what acicular ferrite in line pipe steels really is, is supported by the results of this work here below where two different morphologies of intragranularly nucleated ferrite laths were found, i.e. a "chaotic" arrangement (as in the "classical" acicular ferrite in welds) as well as an arrangement of "parallel laths" somewhat similar to classical bainite except for its nucleation intragranularly.

8.1.1 Acicular ferrite and polygonal ferrite in alloy #6 (Mo-free)

(i) Acicular ferrite and polygonal ferrite

Figure 8.1 below represents the thin foil TEM micrographs of the Mo-free alloy #6 after a rapid cooling rate of 39 $°Cs^{-1}$ after the hot rolling process. A "polygonal" shaped phase could be observed in figure 8.1-(a) (marked with "PF"). According to its shape it appears to be polygonal ferrite with a size of approximately 5 μm in diameter. Many laths in the structure (marked "lath" in the figure) were found beside the polygonal ferrite. The shape of the "PF" is quite different from that of the laths in this figure with the latter more elongated in their shape. This is consistent with the observation from figure 7.34 and discussed in the introduction in section 8.1 above.

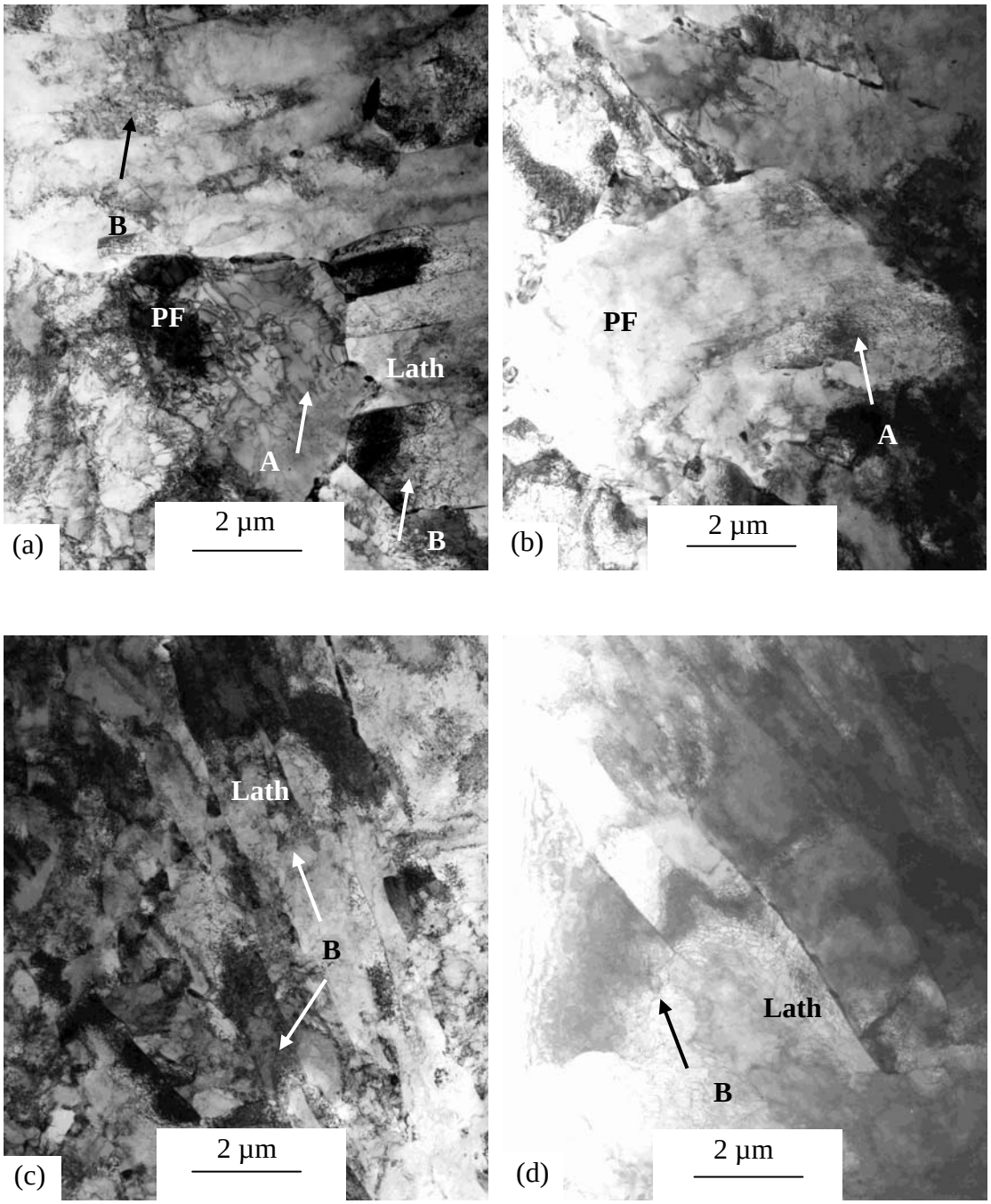

Figure 8.1 Thin foil TEM micrographs of alloy #6 (Mo-free) after a rapid cooling rate of 39 °Cs^{-1} after hot rolling, (a) polygonal ferrite + laths, (b) polygonal ferrite with dislocations and, (c),(d) laths with dislocations. PF-polygonal ferrite, AF-acicular ferrite, A and B-dislocations in polygonal ferrite and an acicular ferrite , respectively.

Another polygonal ferrite grain with size of about 5.8 µm in figure 8.1-(b) is also evident. No cementite was found within the laths or on inter-lath boundaries. This means that the laths are in all likelihood part of acicular ferrite instead of bainite where cementite would be present within the laths in lower bainite and on inter-lath

position in upper bainite[97]. The carbon rejected from the acicular ferrite laths may possibly be in martensite/austenite islands enriched in carbon as no cementite was found in the thin foils. A further study of the martensite/austenite islands in these steels probably needs further thin foil TEM work to confirm it.

According to the CCT diagrams of alloy #6 (see figure 7.22), the polygonal ferrite probably forms during cooling first at higher temperature and the acicular ferrite later. The acicular ferrite is, therefore, mixed in between the polygonal ferrite. Polygonal ferrite can not be fully distinguished from an acicular ferrite on optical micrographs alone such as in figure 7.29-(f), but combining optical and TEM observations of alloy #6 in figure 7.29-(f), it appears that the laths (see figure 8.1) are most likely from an acicular ferrite and not bainite because of the less visible grain boundaries[131,135] and no cementite within or between the laths was observed after deep etching. A further study on this lath structure is made below. It is, therefore, concluded that the microstructure of alloy #6 is most probably a mixture of acicular ferrite and polygonal ferrite.

(ii) Dislocations within the polygonal ferrite

Dislocations were also observed within the polygonal ferrite (see figures 8.1 and 8.2) in these line pipe steels. This is somewhat different, for instance, from polygonal ferrite found in plain low carbon steels where generally dislocation-free polygonal ferrite is usually found. This has led to some researchers even referring to “quasi-polygonal ferrite” in wrought low alloy steels. The reason for this difference caused by alloying elements, requires further investigation but may be associated with solute drag of dislocations by alloying elements, thereby hindering their movement and recovery whereas this is largely absent in plain low carbon steels.

Figure 8.2 showed that there were dislocations apparently being emitted (marked with “M”) from the area close to the moving interface of the PF. There were also more dislocations near this moving interface than within the central regions of the PF (marked with “L”). These dislocations were possibly generated during the formation of polygonal ferrite within the austenite. Firstly, according to the CCT diagram of alloy #6 (see figure 7.26), the polygonal ferrite was formed in a higher temperature

range than that of acicular ferrite. Secondly, there was a volume expansion of about 3.6% (calculated for a 0.06% C steel) during polygonal ferrite formation from austenite as the lattice changed from face-centered cubic (austenite) to body-centered cubic (polygonal ferrite). This will lead to the transformed polygonal ferrite that was surrounded by the parent austenite, to undergo a compression strain of about 1.2% from the austenite. Because of the relatively high temperatures at this stage and hence a low flow stress in the ferrite, this linear strain will probably be a plastic one, thereby creating interface dislocations in the ferrite near the interface as it advances into the austenite.

In addition, however, a second volume expansion again of about 3.6% occurs at a slightly lower temperature as the surrounding austenite now transforms to the bcc acicular ferrite, with the less dense acicular ferrite now creating a further strain field[74,76] on the already formed polygonal ferrite. Such a strain field from acicular ferrite formation leads to a high dislocation content in the acicular ferrite from the displacive transformation but also from some plastic strain within the adjacent austenite[75] or the already existing polygonal ferrite due to the lattice volume change.

Both of these volume expansion processes will result in strain or deformation to be concentrated within the outer edges of the polygonal ferrite rather than in the centre. Therefore, there were more dislocations found in the edge region (marked by “M”) than in the centre region of the polygonal ferrite (marked by “L”). Figures 8.1-(a) and 8.2 show the acicular ferrite that was situated around the polygonal ferrite.

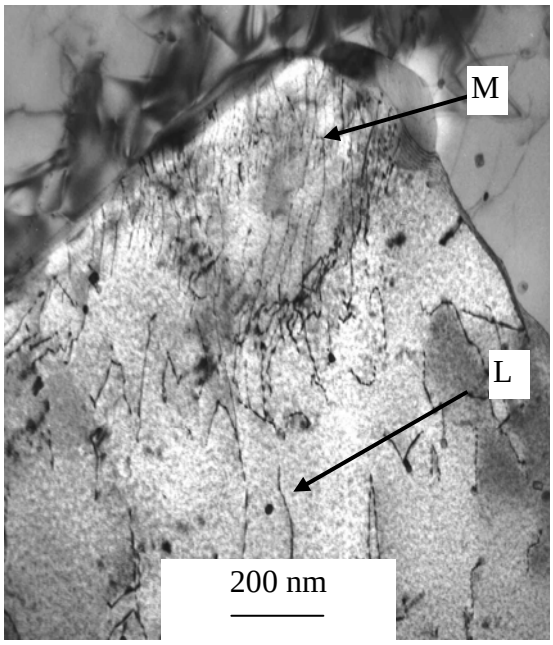

Figure 8.2 Dislocations within the polygonal ferrite in thin foil of the Mo-free alloy #6. The area M shows a high density of dislocations possibly being emitted from the moving PF interface while the central regions L of the PF have less dislocations.

8.1.2 Acicular ferrite and polygonal ferrite in alloy #1

Alloy #6 was the current Mittal Steel's line pipe steel, i.e. V-Nb-Ti micro-alloyed. The main difference between the experimental alloy #1 and the reference alloy #6 was in the niobium and carbon contents. The niobium content in alloy #1 had been increased to 0.055%wt Nb and the carbon content lowered to 0.05%wt C in order to obtain a higher degree of dispersion hardening in the ferrite. TEM thin foil micrographs of polygonal ferrite in this study are shown in figure 8.3, in which a high density of dislocations was also observed with a high magnification.

Figure 8.4 represents an interwoven lath structure from alloy #1 and a high density of dislocations was found within laths B and C. Lath A is not parallel to laths B and C. This is a typical interwoven structure of acicular ferrite, also reported in the literature[4,65,131,134]. Another interwoven lath structure with PF present in this alloy #1, is also shown in figure 8.5. Consequently, it is confirmed that the microstructures of alloy #1 with rapid cooling after hot rolling, also consists of a mixture of an acicular ferrite plus polygonal ferrite.

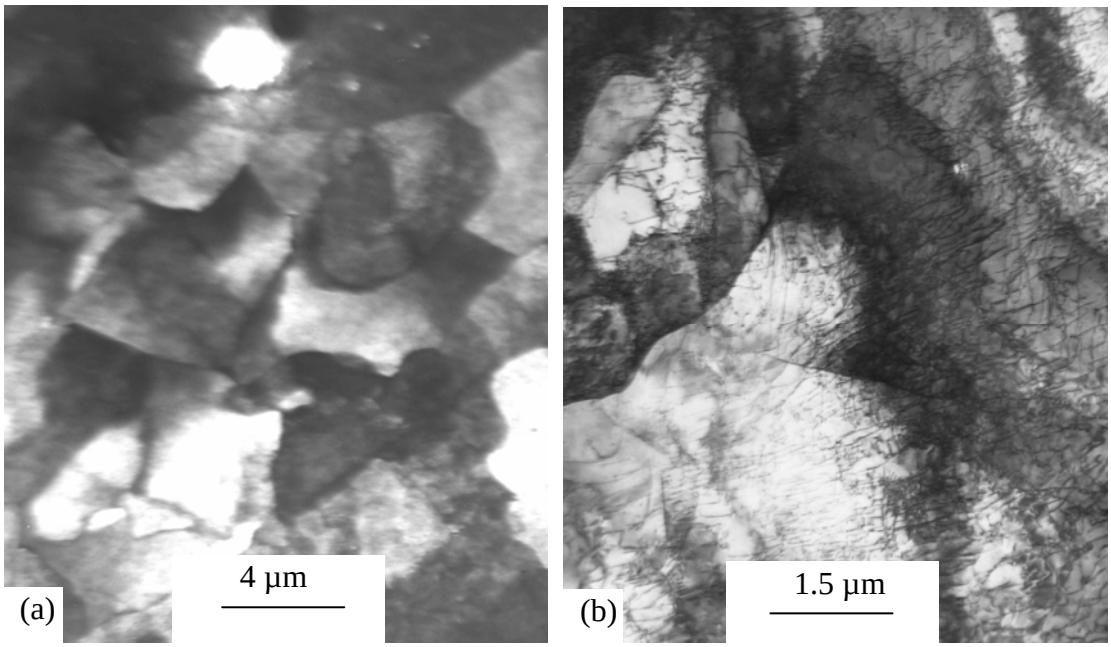

Figure 8.3 Polygonal ferrite in a TEM thin foil micrograph from the experimental alloy #1 after a rapid cooling rate of 47 $^{o}Cs^{-1}$ after the hot rolling process.

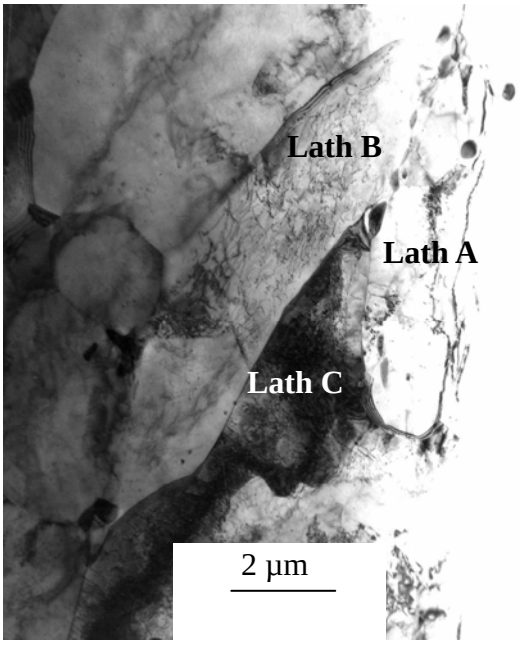

Figure 8.4 TEM thin foil micrograph with laths from alloy #1 after a rapid cooling rate of 47 $^{o}Cs^{-1}$ after the hot rolling process.

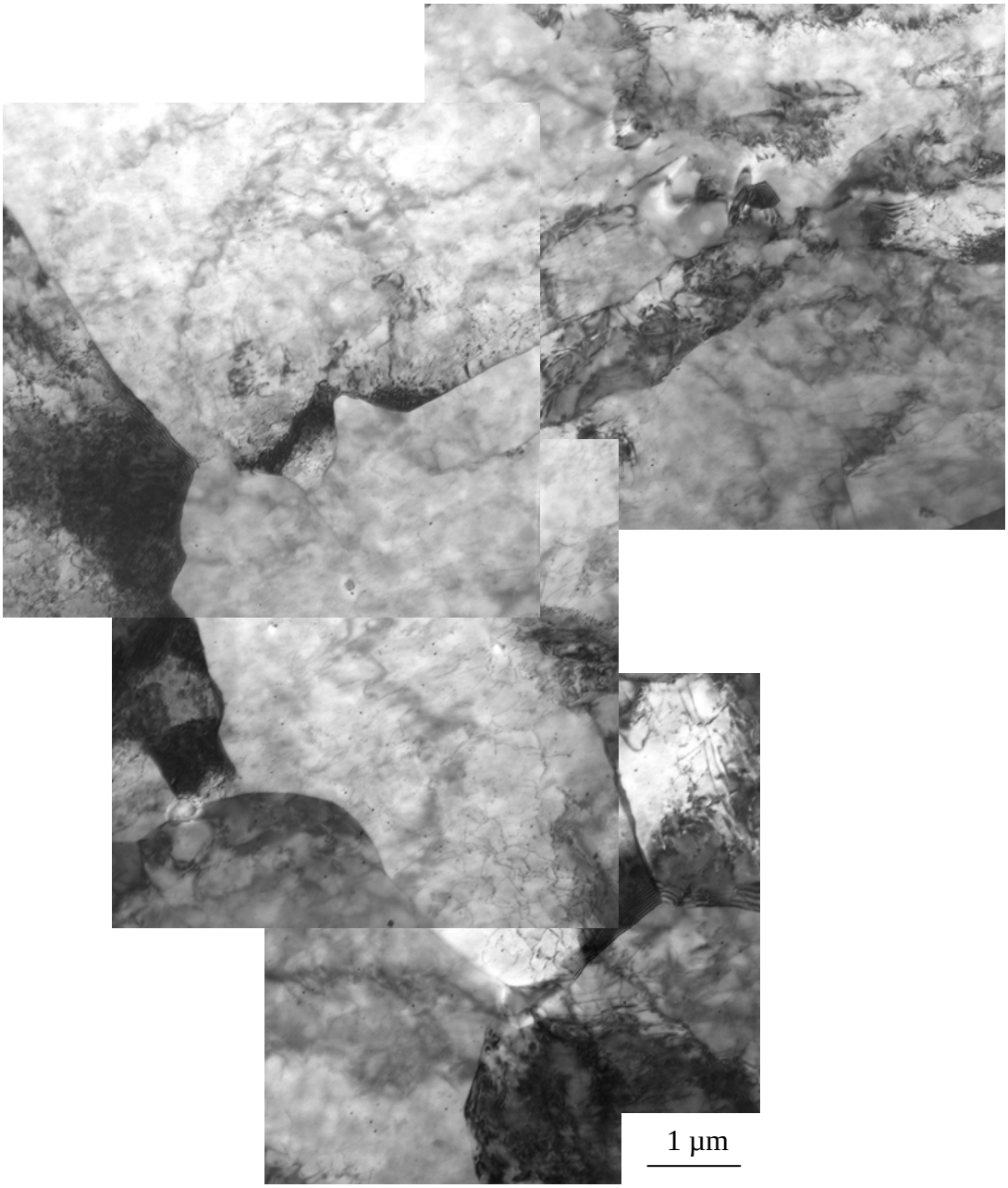

Figure 8.5 TEM thin foil micrograph of the lath plus PF structure in alloy #1 after a rapid cooling rate of 47 $^{o}Cs^{-1}$ after the hot rolling process.

8.1.3 Acicular ferrite in alloys #2 to #5

The lath structures of alloy #2 with an 0.09% Mo + 0.05% Nb addition, are shown in figures 8.6 and 8.7 from TEM thin foils after a rapid cooling rate of 47 ºCs^{-1} after the hot rolling. Parallel laths were found in figure 8.7.

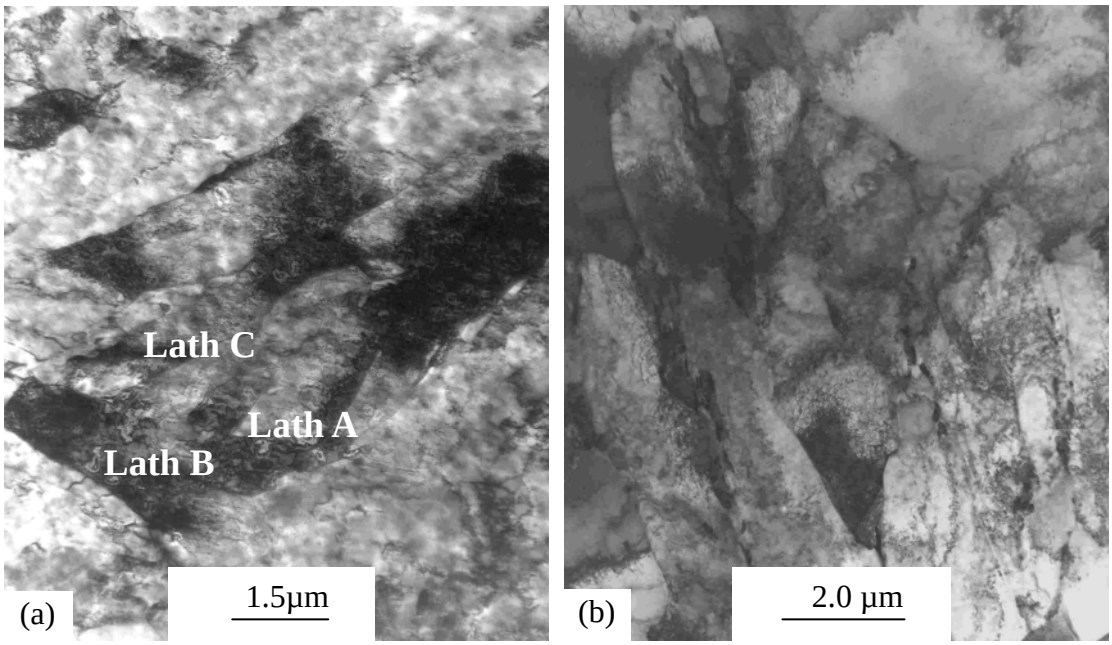

Figure 8.6 Thin foil TEM micrographs of the lath structure in alloy #2 after a rapid cooling rate of 47 ºCs^{-1} after the rolling process.

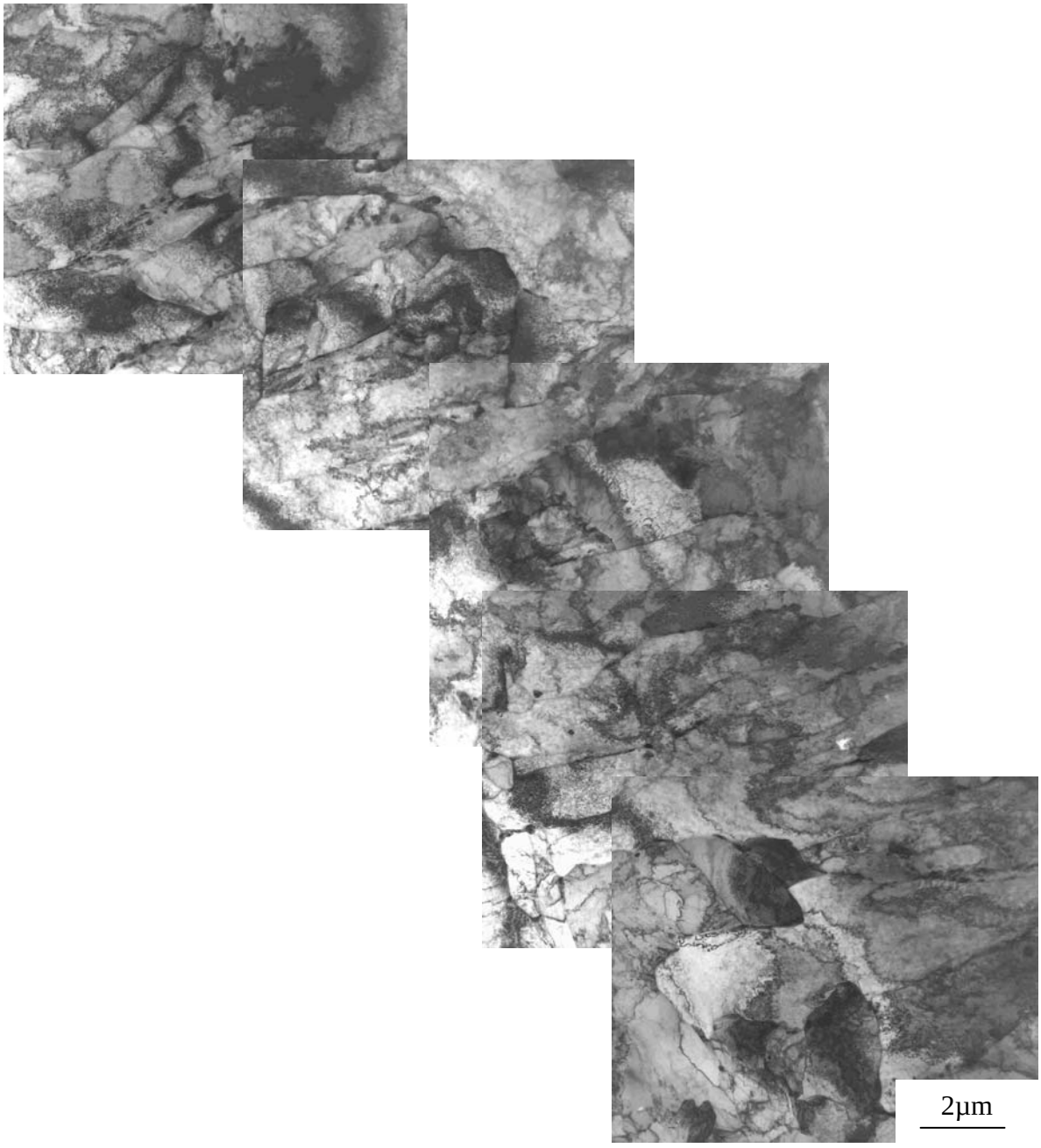

Figure 8.7 Thin foil TEM composite micrographs of parallel laths of an acicular ferrite in alloy #2 after a rapid cooling rate of 47 $^{o}Cs^{-1}$ after the hot rolling process.

Figure 8.8 shows the polygonal ferrite (plus a few isolated laths) found in alloy #3 after a rapid cooling rate of 47 $^{o}Cs^{-1}$ after the hot rolling process. Some dislocations can be found within the polygonal ferrite as well although of a lesser density than in the AF laths. The micrographs with a parallel lath structure of alloy #3 are shown in figure 8.9.

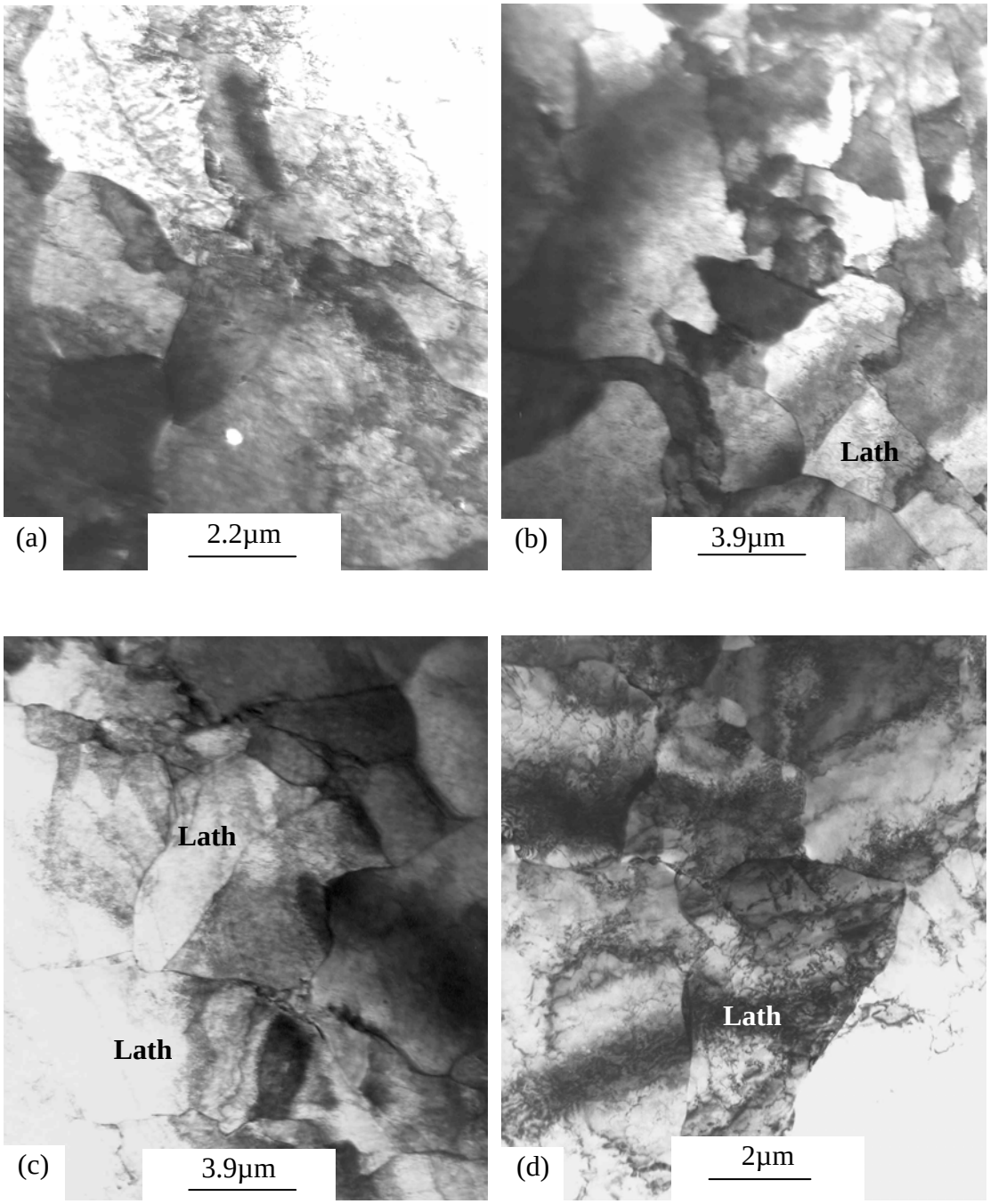

Figure 8.8 Polygonal ferrite (with a few isolated laths) in alloy #3 with a rapid cooling rate of 47 $^{o}Cs^{-1}$ after the hot rolling process.

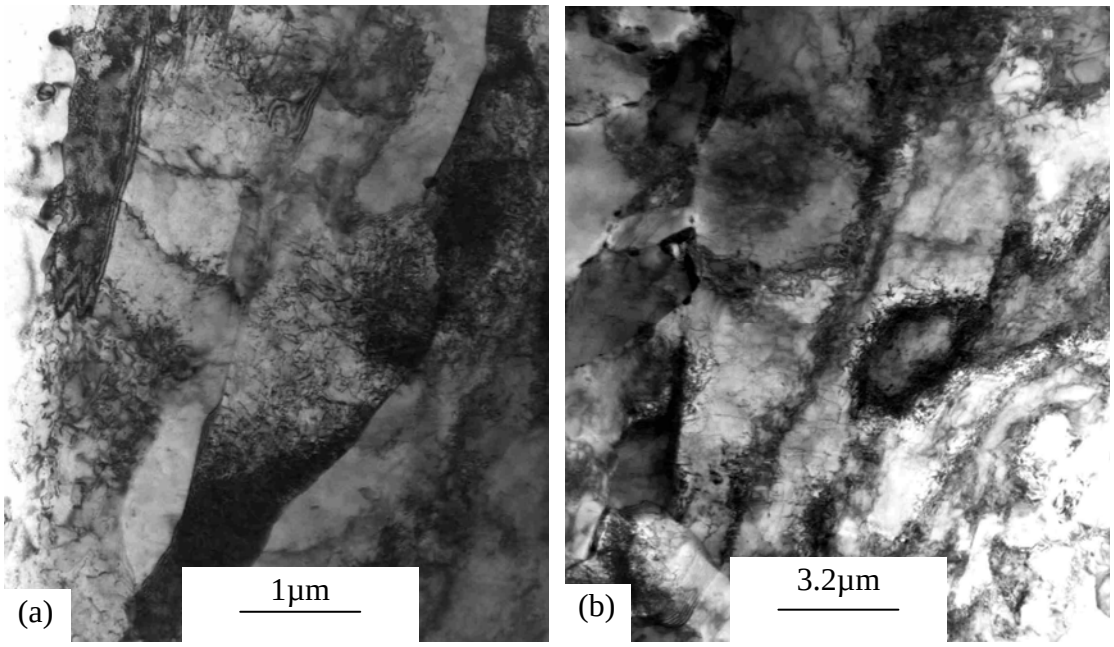

Figure 8.9 The parallel lath morphology in alloy #3 after a rapid cooling rate of 47 $^{o}Cs^{-1}$ after the hot rolling process.

Figure 8.10 shows a composite micrograph of a mixed polygonal ferrite and an acicular ferrite microstructure in alloy #3. Polygonal ferrite is marked with PF in the figure. The interwoven laths are clearly seen, where lath A is crossed by laths B and C.

Figure 8.11 represents the lath structure in alloy #4. Polygonal ferrite with dislocations, can also be found in alloy #5 (with 0.22% Mo) after a rapid cooling rate of 47 $^{o}Cs^{-1}$ (figure 8.12-(a)). An interwoven lath structure of an acicular ferrite in alloy #5 can also be observed in figures 8.12-(b) and (c). It is, therefore, confirmed that the microstructure of alloy #5 (with 0.22%Mo) is also one of polygonal ferrite plus acicular ferrite.

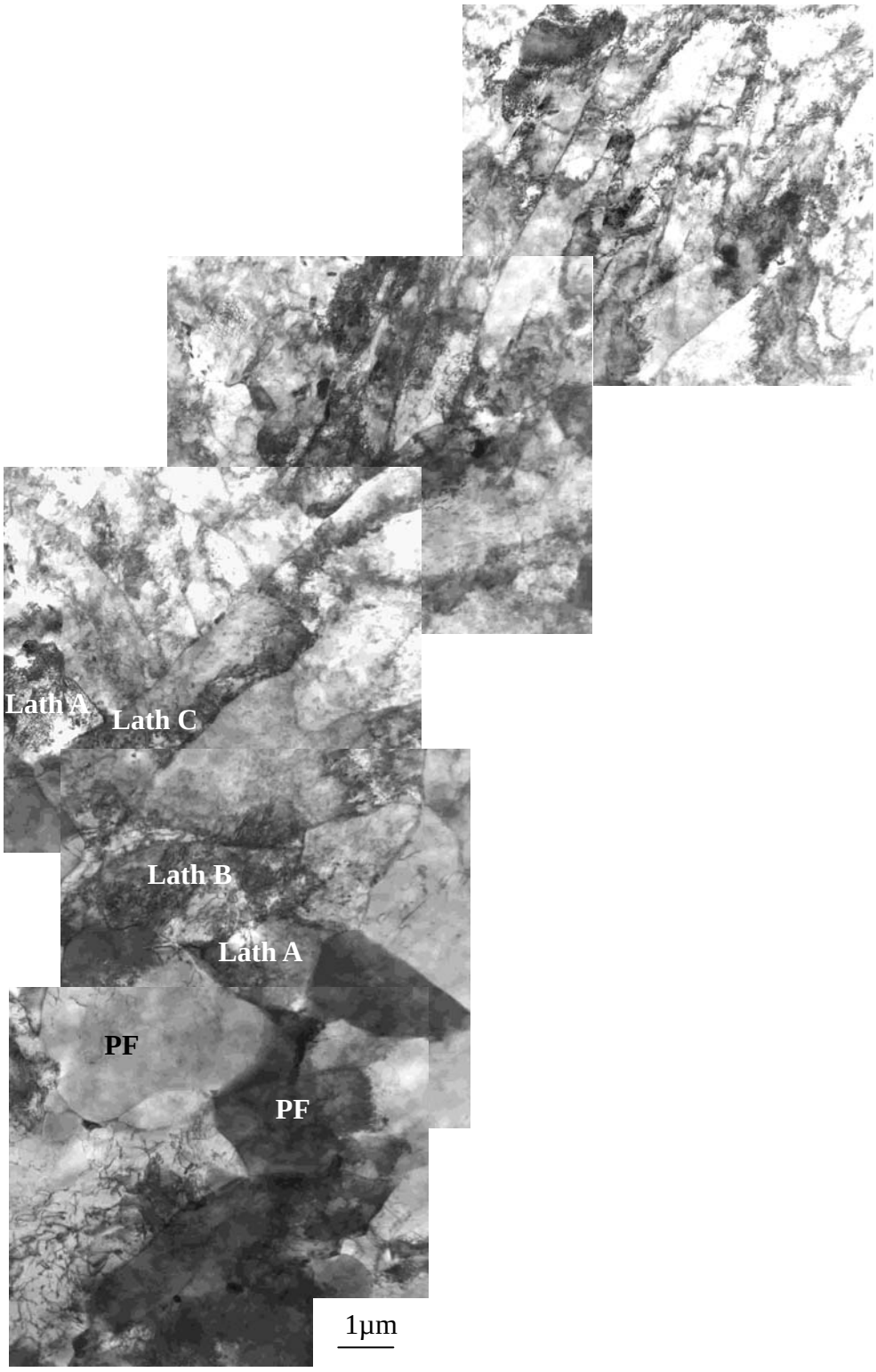

Figure 8.10 Thin foil TEM micrographs of a mixture of polygonal ferrite and an acicular ferrite in alloy #3 after a rapid cooling rate of 47 $^{o}Cs^{-1}$ after the hot rolling process.

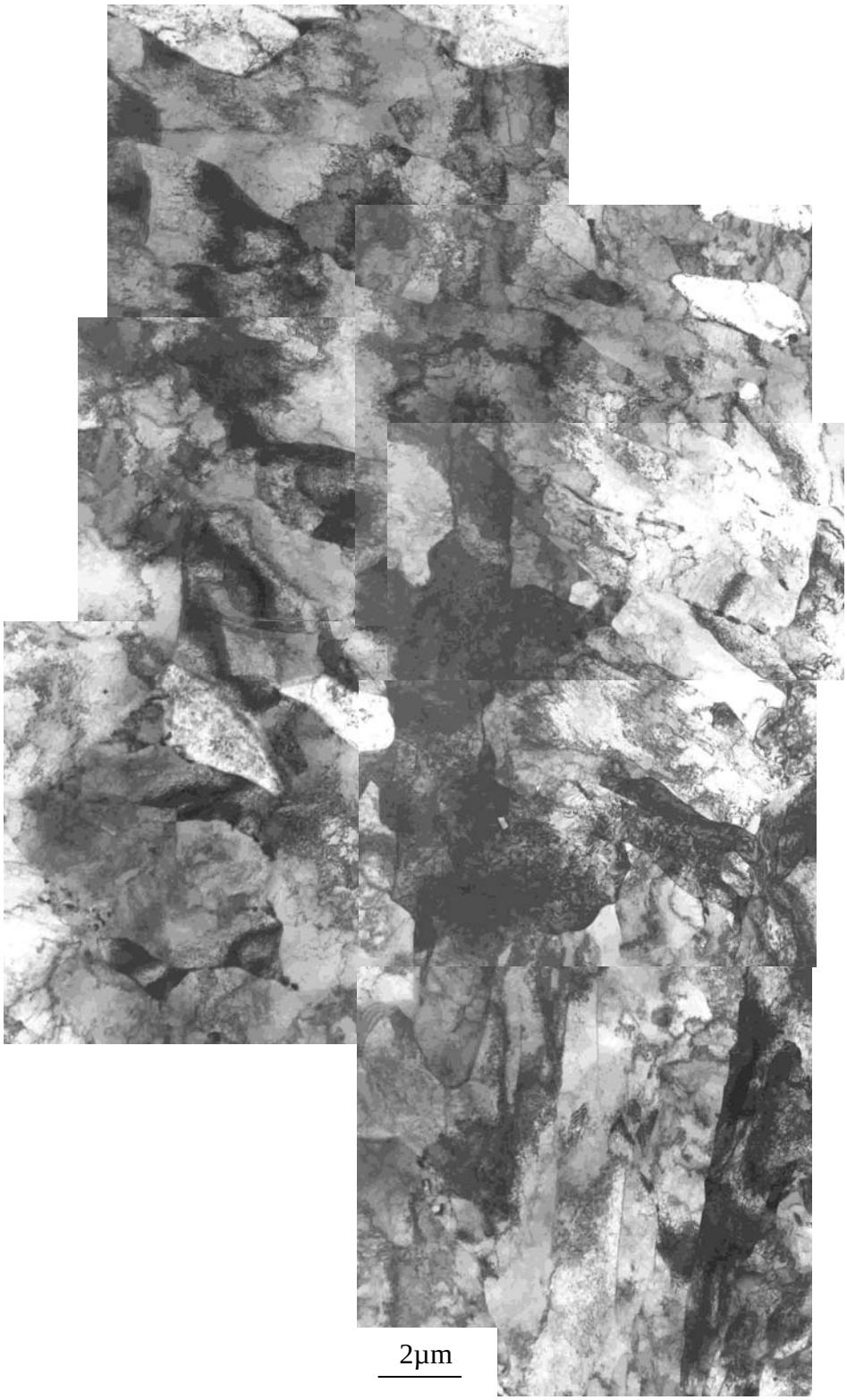

Figure 8.11 Thin foil TEM composite micrographs of the acicular ferrite in alloy #4 after a rapid cooling rate of 47 $^{o}Cs^{-1}$ after the hot rolling process.

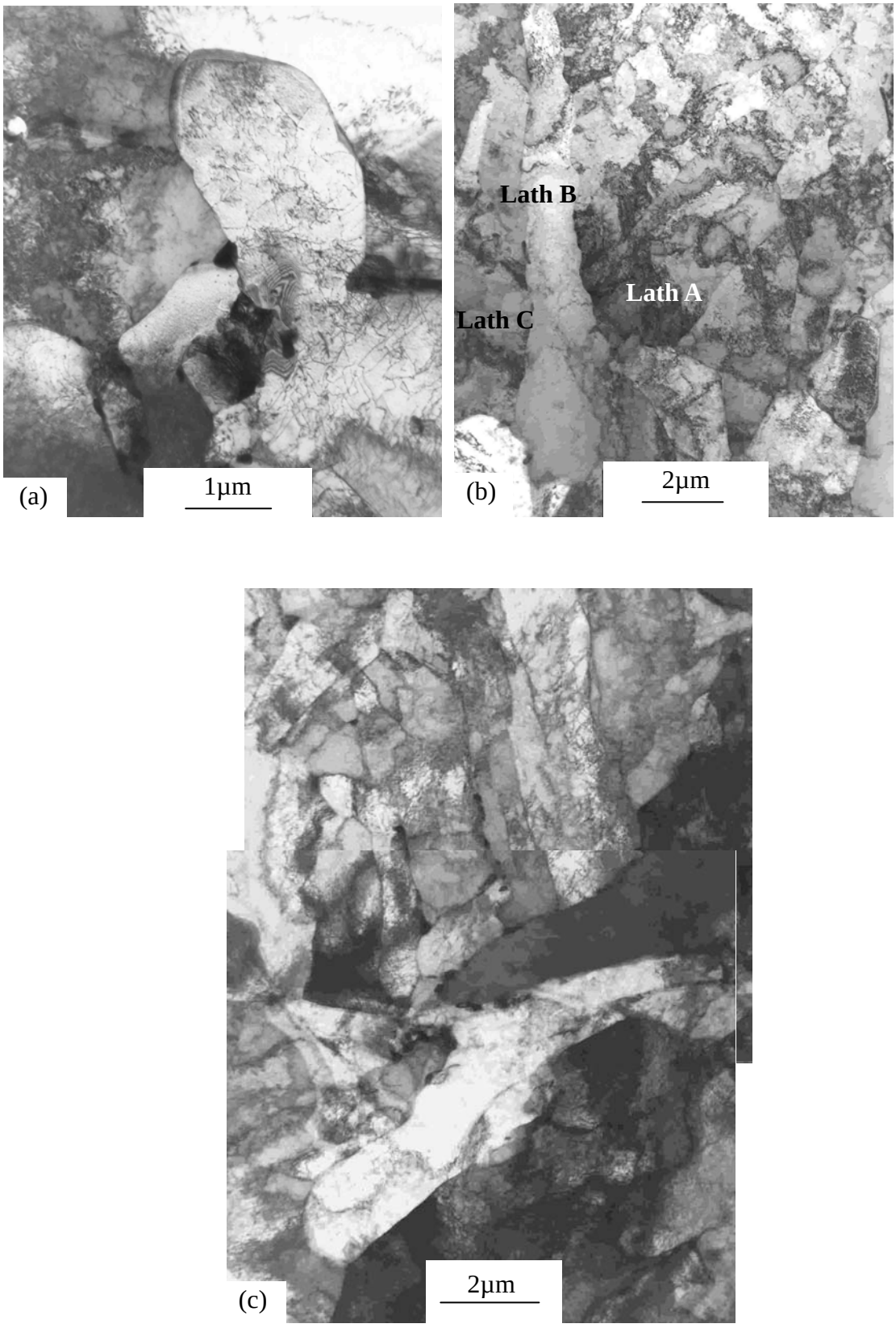

Figure 8.12 Thin foil TEM micrographs from alloy #5 with 0.22% Mo (a) polygonal ferrite, (b) and (c) acicular ferrite with interwoven laths.

Conclusions

Summarising these thin foils results shown above, the following conclusions can be drawn:

- All experimental alloys cooled at a rapid cooling rate of 47 $^{o}Cs^{-1}$ after hot rolling, had a mixed microstructure of polygonal ferrite and an acicular ferrite, as confirmed by thin foil TEM micrographs.
- This confirmed the tentative observation made from the optical micrographs in figure 7.28 that the structure did not appear to be a 100% acicular ferrite but that it rather consisted of a mixture of polygonal ferrite and an acicular ferrite.
- There were no visible etched boundaries between polygonal ferrite and the acicular ferrite microstructure on the optical micrographs. Accordingly, optical micrographs such as in figure 7.29, can not decisively prove by themselves whether there is any polygonal ferrite in a largely acicular ferrite microstructure, as is apparently sometimes inadvertently done in the literature. It can only be confirmed by TEM work on thin foils and shadowed carbon replicas.
- Acicular ferrite has an interwoven lath structure with a high density of dislocations but contained no cementite, neither in the interlath positions or within the laths.
- Polygonal ferrite has a significantly lower dislocation content than the acicular ferrite but some apparent interface emission of dislocations in regions near to the interface into the polygonal ferrite has been observed.

8.2 Two types of acicular ferrite

8.2.1 Structure with parallel laths

There appeared to be two types of acicular ferrite laths that were observed in those alloys cooled with a rapid cooling rate of 47 ºCs^{-1} after the hot rolling. Diaz-Fuentes[78] has also found similarly two types of acicular ferrite by isothermal treatment in a medium carbon steel. Figure 8.13 shows some parallel laths in a lath colony in which some parallel laths interweave with one another. This can be clearly seen in figures 8.13 and 8.14. The apparent preferred habit plane of the laths in colony 1 appears to be different from that of the nearby colony 2 in figure 8.13. Combining this conclusion with the optical micrographs of this alloy (in figure 7.29), these parallel laths are possibly not from a bainite structure. This conclusion is based on no grain boundaries that can be observed in optical metallography (figure 7.29), and no cementite within the laths or on interlath positions by TEM. Acicular ferrite nucleates intragranularly on inclusions[71,74,136,137] in weld pools and not intergranularly, while its nucleation may possibly also be enhanced by dislocations resulting from prior deformation, as was described in section 7.5. The different parallel laths are possibly primary laths which have the same growth direction[75] and with a secondary lath that may nucleate at the tip of the primary one but with both having the same habit plane and orientation, resulting in a parallel sheaf morphology.

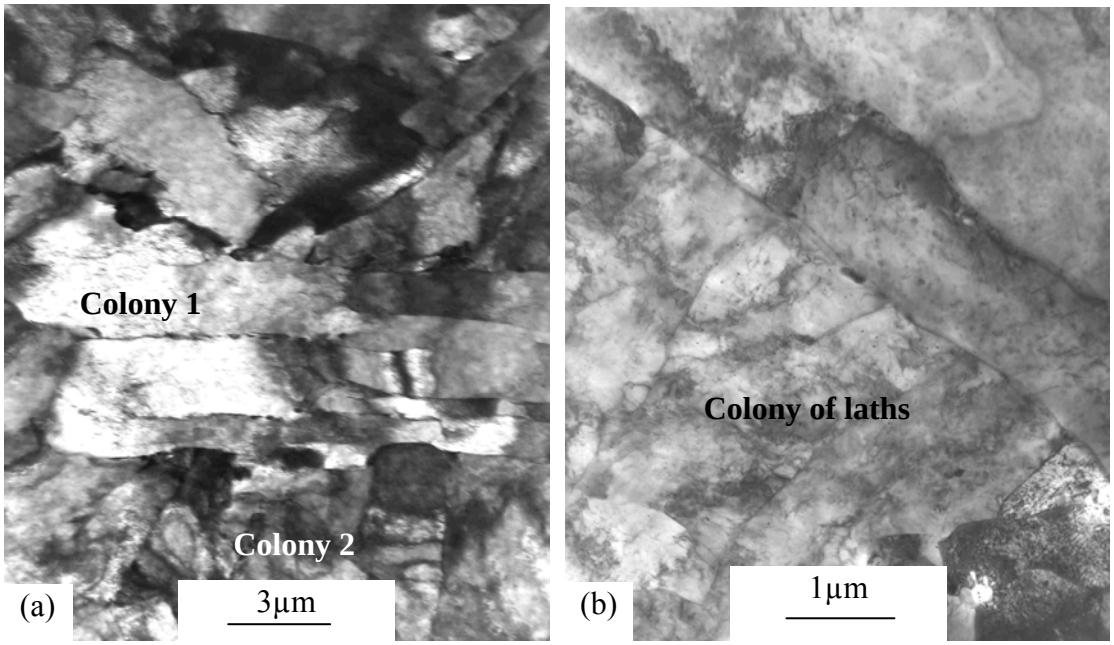

Figure 8.13 Parallel lath morphology in a colony in alloy #3 after rapid cooling at a rate of 47 ºCs^{-1} after the hot rolling process.

Madariaga and Bhadeshia[75] reported a similar parallel lath morphology of acicular ferrite in a medium carbon micro-alloyed steel that was isothermally treated at a relatively low temperature of 400 ºC. The two reasons given by the authors for the formation of a parallel lath microstructure are:

(1) The lower stability of the austenite with low carbon enrichment close to the ferrite tip rather than on the face of the lath, leading to the secondary plate of ferrite nucleating at the tip of previous one.
(2) Madariaga[75] reported that some retained austenite and cementite was found between the ferrite platelets. In that case, there was enough time for diffusion of carbon after the acicular ferrite formation because of the isothermal treatment. The excess carbon in acicular ferrite may be rejected into the austenite after the acicular ferrite formation and the cementite can be formed from the carbon-enriched austenite during this continued isothermal treatment. The austenite close to the face of the platelet has more carbon than the tip and as a result, cementite is distributed differently in the different sections of the boundary between adjacent platelets.

On the contrary, however, the parallel laths found in this study appear to be different from those in Madariaga's study[75]. No cementite was observed here on boundaries between laths or within the laths in any of the alloys in this study. Furthermore, the phase transformation in this study must have taken place in a few seconds due to the rapid cooling rate of 47 ºCs^{-1}, far less than in any isothermal treatment as was used by Madariaga. Consequently, the nucleation and growth of laths in the alloys studied here are probably different from those in Madariaga's study. The nucleation of a secondary lath is dependent not only on the carbon depletion into the parent austenite in front of the interface with the primary lath (the excess carbon from the primary lath will be rejected into the adjacent austenite[75,78], which then is not suited for the formation of a secondary lath), but also on the defects in the austenite adjacent to the primary lath, which resulted from the hot rolling process below the T_{nr}. These defects, therefore,

assist in the nucleation of the ferrite nuclei[134]. On the other hand, the secondary lath was possibly formed heterogeneously along the primary one in order to decrease the activation energy of transformation. A set of parallel laths that composes a colony, is typical of acicular ferrite found in this study. The boundary between the colonies could not be observed under the optical microscope (figure 7.29) because the size of the colonies was too small and the orientation differences between colonies were chaotic. The morphology at the end of the laths in figure 8.14 may not support the assumption that they had nucleated on the boundary of the austenite.

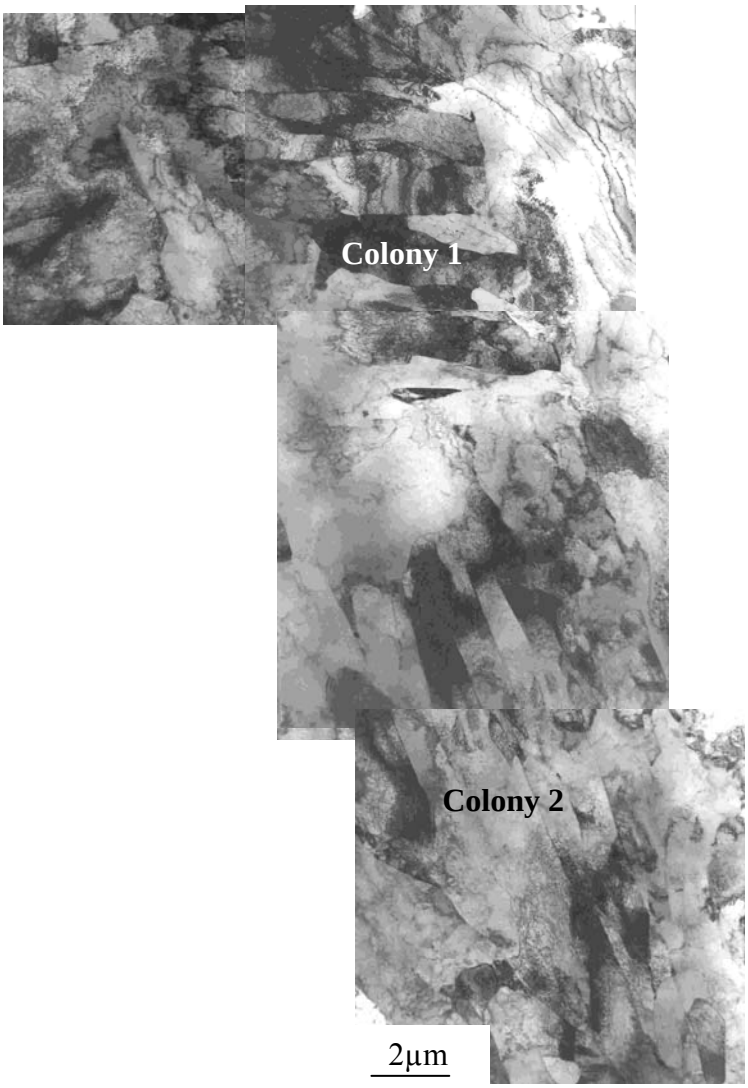

Figure 8.14 Interwoven arrangement between lath colonies in alloy #4 after a fast cooling rate of 47 ºCs^{-1} after the hot rolling process.

8.2.2 Structure with interwoven laths

Another type of lath structure may be seen in figures 8.15 and 8.16. Laths are chaotically arranged and interwoven in between each other (marked with A, B, C, D, E and F). Each lath had its own apparent growth direction. This lath morphology appears to be the same[69,90,134] as that which other researchers have observed in welds in which many non-metallic inclusions in the weld pool act as high density nucleation sites for acicular ferrite[57,81,138]. Such a nucleation process will result in various orientations, interwoven in the nature of acicular ferrite formation.

Although there were relatively few non-metallic inclusions in the alloys in the present study, some interwoven laths were still observed even though this was not typical acicular ferrite morphology in these alloys. Where this did occur, the primary acicular ferrite (AF) lath may have nucleated on an inclusion with the next lath then nucleated on the face of the previous lath, i.e. on the interface of the primary AF lath and the untransformed austenite. The direction of growth will favour the direction in which the retarding forces of the transformation are the lowest. Figure 8.15 shows that laths B, C and F apparently nucleated on the face of lath A, while lath G probably nucleated on lath F.

It, therefore, may be concluded that there are two types of laths of acicular ferrite present in the alloys studied in this work, namely, parallel and interwoven laths with the former being the dominant type.

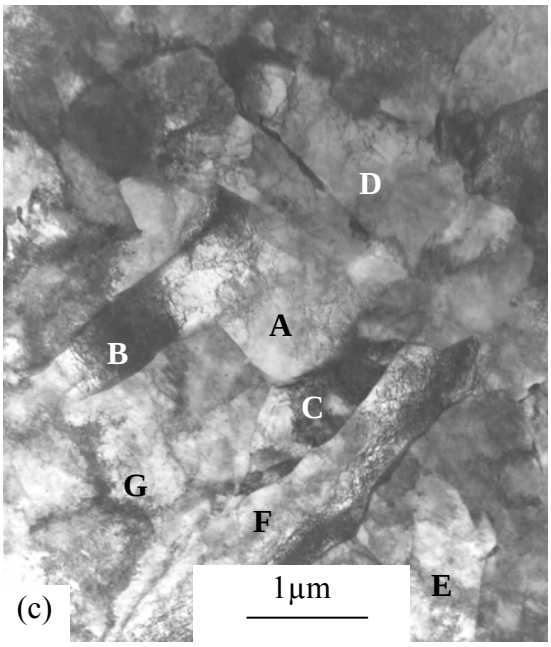

Figure 8.15 Interwoven laths micrographs in alloy #3 after fast cooling of 47 ºCs^{-1} after hot rolling process.

Figure 8.16 Acicular ferrite morphology in alloy #5 after fast cooling of 47ºCs^{-1} after the hot rolling process.

8.3 Nucleation of acicular ferrite

8.3.1 Nucleation on non-metallic inclusions

Both acicular ferrite and bainite have a lath-like structure when observed in thin foil samples by Transmission Electron Microscopy, i.e. both belong to a group of transformations that proceed basically by a displacive mechanism[139]. The main differences between the nucleation and growth of these two phases are the nucleation sites and the presence of cementite inside the laths or at inter-lath positions. Bainite nucleates on an austenite grain boundary[65,66,78], forming sheaves of parallel plates or laths with all essentially of the same crystallographic orientation. The boundaries and the general orientation of the plates are generally visible by optical microscopy (see figure 7.21-(k) in section 7.4 above).

The nucleation of an acicular ferrite structure, on the other hand, generally occurs intragranularly and often on non-metallic inclusions[70,136] as found in weld pools. As described in section 8.4, the morphologies found in this study were either parallel laths (figure 8.13) or interwoven laths (figure 8.15). Such intricate structural features, however, could not be identified by optical microscopy (see figure 7.29 in section 7.9) because of a lack of resolution of visible boundaries[131,135,140]. No precipitation of cementite was also found by thin foil TEM between or within the laths of the acicular ferrite. Accordingly, the lath morphologies in the present work differ significantly from that of bainite. These differences stem basically from differences in their nucleation mechanisms. Such differences in nucleation sites between bainite and acicular ferrite formation were also found by other authors [65,66,78,134]. A reduction of the austenite grain boundary surface area per unit volume, favours the formation of acicular ferrite and is detrimental to the formation of bainite due to the decrease in the number of potential bainite nucleation sites[65] on the austenite grain boundaries. A similar result in enhancing acicular ferrite formation was achieved by increasing the quantity of inclusions in the steel[141]. It has, therefore, been generally accepted that inclusions are the favoured sites for the nucleation of acicular ferrite[53,54,84,141,142], at least in the case of weld pools.

As described in section 8.3 above, the microstructures of the alloys studied here consisted in general of a mixture of acicular ferrite plus polygonal ferrite. An attempt

was made to find any non-metallic inclusions that existed within the laths. Figures 8.17 to 8.20 show acicular ferrite laths around such non-metallic inclusions. The analysis by Energy Dispersive Spectroscopy (EDS) on the TEM of the inclusion in figure 8.17-(a) showed that it consisted of manganese and iron oxides. The iron peak in figure 8.17-(b) was not thought to arise entirely from the steel matrix as the size of the inclusion of about 1.1 µm was large enough for the electron beam to strike primarily on the inclusion during the EDS analysis, although the beam had to penetrate through some matrix material to arrive at the inclusion. No diffraction pattern could be obtained on the TEM as the inclusion was too thick. The inclusion was centered inside the 50 to 80 µm thickness of the thin foil which made it even more difficult for the electron beam to transmit through the inclusion. Consequently, any information on the structure or molecular formula of the inclusion could not be obtained from a diffraction pattern.

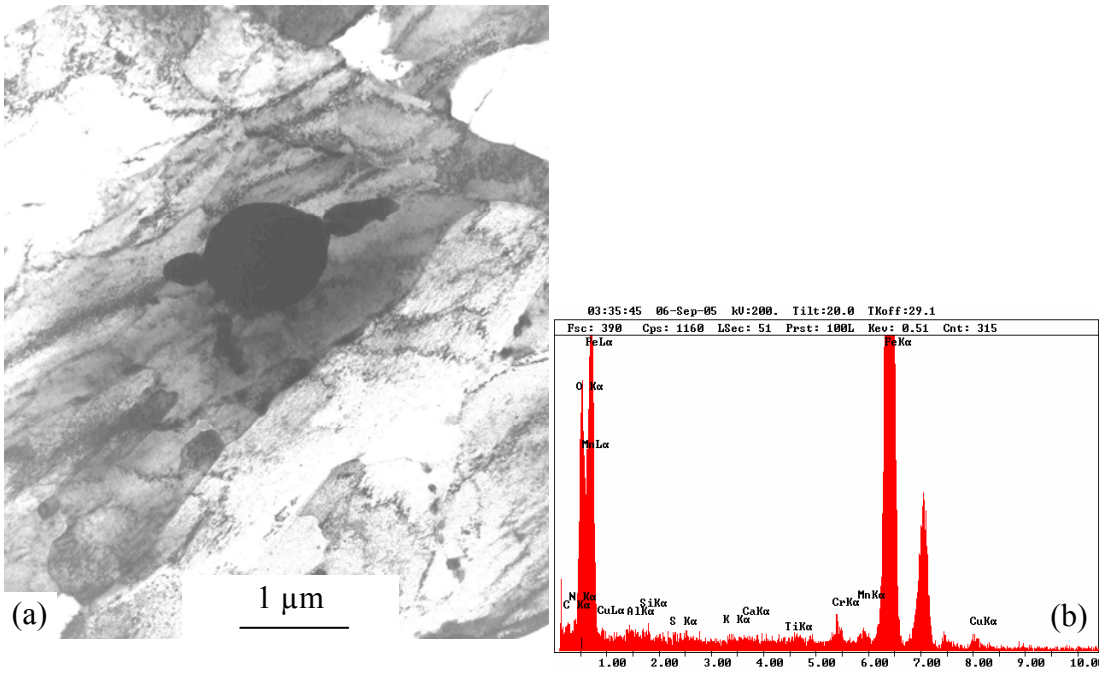

Figure 8.17 (a) TEM image of acicular ferrite and a large non-metallic inclusion in alloy #5 after a rapid cooling rate of 47 $^{o}Cs^{-1}$ after the hot rolling, (b) EDS analysis on the inclusion in this figure (a).

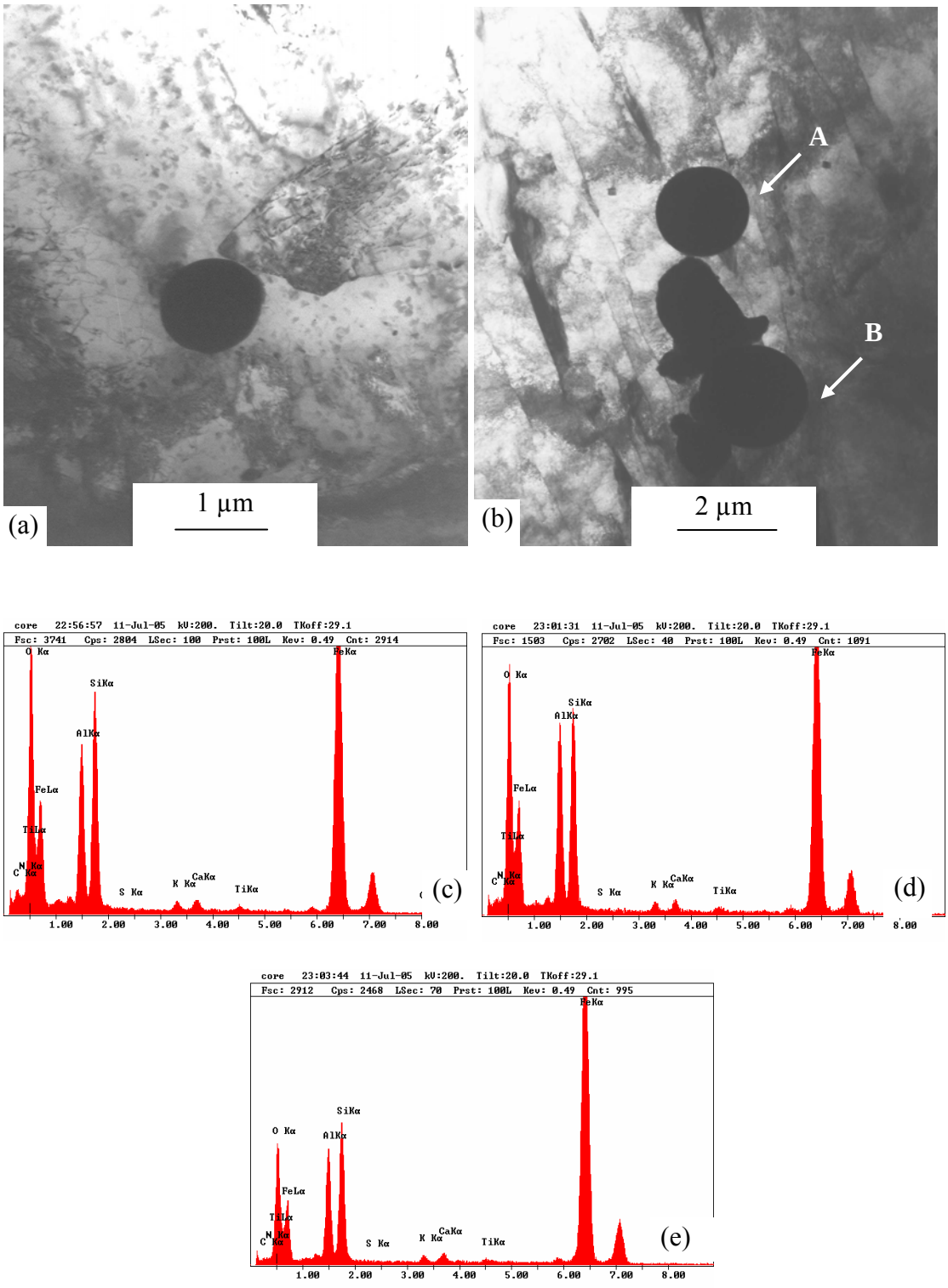

Figure 8.18 Laths nucleated on non-metallic inclusions (a) in alloy #1 after a rapid cooling rate of 47 ºCs^{-1} after the hot rolling, (b) in alloy #3 after a rapid cooling rate of 40 ºCs^{-1} from 980 ºC down to room temperature without deformation, (c) EDS analysis on the inclusion in this figure (a), (d) and (e) EDS analysis on the inclusions A and B in this figure (b), respectively.

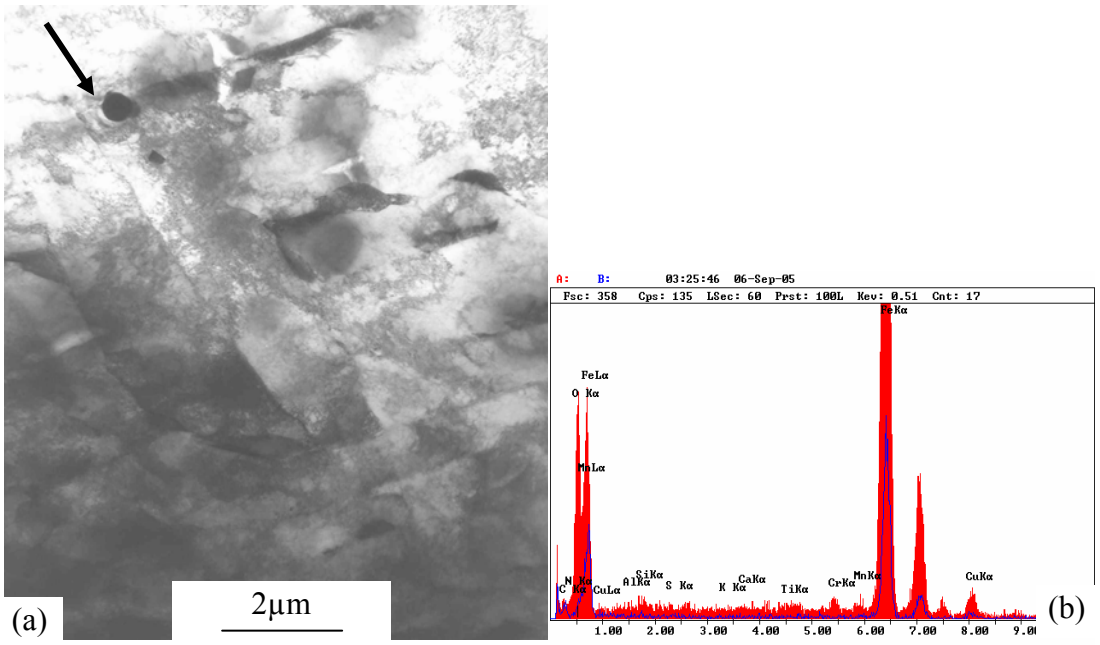

Figure 8.19 (a) Nucleation of interwoven laths of acicular ferrite in sample #AF3F of alloy #3 after a cooling rate of 20 ºCs^{-1} from 980 ºC down to room temperature without deformation, (b) EDS analysis of red peak was from on the inclusion indicated by an arrow in this figure (a), while blue peak was from the matrix steel.

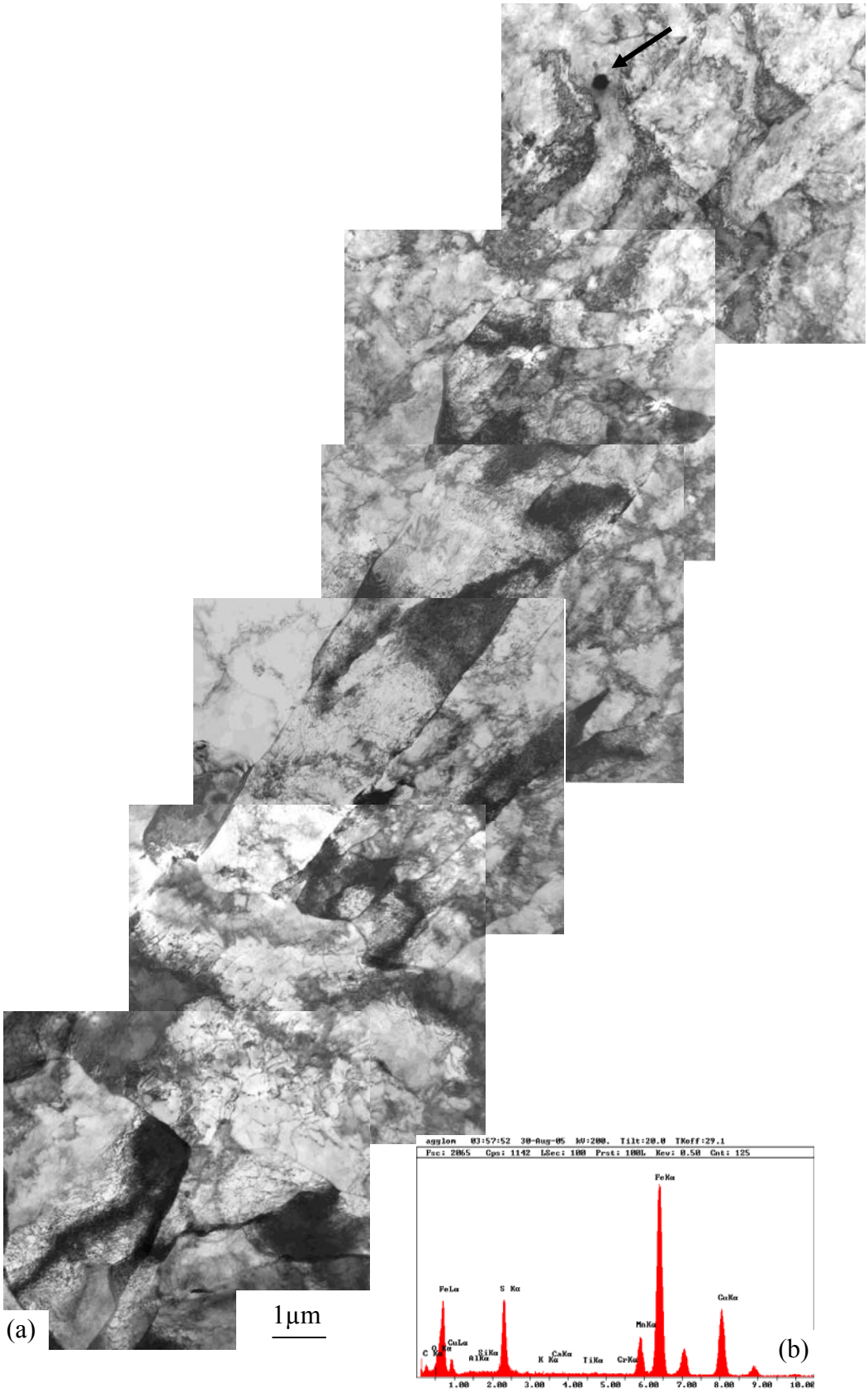

Figure 8.20 (a) Non-metallic inclusion and acicular ferrite in alloy #3 after a rapid cooling rate of 47 ºCs^{-1} after the hot rolling, (b) EDS analysis on the inclusion indicated by an arrow in this figure (a).

Similar nucleation of laths of acicular ferrite on inclusions was also found in alloy #1 (figure 8.18-(a) above). The inclusions in this case were generally round in shape, with a size of about 1.2 μm. The EDS image in figure 8.18-(c) reveals that the composition of these inclusions was apparently a complex oxide containing silicon, aluminium and iron.

Further nucleation of acicular ferrite on non-metallic inclusions is shown in figure 8.18-(b) for sample #AF3F of alloy #3 (0.09% Mo) that was cooled at 40 $^{o}Cs^{-1}$ from 980ºC down to room temperature (figure 6.14 in section 6.9). The acicular ferrite had once more, a typical lath structure nucleated around non-metallic inclusions with rounded shapes. The diameter of the inclusions ranged from 1.9 μm to 2.2 μm (see figure 8.18-(b)). The EDS image in figure 8.18-(d) and (e) revealed that they were complex oxides containing silicon, aluminium and iron. From the figure it appears that the two primary parallel laths of acicular ferrite nucleated on the non-metallic inclusion. The secondary lath, however, nucleated at the tip of the primary one, possibly owing to a lower carbon content in this area and then grew in the same direction as the primary one.

The nucleation of interlocked laths of acicular ferrite is shown in figure 8.19 for another sample in group #AF3F of alloy #3 (0.09% Mo) (figure 6.14 in section 6.9). The cooling rate was 20 $^{o}Cs^{-1}$ from 980 ºC down to room temperature. The inclusions were about 0.5 μm in diameter and, therefore, quite small to be analysed with confidence by EDS in the thin foil. The blue peak for iron in figure 8.19-(b) probably arose from the matrix of the steel surrounding the inclusion. There is a difference in the iron peak between the red and blue lines in the EDS image. Therefore, it appears that the non-metallic inclusion shown by an arrow in the figure was a mixture of manganese, iron and copper oxide.

Figure 8.20 shows the nucleation of an acicular ferrite colony on an inclusion of about 0.35 μm in diameter. For such an inclusion, the iron peak in figure 8.20-(b) is probably from the steel matrix and not from the inclusion. Thus, the acicular ferrite nucleated on an inclusion consisting probably of manganese and copper sulphide.

Summarising the results above, a number of inclusions were found that were associated with acicular ferrite laths. Previous researchers have also found that acicular ferrite nucleates on non-metallic inclusions[75,77,141] and their nucleation frequency increases with an increasing quantity of inclusions in a weld pool[141,143]. In this work the nucleation sites for acicular ferrite were generally oxide and sulphide inclusions with generally a rounded shape whereas the size of these inclusions ranged from 0.35 to 2.2 μm. The chemical compositions of these non-metallic inclusions were complex containing silicon, aluminium, iron, manganese and copper.

8.3.2 Type of non-metallic inclusion as nucleants

Other researchers have reported that acicular ferrite nucleates on inclusions or particles, such as TiO[141,144,145], BN plus rare earth metal oxysulphides[148], aluminium-rich inclusions[147,148], and TiN[149]. Most of the work, however, focused on weld pools where a larger quantity of non-metallic inclusions is readily introduced. Bhatti[147] has reported that inclusions rich in manganese and inclusions covered by a skin of sulphide are ineffective nucleants for acicular ferrite. Inclusions which are covered by or are rich in copper-sulphur or silicon and which were effective as a nucleant[65,66,70] for acicular ferrite, however, were found by Zhang and Farrar[141], Dowling et al[144], Court[150], Harbottl[151], Madariaga[69] and Kayali et al[152]. Similar oxide inclusions of manganese plus iron and containing copper and also manganese sulphides containing copper have been found in this work (see figures 8.19 and 8.20 respectively). It may, therefore, be concluded that the type of inclusions that had formed nucleation sites for acicular ferrite in these steels studied here, were most likely complex oxides or sulphides.

8.3.3 Nucleation mechanisms of acicular ferrite

Three nucleation mechanisms of acicular ferrite on inclusions have been proposed by previous researchers: (1) the existence of local variations in the chemistry of the matrix[90]; (2) the generation of high strain fields around the inclusion due to the different thermal expansion coefficients between austenite and the inclusion[153,154] or deformation in the austenite region; and (3) the creation of a low energy interface between acicular ferrite and the inclusion owing to a low lattice mismatch between them[69, 155-158].

When acicular ferrite is formed, the total system's Gibbs free energy must be lowered for the nucleus to become thermodynamically stable. This total energy includes the decrease in the chemical free energy, the disappearance of an interface between the inclusion and the austenite, and two new interfaces created of austenite-acicular ferrite and inclusion-acicular ferrite. This change in total energy can be described by the following equation:

$$\Delta G_{total} = -\Delta G_v V_{AF} + \sigma_{AF/\gamma} A_{AF/\gamma} + \sigma_{AF/I} A_{AF/I} + \Delta G_\varepsilon V_{AF} - \sigma_{I/\gamma} A_{I/\gamma} - \Delta G_{defect} V_{AF} \qquad (8.1)$$

where ΔG_v is the decrease in Gibbs free energy per unit volume owing to the transformation from austenite to acicular ferrite, also often termed the "chemical free energy",

V_{AF} is the volume of transformed acicular ferrite,

$\sigma_{AF/\gamma}$, $\sigma_{AF/I}$, $\sigma_{I/\gamma}$ are interface energies per unit area between acicular ferrite and austenite, acicular ferrite and an inclusion and an inclusion and austenite, respectively;

$A_{AF/\gamma}$, $A_{AF/I}$, $A_{I/\gamma}$ are the interface areas between acicular ferrite and austenite, acicular ferrite and an inclusion and, an inclusion and austenite, respectively,

ΔG_ε is the strain energy per unit volume around the new AF nucleus due to the volume expansion during the transformation from a face-centered cubic lattice (fcc) to a body-centered cubic lattice (bcc) and

ΔG_{defect} is the stored defect elastic energy per unit volume in austenite around the inclusion due to deformation in the austenite, such as dislocation or point defects.

$-\Delta G_v V_{AF}$ is the chemical Gibbs driving force for the transformation that is dependent on the degree of under-cooling of the austenite as well as the chemical composition of the austenite and is generally independent of the inclusions present in the austenite. $\sigma_{AF/I} A_{AF/I}$ and $\sigma_{I/\gamma} A_{I/\gamma}$ are only affected by inclusions where acicular ferrite nucleates and is primarily determined by the mismatch of the interface between acicular ferrite and an inclusion. The transformation will proceed more readily through an increasing absolute value of $-\Delta G_v V_{AF}$ and become stable when the embryo size of acicular ferrite (r) reaches the critical size (r^*) (r^* is determined according to $\frac{d\Delta G_{total}}{dr} = 0$). This driving force is increased by increasing the under-cooling ΔT which again is increased by a higher cooling rate on the rising part of the "nose" on a CCT diagram. That this

is so, is confirmed by the results shown on the CCT diagrams in figures 7.26 and 7.28 in section 7.5 where it was found that a faster cooling rate after deformation of the austenite is more favourable for acicular ferrite formation because the under-cooling increases with an increase in cooling rate.

$\sigma_{AF/\gamma}A_{AF/\gamma}$, $\sigma_{AF/I}A_{AF/I}$ and $\Delta G_{\varepsilon}V_{AF}$ are the barriers to the nucleation of AF. It means that low values of the surface energies $\sigma_{AF/\gamma}$ and $\sigma_{AF/I}$ are beneficial to the nucleation of acicular ferrite on inclusions. $\sigma_{AF/\gamma}$ is dependent on the crystal lattice mismatch between acicular ferrite and austenite and will, therefore, determine the crystallographic orientation of the laths. For instance, a low $\sigma_{AF/\gamma}$ will arise from a low lattice mismatch between them.

In the present case where a lack of sufficient inclusions in the steels may occur, the typical acicular ferrite will be the parallel lath structure due to a low mismatch between austenite and acicular ferrite (also leading to a low $\sigma_{AF/\gamma}$) in this direction which is parallel to the primary one. $\sigma_{AF/I}$, however, is dependent on the lattice structure of the inclusion. An inclusion that has a lower mismatch with an acicular ferrite nucleus, is favoured more to nucleate acicular ferrite. Some researchers[141,144,159] have observed that an inclusion with a manganese sulphide core covered by a skin of copper sulphide acts as a nucleant for acicular ferrite, instead of manganese sulphide only.

Considering the surface energy $\sigma_{I/\gamma}$ between an inclusion and austenite only (which effectively becomes an additional driving force as it is removed from the system upon forming an acicular ferrite nucleus), on the other hand, this energy increases with an increase in their melting temperature[141]. The melting temperature is 1620 ºC for manganese sulphide, while it is 1125 ºC for copper sulphide[141], which means that $\sigma_{MnS/\gamma}$ is higher than $\sigma_{CuS/\gamma}$, and this will result in manganese sulphide being a more effective nucleant than copper sulphide as it provides a higher additional driving force. However, Evans[160] has reported that a high lattice mismatch exists between

manganese sulphide and ferrite, leading to a high retarding force $\sigma_{MnS/AF}$. Therefore, copper sulphide may be more favourable to nucleate acicular ferrite than manganese sulphide owing to the lower mismatch between it and the ferrite[65]. A similar inclusion has also been found in the present study in alloy #3 (see figure 8.20). It is believed that the inclusion may possibly also have been manganese sulphide in the core and copper sulphide on the outer skin although the difference between core and skin were not resolved by EDS owing to the small size of the inclusion. Accordingly, it can only be speculated that the surface layer of this inclusion may have been favourable for the nucleation of acicular ferrite as found by others for such types of inclusions.

As indicated above, $-\sigma_{I/\gamma}A_{I/\gamma}$ is another driving force for the transformation because of its negative sign. A high energy interface would preferably be replaced by a low energy one during the phase transformation, thus lowering the effective energy barrier for nucleation according to classical nucleation theory. Using the general assumption that the interface energy of phases or particles increase with their melting temperature, Dowling[144] has proposed that Al_2O_3 and SiO_2 would be expected to have high interface energies. These inclusions would, therefore, be efficient nucleants for acicular ferrite. In this work some aluminium, silicon and manganese oxides were found within the acicular ferrite laths (see figures 8.17 to 8.19) which were effective nucleants because these inclusions are of higher melting temperatures, 2015 ºC for Al_2O_3, 1713 ºC for SiO_2 and 1650 ºC for MnO[65].

The additional driving force $-\Delta G_{defect}$ arises from any defects in the austenite around inclusions from the deformation in the parent austenite during hot rolling below the T_{nr}. Most of these defects are likely to be dislocations as point defects will probably already anneal out during the hot rolling, even below the T_{nr}. The total strain in the finish rolling process below the T_{nr} of 0.54 that was applied here, would have resulted in a relatively high dislocation density within the austenite at the point of deformation. Furthermore, the density of dislocations immediately around inclusions will be higher than further away because of a concentration in deformation behaviour in the austenite in those areas. That this is likely to occur, has been shown by a number of authors in the theory of Particle Stimulated Nucleation (PSN) around large

precipitates after cold working in aluminium alloys[97]. In the PSN theories[161,162], it has been shown that the deformation zones around large second phase particles contain a larger number of "geometrically necessary" dislocations than further away and this leads to a higher driving force for nucleation during recrystallisation at the surfaces of these particles.

Similar to the above case of PSN, a higher stored defect energy, therefore, possibly exists in the area of austenite around an inclusion than further away or in undeformed austenite. This stored energy provides an additional driving force for acicular ferrite nucleation. It also means that the nucleation barrier for acicular ferrite may be reduced in the strain and dislocation field around the inclusion, leading to the observation that deformation in the austenite accelerates the nucleation of acicular ferrite or generates suitable nucleation sites[134,141]. This point has been demonstrated clearly by the results of the strain affected CCT diagrams in this study, in which it was demonstrated in section 7.5 that deformation in the austenite is beneficial to acicular ferrite formation instead of bainite.

$\Delta G_\varepsilon V_{AF}$ is another retarding force of strain energy due to the volume expansion during the transformation because there is a lattice change from fcc (austenite) to bcc (acicular ferrite). The amount of this strain energy is dependent on the temperature of the transformation and lower transformation temperatures will result in a higher strain energy because the untransformed austenite around acicular ferrite will strain harden more than at higher temperatures.

Acicular ferrite, however, is a displacive transformation and it is also possible that defects in the austenite prior to the transformation that may promote the nucleation, can also retard the growth[76]. The nucleated primary laths formed around inclusions may, therefore, grow to a smaller size in deformed austenite (see figure 7.27 of alloy #5 in section 7.5) than in a well annealed austenite. This will result in an overall finer ferrite grain size after transformation. A coarse acicular ferrite microstructure was only observed in alloy #5 without prior deformation (figure 7.23 in section 7.4).

In summary, therefore, deformation in the austenite prior to the transformation appears to accelerate the nucleation of acicular ferrite and thereafter possibly limits its growth, so that the size of the formed acicular ferrite packets or grains becomes finer.

CHAPTER 9 DISCUSSION

9.1 Effect of molybdenum additions on the continuous cooling transformations

9.1.1 Effect of molybdenum on polygonal ferrite formation

(i) With no prior deformation

From figures 7.22 and 7.24 (in section 7.4 above), it is evident that the polygonal ferrite region in the CCT diagram is more extended at the expense of the pearlite region in alloy #5 (with 0.22% Mo) than in the Mo-free alloy #6 for a condition of no prior deformation. From these figures it may be concluded that the temperature range for polygonal ferrite formation is enlarged in the case of alloy #5 with an 0.22% Mo addition, although the cooling rate range for polygonal ferrite formation is very similar (ranging from 0.1 to 4 $^{o}Cs^{-1}$ for alloy #6 and from 0.1 to 5 $^{o}Cs^{-1}$ for alloy #5). Formation of pearlite takes place within the cooling rate range of 0.1 to 1.5 $^{o}Cs^{-1}$ for the Mo-free alloy #6. Pearlite, however, can be observed between the cooling rates of 0.1 and 0.4 $^{o}Cs^{-1}$ with an 0.22% Mo addition in alloy #5. This is clearly due to the Mo addition in the alloy. Molybdenum is a ferrite forming element and diminishes the austenite phase field[97]. It can, therefore, promote polygonal ferrite and hinder pearlite formation under no prior deformation conditions in austenite.

(ii) With prior 45% reduction deformation at 860 ^{o}C below the T_{nr}

A similar result was obtained with a prior 45% reduction deformation in alloys #5 and #6 (see figures 7.28 and 7.26 in section 7.5). Polygonal ferrite was observed after all cooling rates, but formed within a wider temperature range in alloy #5 (with 0.22% Mo) than in the Mo-free alloy #6 during continuous cooling. The transformation temperature range for pearlite formation, however, was suppressed in alloy #5 (with 0.22% Mo) in the case of a prior deformation (see figure 7.28). This was an indication that the pearlite formation region was reduced by the molybdenum addition. It can, therefore, be concluded that molybdenum addition to Nb-containing low carbon line pipe alloys with prior deformation, promotes the formation of polygonal ferrite and inhibits pearlite formation.

9.1.2 Effect of molybdenum on acicular ferrite formation

(i) With a prior deformation

Figure 7.26 shows the strain affected CCT diagram for the Mo-free alloy #6 after solution treatment at 1225 ºC to completely dissolve the Nb(C,N) prior to a deformation of 45% reduction at 860 ºC. The non-recrystallisation temperature T_{nr} of alloy #6 ranged from 900 to 930 ºC and was dependent on the deformation parameters of pass strain, strain rate and inter pass time etc. The deformation prior to cooling for the CCT determination was, therefore, applied in the non-recrystallisation region. Figure 7.26 (in section 7.5) showed that the lowest cooling rate limit for acicular ferrite formation for alloy #6 (Mo-free) was approximately 0.7 ºCs^{-1} while almost the same limit for alloy #5 (0.22% Mo) (figure 7.28 in section 7.5), with a prior 45% reduction, was about 0.5 ºCs^{-1}. These two limits for the lowest cooling rates for acicular ferrite formation after prior deformation are, therefore, very close to each other. Furthermore, there was also no measurable difference in cooling rate range (almost 1 to 40 ºCs^{-1}) for acicular ferrite formation during cooling between the alloys #5 and #6 (see figures 7.28 and 7.26). It appears, therefore, that a molybdenum addition of about 0.22% Mo to Nb-bearing line pipe alloys does neither promote or retard acicular ferrite formation after a 45% prior reduction at 860 ºC below the non-recrystallisation temperature.

(ii) With no prior deformation

In contrast with the above effects of a prior deformation, the formation of acicular ferrite is affected by molybdenum additions with no prior deformation. The difference can be recognised from figures 7.22 and 7.24 (see section 7.4). Acicular ferrite was found in a wider cooling rate range from 0.1 to 15 ºCs^{-1} for alloy #5 (with 0.22% Mo) if compared to the Mo-free alloy #6 in which the region for acicular ferrite formation was smaller and was observed only within the narrower cooling rate range from 0.3 to 5 ºCs^{-1}.

(iii) Conclusions

On one hand there is, therefore, clear evidence that molybdenum additions to Nb-bearing line pipe steels promote acicular ferrite formation under no prior deformation conditions, as has been observed by a number of other researchers[78, 131,163-165]. On the

other hand, the contribution of molybdenum additions appears to be over-shadowed by the effect of deformation in the 0.22% Mo alloy #5 since there was no difference in the AF-forming regions in the CCT diagrams from that of the Mo-free reference alloy #6 (figures 7.26 and 7.28) after a prior deformation below the T_{nr}. It is evident, therefore, that both molybdenum additions and retained strain in the austenite can independently promote acicular ferrite formation. A high density of dislocations induced by the deformation in the austenite prior to transformation is, therefore, beneficial to the nucleation of acicular ferrite. This effect of retained strain on promoting acicular ferrite appears to be stronger than the effect of molybdenum additions.

9.2 Effect of deformation in austenite on acicular ferrite formation

Comparing figures 7.22 (section 7.4) and 7.26 (see section 7.5), the cooling rate range in which acicular ferrite formed, shifted from 0.3 to 5 $^{o}Cs^{-1}$ with no prior deformation, to 0.7 to 40 $^{o}Cs^{-1}$ with prior deformation, for the Mo-free alloy #6. It is, therefore, clear that the acicular ferrite region is expanded due to retained strain in the austenite prior to the phase transformation. It seems that the high density of dislocations in the deformed austenite is beneficial to the formation of acicular ferrite instead of bainite[75]. Bainite formation is completely suppressed in deformed austenite (figures 7.25 and 7.26 in section 7.5). Both bainite and acicular ferrite belong to the group that transform by a displacive transformation[74,76] that may be suppressed by pre-deformation in the austenite[166-168]. From these observations, however, it appears that the bainite displacive transformation must have been suppressed in the deformed austenite whereas the acicular ferrite formation was enhanced.

The main differences between bainite and acicular ferrite formation are related to their nucleation sites and growth directions. Bainite nucleates on austenite grain boundaries and grows as a sheaf of parallel plates with the same growth direction within the austenite grains (figure 7.21-(q) in section 7.4). Acicular ferrite generally nucleates intragranularly on non-metallic inclusions[70, 144,159, 169,170] and grows as primary plates in the same[75,78] or many different orientations[75,76] from these inclusions. Then a new generation of secondary plates nucleates at the austenite/primary acicular plate's interface[75,77]. Consequently, acicular ferrite is characterised by a chaotic arrangement

of plates showing fine grained interwoven morphologies (figure 7.25-(k) to (t) in section 7.5). The grain structures of acicular ferrite laths are also smaller than those of bainite. This may be related to the effect of dislocations adjacent to inclusions/primary plates in deformed austenite that can act as the nucleation sites for secondary plates of acicular ferrite. The retained strain energy[74] in the areas with a high density of dislocations can contribute to the mechanical driving force[51] for acicular ferrite nucleus formation[134]. Dislocations, however, can also hinder the growth of a nucleus of acicular ferrite[76] owing to the displacive nature of the transformation. Thus both of the effects of dislocations of, firstly, promoting nucleation of an acicular ferrite lath and, secondly, suppressing its growth, will lead to an eventual finer acicular ferrite lath structures. Shipway and Bhadeshia[171] have found that a large enough dislocation density in austenite introduced by prior deformation, appears to act as a further nucleation source for Widmanstätten ferrite which forms also by a displacive transformation mechanism, leading to a refinement of microstructure. Sugden[74] has also found that acicular ferrite never grows across austenite grain boundaries.

Figure 7.22 in section 7.4 shows that the cooling rate for the formation of bainite is higher than that required for acicular ferrite. It means that bainite formation requires a higher degree of under-cooling for nucleation, but once it has nucleated, it grows relatively quickly. On the contrary, the undercooling required for the formation of acicular ferrite is lower than that for bainite and its formation might be rate controlled by both nucleation and growth for the primary plates or secondary nucleation on the interface between the plate and austenite. Its transformation model is a mixture of diffusion and shear transformation[4,9,11,43]. Figure 7.22 also shows that the acicular ferrite formation temperature is higher than that of bainite, which is in agreement with the work of Zhao[4] and Kim[11]. This higher transformation temperature is helpful for the carbon diffusion in its rejection from the acicular ferrite primary laths with its lower solubility for carbon than the untransformed austenite.

The same result was obtained in alloy #5 (with 0.22% Mo) (see figures 7.24 in section 7.4 and 7.28 in section 7.5). The bainite transformation was completely suppressed in deformed austenite, while the acicular ferrite formation was promoted, even more with prior deformation than in alloy #6 (Mo-free).

In summary, retained strain in the austenite promotes the nucleation of acicular ferrite, hinders its growth, and at the same time, suppresses the formation of bainite. This results in a shorter lath size of acicular ferrite, which may be beneficial to the toughness of the steel. An addition of 0.22% Mo to Nb-bearing low carbon line pipe steels, therefore, does not markedly affect the formation of acicular ferrite to the same extent as prior deformation of the austenite does.

9.3 Ratio of yield strength to ultimate tensile strength and its effect

The ratio of yield strength to ultimate tensile strength (YS/UTS) is one of the properties sometimes specified for low carbon structural steel. In particular, a low YS/UTS ratio is a very important parameter in the API specifications for line pipe steels as a high work hardening rate is required in this application. In the present work a number of differently alloyed steels treated at various cooling rates, two coiling temperatures and with and without prior deformation in the austenite, were tensile tested in order to establish the relationships between their YS/UTS ratios and these materials and process parameters.

9.3.1 The effect of cooling rate

The cooling rate after austenitisation affects the transformed microstructures that result in different mechanical properties in line pipe steels, such as yield strength (YS), ultimate tensile strength (UTS), elongation and impact toughness. The two alloys #3 (0.09% Mo) and the reference Mo-free alloy #6 were selected for studying the effect of cooling rate on the YS/UTS ratio. The temperature range of varying cooling rates was from 980 ºC down to room temperature.

The effects of cooling rate on the yield strength and ultimate tensile strength are shown in figures 9.1 and 9.2, respectively. Both the yield strength and ultimate tensile strength increase with increasing cooling rate after soaking at 980 ºC, as predicted by the two fitted equations (9.1) and (9.2). The microstructures also changed with cooling rate. Polygonal ferrite dominated the microstructure at lower cooling rates, whereas acicular ferrite plus bainite dominated at high cooling rates. The amount of bainite and acicular ferrite constituents increased with an increase in cooling rate (see figure 7.22 in section 7.4.1) and this increased the strength of the alloy.

$$YS = 4.1CR + 445 \quad \text{(in MPa)} \qquad R^2 = 0.98 \qquad (9.1)$$

$$UTS = 3.9CR + 572 \quad \text{(in MPa)} \qquad R^2 = 0.99 \qquad (9.2)$$

where CR is cooling rate in $^{o}Cs^{-1}$

R^2 is the Regression Coefficient

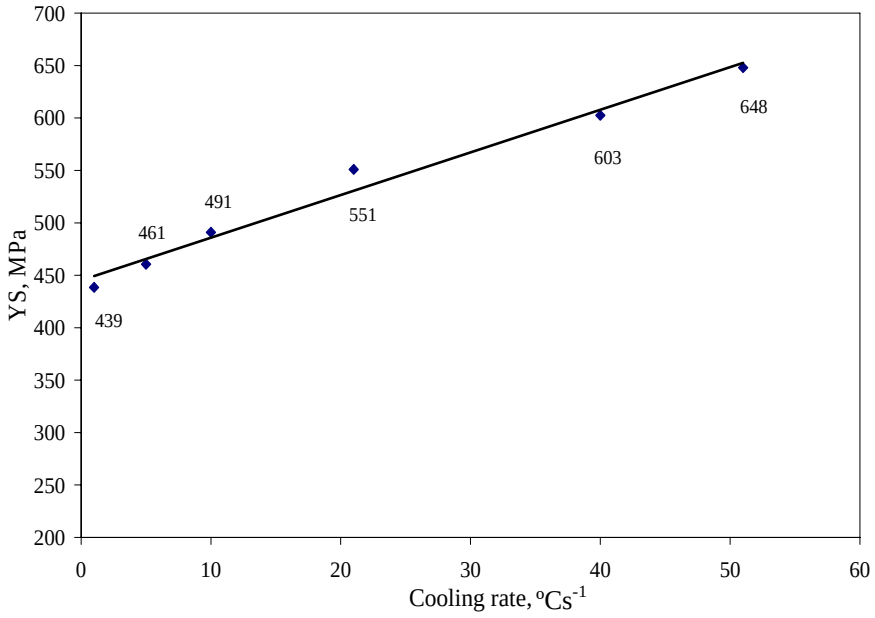

Figure 9.1 The yield strength of the reference Mo-free alloy #6 as a function of the cooling rate from 980 ºC with no prior deformation before the transformation and with no coiling simulation.

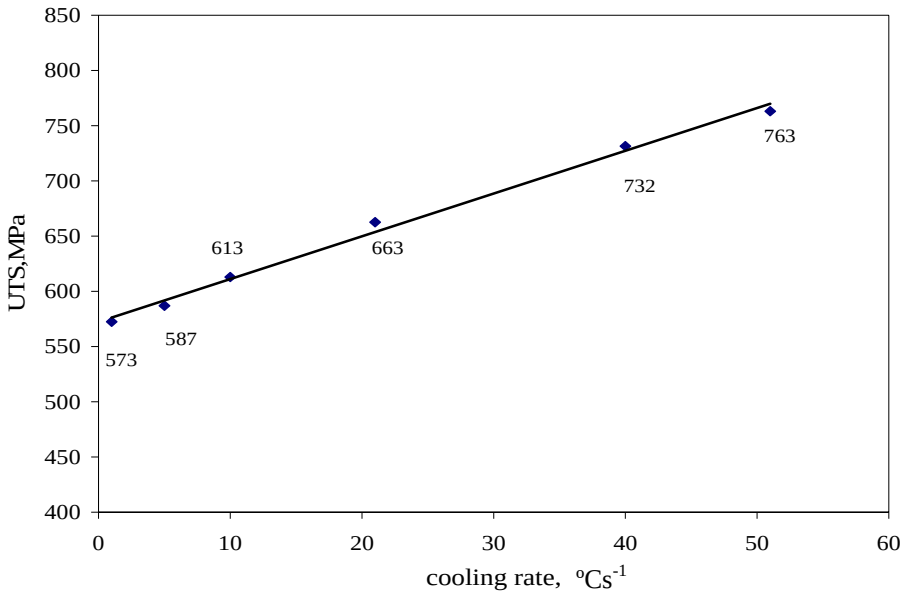

Figure 9.2 The ultimate tensile strength of the reference alloy #6 as a function of cooling rate from 980 ºC with no prior deformation before the transformation and with no coiling simulation.

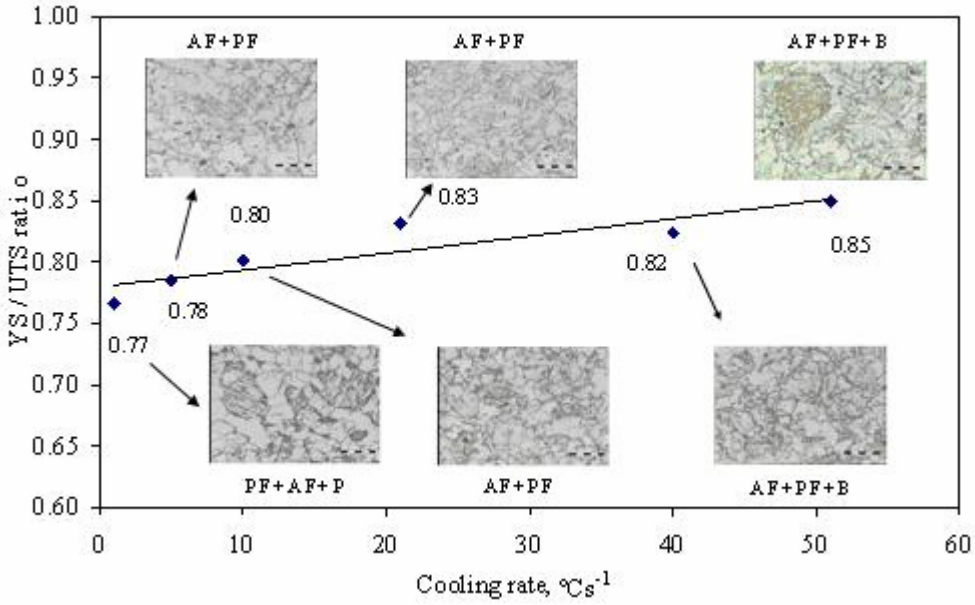

Figure 9.3 The YS/UTS ratio of the reference alloy #6 as a function of cooling rate from 980 ºC with no prior deformation before the transformation and with no coiling simulation. PF-polygonal ferrite, AF-acicular ferrite and P-pearlite.

As may be seen in figure 9.3, it appears that the ratio of YS/UTS increases slowly with increasing cooling rate under conditions of no coiling simulation and no deformation prior to the transformation. Equations (9.1) and (9.2) show that the slope of the YS versus CR line is higher than that of the UTS versus CR, i.e. the cooling rate may affect the YS more than the UTS. This suggests that the dominant structure of acicular ferrite plus bainite could improve the yield strength more than the ultimate tensile strength of these steels. Furthermore, the grain size of the steel will also be finer with increasing cooling rate because of the higher under-cooling at a faster cooling rate. A high density of dislocations and other crystal defects could also have been introduced by an acicular ferrite microstructure or bainite formation due to their displacive formation mechanisms. Such a high density of dislocations has been found in sample #AF3F from alloy #3 with a cooling rate of 40 $^{o}Cs^{-1}$ (seen figure 8.18-(b)). These “prior” defects may interact with other dislocations during early plastic straining, leading to a high yield strength. Therefore, the finer grain size and a high density of dislocations after a rapid cooling rate are useful to raise the YS, thereby increasing the YS/UTS ratio with increasing cooling rate.

A similar result (see figures 9.4 to 9.6) between YS, UTS, YS/UTS and the cooling rate was obtained for alloy #3 containing 0.09% Mo after the same treatment as above for alloy #6. The YS/UTS ratio in alloy #3, however, was not affected to the same degree by the cooling rate as was the case in alloy #6, compare figures 9.6 with 9.3.

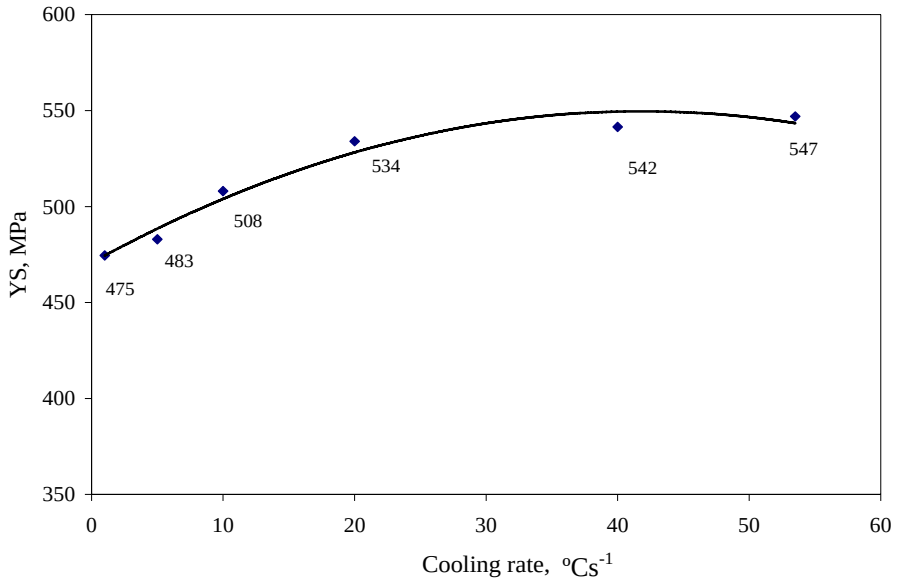

Figure 9.4 The yield strength of alloy #3 as a function of cooling rate from 980 ºC under conditions of no prior deformation to the transformation and no coiling simulation.

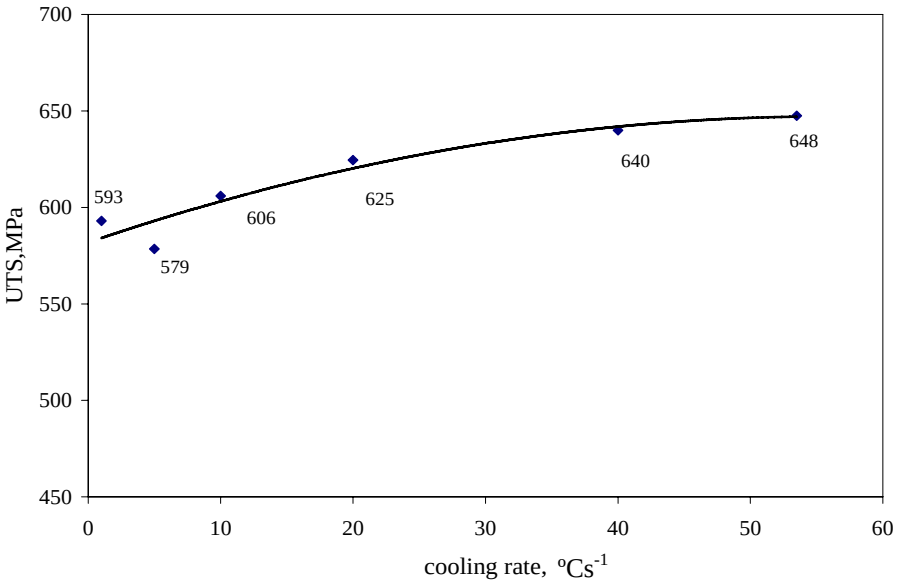

Figure 9.5 The ultimate tensile strength of alloy #3 as a function of cooling rate from 980 ºC under conditions of no prior deformation to the transformation and no coiling simulation.

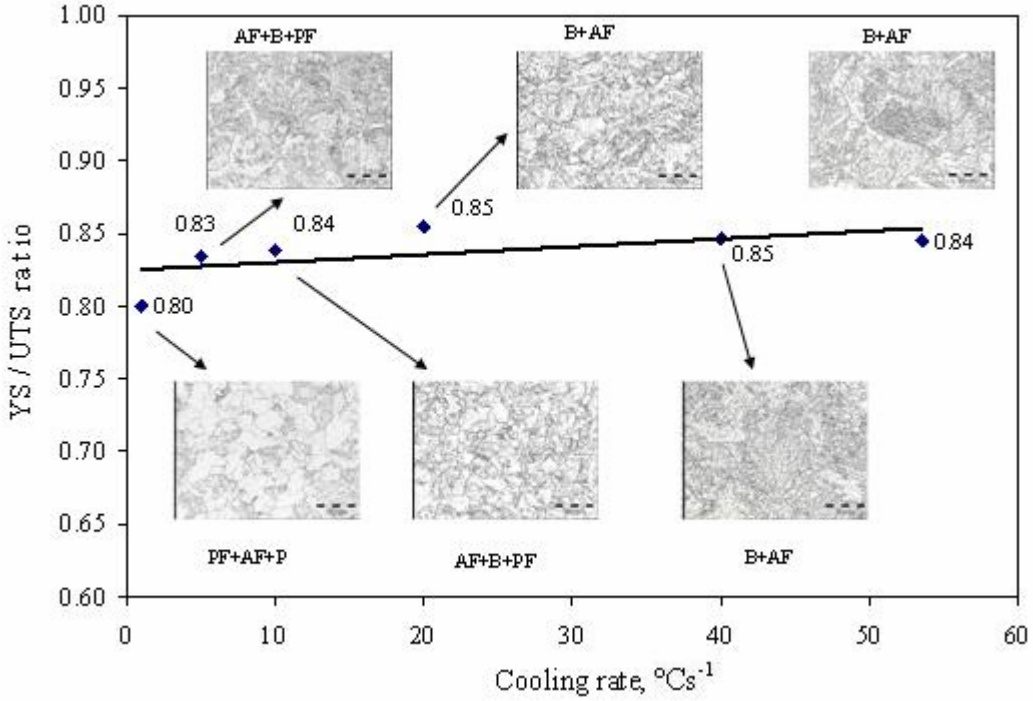

Figure 9.6 The YS/UTS of alloy #3 as a function of cooling rate from 980 ºC under conditions of no prior deformation to the transformation and no coiling simulation. PF-polygonal ferrite, AF-acicular ferrite, B-bainite and P-pearlite

9.3.2 The effect of coiling temperature

Two sets of specimens were treated for coiling simulations at 575 and 600 ºC, respectively, without deformation prior to the transformation. The latter coiling temperature of 600 ºC has recently been lowered to 575 ºC by Mittal Steel SA in their line pipe process. The results of alloy #6 are given in figures 9.7 to 9.9 for the coiling temperature of 600 ºC. It seems that the cooling rate does not markedly affect the yield strength and ultimate tensile strength of this alloy after coiling at 600 ºC. It was observed that the ratio of YS/UTS was also not a function of the cooling rate, with the ratio almost constant, ranging from 0.76 to 0.78. This could be due to the annealing out of the dislocations and other crystal defects introduced by the displacive transformation in acicular ferrite or bainite during the coiling simulation process.

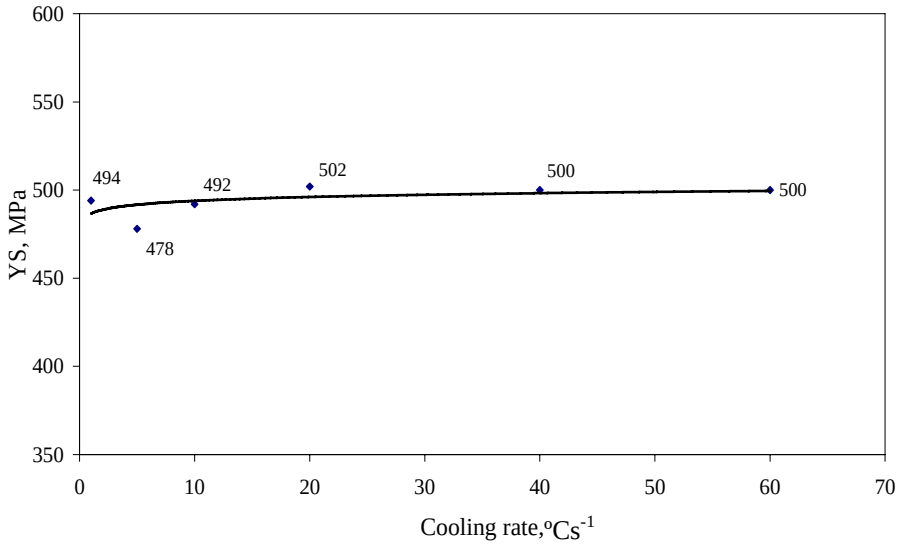

Figure 9.7 The yield strength of alloy #6 as a function of the cooling rate from 980 ºC to 600 ºC under conditions of no prior deformation to the transformation but with a coiling simulation at 600 ºC for 1 hour.

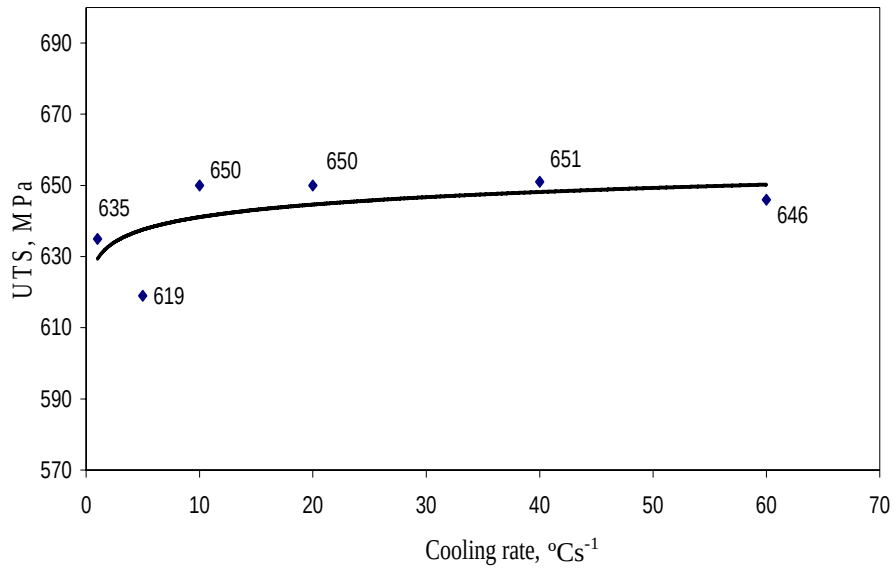

Figure 9.8 The ultimate tensile strength of alloy #6 as a function of cooling rate from 980 ºC to 600 ºC under conditions of no prior deformation to the transformation but with a coiling simulation at 600 ºC for 1 hour.

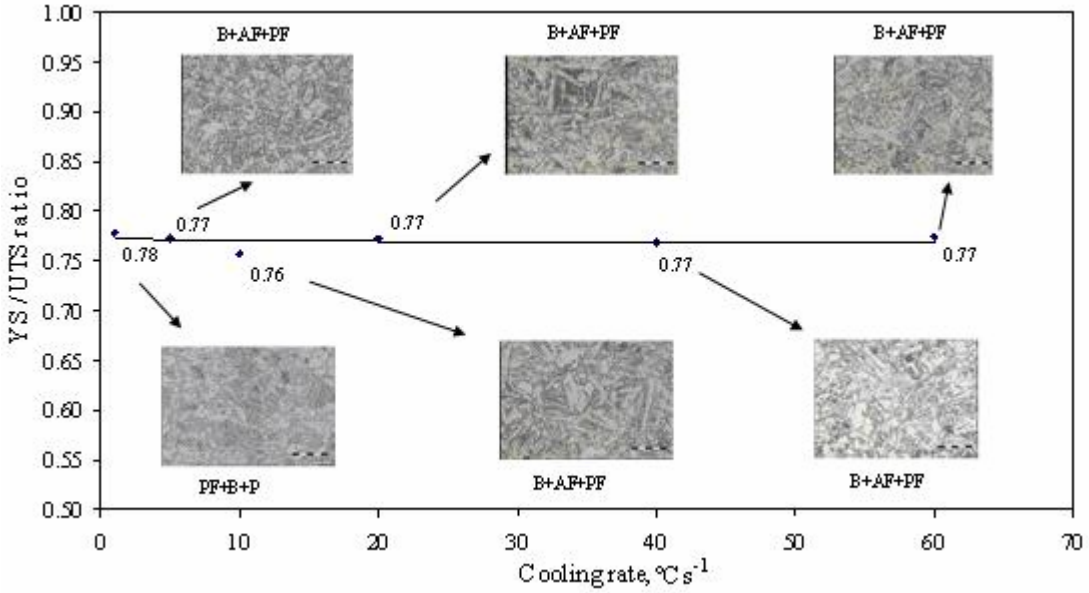

Figure 9.9 The YS/UTS ratio of alloy #6 as a function of the cooling from 980 ºC to 600 ºC under conditions of no prior deformation to the transformation but with a coiling simulation at 600ºC for 1 hour. PF-polygonal ferrite, AF-acicular ferrite, B-bainite and P-pearlite.

Figures 9.10 to 9.12 show the results of the tensile tests of alloy #6 for a coiling temperature of 575 ºC. Similar results were obtained for the coiling simulation at 600 ºC with the ratio of YS/UTS ranging from 0.75 to 0.80. It was concluded that varying the coiling temperature within the range of 575 to 600 ºC did not substantially influence the ratio of YS/UTS for the entire cooling range of 1 to 60 ºCs^{-1}.

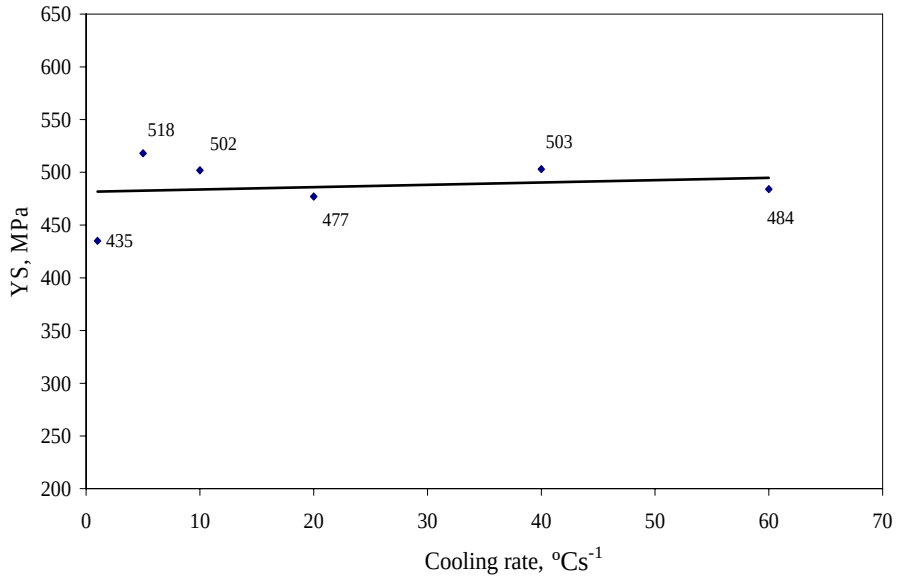

Figure 9.10 The yield strength of alloy #6 as a function of the cooling rate from 980 ºC to 575 ºC under conditions of no prior deformation to the transformation but with a coiling simulation at 575 ºC for 1 hour.

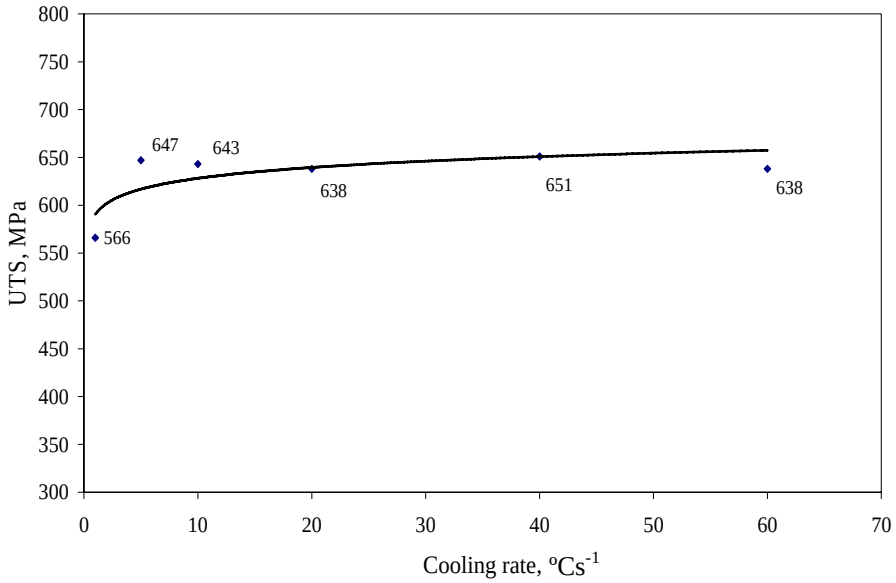

Figure 9.11 The ultimate tensile strength of alloy #6 as a function of the cooling rate from 980 ºC to 575 ºC under conditions of no prior deformation to the transformation but with a coiling simulation at 575 ºC for 1 hour.

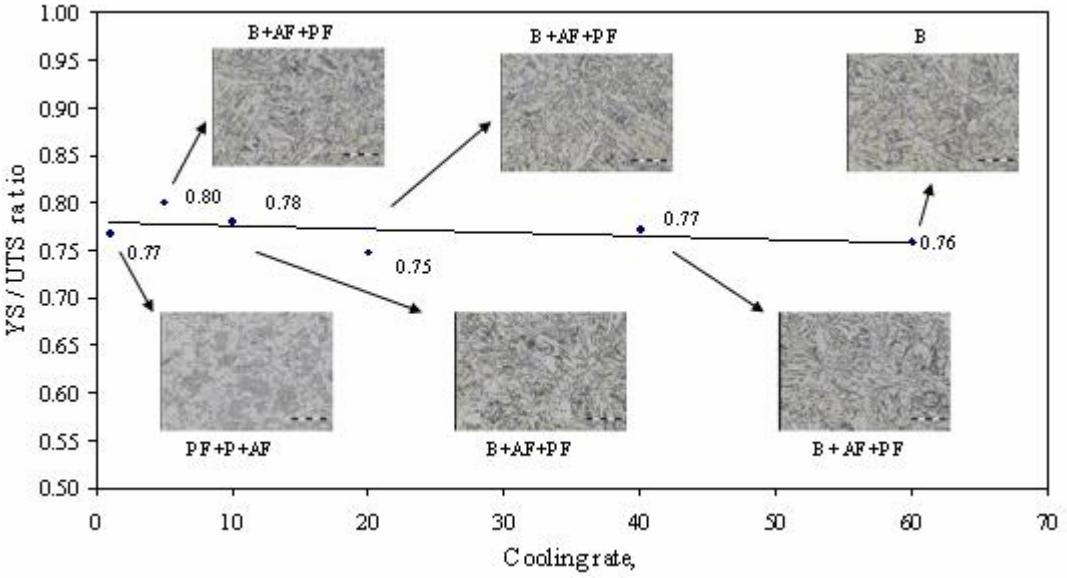

Figure 9.12 The YS/UTS ratio alloy #6 as a function of the cooling rate from 980 ºC to 575 ºC under conditions of no prior deformation to the transformation but with a coiling simulation at 575 ºC for 1 hour. PF-polygonal ferrite, AF-acicular ferrite, B-bainite and P-pearlite.

9.3.3 The effect of prior deformation in the austenite and coiling simulation

This group of specimens was subjected to a deformation in the austenite region with 33% reduction below the T_{nr}, before cooling through the transformation to ferrite from 860 to 575 ºC and then applying a coiling simulation at 575 ºC for 1 hour. The results from these tests are given figures 9.13 to 9.15. As may be seen, the yield strength and ultimate tensile strength were affected by cooling rate as well.

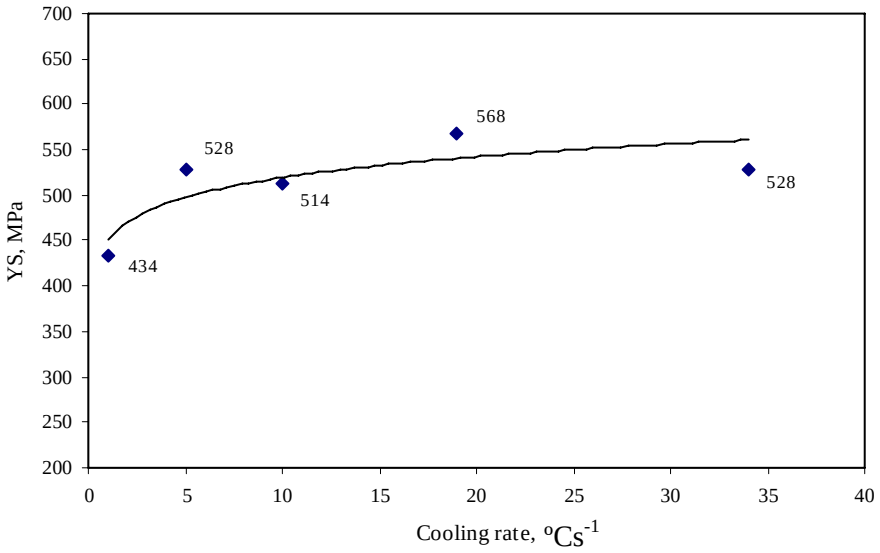

Figure 9.13 Effect of the cooling rate on the yield strength of the reference alloy #6 after prior deformation of 33 % reduction in the austenite below the T_{nr}, cooling to 575 ºC at different cooling rates and simulation of the coiling at 575 ºC for 1 hour.

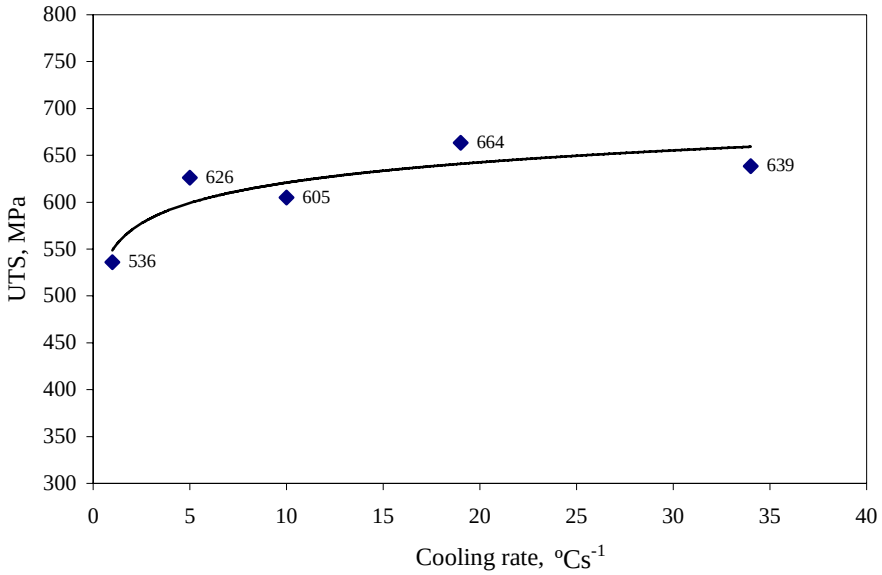

Figure 9.14 Effect of the cooling rate on the ultimate tensile strength of the reference alloy #6 after prior deformation of 33 % reduction in the austenite below the T_{nr}, cooling to 575 ºC at different cooling rates and simulation the coiling at 575 ºC for 1 hour.

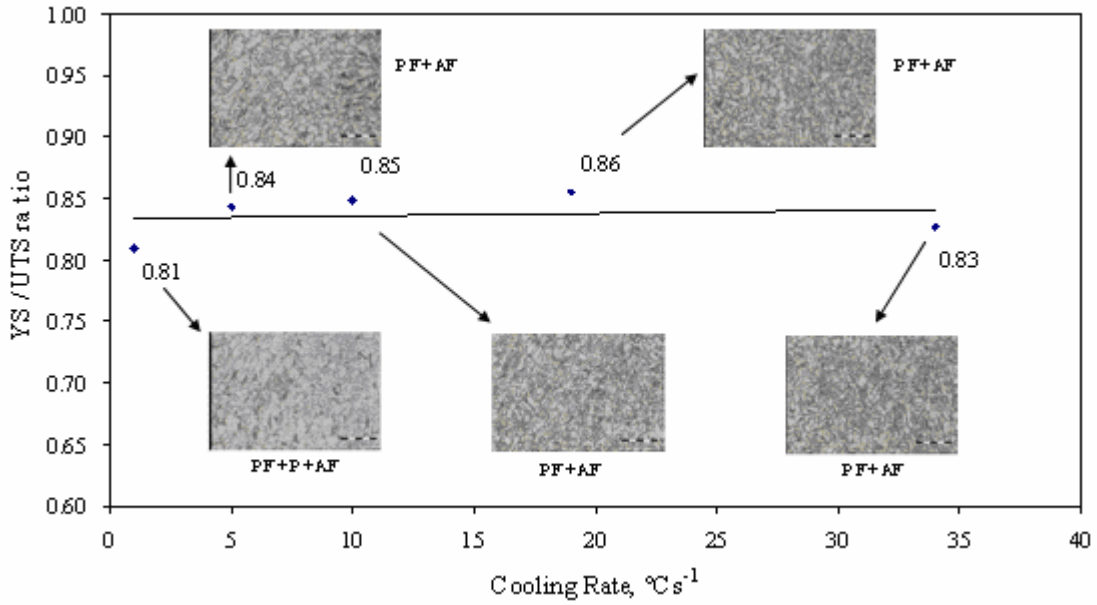

Figure 9.15 Effect of the cooling rate on the YS/UTS ratio of the reference alloy #6 after prior deformation of 33 % reduction in the austenite below the T_{nr}, cooling to 575 ºC at different cooling rates and simulation the coiling at 575 ºC for 1 hour. PF-polygonal ferrite, AF-acicular ferrite and P-pearlite.

Comparing the two cases, in the first case without prior deformation (figure 9.12), a high cooling rate introduces more dislocations into the microstructures because of the acicular ferrite or bainite microstructures which undergo displacive transformation from the austenite. The effect of any difference in dislocation density between a low and a high cooling rate, however, decreased thereafter due to the 60 minutes coiling simulation at 575 ºC, in spite of the fact that a higher dislocation density had initially been introduced by the high cooling rate. In other words, the coiling process decreases the effects of any initial difference in dislocation density in the microstructures caused by low and high cooling rates.

In the case of the prior deformed alloy (figure 9.15), the dislocations are not only from the high cooling rate, but also from the prior deformation. However, the dislocations introduced from the deformation in the austenite do not lead directly to a higher dislocation content in the acicular ferrite, but it does induce a finer (one pass deformation at 1050 ºC above the T_{nr}) and flattened (two passes deformation at 900 and 860 ºC, respectively, below the T_{nr}) austenite grain size that will provide a high nucleation rate of the acicular ferrite during the transformation, leading to a finer

ferrite grain size. The yield strength is sensitive to ferrite grain size[28,172] through the Hall-Petch relationship[174], whereas the ultimate tensile strength is not as sensitive to the grain size[28]. All of these can increase the obstacles for the commencement of plastic deformation and will result in a high yield strength of the steel. Therefore, the YS/UTS ratio could be raised by deformation as it is sensitive to deformation.

Thus, it can be concluded that:

- The YS/UTS ratio was found to be only sensitive to cooling rate or the transformed microstructures in the case without any prior deformation and simulated coiling at 575 and 600 ºC;
- Varying the coiling temperature at 575 and 600 ºC did not affect the YS/UTS ratio but coiling in general diminishes the effect of cooling rate on this ratio;
- Coiling decreases the YS/UTS ratio in the case without prior deformation; and
- A prior deformation of 33% below the T_{nr} in the austenite strongly increases the YS/UTS ratio at all cooling rates from 1 to 34 $^{o}Cs^{-1}$ and overshadows the effect of microstructure or cooling rate.

9.3.4 The effect of acicular ferrite on the ratio of yield strength to ultimate tensile strength

The relationship between the volume fraction of acicular ferrite and the YS/UTS (longitudinal specimens) is shown in figure 9.16. The volume fraction of acicular ferrite was measured on the experimental alloys #1 to #5 after laboratory hot rolling with an 86% reduction and cooling at a rate of 47 $^{o}Cs^{-1}$. These microstructures revealed mainly acicular ferrite mixed with some polygonal ferrite. It appears that the YS/UTS ratio was not markedly influenced by the quantity of acicular ferrite, although the range over which the AF content could be varied, was very limited. This observation is not in agreement with results of other researchers[173] that reported that there is a high density of mobile dislocations in acicular ferrite which result in a high work hardening rate and this lowers the number of obstacles for the commencement of plastic deformation. For instance, Kim has found[172] that increasing the volume fraction of acicular ferrite or bainite is useful to lower the YS/UTS ratio. Tither[173] has also reported that dominating acicular ferrite in a microstructure of line pipe steel could result in a large work hardening rate.

Summarising the above results, it is concluded that varying the acicular ferrite content from both undeformed and deformed austenite in these alloys was not measurably beneficial to lower the YS/UTS ratio, at least not in the quantities used here. An unresolved question remains, however, whether the effect of the quantity of acicular ferrite amount is weaker than that of a prior deformation in austenite? This needs further study with larger variations in the quantity of acicular ferrite than was found possible here.

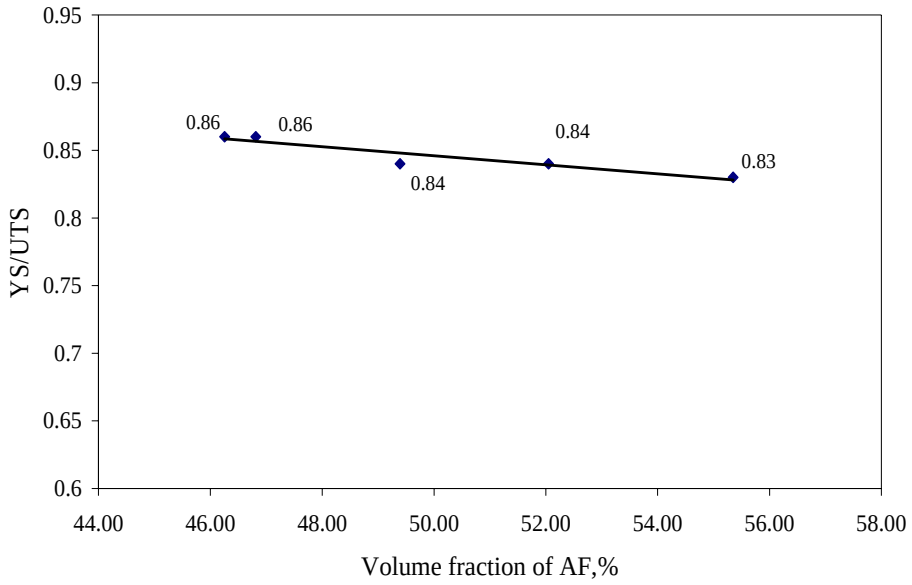

Figure 9.16 Relationship between the YS/UTS ratio (longitudinal specimens) and the measured volume fraction of acicular ferrite in the experimental alloys #1 to #5 after laboratory hot rolling with an 86% reduction in total and rapid cooling at a rate of 47 $^{o}Cs^{-1}$.

CHAPTER 10 CONCLUSIONS

The objective of this study was to establish the relationship between micro-alloying elements, the microstructure and process variables such as cooling rate, prior deformation in the austenite and coiling conditions, on the ratio of YS/UTS and other mechanical properties. Therefore, a study was undertaken on the austenite to acicular ferrite transformation with particular emphasis on the kinetics of the acicular ferrite formation and as affected by the above process variables. The following conclusions could be drawn from the present study:

9.1: The type of undissolved particles are mainly (Ti,Nb)(C,N) and Ti(C,N) after reheating at 1225 ºC for 120 minutes and the smallest size of 46 nm was found in the Nb-Ti-containing reference alloy #6. The volume fraction of undissolved particles decreased with increasing reheating temperatures as follows:

$f_v = 10^{-6} T^2 - 0.0038T + 3.2258$ $R^2=0.97$ for 15 minutes soaking time

$f_v = 10^{-6} T^2 - 0.0043T + 3.3251$ $R^2=0.99$ for 60 minutes soaking time

$f_v = 4\times10^{-6} T^2 - 0.0103T + 6.862$ $R^2=0.97$ for 120 minutes soaking time

9.2: The austenite grain size increased with increasing austenitisation temperature and soaking time. For alloy #6, however, the effect of the temperature is larger than the effect of soaking time. When the temperature reaches above 1225 ºC, coarsening of the particles sets in.

9.3: The non-recrystallisation temperature (T_{nr}) for the Mo-free reference alloy #6 was affected by the pass strain and the inter-pass time. These relationships between the T_{nr} and the pass strain ε and the inter-pass time t_{ip} can be described by the following respective equations:

$$T_{nr} = -210\,\varepsilon + 972$$

$$T_{nr} = 961 t_{ip}^{-0.0128}$$

9.4: The strain-free and strain affected CCT diagrams for alloy #5 (with 0.22% Mo) and alloy #6 (Mo-free), have shown that molybdenum additions can shift the acicular ferrite region on the strain-free CCT diagram to longer times and expand the region

for the formation of acicular ferrite. The dominant microstructures with no deformation in the austenite, were found to have changed from polygonal to an acicular ferrite microstructure and bainite with increasing cooling rate. A 45% deformation in the austenite below the T_{nr} is beneficial to acicular ferrite formation as the deformation promoted the nucleation of an acicular ferrite microstructure and hindered the growth of its constituents at the same time, and substantially suppressed the transformation to bainite. The effect of molybdenum additions on acicular ferrite transformation in these steels is overshadowed by the stronger effect of the prior deformation in alloys #5 (with 0.22% Mo) and the Mo-free reference alloy #6.

9.5: The transformed microstructures of all alloys were found to be a mixture of polygonal ferrite plus an acicular ferrite microstructure. The technique of TEM examination of shadowed carbon extraction replicas was found to be a superior method to identify these microstructures, rather than optical microscopy and SEM.

9.6: The acicular ferrite microstructure in the present study was found to have a lath morphology with two types: parallel laths and interwoven laths but with the more typical one of parallel laths. A high density of dislocations was found inside the laths. However, no cementite was observed between laths and within the laths. The nucleation sites for acicular ferrite were often oxide and sulphide inclusions with mostly round shape and the observed sizes of these inclusions ranged from 0.35 to 2.2 μm.

9.7: The YS/UTS ratio ranged from 0.83 to 0.86 for the alloys with microstructures of polygonal ferrite plus acicular ferrite after hot rolling and rapid cooling. However, an acicular ferrite microstructure or bainite was found to be not beneficial in lowering the YS/UTS ratio. This ratio was only sensitive to the microstructure or the cooling rate in the case with no prior deformation and without any simulated coiling process. The YS/UTS, yield strength and ultimate tensile strength by themselves, however, were not sensitive to the cooling rate after a simulated coiling process.

9.8: Varying the temperature of the coiling process between 575 and 600 ºC did not affect the YS/UTS ratio and the simulated coiling process itself diminished the effect

of cooling rate and decreased the ratio in the case with no prior deformation.

9.9: Prior deformation with a 33% reduction below the T_{nr} in the austenite strongly increased the YS/UTS ratio at all cooling rates from 1 to 34 $^{o}Cs^{-1}$ and overshadowed the effect of microstructures or cooling rate on this ratio.

9.10: Molybdenum additions to Nb-Ti micro alloyed steels did not markedly affect the YS/UTS ratio after a simulated coiling process.

CHAPTER 11 RECOMMENDATIONS FOR FUTURE WORK

1. The influence of the strain rate on the non-recrystallisation temperature in torsion tests at higher strain rates of more than 2.5 s^{-1}, to simulate strip rolling mill strain rates more closely.
2. The use of selected area diffraction pattern analysis and misorientation measurements on acicular ferrite lath structures in thin foil TEM work to determine whether the parallel laths have the same crystal orientation and or habit planes.
3. More thin foil TEM work to confirm the role played by non-metallic inclusions as the preferred nucleation sites for acicular ferrite.
4. Larger variations in the quantity of acicular ferrite in these steels to study the effect of this on the YS/UTS ratio by changing the cooling rate after hot rolling or changing the parameters of the hot rolling schedule.

References

1. M. Pontremoli et al: Met. Tech., Nov.,11(1984), pp504-514

2. J.G. Williams et al: Micro alloying ’95 Conference Proceeding, pp117-139

3. Jon P. Orton: Micro-alloying 75 Proceedings, Publ. Union Carbide Corp., Washington, D.C. USA, 1977, pp334-347

4. Ming-Chun Zhao, Ke Yang, Fu-Ren Xiao and Yi-Yin Shan: Mater. Sci. Eng., A355 (2003), pp126-136

5.William Roberts: Conference Proceedings of International Conference on Technology and Applications of HSLA Steels, American Society for Metals, Metals Park, Ohio 44073, 3 - 6 Oct., 1983, pp33-65

6. J.G. Williams et al: Materials Forum, 20(1996), pp13-28

7. R. Mendoza and M. Alanis et al: Mater. Sci. Eng., A337(2002), pp115-120

8. Andreas Kern, Joachim Degenkolbe, Bruno Musgen and Udo Schriever: ISIJ Int., 32(3)(1992), pp387-394

9. Min-Chun Zhao, Ke Yang and Yi-Yin Shan: Mater. Sci. Eng., A335(2002), pp14-20

10. Akihiko Takahashi and Makio Iino: ISIJ Int., 36(2)(1996), pp235-240

11. N.J. Kim: Journal of Metals, April (1983), pp21-27

12. J.J.Withfield: Options for manufacturing X70-X80 line pipe, Internal report ISCOR (new Mittal Steel (SA)), South Africa, (1998)

13. C.S. Chiou et al: Materials Chemistry and Physics, 69(2001), pp113-124

14. Yu Matrosov: Metal Science and Heat Treatment of Metals, Issue 28, 3-4(1986), pp173-180

15. C.O.I.Emenike and J.C.Billington: Mater. Sci. and Tech., May, 5(1989), pp450-456

16. Matrosov, Yu: Metal Science and Heat Treatment (English) Translation of Metallovedenie i Termicheskaya Obrabotka, Issue 11-12, Nov-Dec., 26(1984), pp798-807

17. W.P.Sun, M.Militzer, D.Q.Bai and J.J.Jonas: Acta Metall. Mater., 41(1993),

pp3595-3604

18. S.F.Medina: Mater. Sci. Tech., 14(1998), pp217-221
19. S.F.Medina and J.E.Mancilla: Acta Metall. Mater., 42(1994), p3945-3951
20. M.G.Mecozzi, J.Sietsma and S.van der Zwaag: Acta Materialia, 54(2006), pp1431-1440
21. P.Cizek, B.P.Wynne, C.H.J.Dvies, B.C.Muddle, P.D.Hodgson: Metall. Mater. Trans., A, 33A(2002), pp1331-1349
22. A.I. Fernandez et al: Mater. Sci. Eng., A361(2003), pp367-376
23. C.I.Smith, R.R.Preston and N.L.Richards: Met. Tech., 5(1978), pp341-350
24. F. Heisterkamp AND k.hULKA: Metals Tech., Dec.,11(1984), pp535-544
25. B.de.Meester: ISIJ Int. 37(6) (1997), pp537-551
26. D.Dormagen: Steel Res., 59(8) (1988), pp368-374
27. J.J.Jonas and I.Weiss: Met. Sci., 13(1979), pp238-245
28. S.N.Prasad, D.S.Sarma: Mater. Sci. Eng., A408(2005), pp53-63
29. S.F.Medina, M.Chapa, P.Valles, A.Quispe and M.I.Vega: ISIJ Int., 39(9)(1999), pp930-936
30. T.J.George and N.F.Kennon: Aust. Inst. Met., 17(1972), pp73-80
31. T.George and J.J.Irani: J. Aust. Inst. Met., 13(1968), pp94-106
32. Kong Junhua, Zhen Lin, Guo Bin, Li Pinghe, wang Aihua and Xie Changsheng: Materials and design, 25(2004), pp723-728
33. Michel L. Lafrance, Francis A Caron and Guy R. Lamant “use of Microalloyed Steels in the Manufacture of Controlled Rolled Plates for Pipe” Micro-alloying 75 Proceedings, Publ. Union Carbide Corp., Washington, D.C. USA, 1977, pp367-374
34. He Kejian and T.N. Baker: Mater. Sci. Tech., Dec.,8(1992), pp1082-1089
35. C.O.I.EMENIKE: J. Mater. Sci. Letters, 9(1990), pp406-409
36. P.D. Hodgson et al: ISIJ Int., 32(12)(1992), pp1329-1338
37. Shuji OKAGUCHI and Tamotsu HASHIMOTO: ISIJ Int., 32(3)(1992), pp283-290

38. C.O.I. Emenike: Pipes & Pipelines International, Nov. - Dec., (1988), pp15-22

39. Atsuhiko YOSHIE, Masaaki Fujioka, Yoshiyuki Watanabe, Kiyoshi and Hirofumi Morikawa: ISIJ Inter., 32(3)(1992), pp395-404

40. Ming-Chun Zhao, Ke Yang and Yi-Yin Shan: Materials Letters, 57(2003), pp1496-1500

41. A.M. Sage : Metals Technology , March (1981), pp94-102

42. C.O.I. Emenike et al: Pipes & Pipelines International Jan. - Feb. (1990), pp24-27

43. Sunghak Lee, Dongil Kwon, Young Kook Lee and Ohjoon Kwon: Metall. Mater. Trans. A, May, 26A(1995), pp1093-1100

44. M. Charleux et al: Metall. Mater. Trans. A, July, 32A(2001), pp1635-1647

45. A.Yoshie and M.Fujioka: ISIJ Int. 32(1992), pp395-404

46. J.J.Withfield: Thermo-mechanical Processing, Report number: TMP98/040, Internal report, ISCOR (new Mittal Steel (SA)), South Africa, (1998)

47. S.F.Medina and A.Quispe: Mater. Sci. Tech., June, 16(2000), pp635-642

48. D.Q. Bai et al: ISIJ Int., 36(8) (1996), pp1084-1093

49. C. Ouchi et al: ISIJ. Int., 20 (1980), pp833-842

50. H.L. Andrade, M.G. Akben, and J.J. Jonas: Metall. Trans. A, Oct, 14A(1983), pp1967-1977

51. S.S.Babu and H.K.D.H. Bhadeshia: Mater. Sci. Eng., A156(1992), pp1-9

52. F.J.Barbaro, P.Kraulis, K.E.Easterling: Mat. Sci. Tech., 5(1989), pp1057-1068

53. A.O.Kluken, O.Grong and G.Rorvik: Metall. Trans. A, 21A(1990), pp2047-2058

54. J.M.Gregg and H.K.D.H.Bhadeshia: Acta Mater., 45(1997), pp739-748

55. F.Ishikawa and T.Takahashi: ISIJ Int., 35(1995), pp1128-1133

56. F.Ishikawa, T.Takahashi and T.Ochi: Metall. Mater. Trans., A, 25A(1994), pp929-936

57. S.Ohkita, H.Homma, S.Tsushima and N.Mori: Aus. Welding J., (1984), pp29-36

58. S.Liu and D.L.Olson: Weld. J., 65(1986), pp139s-149s

59. D.W.Oh, D.L.Olson and R.H.Frost: Weld. J., 69(1990), pp151s-158s

60. R.B.Oldland: Aust. Weld. Res., 14(1985), pp44-56

References

61. G.M.evans: Weld. J., 70(1991), pp32s-39s

62. H.Terashima and P.H.M.Hart: Weld. J., 63(1984), pp173s-182s

63. S.Ohkita, H.Homma, S.Tsushima and N.Mori: Aust. Weld. J., 29(1984), pp29-36

64. A.G.Glover, J.T.McGRATH, M.J.Tinkler and G.C.Weatherly: Weld. J., 56(1977), pp267s-273s

65. M.Diaz-Fuentes, I.Madariaga and I.Gutierrez: Materials science Forum, 284-286, (1998), pp245-252

66. I.Madariaga and I.Gutierrez: Materials science Forum, 284-286(1998), pp419-426

67. M.A.Linaza, J.L.Romero. J.M.Rodriguez-Ibabe and J.J.Urcola: Scripta Metall. Mater., 29(1993), pp1217-1222

68. M.A.Linaza, J.L.Romero. J.M.Rodriguez-Ibabe and J.J.Urcola: Scripta Metall. Mater., 32(1995), pp395-400

69. I.Madariaga and I.Gutierrez: Scripta Mater., 37(8), (1997), pp1185-1192

70. I.Madariaga, J.L.Romero and I.Gutierrez: Metall. Trans., 29A(1998), pp1003-1015

71. S.Hoekstra, M.A.Munnigschmidt-van der Berg and G.Denouden: Met. Contr., 18(12) (1986), pp771-775

72. S.W.Thompson, D.J.Colvin and G.Krauss: Metall. Tran. A, 21A(1990), pp1493-1507

73. Ming-chun Zhao, Ke Yang and Yi-Yin Shan : Mater. Sci. Eng., A335 (2002), pp 14-20

74. A.A.B. Sugden and H.K.D.H Bahadeshia: Metall. Trans. A, Sept, 20A(1989), pp1811-1818

75. Madariaga, I. Gutierrez and H.K.D.H. Bhadesia: Metall. Mater. Trans. A, Sept, 32A(2001), pp2187-2197

76. C.H. Lee and H.K.D.H. Bhadeshia: Mater. Sci. Eng., A360(2003), pp249-257

77. J.R.Yang and H.K.D.H.Bhadeshia: Mater. Sci. Tech., 5(1989), pp93-97

78. M. Diaz-Fuentes et al: Mater. Sci. Eng., A363(2003), pp316-324

79. J.M.Gregg and H.K.D.H.Bhadeshia: Acta Mater., 45(2)(1997), pp739-748

80. A.A.B.Sugden and H.K.D.H.Bhadeshia: Metall. Trans.A, 20A(1989), pp1811-1818

81. J.G.Garland and P.R.Kirkwood: Met. Constr., 7(5), (1975), pp275-283

82. R.A.Farrar and P.L.Harrison: J. Mater. Sci., 22(1987), pp3812-3820

83. T. Mohandas and GM.Reddy: J. Mater Process Techol., 69(1-3)(1998), pp222-226

84. K.Yamamoto, T.Hasegawa and J.Takamura: ISIJ Int., 36(1996), pp80-86

85. M.Ferrante and R.A.Farrar: J. Mater. Sci., 17(1982), pp3293-3298

86. D.J.Abson and R.E.Dolby: Weld. Inst.Res. Bull., 19(1978), pp202-207

87. R.A.Ricks, P.R.Howell and G.S.Barritte: J. Mater. Sci., 17(1982), pp2218-2226

88. S.A.Court and G.Pollard: Metallography, 22(1989), pp219-243

89. R.C.Cochrane: Weld. World, 21(1983), pp16-24

90. R.A.Ricks, P.R.Howell and G.S.Barritte: J. Mater. Sci., 17 (1982), pp732-740

91. J.M.Chilton and M.J.Roberts: Metall. Trans. A, 11A(1980), pp1711-1721

92. Simith Ye, Coldren AP and Cryderman RL: Met. Sci. Heat Treat., 18(1-2)(1976), pp59-65

93. Tomo Tanaka: "Bauschinger Effect during Pipe-forming Operations", Micro-alloying 75 Proceedings, Publ. Union Carbide Corp., Washington, D.C. USA, 1977, pp350-352

94 Franz M. Oberhauser: "Bauschinger effect under Multi-axial Loading Conditions", Micro-alloying 75 Proceedings, Publ. Union Carbide Corp., Washington, D.C. USA, 1977, pp349-349

95. M. Grumach: "Influence of work hardening and Bauschinger effect on plate-to-pipe yield-strength differences", Micro-alloying 75 Proceedings, Publ. Union Carbide Corp., Washington, D.C. USA, 1977, pp348-348

96. Tetsuo Yamaguchi: "Relative Importance of Work Hardening and Bauschinger Effect on Strength during Pipe Forming" Micro-alloying 75 Proceedings, Publ. Union Carbide Corp., Washington, D.C. USA, 1977, pp352-353

References

97. Waldo Stumpf: Class notes on Phase Transformations in Metals and Their Alloys, University of Pretoria, RSA, (2003), p1.9-12, p5.1-1, p5.15-2, p8.1-10, p11.7-3

98. M.F.Ashby and R.Ebeling: Transactions of the Metallurgical Society of AIME, Oct, 236(1966), pp1396-1404

99. D.R.Barraclough and C.M.Sellar: Met. Sci., 13(1979), pp257-267

100. M.J.Luton, R.A.Petkovie and J.J.Jonas: Acta Metall., 28(1979), pp729-743

101. G.G.Glover and C.M.Sellars: Metall. Trans., 4(1973), pp765-775

102. R.A.P.Djaic and J.J.Jonas: Metall. Trans., 4(1973), pp621-625

103. Y.Iwahashi, Z.Horita, M.Nemoto and T.G.Langdon: Acta Mater., 45(1997), pp4733-4741

104. S.F.Medina A.Quispe, P.Valles and J.L.Banos: ISIJ Int., 39(1999), pp913-922

105. A.Quispe, S.F.Medina and P.Valles: ISIJ Int., 37(1997), pp783-788

106. S.S.Hansen, J.B.Vandersande and M.Cohen: Metall. Trans. A, 11A(1980), pp387-402

107.A.LeBon, J.Rofes-Vernis and C.Rossard: Met. Sci., 9(1975), pp36-40

108. T.Sakai and J.J.Jonas: Acta Metall., 32(1984), pp189-209

109. G.Gottstein and U.F.Kocks: Acta Metall., 31(1983), pp175-188

110. A.Belyakov, R.Kaibyshev and T.Sakai: Metall. Trans. A, 29A(1998), pp161-167

111. W.P.Sun, M.Militzer and J.J.Jonas: Metall. Trans. A, 23A(1992), pp3013-3023

112. I.Weiss and J.J.Jonas: Metall. Trans. A, 11A(1980), pp403-410

113. J.G.Speer and S.S.Hansen: Metall. Trans. A, 20A(1989), pp25-38

114. L.J. Cuddy: Metall. Trans., A, 12A(1981), pp1313-1320

115. C.M.Sellars and J.A.Whiteman: Metal Sci., 13(1979), pp187-194

116. L.J.Cuddy: Metall. Trans. A, 15A(1984), pp87-98

117. L.N.Pussegoda, S.yue, and J.J.Jonas: Metall. Trans. A, 21A(1990), pp153-164

118. L.N.Pussegoda and J.J.Jonas: ISIJ. Int., 31(3)(1991), pp278-288

119. F.H.Samuel, S.Yue, J.J.Jonas, and B.A.Zbinden: ISIJ. Int., 29(10)(1989), pp 878-886

120. F.H.Samuel, S.Yue, J.J.Jonas, and K.R.Barnes: ISIJ. Int., 30(3)(1990),

pp 216-225

121. S.Yue and J.J.Jonas: Mater. Forum, 14(1990), pp245-252

122. K.J. Irvine, F.B.Pickering, and T.Gladman: J. Iron Steel Inst., 205(1967), pp161-182

123. B.Dutta and C.M.Sellars: Mater. Sci. Tech., 3(1987), pp197-206

124. A.Laasraoui and J.J.Jonas: Metall. Trans. A, 22A(1991), pp151-160

125. D.Q.Bai, S.Yue, W.P.Sun and J.J.Jonas: Metall. Trans. A, Oct, 24A(1993), pp2151-2159

126. G.K.Prior: Materials Forum, 18(1994), pp265-276

127. T.Mukherjee, W.E.Stumpf and C.M.Sellars: J. of Mater. Sci. 3(1968), pp127-135

128. L.J.Cuddy, J.J.Bauwin and J.C.Raley: Metall. Trans. A, 11A(1980), pp381-386

129. M.G.Akben, I.Weiss, and J.J.Jonas: Acta Met., 29(1981), pp111-121

130. A.Le. Bon,J.Rofes-Vernis and C.Rossard: Metal Sci., 9(1975), pp36-40

131. Furen Xiao, Bo Liao Deliang Ren, Yiyin Shan and Ke yang: Materials Characterization, 54 (2005), pp205-314

132. P.H.Shipway and H.K.D.H.Bhadeshia: Mater. Sci. Tech., 11(1995), pp1116-1128

133. S.B.Singh and H.D.K.H. Bhadeshia: Mater. Sci. Tech., 12 (1996), pp610-612

134. G.I.Rees and H.K.D.H.Bhadeshia: Mater. Sci. Tech., May, 10(1994), pp353-358

135. V.Biss and R.L.Cryderman: Metall. Trans., 2(1971), pp2267-2276

136. S.S.Babu and H.K.D.H.Bhadeshia: Mater. Sci. Tech., 6(1990), pp1005-1020

137. H.K.D.H.Bhadeshia, L.E.Svensson and B.Gretoft: Acta Metall., 33(1985), pp1271-1283

138. J.G.Garland and P.R.Kirkwood: Met. Constr., 7(6)(1975), pp320-330

139. H.K.D.H.Bhadeshia: Scripta Metall., 21(1987), pp1017-1022

140. P.L.Mangonon: Metall. Trans. A, 7A (1976), pp1389-1400

141. Z.Zhang and R.A.Farrar: Mater. Sci. Tech., 12(1996), pp237-260

142. A.R.Mills, G.Thewlis and J.A.Whiteman: Mat. Sci. Tech., 3(1987),

pp1051-1061

143. P.L.Harrison and R.A.Farrar: J. Mater. Sci., 16(1981), pp2218-2226

144. J.M.Dowling J.M.Corbett and H.W.Kerr: Mettal. Trans. A, 17A(1986), pp1611-1623

145. G.M.Evans: Weld. J., 71(1992), pp447s-454s

146. T.Funakoshi, T.Tanaka, S.Ueda, M.Ishikawa, N.Koshizuka and K.Kobayashi: Transactions ISIJ., 17(1977), pp419-427

147. A.R.Bhatti, M.E.Saggese, D.N.Hawkins, J.A.Whiteman and M.S.Golding: Welding Journal, 63(1984), pp224s-230s

148. G.M.Evans: Weld. J., 72(1993), pp123s-133s

149. T.N.North, H.B.Bell, A.Koukabi and I.Craig: Welding Journal, 58(1979), pp343s-354s

150. S.G.Court and G.Pollard: J. Mater. Sci. Letters, 4(1985), pp427-430

151. J.E.Harbottl and S.B.fisher: Nature, 299(1982), pp139-140

152. E.S.Kayali, I.M.Corbett and H.W.Kerr: J. Mater. Sci. Letters, 2(1983), pp123-128

153. G.S.Barritte and D.V.Edmonds: "Advances in the Physical Metallurgy and Applications of Steel", 1982, London, The Metals Society, pp126-135

154. B.Ralph: Mater. Sci. Tech., 6(1990), pp1139-1144

155. D.J.Abson: weld World, 27(1989), pp76-100

156. G.Thewlis: Join. Mater., 2(1989), pp25-32

157. G.Thewlis: Join. Mater., 2(1989), pp125-129

158. A.R.Bhatti, M.E.Saggese, D.N.Hawkins, J.A.Whiteman and M.S.Golding: Weld. J., 63(1984), pp224s-230s

159. I.Madariaga and Gutierrez: Acta Mater., 47(3), (1999), pp951-960

160. G.M.Evans: Met. Constr., 18(1986), pp631R-636R

161. R.D.Doherty: Mater. Sci. Eng., A238(1997), pp219-274

162. J.D.Embury: Met. Trans., 16A (1985), pp2191-2200

163. C.García de Andres, C.Capdevila, I.Madariaga and I.Gutierrez: Scripta

Materialia, 45(2001), pp709-716

164. Pavel Morcinek: Micro-alloying 75 Proceedings, Publ. Union Carbide Corp., Washington, D.C. USA, 1977, pp272-278

165. E.C.Hamre and A.M.Gilroy-Scott: Micro-alloying 75 Proceedings, Publ. Union Carbide Corp., Washington, D.C. USA, pp375-381

166. C.Y.huang, J.R.Yang and S.C.Wang: Mater. Trans., JIM, 34(1993), pp658-668

167. R.H.Edwards and N.F.Kennon: Metall. Trans. A, 9A(1978), pp1801-1809

168. R.Freiwillig, J.kudraman and P.chraska: Metall. Trans. A, 7A(1976), pp1091-1097

169. O.Grong and D.K.Matlock: Int. Met.Rev., 31(1)(1986), pp27-44

170. E.S.Kayali, J.M.Corbett and H.W.Kerr: J. Mater. Sci. Lett., 2(1983), pp123-128

171. P.H.Shipway and H.K.D.H.Bhadeshia: Mater. Sci. Eng., A223(1997), pp179-185

172. Y.M.Kim, S.K.Kim, Y.J.Lim and N.J.Kim: ISIJ Int., 42(12) (2002), pp1571-1577

173. G.Tither and M.Lavite: J. of Met. (JOM), (1975), p15-23

174. Waldo Stumpf: Class notes on Mechanical Metallurgy, University of Pretoria, South Africa, (2002), p3.3-11

Appendix A

Parameters of the laboratory hot rolling process

Table A-1 The hot rolling parameters for alloy #2

Pass No		R1	R2	reheating	R3	R4	R5	F1	reheating	F2	reheating	F3
Temperature (°C)	in	1165	1050	1225 5 min	1080	1030	990	910	930 5 min	880	930 5 min	890
	out											865
t_{ip} (s)		23	--		20	10	13	--		--		--
Gauge (mm)	in	43	37		28	20	13.6	10.3		8.3		6.9
	out	37	28		20	13.6	10.3	8.3		6.9		6
Pass ε		0.15	0.28		0.34	0.38	0.28	0.22		0.18		0.14
Total ε		1.43						0.54				
Reduction (%)		76						42				
$\dot{\varepsilon}$ (s^{-1})		1.67	2.43		3.15	3.92	4.00	4.07		4.00		3.89

Table A-2 The hot rolling parameters for alloy #3

Pass No		R1	R2	reheating	R3	R4	R5	F1	reheating	F2	reheating	F3
Temperature (°C)	in	1162	1043	1225 5 min	1045	1032	980	910	930 5 min	885	930 5 min	890
	out											861
t_{ip} (s)		24	--		18	12	18	--		--		--
Gauge (mm)	in	43	37		28	20	13.6	10.3		8.3		6.9
	out	37	28		20	13.6	10.3	8.3		6.9		6
Pass ε		0.15	0.28		0.34	0.38	0.28	0.22		0.18		0.14
Total ε		1.43						0.54				
Reduction (%)		76						42				
$\dot{\varepsilon}$ (s^{-1})		1.67	2.43		3.15	3.92	4.00	4.07		4.00		3.89

Table A-3 The hot rolling parameters for alloy #4

Pass No		**R1**	**R2**	**reheating**	**R3**	**R4**	**R5**	**F1**	**reheating**	**F2**	**reheating**	**F3**
Tempera-Ture (°C)	in	1165	1065	1225 5min	1082	1050	1000	910	930 5min	890	930 5min	889
	out											860
t_{ip} (s)		22	--		19	14	17	--		--		--
Gauge (mm)	in	43	37		28	20	13.6	10.3		8.3		6.9
	out	37	28		20	13.6	10.3	8.3		6.9		6
Pass ε		0.15	0.28		0.34	0.38	0.28	0.22		0.18		0.14
Total ε		1.43						0.54				
Reduction (%)		76						42				
$\dot{\varepsilon}$ (s^{-1})		1.67	2.43		3.15	3.92	4.00	4.07		4.00		3.89

Table A-4 The hot rolling parameters for alloy #5

Pass No		**R1**	**R2**	**reheating**	**R3**	**R4**	**R5**	**F1**	**reheating**	**F2**	**reheating**	**F3**
Tempera-ture (°C)	**in**	1148	1058	1225 5 min	1081	1020	1010	910	930 5 min	870	930 5 min	885
	out											857
t_{ip} (s)		22	--		17	13	23	--		--		--
Gauge (mm)	**in**	43	37		28	20	13.6	10.3		8.3		6.9
	out	37	28		20	13.6	10.3	8.3		6.9		6
Pass ε		0.15	0.28		0.34	0.38	0.28	0.22		0.18		0.14
Total ε		1.43						0.54				
Reduction (%)		76						42				
$\dot{\varepsilon}$ (s^{-1})		1.67	2.43		3.15	3.92	4.00	4.07		4.00		3.89

Table A-5 The hot rolling parameters for sample #M1-11 of alloy #6

Pass No		**R1**	**R2**	**R3**	**Rehea t-ing**	**R4**	**R5**	**R6**	**Rehea t-ing**	**F1**	**F2**	**Rehea t-ing**	**F3**
Tempera-ture (°C)	**in**	1140	1108	1008	1200 5 min	1085	940	901	1200 30 s	925	--	1200 60 s	920
	out										--		870
t_{ip} (s)		18	22	--		20	--	--		--	--		
Gauge (mm)	**in**	45	37	30		25	20	15		10	8.3		6.9
	out	37	30	25		20	15	10		8.3	6.9		6
Pass ε		0.196	0.21	0.182		0.223	0.288	0.405		0.186	0.18		0.14
Total ε		1.50							0.51				
Reduction (%)		78							40				
$\dot{\varepsilon}$ (s^{-1})		1.82	2.08	2.09		2.56	3.31	4.66		3.05	4.00		3.89

Appendix B
Curves of tensile tests

Conditions on the Gleeble:

Reheating temperature: 1225 ºC

No prior deformation and coiling simulation

Alloy #6

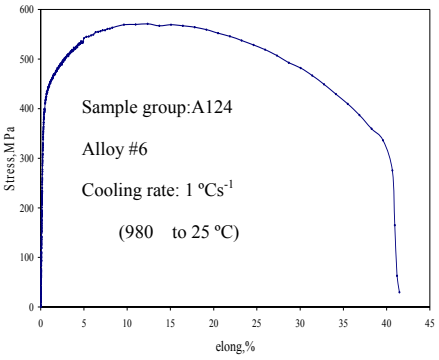

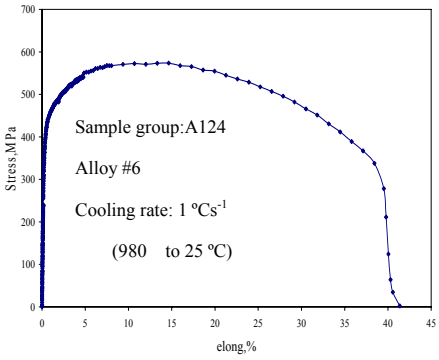

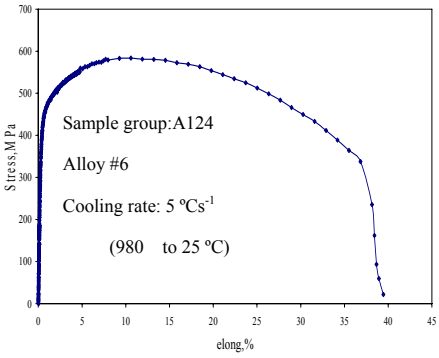

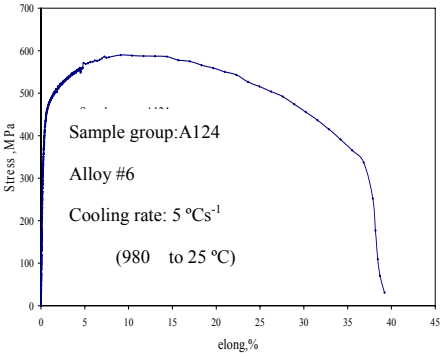

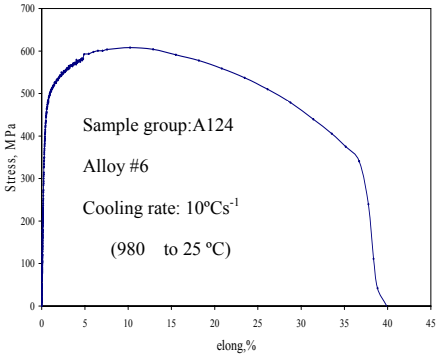

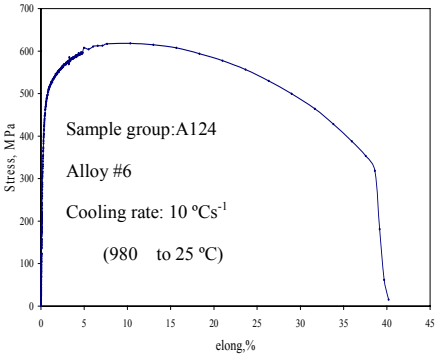

Appendix

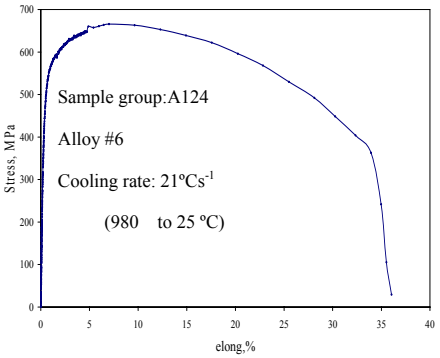
Sample group:A124
Alloy #6
Cooling rate: 21ºCs-1
(980 to 25 ºC)
Stress, MPa
elong,%

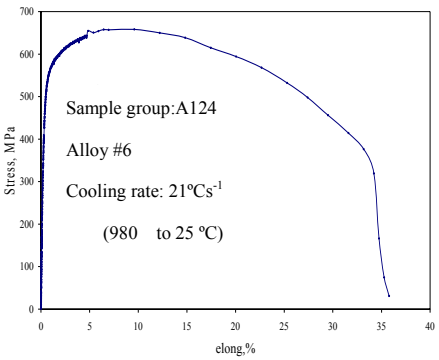
Sample group:A124
Alloy #6
Cooling rate: 21ºCs-1
(980 to 25 ºC)
Stress, MPa
elong,%

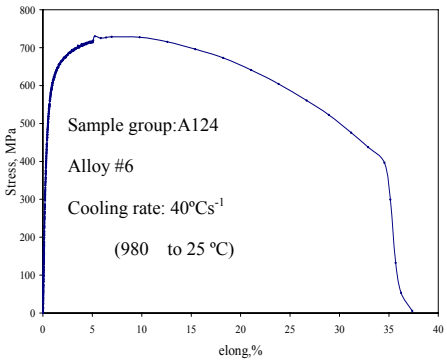
Sample group:A124
Alloy #6
Cooling rate: 40ºCs-1
(980 to 25 ºC)
Stress, MPa
elong,%

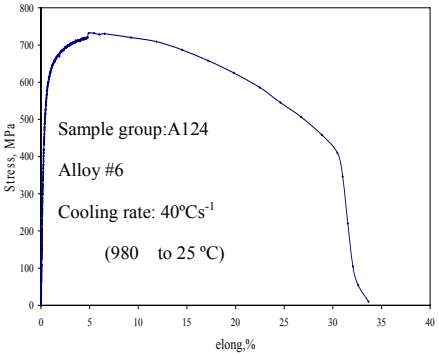
Sample group:A124
Alloy #6
Cooling rate: 40ºCs-1
(980 to 25 ºC)
Stress, MPa
elong,%

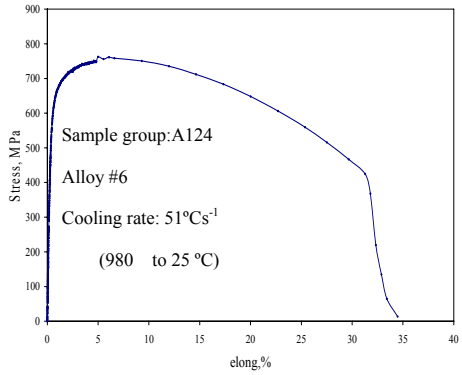
Sample group:A124
Alloy #6
Cooling rate: 51ºCs-1
(980 to 25 ºC)
Stress, MPa
elong,%

Appendix C
Curves of tensile tests

Conditions on the Gleeble:

Reheating temperature: 1225 ºC

No prior deformation and coiling simulation

Alloy #3

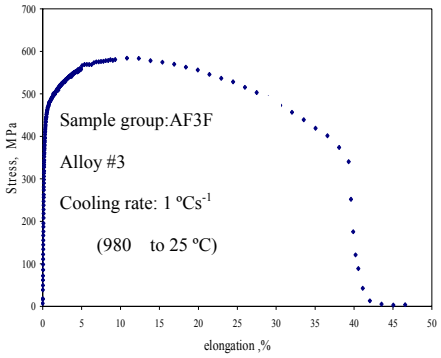

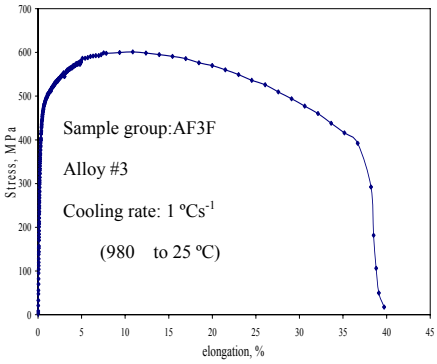

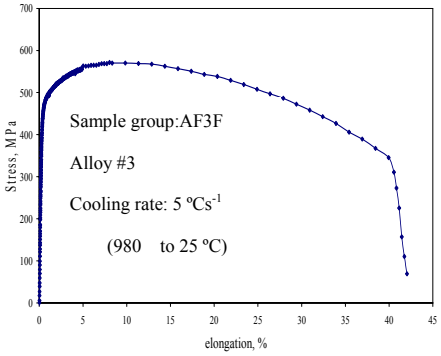

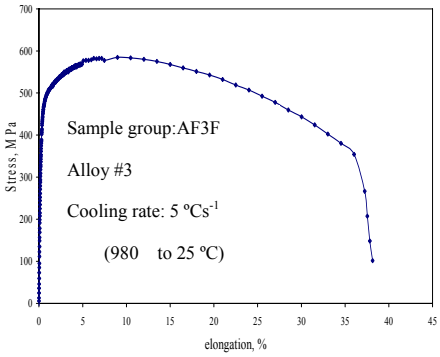

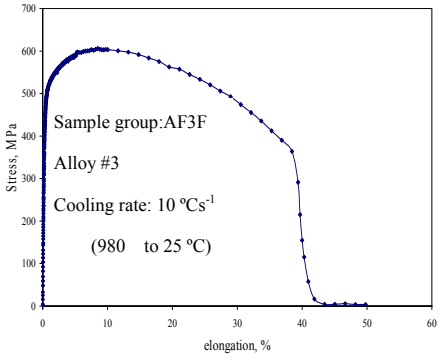

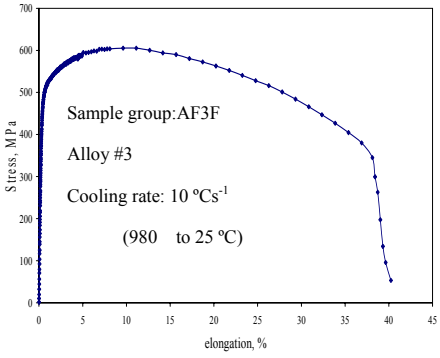

Appendix

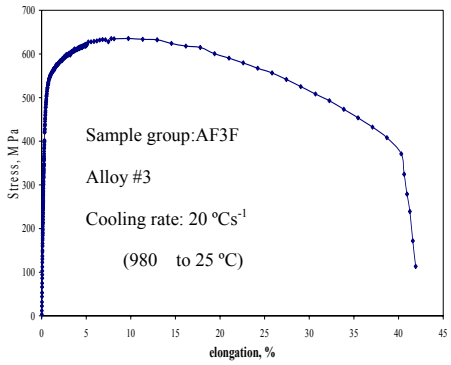
Sample group:AF3F
Alloy #3
Cooling rate: 20 ºCs-1
(980 to 25 ºC)
Stress, MPa
elongation, %

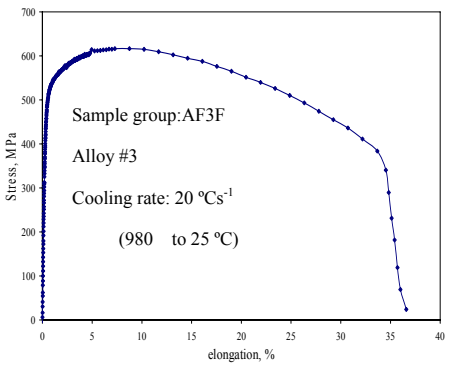
Sample group:AF3F
Alloy #3
Cooling rate: 20 ºCs-1
(980 to 25 ºC)
Stress, MPa
elongation, %

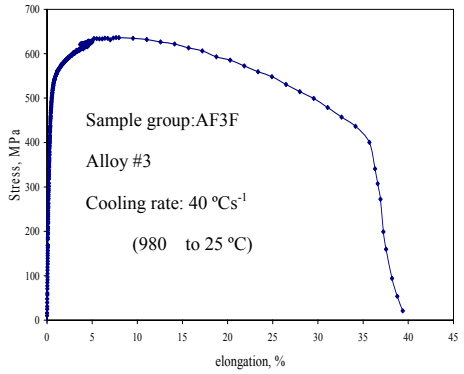
Sample group:AF3F
Alloy #3
Cooling rate: 40 ºCs-1
(980 to 25 ºC)
Stress, MPa
elongation, %

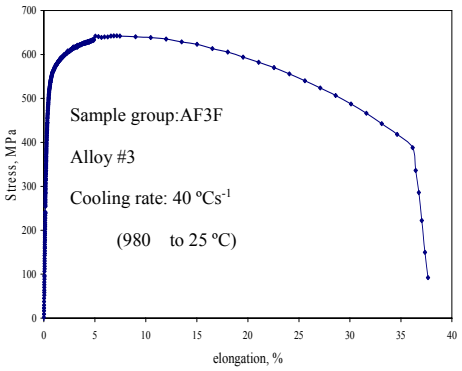
Sample group:AF3F
Alloy #3
Cooling rate: 40 ºCs-1
(980 to 25 ºC)
Stress, MPa
elongation, %

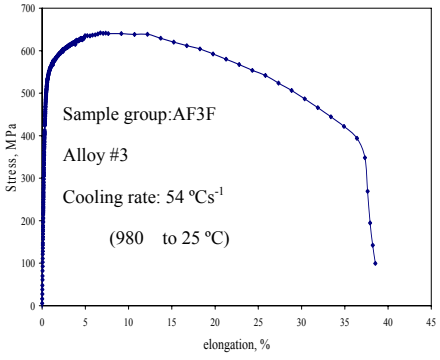
Sample group:AF3F
Alloy #3
Cooling rate: 54 ºCs-1
(980 to 25 ºC)
Stress, MPa
elongation, %

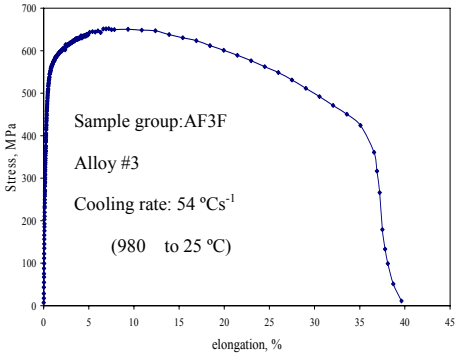
Sample group:AF3F
Alloy #3
Cooling rate: 54 ºCs-1
(980 to 25 ºC)
Stress, MPa
elongation, %

Appendix D
Curves of tensile tests

Conditions on the Gleeble:

Reheating temperature: 1225 ºC

Coiling at 600 º for 1 h

No prior deformation

Alloy #6

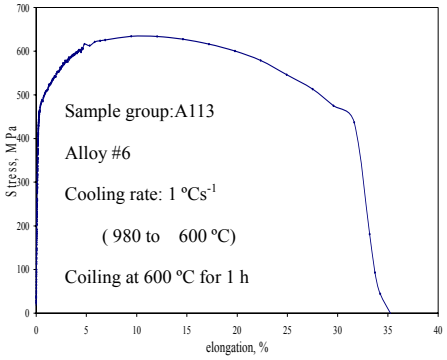

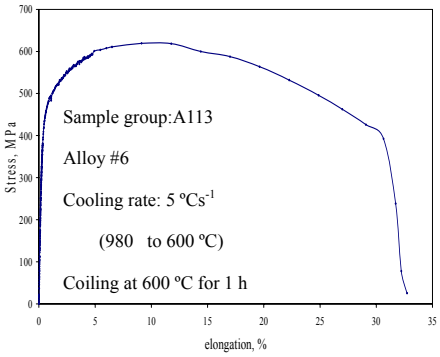

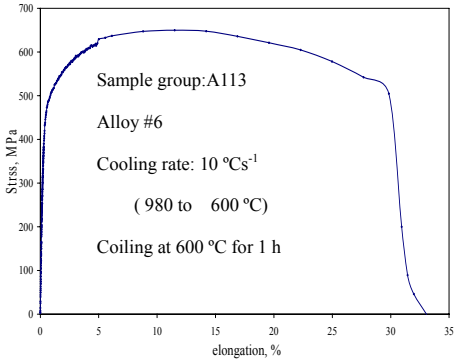

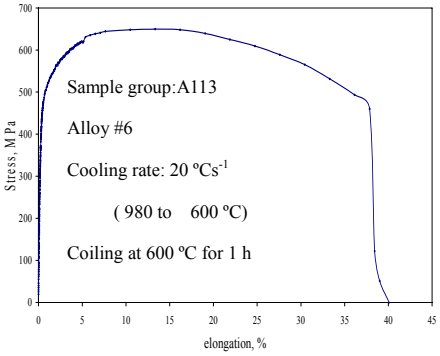

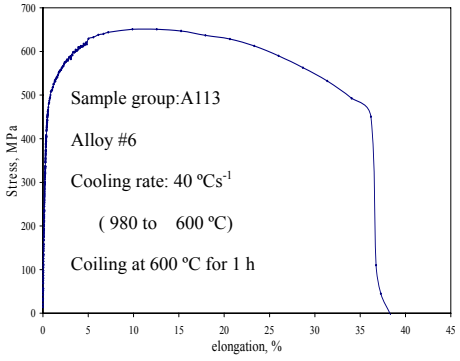

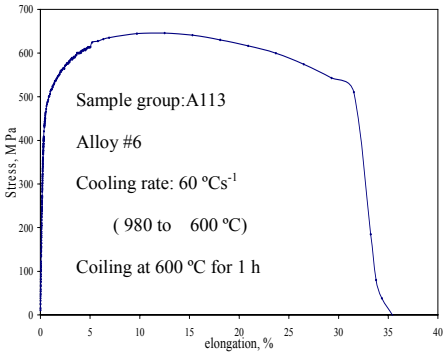

Appendix E
Curves of tensile tests

Conditions on the Gleeble:

Reheating temperature: 1225 ºC

Coiling at 575 º for 1 h

No prior deformation

Alloy #6

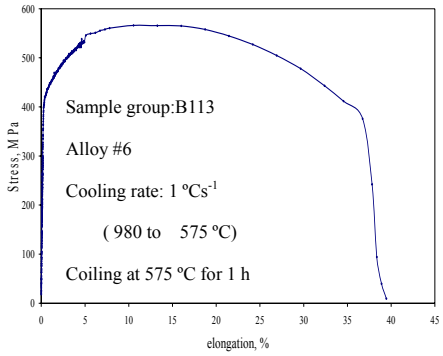

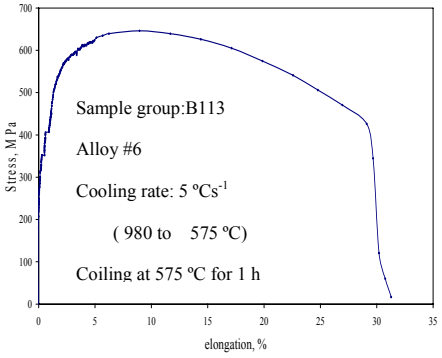

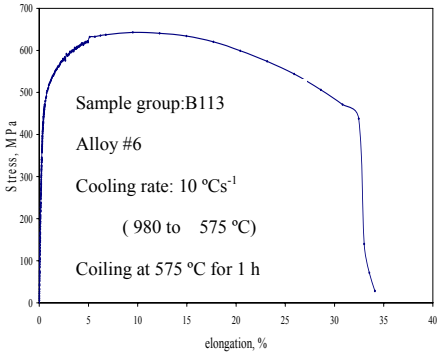

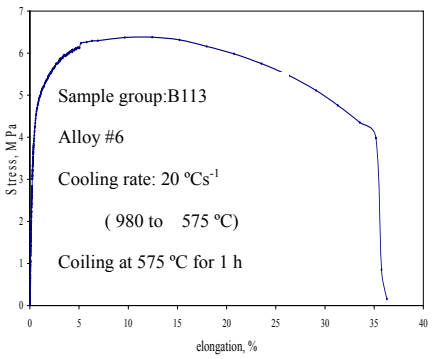

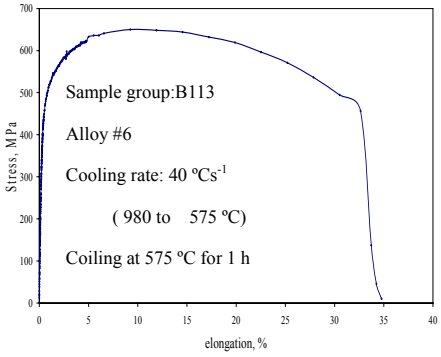

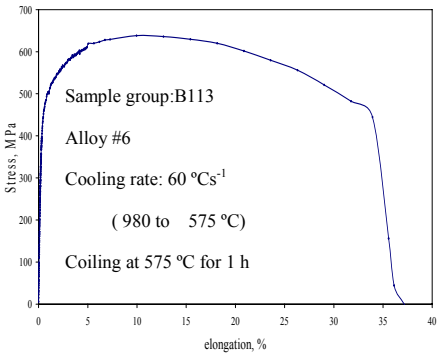

Appendix F
Curves of tensile tests (Instrumented Hounsfield)

Conditions on the Gleeble:

Reheating temperature: 1225 ºC

45% and 33% prior deformation in total and below the T_{nr}, respectively

cooling from 860 down to 575 ºC

Coiling at 575 º for 1 h

Alloy #6

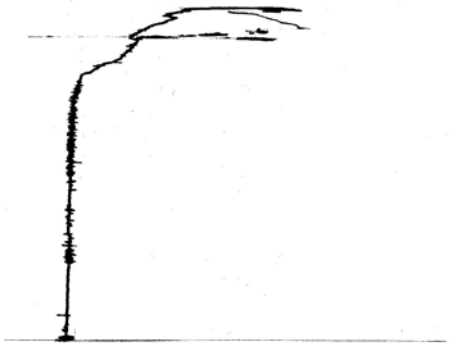

cooling rate : 1 $ºCs^{-1}$

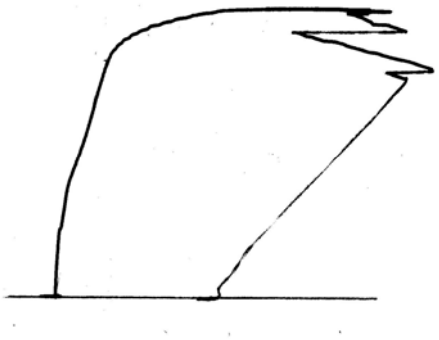

cooling rate : 1 $ºCs^{-1}$

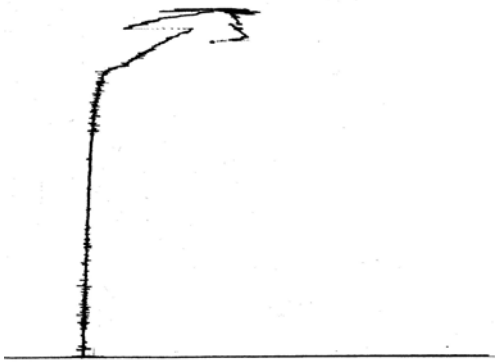

cooling rate : 5 $ºCs^{-1}$

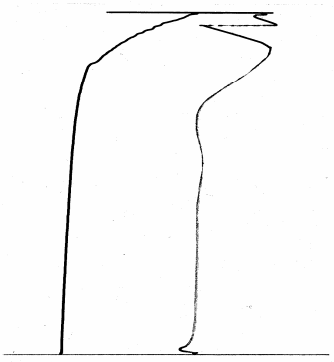

cooling rate : 5 $ºCs^{-1}$

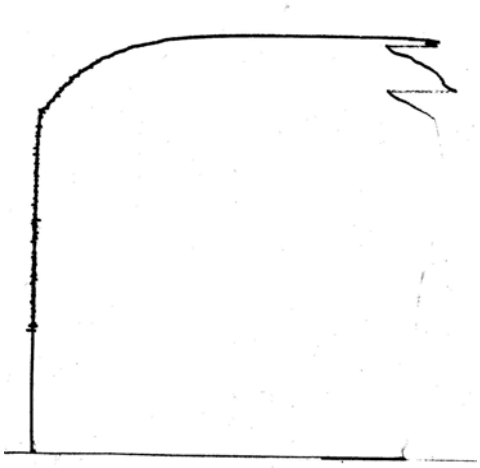

cooling rate : 10 ºCs^{-1}

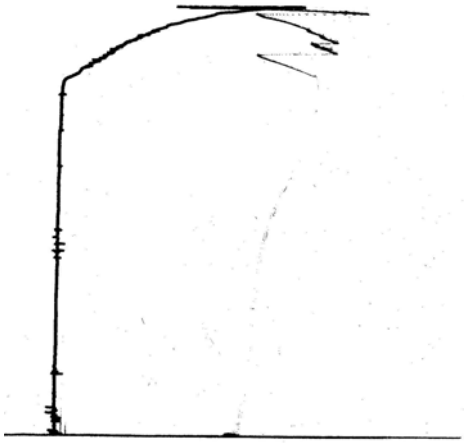

cooling rate : 10 ºCs^{-1}

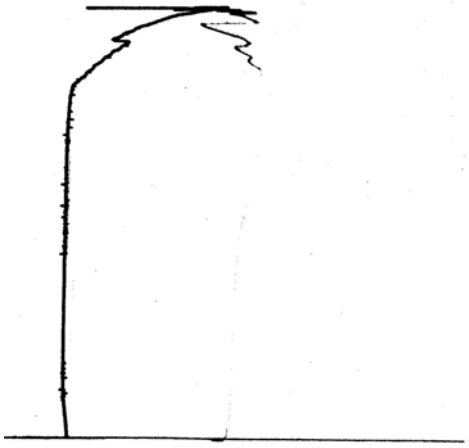

cooling rate : 19 ºCs^{-1}

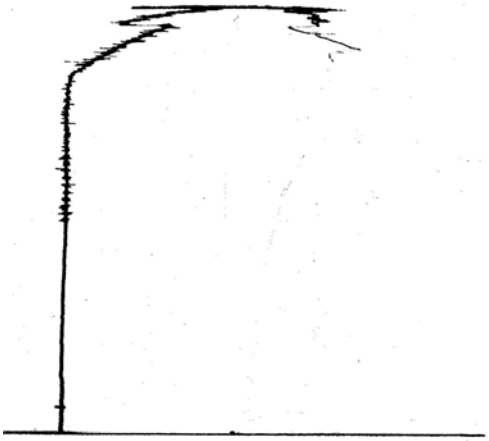

cooling rate : 19 ºCs^{-1}

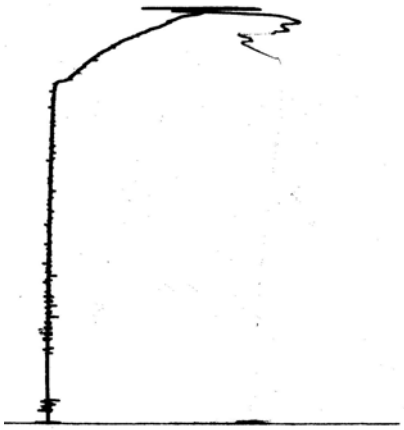

cooling rate : 34 ºCs^{-1}

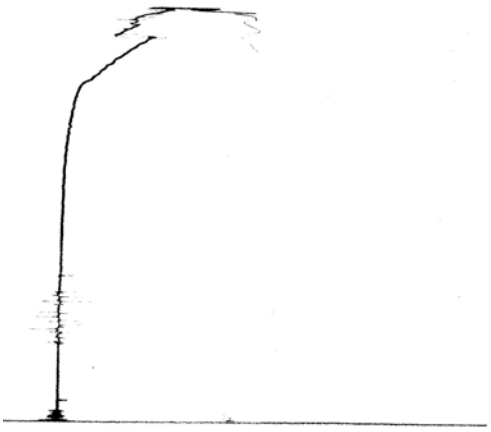

cooling rate : 34 ºCs^{-1}

Appendix G
Curves of tensile tests

Conditions : all experimental alloys #1 to #5

1. Alloy #1:

1.1 Longitudinal specimen:

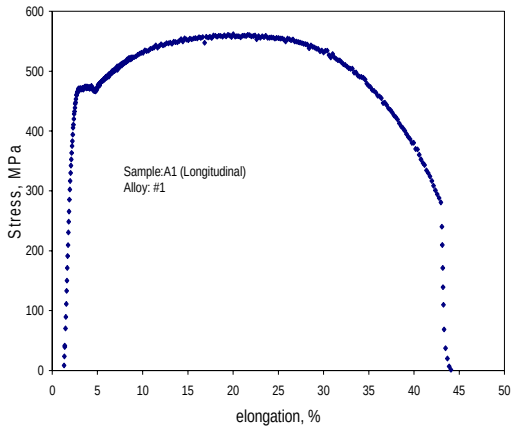

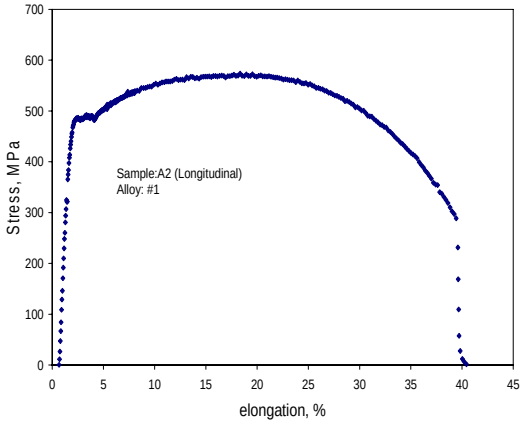

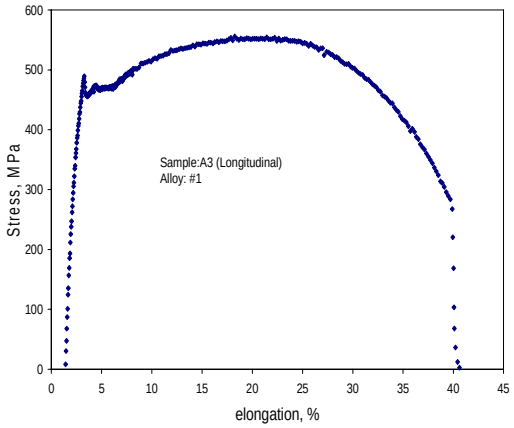

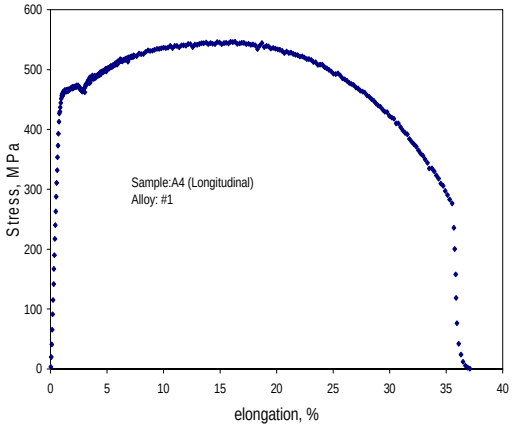

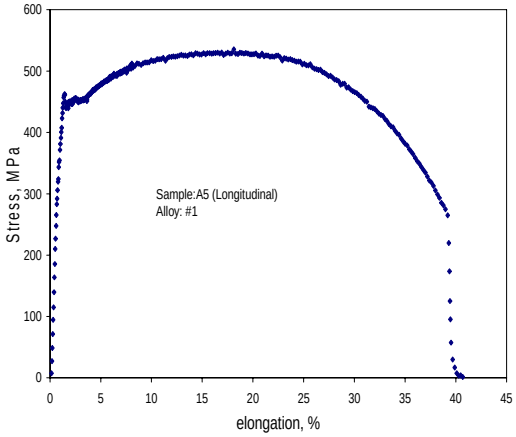

1.2 Transverse specimen:

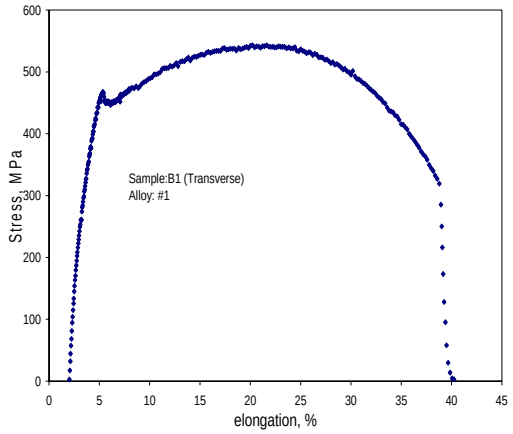

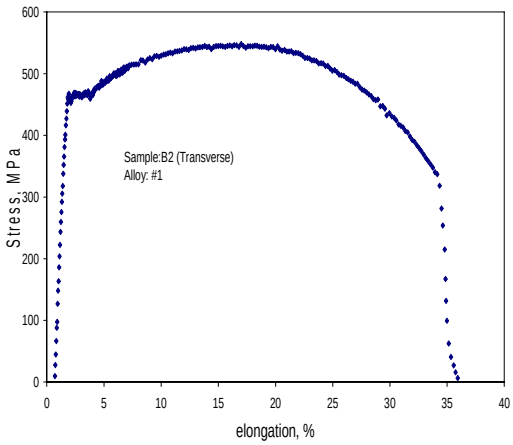

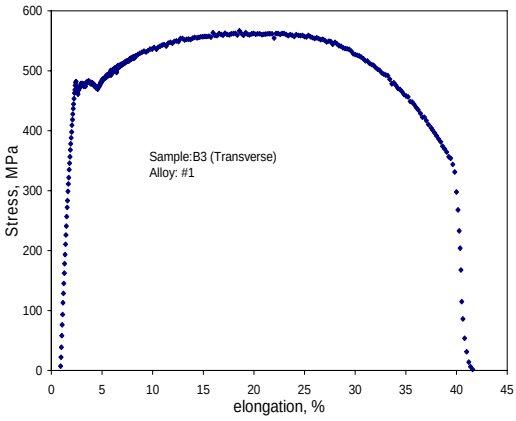

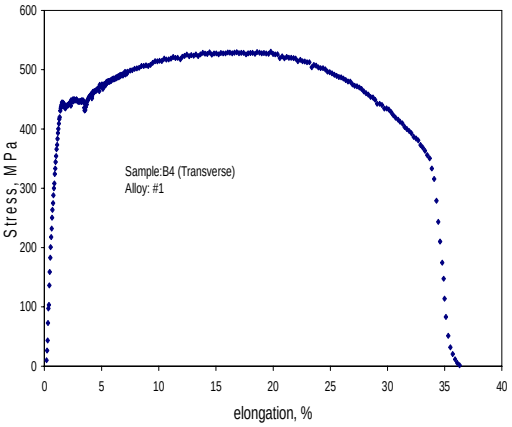

2. Alloy #2:

2.1 Longitudinal specimen

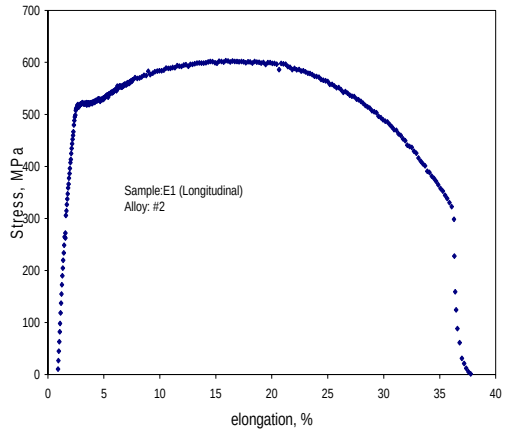

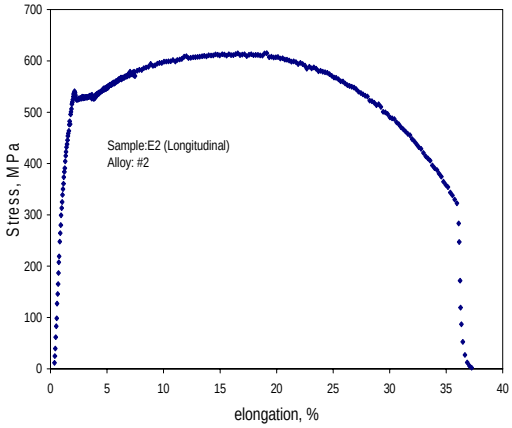

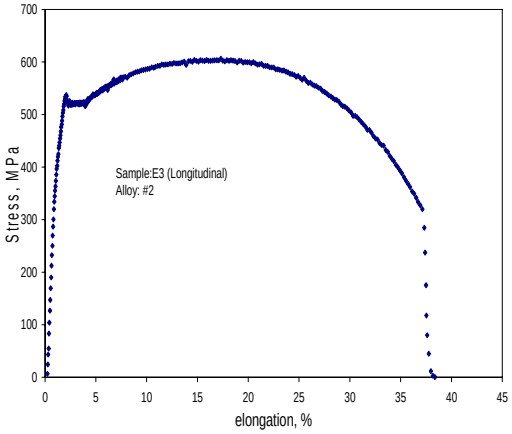

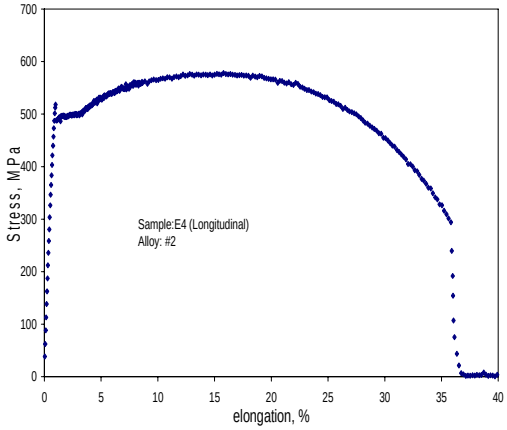

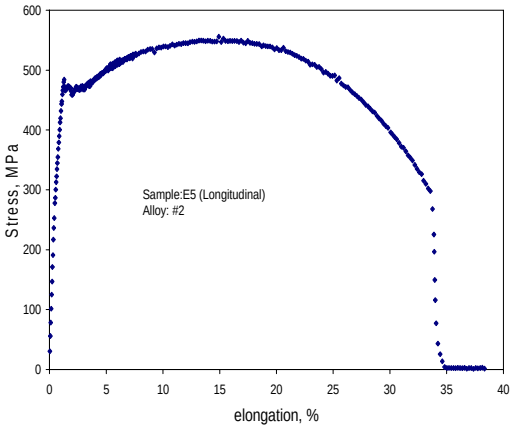

2.2 Transverse specimen:

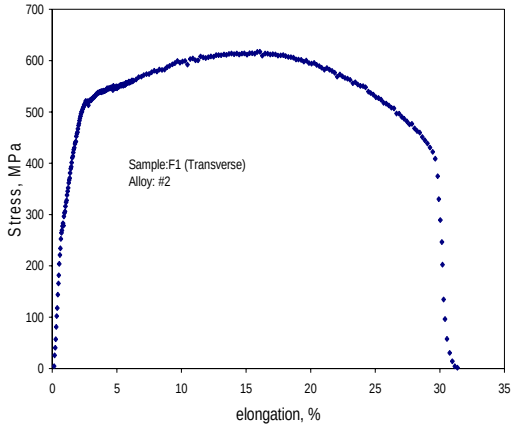

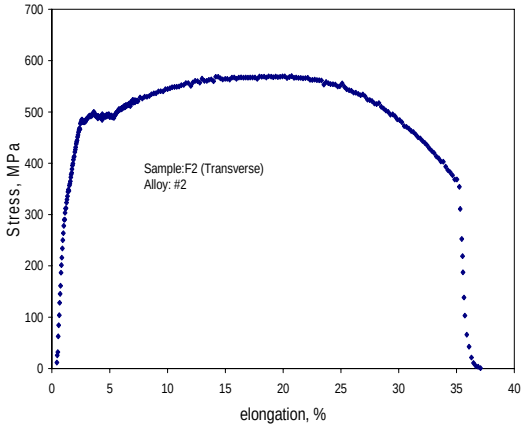

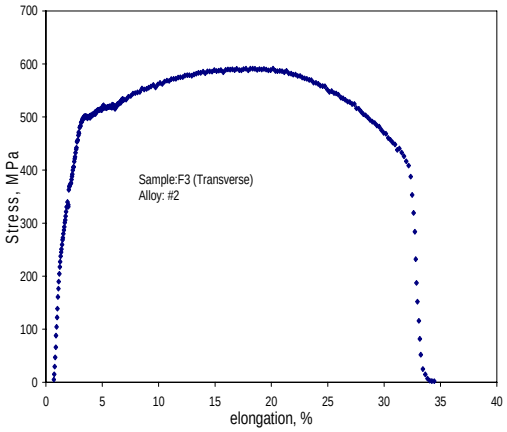

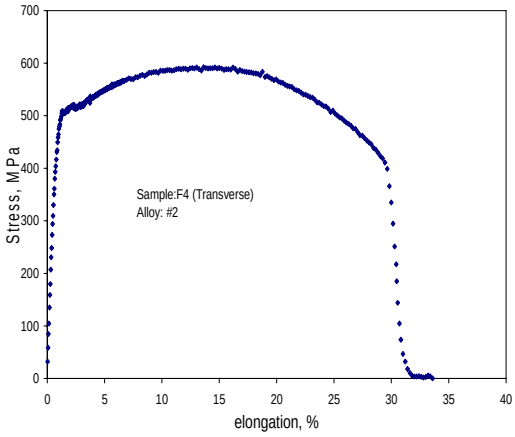

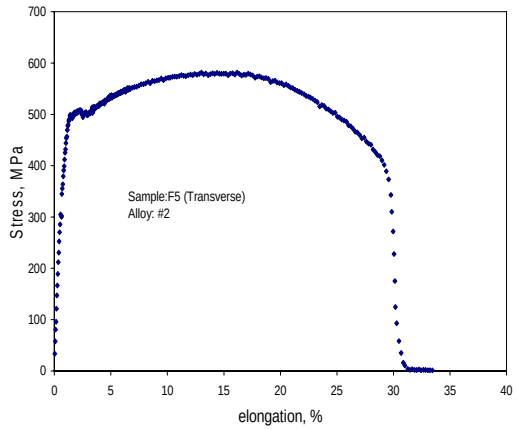

3. Alloy #3:

3.1 Longitudinal specimen:

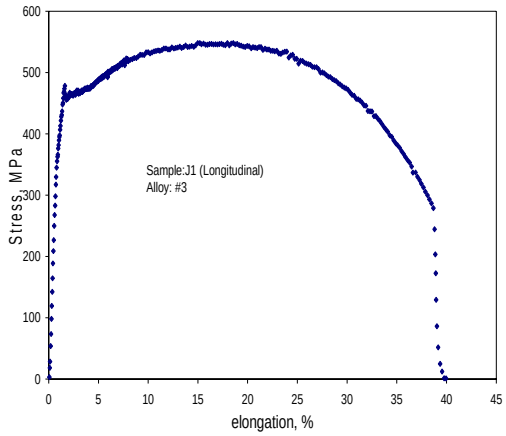

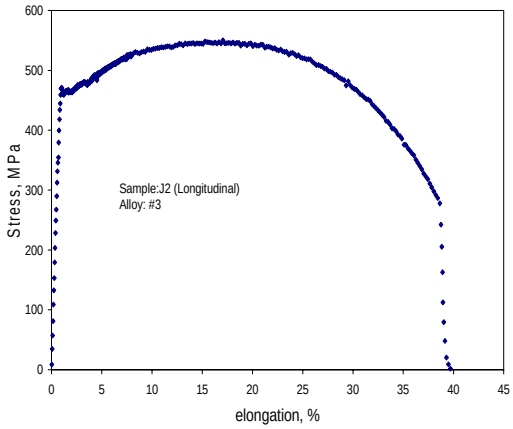

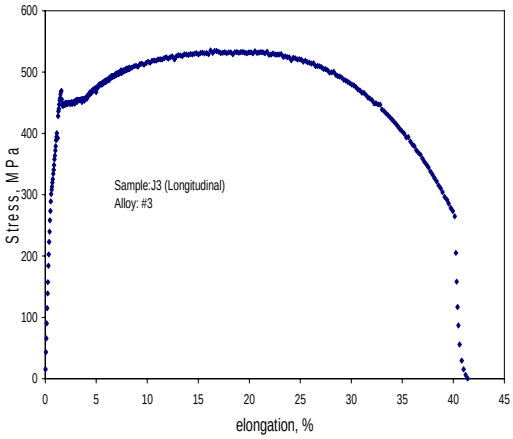

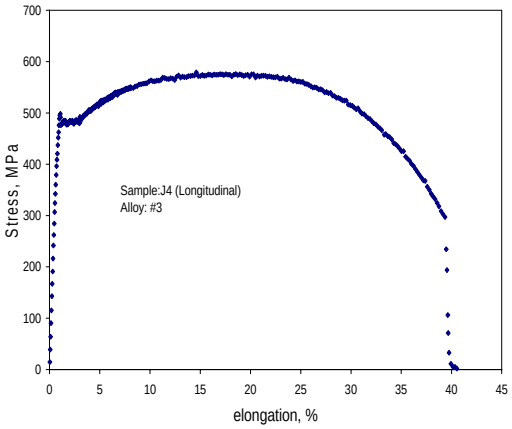

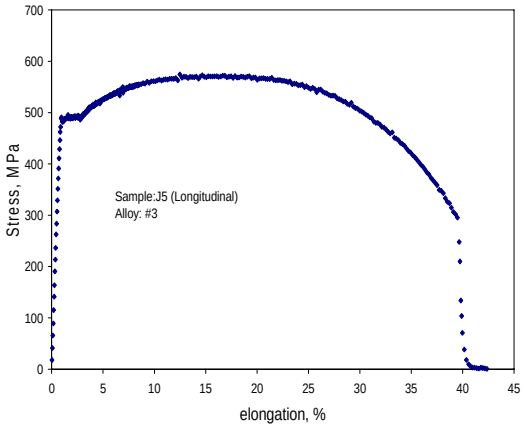

3.2 Transverse specimen:

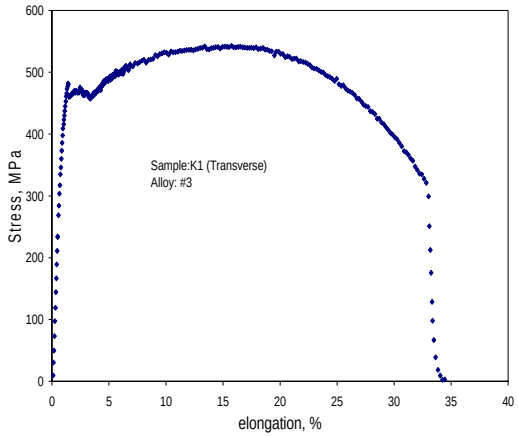

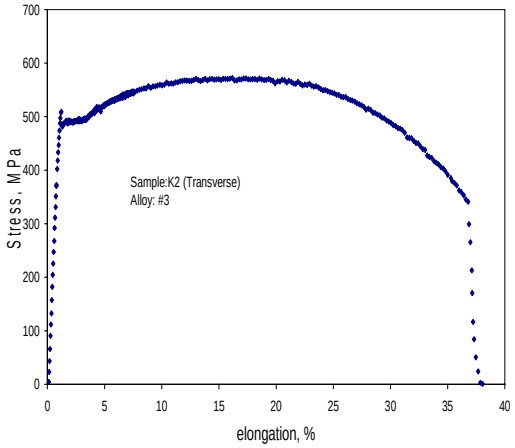

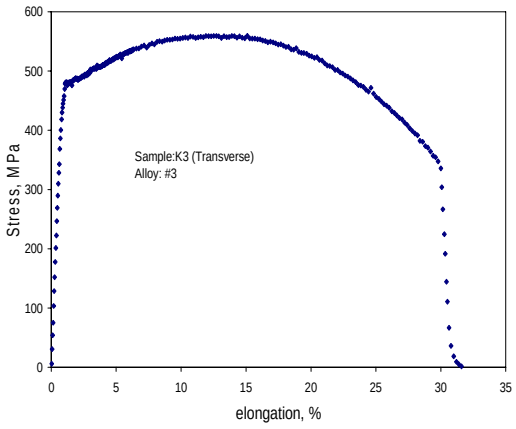

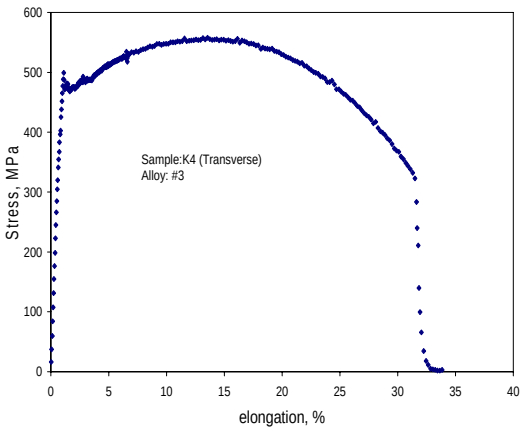

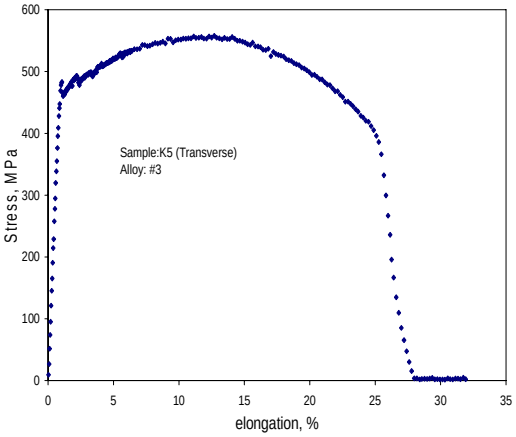

4. Alloy #4

4.1 Longitudinal specimen:

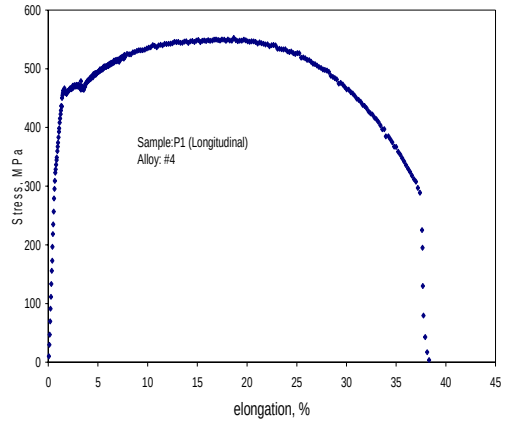

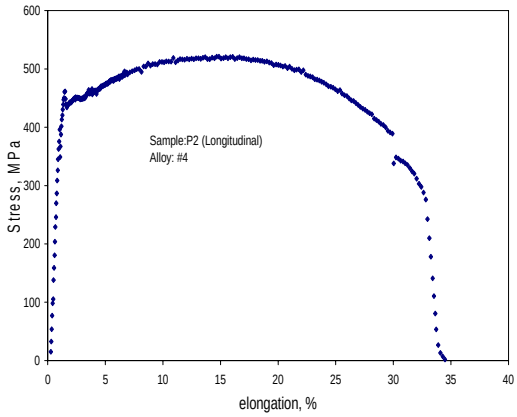

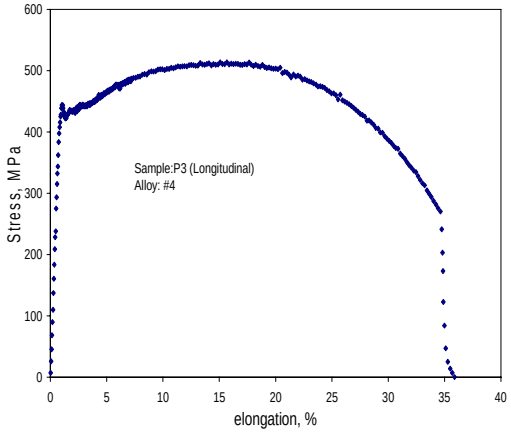

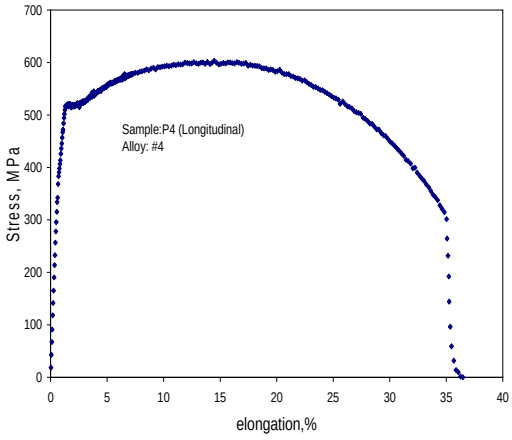

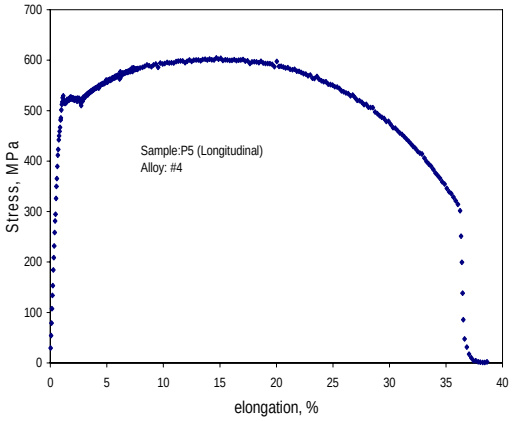

4.2 Transverse specimen:

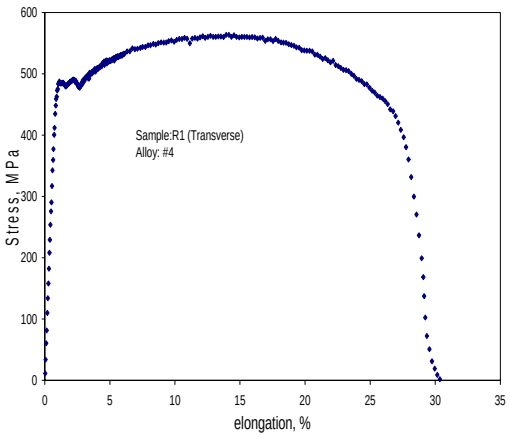

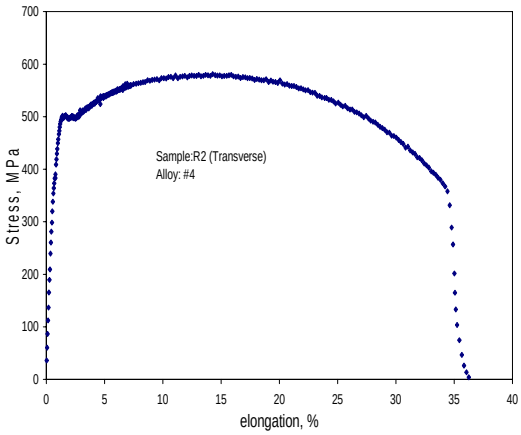

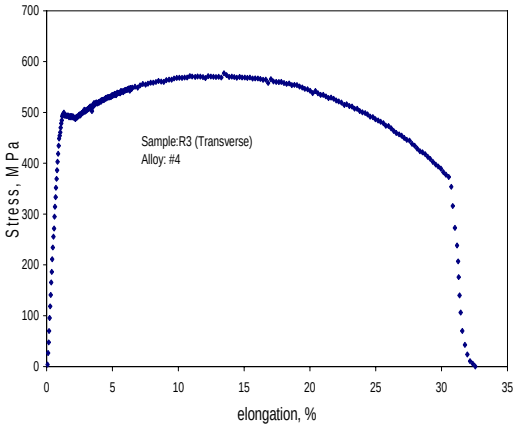

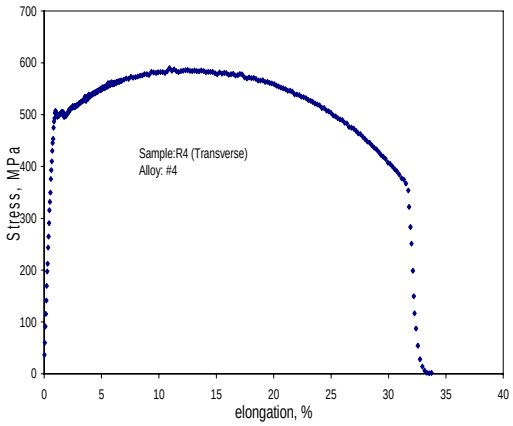

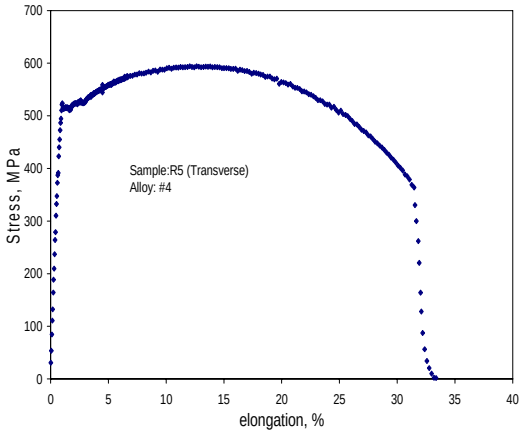

5. Alloy #5

5.1 Longitudinal specimen:

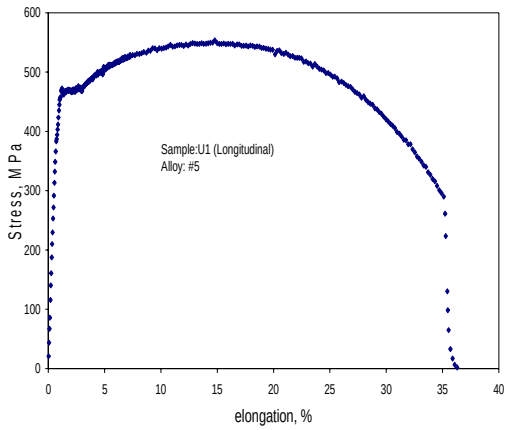

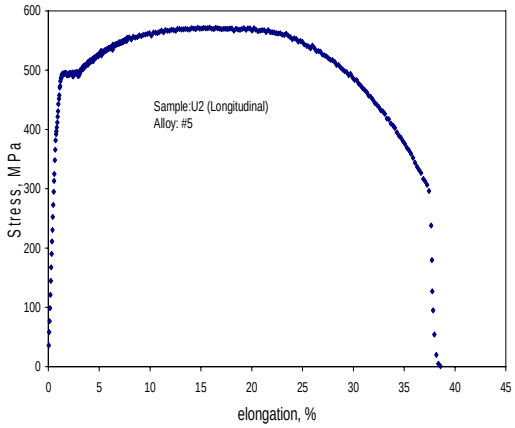

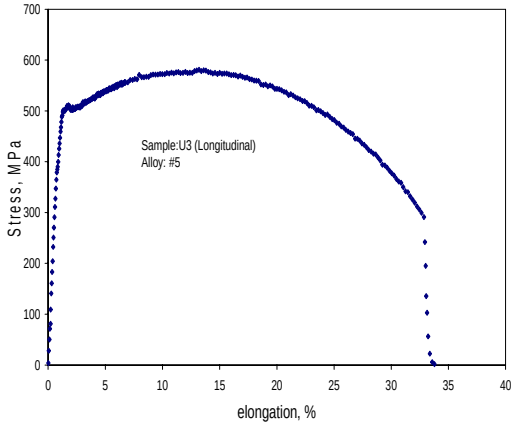

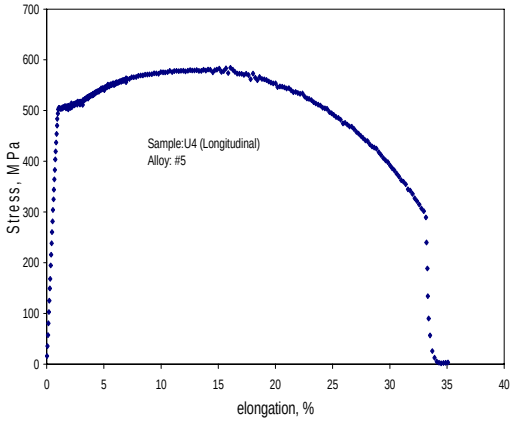

5.2 Transverse specimen:

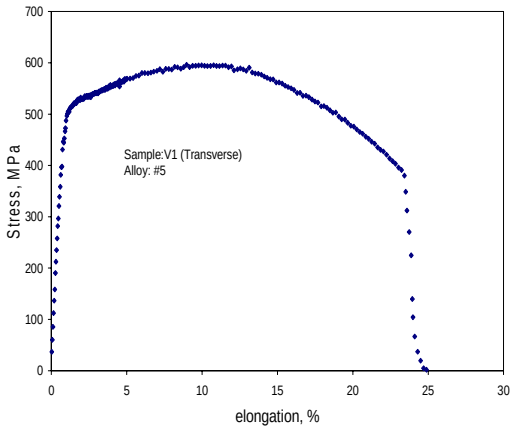

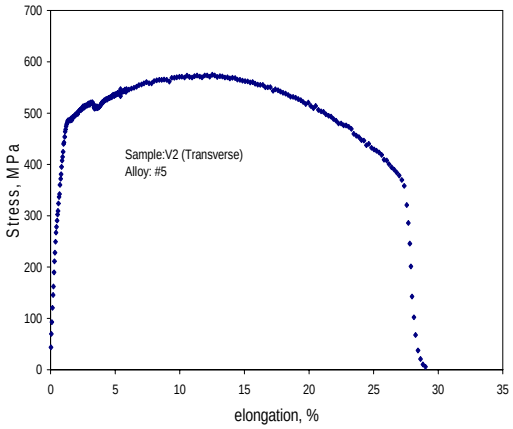

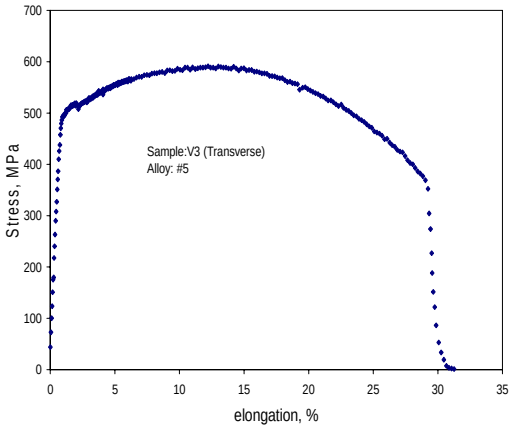

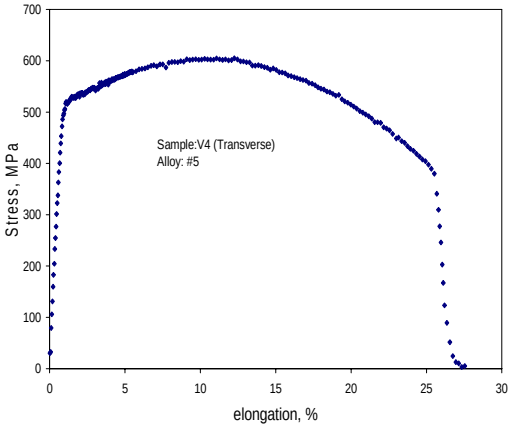

Appendix H

Parameters of the laboratory hot rolling process for tests samples on Gleeble:

Tables H-1 to H-4 show the hot rolling details for the test samples of type A and B for the YS/UTS ratio versus cooling rates, coiling temperatures and deformation values after compression deformation. These coiling temperatures were inadvertently too high. These particular plates were, therefore, not used for the YS/UTS tests directly, but were later used for studying the effect of cooling rate, coiling temperature and prior deformation on the YS/UTS ratio on the Gleeble (see section 6.9.2).

Table H-1 The laboratory hot rolling parameters for sample #A124 of the Mo-free reference alloy #6

Pass No		**R1**	**R2**	**reheating**	**R3**	**R4**	**R5**	**F1**	**reheating**	**F2**	**reheating**	**F3**
Tempera-ture (ºC)	**in**	1132	1075	1225 5 min	1157	1112	1058	910	930 5 min	870	930 5 min	880
	out											860
t_{ip} (s)		26	--		18	32	58	--		--		--
Gauge (mm)	**in**	45	37		28	20	13.6	10.3		8.3		6.9
	out	37	28		20	13.6	10.3	8.3		6.9		6
Pass ε		0.196	0.28		0.34	0.38	0.28	0.22		0.18		0.14
Total ε		1.48						0.54				
Reduction(%)		77						42				
$\dot{\varepsilon}$ (s^{-1})		1.82	2.43		3.15	3.92	4.00	4.07		4.00		3.89

Reheating: 1220 ºC for 60 min

Fast cooling: 35 ºCs^{-1} (860 down to 650 ºC)

Coiling: 650 ºC for 24 hrs

Table H-2 The laboratory hot rolling parameters for sample #AF3F of alloy #3 (with 0.09% Mo)

Pass No		R1	R2	reheating	R3	R4	R5	F1	reheating	F2	reheating	F3
Tempera-ture (ºC)	in	1170	1060	1225 5 min	1120	1070	1000	910	930 5 min	890	930 5 min	880
	out											--
t_{ip} (s)												
Gauge (mm)	in	43	37		28	20	13.6	10.3		8.3		6.9
	out	37	28		20	13.6	10.3	8.3		6.9		6
Pass ε		0.15	0.28		0.34	0.38	0.28	0.22		0.18		0.14
Total ε		1.43						0.54				
Reduction(%)		76						42				
$\dot{\varepsilon}$ (s^{-1})		1.67	2.43		3.15	3.92	4.00	4.07		4.00		3.89

Reheating: 1225 ºC for 60 min

water quench down to room temperature

Table H-3 The laboratory hot rolling parameters for sample #A113 and B113 of the Mo-free alloy #6

Pass No		R1	R2	R3	Reheat-ing	R4	R5	R6	Reheat-ing	F2	F2	Rehea t-ing	F3
Tempera-ture (ºC)	in	1141	1096	1013	1200 5 min	1119	1049	1002	925 5 min	880	840	925 5 min	870
	out												840
t_{ip} (s)		10	20	--		15	15	--		10	--		--
Gauge (mm)	in	45	37	30		25	20	15		10	8.3		6.9
	out	37	30	25		20	15	10		8.3	6.9		6
Pass ε		0.196	0.21	0.182		0.223	0.288	0.405		0.186	0.18		0.14
Total ε		1.50							0.51				
Reduction(%)		78							40				
$\dot{\varepsilon}$ (s^{-1})		1.82	2.08	2.09		2.56	3.31	4.66		3.05	4.00		3.89

Reheating: 1178 ºC for 60 min

Fast cooling: 29 ºCs^{-1} (840 down to 640 ºC)

Coiling: 640 ºC for 24 hrs

Table H-4 The laboratory hot rolling parameters for sample #TEN06 of the Mo-free alloy #6

Pass No		**R1**	**R2**	**R3**	**Reheat-ing**	**R4**	**R5**	**R6**	**Reheat-ing**	**F2**	**F2**	**Reheat-ing**	**F3**
Tempera-ture (ºC)	**in**	1135	1026	968	1200 5 min	1040	980	940	1200 30 s	870	820	1200 60 s	840
	out												820
t_{ip} (s)		15	18	--		15	13	--		14	--		--
Gauge (mm)	**in**	45	37	30		25	20	15		10	8.3		6.9
	out	37	30	25		20	15	10		8.3	6.9		6
Pass ε		0.196	0.21	0.182		0.223	0.288	0.405		0.186	0.18		0.14
Total ε		1.50							0.51				
Reduction(%)		78							40				
$\dot{\varepsilon}$ (s^{-1})		1.82	2.08	2.09		2.56	3.31	4.66		3.05	4.00		3.89

Reheating: 1178 ºC for 60 min

Fast cooling: 33 ºCs^{-1} (820 down to 620 ºC)

Coiling: 620 ºC for 24 hrs